UC Riverside

UC Riverside Electronic Theses and Dissertations

Title

Enhanced Cooling for High Heat Flux Applications Using Droplet Impact and Optical Cavitation

Permalink

Author

Banks, Darren

Publication Date

2015

Peer reviewed|Thesis/dissertation

UNIVERSITY OF CALIFORNIA
RIVERSIDE

Enhanced Cooling for High Heat Flux Applications Using Droplet Impact and Optical Cavitation

A Dissertation submitted in partial satisfaction
of the requirements for the degree of

Doctor of Philosophy

in

Mechanical Engineering

by

Darren Keith Banks

August 2015

Dissertation Committee:
      Dr. Guillermo Aguilar, Chairperson
      Dr. Lorenzo Mangolini
      Dr. Marko Princevac

The Dissertation of Darren Keith Banks is approved:

_____

_____

_____
Committee Chairperson

University of California, Riverside

Acknowledgements

1. Vu, H., D. Banks, and G. Aguilar, Examining Viscosity and Surface Wettability in Lamella Lift Dynamics and Droplet Splashing. Atomization and Sprays, 2011. 21(4).

2. Banks, D., et al., Effects of Liquid and Surface Characteristics on Oscillation Behavior of Droplets Upon Impact. Atomization and Sprays, 2014. 24(10): p. 895-913.

3. Banks, D., et al., Effects of drop and film viscosity on drop impacts onto liquid films. Atomization and Sprays, 2013. 23(6): p. 525-540.

4. Banks, D., et al. Optical Transmission Measurement of Thermocavitation. in Conference on Liquid Atomization and Spray Systems. 2013. Pittsburgh, PA.

5. Banks, D., et al. Frequency and Bubble Size in CW Optical Cavitation. in ILASS Americas 27th Annual Conference. 2015. Rayleigh, NC.

6. Padilla-Martinez, J.P., et al., Towards the enhancement of transdermal drug delivery through thermocavitation. Photonics and Lasers in Medicine, 2012. 1(3): p. 183-193.

Dedication

I dedicate this dissertation to my family, especially my wife and my parents, without whose love and support I would not completed this.

In addition, the mentorship, guidance, and assistance of a few people at UCR have been invaluable during my graduate career. The many discussions I had with Dr. Campbell Dinsmore during the last couple years of my Ph.D. shaped my growth and pursuit of the degree for the better. I would like to credit the UCLEADS program at UCR, and the wonderful lady at the helm of it, Maria Franco-Aguilar, for developing an outstanding program which steered me into graduate school.

ABSTRACT OF THE DISSERTATION

Enhanced Cooling for High Heat Flux Applications Using Droplet Impact and Optical Cavitation

by

Darren Keith Banks

Doctor of Philosophy, Graduate Program in Mechanical Engineering
University of California, Riverside, August 2015
Dr. Guillermo Aguilar, Chairperson

Demand for increased heat fluxes in high-power thermal management applications drives research into improved cooling techniques. Liquid and two-phase cooling methods provide cost-effective and potent means of heat extraction. Sprays of atomized liquid, in particular, deliver very high heat flux due to large cooling surface area, rapid evaporation, and continuous delivery of fresh cold liquid to the target. Sprays are difficult to model and study due to the inherent complexity of highly dynamic two-phase flows and the wide range of factors which influence the cooling effects. A detailed study of the impact of liquid droplets, alone and in sequential trains, onto a variety of impact surfaces is presented, with examination of the fluid properties, impact characteristics, and environmental conditions that govern the dynamics of the liquid after impact and the overall cooling effect. The interaction of successive droplets in a train is found to dramatically influence heat transfer, depending on the frequency of impacts.

As a spray is used to cool a target surface, a liquid film will often develop. A thermal boundary layer develops within the liquid film, reducing the effective cooling rate by isolating hot liquid near the surface. Agitation will minimize the thermal boundary layer, restoring the heat flux. Optical cavitation presents a unique method of non-intrusively breaking down the thermal boundary layer. By inducing cavitation within the layer, near the surface, the growth and col-

lapse of the bubble will draw cool liquid from outside the boundary layer and deposit it near the surface. To achieve this effect, the optical and fluid conditions that contribute to cavitation are explored, in particular looking at the growth and collapse dynamics and the sequences of bubbles resulting from irradiation by a continuous wave laser. Novel experimental observations of asymmetric collapse phenomena are reported, and among the first measurements of cavitation frequency for continuous wave laser irradiation are reported.

Table of Contents

List of Figures

List of Tables

Nomenclature

Symbol	Definition	Typical Units
c	Specific heat	kJ/kg K
d	Droplet or bubble diameter	mm
f	Frequency	Hz
h	Pool depth	mm
k	Thermal conductivity	W/m K
q″	Heat flux	W/m^2
t	Time	s
T	Temperature	K
U	Velocity	m/s
α	Absorptivity	cm^{-1}
γ	Standoff distance	-
θ	Dimensionless temperature	-
λ	Wavelength	nm
μ	Dynamic viscosity	N s/m^2
ν	Kinematic viscosity	m^2/s
ρ	Density	kg/m^3
σ	Surface tension	N/m

	Dimensionless Groups	
Oh	Ohnesorge number	$\dfrac{\mu}{\sqrt{\rho U d}}$
Re	Reynolds number	$\dfrac{Ud}{\nu}$
St	Strouhal number	$\dfrac{fd}{U}$
We	Weber number	$\dfrac{\rho U^2 d}{\sigma}$

1. INTRODUCTION

1.1. Prelude: Two-Phase Cooling

Many of the challenges facing modern technology are in the field of thermal management. The combination of high power and miniaturization necessitates cooling at a rate that traditional methods cannot provide. For example, Moore's Law dictates that the number of transistors in a single computer processor doubles every two years, a statement which has empirically proven true since 1959 (Mack 2011). Transistor counts on present-day consumer CPUs number in the billions, while the size of the CPU has not grown significantly due to limitations in silicon wafer fabrication (Ferain, Colinge et al. 2011). The heat dissipated by these processors is tremendous. Heat sinks for the CPUs have grown from passive metal fin sinks to large fan-cooled fin-and-heat-pipe arrays to closed loop liquid cooling systems (Faulkner, Khotan et al. 2003). The next step in thermal management is two-phase cooling. By exploiting the latent heat capacity and evaporative processes, the effective heat flux can be dramatically enhanced over single-phase cooling (Kim 2007). To reap the benefits of two phase cooling, a thorough exploration of the dynamics will lead to optimal application of these flows.

Two phase flows, however, introduce analytical and experimental complexity beyond single phase cooling. The transitions between the phases and the interactions between gas and liquid are nontrivial, and vary widely from application to application and from fluid to fluid. The dynamics are often characterized by small time and length scales, challenging traditional techniques of experimental measurements. Numerical methods have yet to be developed that can accurately follow the rapidly moving boundaries between phases at a reasonable computational cost. New methods to characterize the dynamics of two phase cooling techniques are needed.

1.2. Motivation

High heat flux thermal management is a growing necessity in the modern era of electronics and optics. The cooling requirements for many applications are ever-increasing as a consequence of growing capabilities and demands for more power in smaller volumes. Orthodox, generally single-phase, cooling mechanisms, notably air-cooled heat sinks and liquid immersion cooling, cannot deliver improved heat flux due to physical limitations on their designs. In general, increasing the size or fluid flow of these types of heat sinks will increase the heat removal rate, but with diminishing returns. Past a certain point, the limiting factor in the cooling processes becomes the heat flux at the target surface – regardless of the sink's dissipation capacity, there is no corresponding increase in the ability to move that heat from the chip into the sink. Two-phase cooling techniques overcome this bottleneck by exploiting phase change processes and latent heat capacity to improve cooling at the target surface.

Spray cooling uses the combination of evaporation, forced convection, and large surface area to provide heat fluxes in excess of 100 W/cm^2 (Kim 2007). Atomizing a stream of liquid into thousands of micro-scale droplets provides a liquid surface area unmatched by any other fluid-based cooling method. The exposed area magnifies heat transfer to the liquid. Evaporation occurs rapidly, absorbing heat from the target. Subsequently, incoming droplets in the spray displace the heated liquid and vapor. Sprays provide a powerful cooling effect using a minimal volume of liquid.

Many applications challenge current thermal management techniques with restricted space and the lack of power to drive flows at very small scales. Control and enhancement of fluid flow through microfluidic channels has been the subject of many studies (Ex., (Zhou, Hom et al. 2004, Hellman, Rau et al. 2007, Wu, Gao et al. 2008, Zhang, Jian et al. 2011, Jian, Zhang et al. 2012,

Nagel, Brun et al. 2014)). Optical cavitation presents a non-intrusive method to induce high-velocity flow in small spaces. By focusing a laser into a small volume of liquid, an explosive bubble forms and displaces the surrounding liquid quite rapidly. Optical cavitation has already been demonstrated as a periodic pump and a switch in microfluidic channels (Jian, Zhang et al. 2012). The potency of optical cavitation for localized fluid control has only begun to be explored. In a thermal management context, the cavitation bubble's motion can induce strong convective heat transfer in the area around the bubble. With this convection and mixing, cavitation can be a novel method for enhancing heat transfer near liquid-solid boundaries.

1.3. Interrupting the Thermal Boundary Layer

The theme of this study is enhancement of local heat flux through manipulation of the thermal boundary layer. Cavitation and droplet impact each can disrupt the boundary layer, delivering cool fluid to a heated surface that would otherwise be relatively insulated by a growing zone of warm liquid. The goals of this study are intended to optimize the methods and dynamics of each phenomenon for the purpose of maximizing heat transfer.

In nearly every liquid-based cooling mechanism, the intent is to induce a heat flux at a liquid-to-solid boundary. A heat flux will only occur when the solid and the liquid are at different temperatures. For the sake of discussion, we will assume that the solid boundary is at a higher temperature than the bulk liquid, leading to a cooling effect on the solid boundary. The magnitude of this heat flux depends on the magnitude of the temperature difference between the solid and liquid, the thermal diffusivity of the liquid and solid, and the convection coefficient of the liquid. The thermal diffusivity of the liquid and solid involved generally are constant or nearly so, as long as the properties on both sides of any phase change are accounted for. Any increase in heat transfer, therefore, must result from a change in the temperature difference

(supplying cold liquid directly to the surface, for example) or the convection coefficient (altering the flow rate of fluid across the surface).

In most cases, convection and cooling liquid supply are the same mechanism; convection occurs as an influx of cold liquid flows across a surface. However, for purposes of this study, each can be separated from the other by the geometry of the flows. Convection in cavitation and droplet impingement occurs radially outward from the point of droplet impact or bubble nucleation, and it can happen with cool liquid or the heated liquid present near the solid boundary – in other words, in the presence or the absence of cooling fluid supply. In both cavitation and droplet impingement, the fluid supply cooling mechanism occurs normal to the radial convective flows. In droplet impingement, the fluid supply is the impact of a cold liquid droplet, which can deposit directly on the substrate and causes cooling independently of any radial flow via conduction. The mechanism of cold liquid supply in cavitation is less obvious but occurs along the axis normal to the solid surface as well. Cavitation bubbles formed near a solid boundary collapse asymmetrically. The pole of the bubble opposite the boundary collapses more quickly than the rest of the bubble, forming a jet that pulls liquid toward the solid surface. Due to the nature of the thermal boundary layer, this liquid will be cooler (e.g., closer to the bulk liquid temperature) than the liquid near the boundary. When this jet reaches the substrate, where the bubble has displaced the liquid which has been heated by the surface, it provides a deposition cooling effect.

Cavitation and droplet impingement both influence the convection coefficient by producing a strong flow of liquid across the solid boundary. While an exact solution for the convection coefficient frequently relies on empirical measurements, a scaling argument can be used to show that the coefficient tends to grow as flow velocity increases.

4
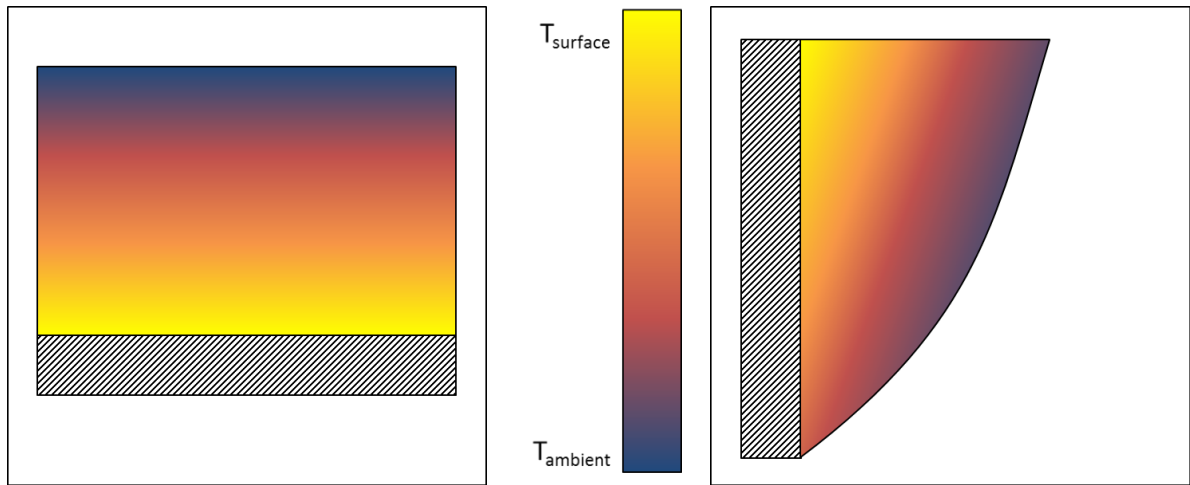
For a horizontal solid plane.

For a vertical solid plane.

Figure 1.1. Temperature distributions of an otherwise unheated liquid near a heated solid plane, based on boundary layer theory and natural convection (SRC).
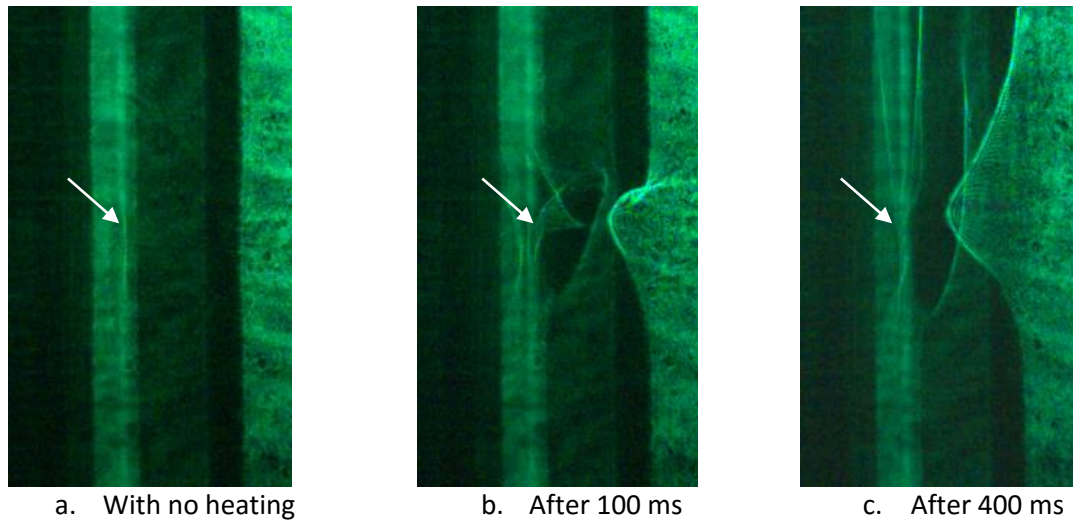
a. With no heating

b. After 100 ms

c. After 400 ms

Figure 1.2. Phase contrast images showing the distribution of liquid heated relative to the bulk temperature during laser irradiation at the indicated point.

In this study, cavitation is usually induced near a vertical wall, similar to that depicted in Figure 1.1.b. As such, a natural convection thermal boundary layer is anticipated, starting from the point of laser heating. Figure 1.2 shows the growth of the thermal boundary layer – a region of heated liquid – near a glass wall during laser irradiation, using a phase contrast technique through which relative temperature differences are made visible as the refractive index of the working liquid changes.

Cavitation bubbles grow and collapse with velocities up to 50 m/s, displacing the surrounding liquid radially outward from the point of nucleation (Kröninger, Köhler et al. 2009). In the area surrounding the bubble nucleation site, the forced flow will create a strong convection coefficient. There are many applications where such flow is useful, but traditional methods of producing those flow velocities are impossible - for example, in micro-scale devices, a traditional pump design to drive flow is impractical, but a cavitation bubble can be easily produced as long as optical access is available.

Droplet impacts onto solid surfaces and sufficiently thin liquid films spread radially from the point of impact outward, creating convection (Figure 1.3). The radial spreading is initially two to five times the axial impact velocity (Liu, Vu et al. 2010). In a thicker film, however, the impact motion is partially or completely used up producing a cavity within the pool, and the droplet fluid contact with the substrate is often minimized (Figure 1.4).

A further consideration in droplet convection is the frequency of droplet impacts. At some droplet train frequencies, the post-impact jet impedes the impact of the successive droplet, preventing the droplet from reaching the substrate. At other frequencies, the prior droplet will open the cavity for the next droplet, reducing the effect of the liquid film on the substrate and maximizing convection and deposition.
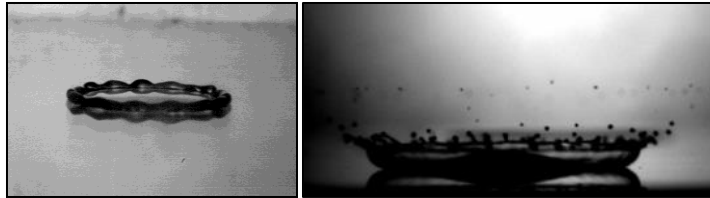
Figure 1.3. Typical droplet dynamics observed during single droplet impact onto a solid surface.
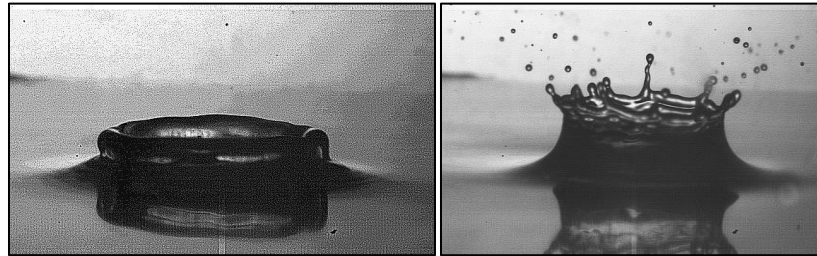
Figure 1.4. Typical cavity dynamics observed during single droplet impact onto a liquid pool.

1.4. Hypothesis

The fundamental cooling event in spray cooling is the impact of a single droplet upon the target. The droplet impact brings in cool liquid and drives heated liquid away from the impact point. In this way, the thermal boundary layer is periodically (occurring with each successive droplet impact) interrupted by successive droplet impacts, as cool fluid displaces previously deposited hot fluid. To optimize spray cooling, the droplet impact dynamics must be effective at penetrating and disrupting the boundary layer. By controlling the frequency and velocity of droplet impacts, the effective heat flux can be increased.

When a cavitation bubble collapses near a solid boundary, the bubble collapses asymmetrically. The pole of the bubble farthest from the boundary collapses more rapidly than the rest of the bubble, forming a jet that is driven toward the boundary. This jet is comprised of liquid from away from the boundary. If the bubble occurs near a heated solid boundary, cool liquid will be drawn inward, enhancing the heat flux near the bubble site.

1.4.1. Aim: Droplet Impact Studies for Spray Cooling

An atomized liquid spray is one of the most potent cooling techniques available. The combination of evaporative and convective heat transfer, a steady influx of cooling liquid, and an unmatched surface area created by thousands of individual liquid droplets can lead to very high heat fluxes. However, sprays are among the most chaotic and complex challenges in the field of fluid mechanics. Experimental studies and computational modeling both struggle to address the two-phase dynamics and the multitude of impact conditions.

This study seeks to improve understanding of spray cooling by investigating droplet impact dynamics. Starting with single droplet impacts onto heated dry and liquid surfaces, the splashing and cooling dynamics will be investigated in detail. Then the interactions between impacts of a train of droplets are investigated, with focus on the frequency of the train and the resultant cavity behavior. The experimental parameters include the droplet diameter, impact velocity, droplet and pool viscosity, and pool thickness. The overall goal is to maximize the heat flux produced by the droplet impacts.

To accomplish this overarching goal, four specific objectives are accomplished:

1. To explore solid surface wettability and its influence on the disposition of liquid following the impact of a droplet.

2. To quantify the effects of droplet and film properties on the fluid dynamics and heat transfer accompanying single droplet impact onto heated solid and liquid surfaces.

3. To study the dynamics of droplet train impacts for a range of train frequencies.

4. To optimize the heat transfer of droplet train impacts based on the dynamics observed.

Explanation of Droplet Impact Objectives

First, to explore solid surface wettability and its influence on the disposition of liquid following the impact of a droplet. One of the fundamentals of all forms of heat transfer is that the surface area is a governing factor in any heat exchange. In the cooling of a surface by an atomized spray, the droplets strike the surface and then spread and often splash, distributing liquid away from the impact point. The factors controlling the dynamics of the droplet after splashing are numerous and entwined together. For this study, the factors explored are the wettability of the solid surface, the viscosity of the droplet liquid, and the impact velocity. Each is found to play a role in the motion and breakup of liquid after it impacts the surface.

Second, to evaluate the effects of droplet and film properties on the dynamics of cavity formation within the liquid film, splashing, and heat transfer to the pool substrate. The single droplet impact is the fundamental element of spray cooling. A thorough understanding of how the droplet fluid becomes distributed on the target substrate and within the liquid film is essential to any thermal effects. Splashing can disperse the droplet liquid across a wide area, leading to a distributed cooling effect; the liquid breakup and ejection of secondary droplets is a fascinating case study on linear instability, capillary effects, and liquid-solid interactions. When the droplet strikes a liquid surface, splashing can occur from the point of impact or from the crown produced from the liquid film. Solid surface impacts are influenced by the wetting characteristics of the surface. The formation of the cavity within the liquid film is a consequence of impact, and the depth and collapse shape of that cavity can eject the cooling droplet fluid or deposit it upon the pool substrate. Both the droplet and film properties are found to play a role in splashing and cavity dynamics; by using distinct liquids for each the droplet and film these effects can be identified.

Third, to study the regimes of droplet train impact dynamics - in particular, the cavity and jetting behavior - as it relates to the frequency of the train. Each droplet in the train can influence the impact conditions for the successive one. At very low frequencies, the effects of sequential droplets are minimal, as the film can come to rest between impacts. As the frequency grows, the droplets can interfere with each other through jet deflection. At the highest frequencies, the droplets impinge into the previous droplet's cavity. This produces a quasi-steady state cavity that deposits cool droplet liquid directly on the substrate without interference from the pool liquid.

Fourth, to quantify the influence of droplet train frequency on the heat flux at the point of impact and radially outward. Tuning a spray to average impact frequencies where this steady cavity is achieved will produce optimal heat flux, whereas if the spray impact frequency leads to jet deflection of the droplets, the heat flux will diminish.

1.4.2. Aim: Optical Cavitation for Convective Cooling and Skin Poration

Optical cavitation induced by continuous wave lasers is a novel and growing field. The overall aim of this study is to explore the fluid and thermal dynamics of cavitation and relate those to the optical parameters used to produce them. Optical cavitation uniquely challenges many conventional experimental measurement methods. The combination of very short-lived bubbles, high temperatures, and powerful shockwaves make in-situ direct measurement nearly impossible. The integral part of this study will be the development and implementation of measurement techniques that are novel and adapted to the rigors of cavitation into a flexible and reliable experimental setup.

Continuous wave laser induced cavitation is a relatively recent development, and the field studying it is growing rapidly. As a contribution to this field, this study will lay out analytical

methods and define vocabulary to discuss the phenomena and dynamics of CW cavitation. The benefits of CW-induced cavitation over the more widely studied pulsed laser induced cavitation are twofold. One, CW lasers are far less expensive and complex than pulsed lasers; any application where a CW laser can be used becomes that much more cost effective. Second, the nature of cavitation induced by CW lasers is different from pulsed. With a pulsed laser, a single cavitation event occurs per pulse, limiting the flexibility of the system. In contrast, a CW laser can produce bubbles frequently for the entire irradiation period, and by simply manipulating the focal point of the laser the frequency and bubble size can be tuned for a given situation.

To accomplish the goal of developing a combined approach to characterize cavitation from a thermal, fluid, and acoustic perspective, the following specific objectives are completed:

1. Explore the nuances of optical factors - absorption coefficients, focusing characteristics, laser power, and how they control cavitation dynamics, in particular the bubble size and frequency of bubble nucleation.

2. Characterize the temperature field surrounding the bubble site before, during, and after cavitation occurs.

A third objective is achieved demonstrating an application of optical cavitation that makes use of the findings from the previous two:

3. To evaluate optical cavitation's capability to porate the skin at the micron scale, opening an avenue for needle-less pharmaceutical delivery.

Explanation of Cavitation Objectives

First, the optical factors influencing cavitation will be explored. The effects of altered absorption characteristics, laser focus, and laser power on the resulting bubble size and frequency will be quantified. Intuitively, because CW cavitation is generally a linear absorption process, a

higher absorption coefficient and increased laser intensity should lead to higher frequency bubbles. The bubble size is also affected by the absorption rate and appears inversely proportional to the frequency. However, there are some unusual effects when the laser focus is altered. These effects are not observed during pulsed laser-induced cavitation, and have not been reported in past studies on CW cavitation.

Second, the temperature field surrounding the bubble site before, during, and after cavitation will be measured using a planar laser induced fluorescence (PLIF) technique. Direct measurement of the liquid temperature during cavitation poses a number of challenges. Fluorescence-based measurement is a non-intrusive characterization technique that allows a high-speed video camera to observe the temperature of liquid surrounding the cavitation bubble, instead of relying on physical sensors or relatively slow infrared cameras. PLIF fits well with the optical setup used for cavitation. Literature reports that high-speed PLIF has seen little use, rarely exceeding 1000 fps, and is novel in cavitation-related applications.

Third, a practical application of optical cavitation in the field of biomedicine is explored. The acoustic shockwaves accompanying cavitation are demonstrated to porate the outer layer of skin, known as the stratum corneum, which is the principal barrier to diffusion through the skin. The lower layers of skin – the dermis - are far more permeable to mass transfer. With the stratum corneum punctured, pharmaceutical particles are likely to be able to diffuse into the dermis and subsequently through capillaries into the bloodstream. The control of cavitation developed in accomplishing the previous two objectives is instrumental in enabling this application of optical cavitation phenomena.

References

Faulkner, D., M. Khotan and R. Shekarriz (2003). Practical design of a 1000 W/cm^2 cooling system [high power electronics]. Semiconductor Thermal Measurement and Management Symposium, 2003. Ninteenth Annual IEEE.

Ferain, I., C. A. Colinge and J. P. Colinge (2011). "Multigate transistors as the future of classical metal-oxide-semiconductor field-effect transistors." Nature **479**(7373): 310-316.

Hellman, A. N., K. R. Rau, H. H. Yoon, S. Bae, J. F. Palmer, K. S. Phillips, N. L. Allbritton and V. Venugopalan (2007). "Laser-Induced Mixing in Microfluidic Channels." Analytical Chemistry **79**(12): 4484-4492.

Jian, A. Q., K. Zhang, Y. Wang, S. P. Lau, Y. H. Tsang and X. M. Zhang (2012). "Microfluidic flow direction control using continuous-wave laser." Sensors and Actuators A: Physical **188**(0): 329-334.

Kim, J. (2007). "Spray cooling heat transfer: The state of the art." International Journal of Heat and Fluid Flow **28**(4): 753-767.

Kröninger, D., K. Köhler, T. Kurz and W. Lauterborn (2009). "Particle tracking velocimetry of the flow field around a collapsing cavitation bubble." Experiments in Fluids **48**(3): 395-408.

Liu, J., H. Vu, S. S. Yoon, R. Jepsen and G. Aguilar (2010). "Splashing Phenomena during Liquid Droplet Impact." Atomization and Sprays **20**(4): 297-310.

Mack, C. A. (2011). "Fifty Years of Moore's Law." Semiconductor Manufacturing, IEEE Transactions on **24**(2): 202-207.

Nagel, M., P.-T. Brun and F. Gallaire (2014). "A numerical study of droplet trapping in microfluidic devices." Physics of Fluids (1994-present) **26**(3): -.

Wu, T.-H., L. Gao, Y. Chen, K. Wei and P.-Y. Chiou (2008). "Pulsed laser triggered high speed microfluidic switch." Applied Physics Letters **93**(14): 144102-144102-144103.

Zhang, K., A. Jian, X. Zhang, Y. Wang, Z. Li and H.-y. Tam (2011). "Laser-induced thermal bubbles for microfluidic applications." Lab on a chip **11**(7): 1389-1395.

Zhou, P., J. Hom, G. Upadhya, K. Goodson and M. Munch (2004). Electro-kinetic microchannel cooling system for desktop computers. Semiconductor Thermal Measurement and Management Symposium, 2004. Twentieth Annual IEEE.

2. Droplet Impact Studies for Spray Cooling

2.1. Background

The starting point for spray dynamics studies has been the behavior of a single droplet impacting a surface. Many studies have been performed in this line, starting from Worthington in 1876 with dust-splat shape studies and continued through the present. Rein's 1993 review marks the beginning of modern droplet study (Rein 1993), with the advent of high speed digital video revolutionizing the field thereafter. Yarin discussed droplet impact onto thin films and dry surfaces and recent insight into the transitions between the phenomena categorized by Rein in his 1993 study, as well as several dynamics that had been discovered since (Yarin 2006).Vu, et al. explored single droplet cooling in shallow heated pools and reported secondary cooling effects, delayed slightly after impact of the droplet into the pool, due to droplet fluid deposition (Vu, Aguilar et al. 2009).

Existing studies on droplet trains describe a quasi-steady cavity within a pool that develops-the walls of the cavity are nearly quiescent as incoming droplets prevent the collapse of the cavity (Trujillo and Lewis 2012). The cited study used high frequency trains (1-10 kHz) of micron scale droplets and found that the steady condition was achieved in the order of milliseconds after the first droplet impact, and after order O(10) droplets had struck, accompanied by heat fluxes ranging from 5 to 35 W/cm^2, increasing with droplet frequency (Trujillo and Lewis 2012). This study builds upon Trujillo, et al's work, extending to larger (O(1) mm diameter) droplets and lower (0.5 – 30 Hz) frequencies. The intent is to provide detailed insight into the interactions between successive droplets that lead to the heat transfer that has been measured.

2.2. Physics

The study of the physics of droplet impact is a tremendously broad undertaking. Both the fluid dynamics and the heat transfer before, during, and following the impact of a single liquid droplet onto a surface are each influenced by a myriad of factors. Adding in the interactions between multiple droplets in a spray only multiplies the challenge. The overall goal of this study is to maximize the heat transfer to a surface resulting from droplet impacts. To accomplish this, the focus of the study will be on the phenomena occurring during and immediately following the impact. To be more specific, the behaviors of splashing, cavity formation, and jet ejection will be investigated. Each of those behaviors is essential to understanding the cooling process.

Before discussing droplet impact dynamics, it is helpful to define the dimensionless groups that are used to characterize these phenomena. Most commonly used in literature to characterize the droplet impact dynamics is the Weber number, which is a ratio of inertia to surface tension (Equation [2-1]):

$$We \equiv \frac{\rho U^2 d}{\sigma} \qquad \text{[2-1]}$$

The second most frequently referenced dimensionless group in droplet impact studies is the Reynolds number, which gages the relative magnitude of inertial characteristics to viscosity (Equation [2-2]):

$$Re \equiv \frac{Ud}{\nu} \qquad \text{[2-2]}$$

The reason the Weber number shows up so frequently in droplet impact studies is that for many common liquids (water, ethanol, octane, etc.) for millimeter-scale and smaller droplets, the Weber number is relatively small, suggesting that capillary effects and other surface tension related dynamics are relevant. To quantify that statement, in the results that will be presented

here, the Weber number ranges from 10 to 1020 for water droplets. For a 4 mm water droplet moving at 2 m/s (a diameter and velocity within the range of this study), the Weber number is 220. In contrast, the Reynolds number range is 1500 to 18400 for water droplets, and for that same example water droplet, Reynolds is 8000. While, as will be demonstrated, viscosity does play a non-negligible role in droplet impact, the role of surface tension is often more pronounced, and thus the convention for characterizing these dynamics has become the Weber number.

There is one other dimensionless group which combines viscous and surface tension effects, and can be formulated as a combination of the Weber and Reynolds number. The Ohnesorge number is defined by Equation [2-3]:

$$Oh \equiv \frac{\mu}{\sqrt{\rho \sigma d}} = \frac{\sqrt{We}}{Re} \qquad [2\text{-}3]$$

For the 4 mm water droplet described above, the Ohnesorge number is 0.00185.

The ranges of dimensionless groups listed here are for droplets composed of water, which is the primary liquid used in most experiments. In some cases, glycerol mixtures and FC-72 are used; the relevant properties and dimensionless groupings are reported in those cases.

A train of droplets adds frequency to the mix of characteristics. The dimensionless number commonly used for discussing periodic flows is the Strouhal number (Equation [2-4]).

$$St \equiv \frac{fd}{U} \qquad [2\text{-}4]$$

Splashing is a complex set of fluid behaviors. It is typically defined as the ejection of secondary droplets of liquid from the bulk. It can occur immediately at impact ('prompt splashing', Figure 2.1.a), during the initial spreading on a dry surface ('corona splashing' Figure 2.1.b) or as the liquid withdraws from its maximum spread ('receding breakup', Figure 2.1.c), from an elevated

liquid crown produced from impact on a liquid film ('crown splashing', Figure 2.2.d), or from the jet produced as the cavity within the liquid film collapses ('jet splashing', Figure 2.2.e). Splashing is often attributed to the growth of linear instability within the liquid, although the exact nature of that instability is not completely understood (Yoon, Jepsen et al. 2009). From a heat transfer perspective, understanding and predicting splashing is important in the fate of impinging cooling liquid; splashing has the potential to disperse cold liquid around a surface, increasing the cooling area but reducing the amount of liquid near the point of impact.
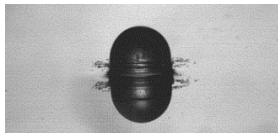
Prompt splashing, from the impact point   Corona splashing, during initial spreading.
Figure 2.1. Splashing modes that occur during liquid droplet impact on a dry solid surface.
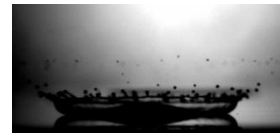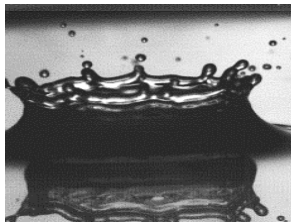
Splashing from the elevated crown produced   Splashing from the jet ejected during cavity
by cavity formation in liquid film.   collapse within a liquid film.
Figure 2.2. Splashing modes that occur during droplet impact on a liquid film.

When a droplet impinges on the surface of a liquid film, a cavity is formed within the film (Figure 2.3). In a cooling situation, the film has been heated by the substrate and the droplet is generally colder than the film. The formation of this cavity is a consequence of the droplet pene-trating the film; the cavity growth and collapse influence the distribution of cold droplet liquid through the film. If the cavity does not get close enough to the substrate, droplet liquid does not reach the substrate and the cooling effect will be negligible. Conversely, in some cases, the iner-

tia of the droplet negate the effects of the film, leading to splashing and cooling dynamics that appear to closely resemble droplet impacts onto dry surfaces. The depth of the cavity relates to the droplet diameter and impact velocity, the maximum thickness of the film, and the viscosity, surface tension, and density of both the droplet and the film.

Quasi-cylindrical cavity formed in a thin film, where motion is redirected radially.
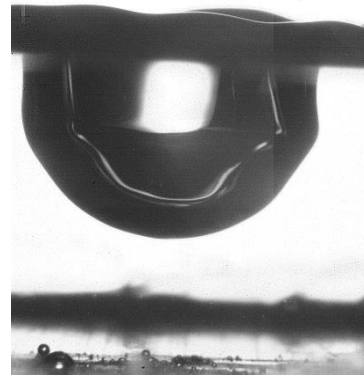
Hemispherical cavity formed in a deep pool with negligible substrate influence.

Figure 2.3. Typical cavity formation due to droplet impact within films of different thicknesses.

Figure 2.4 is an illustration of the typical droplet impact dynamics in chronological order, starting from impact. There is a brief description of the thermal and fluid dynamics that occur during that time. Each chapter of study in this dissertation can be tied to one of the sections in this timeline. The time scales listed are typical for the range of droplet sizes, velocities, and fluids used in this dissertation. The thermal behaviors described will be demonstrated in Section 2.8, starting on page 115.
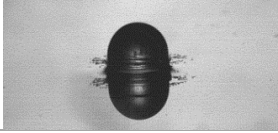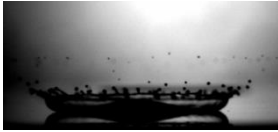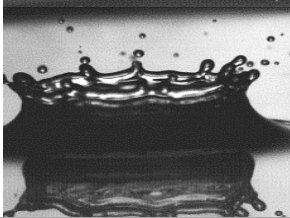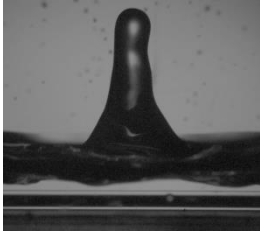
Time Scale	Fluid Dynamics	Thermal Effects
Impact (0-2 ms)	Dry / pool: Prompt splashing	Dry: Large ΔT at point of impact Pool: Little / no effect
2 – 10 ms	Dry: Spreading lamella, corona splashing Pool: Cavity development, crown splashing	Dry: temperature minimum Pool: Decrease of temperature as droplet approaches substrate
10 – 100 ms	Dry: Receding lamella, high amplitude initial oscillation Pool: Cavity collapse, jet formation	Dry: Heating of droplet fluid (boundary layer growth) Pool: Recirculation (secondary cooling) and ejection of droplet fluid
> 100 ms	Dry: Oscillation decay Pool: Jet ejection, capillary waves on pool surface	Dry: droplet fluid heats, reducing heat flux Pool: Loss of heat flux as droplet fluid displaced

Figure 2.4. A generalized timeline of dynamics observed in droplet impacts. Timescales shown are typical for the range of droplet diameters (3 – 5 mm) and impact velocities (0.5 – 5 m/s) used in these studies.

2.3. Experimental Setup

Figure 2.5 shows the droplet production and measurement setup. Droplets and droplet trains are produced using a pneumatic microliter valve (EFI- model SS) and a programmable microcontroller (Arduino Uno R3). The microcontroller can produce voltage pulses with a time resolution on the order of microseconds at set frequencies, and those pulses trigger the valve to open for a prescribed time. The valve is fed from a pressurized liquid reservoir. When actuated, the valve releases pressurized liquid through a steel needle, and a droplet is formed at the tip of that needle. After a set time, the valve closes and liquid ceases passing through the needle. When the droplet is large enough, gravity overcomes the surface tension holding the droplet to the needle and the droplet falls. The duration of the valve's opening is calibrated such that one cycle of the valve results in the production of one droplet. Thus, the valve's cycling frequency, regulated by the microcontroller, corresponds to the droplet production frequency.

Droplets fall under gravity acceleration from the needle when they reach a critical diameter - related to density, surface tension, and the diameter of the droplet, and the impact velocity varies from 0 (deposition) up to 3 m/s based on the height of release.

The impact substrate consists of an aluminum plate, heated by resistance heaters from within. A channel in the face of the aluminum has been filled with cast epoxy resin to hold a fast-response resistance temperature detector (RTD) at the level of the substrate surface. Glass walls surround the plate, retaining a pool of liquid on the aluminum substrate while allowing video recording of the plane of impact. The glass walls are 50 mm tall, allowing pools up to that depth. For this study, the focus is on the heat transfer induced at the substrate, so the focus is on shallow pools, with depth ranging from 0 (dry surface) to 34 mm (approximately 8 times the droplet diameter). Typically, deeper pools appear to prevent interaction between the droplet

and the substrate, minimizing the heat transfer. The less-trivial specifics of droplet-substrate interactions during liquid film impacts are the focus of the second segment of this study – Effects of Droplet and Film Properties on Dynamics of Single Droplet Impacts.
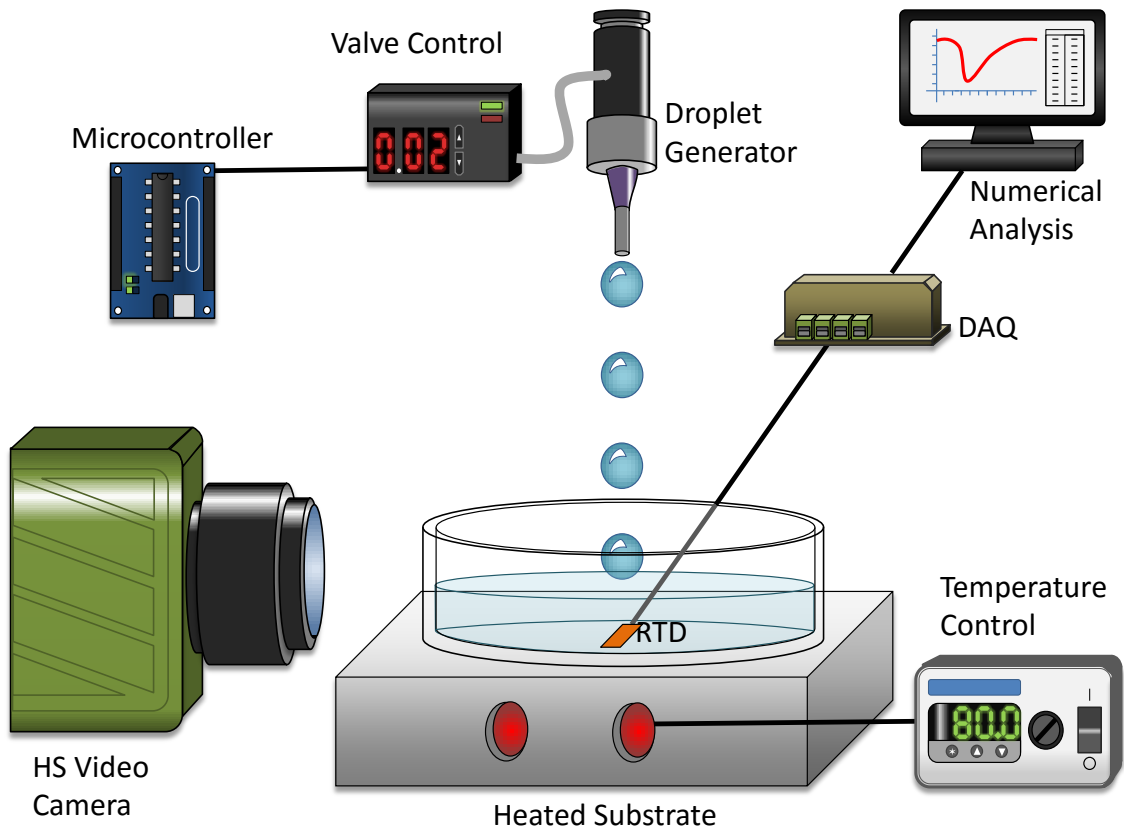
Figure 2.5. Experimental setup for droplet impact studies.

A two-pronged approach is used to measure the dynamics of the droplet impacts. A high speed video camera (Phantom v7.1) is used to record the droplet in freefall and the impact cavity from the side- within the plane of the substrate. The camera and analysis are managed using the Phantom Camera Control software provided with the camera. The camera records at up to 4700 frames per second at a resolution of 800 x 600 pixels maximum resolution; higher framer-

ates are available by reducing the resolution. The exposure time per frame is variable from the frame interval down to 1 microsecond. The camera is equipped with a Micro-Nikkor 105 mm manual focus lens, and optionally magnification lenses producing +1, +2, and +4 zoom factors. Distance and velocity measurements are taken from video using still frames of objects of known dimensions; from these frames the length corresponding to one pixel on video can be calculated. Measuring the distance a droplet moves between successive frames of video at a known interval between those frames gives the velocity the droplet is moving during that time. Measurement of objects of known diameter reveals a less than 1% error in length measurements in still frames. The error in velocity measurements will be proportional to the length. The camera is positioned at a height such that the cavity below the surface of the pool is visible as well. Calibration lengths are taken above and below the surface of the pool to account for refraction.

The second prong is a fast-response RTD cast in epoxy upon the substrate (Minco, S10044PD12 or equivalent Omega, F3145). The layout and dimensions of the RTD are listed in Figure 2.6. It is advertised with a response time of approximately 3 milliseconds, and it is exposed but flush with the substrate. The droplet impacts are centered upon the RTD. The RTD is sampled at 1000 Hz – oversampling by a factor of approximately 3 - and the data is digitally smoothed by a customized moving average filter to reduce noise and eliminate the oversampling. The RTD provides detailed insight into the heat transfer at the point of impact.
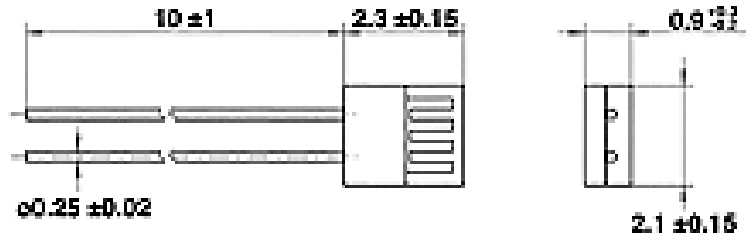
Figure 2.6. Omega Model F3145 RTD.
This model is used for measuring temperature effects during droplet impact. Dimensions are in mm.

The heat flux is calculated using a numerical integration of Duhamel's theorem. Duhamel's theorem is a method of solving the heat equation for time-fluctuating boundary conditions, enabling the heat flux through a surface to be solved based on a measurement of temperature history (Beck, St Clair et al. 1985). If k is the thermal conductivity of the substrate, ρ the density, and c the specific heat, then the heat flux at the surface can be approximated by Equation [2-5].

$$q'' = 2 \sqrt{\frac{k\rho c}{\pi}} \sum_{i-1}^{I} \frac{T_i - T_{i-1}}{t_i - t_{i-1}} \left(\sqrt{t_I - t_{i-1}} - \sqrt{t_I - t_i} \right) \qquad [2\text{-}5]$$

Where T is the temperature at each time step I, t the time, k, ρ, c the thermal conductivity, density, and specific heat of the substrate containing the sensor, respectively, and q'' is the heat flux per unit area.

This solution assumes a finite time step and a semi-infinite planar substrate. Vu, et al, used this method to compute the heat fluxes of single droplets impinging upon shallow heated pool (Vu, Aguilar et al. 2009). Equation [2-5] is used to estimate the heat flux from the temperature history recorded by the embedded RTD.

23

References

Beck, J. V., C. R. St Clair and B. F. Blackwell (1985). <u>Inverse Heat Conduction: Ill-Posed Problems</u>, John Wiley & Sons, Inc.

Rein, M. (1993). "Phenomena of liquid drop impact on solid and liquid surfaces." <u>Fluid Dynamics Research</u> **12**: 61-93.

Trujillo, M. F. and S. R. Lewis (2012). "Thermal boundary layer analysis corresponding to droplet train impingement." <u>Physics of Fluids</u> **24**(11): 112102-112102-112122.

Vu, H., G. Aguilar and R. Jepsen (2009). <u>Single Droplet Heat Transfer through Shallow Liquid Pools</u>. 11th International Conference on Liquid Atomization and Spray Studies, Vail, CO, Institute of Liquid Atomization and Spray Studies.

Yarin, A. L. (2006). "Drop Impact Dynamics: Splashing, Spreading, Receding, Bouncing..." <u>Annual Review of Fluid Mechanics</u> **38**: 159-192.

Yoon, S., R. Jepsen, S. James, J. Liu and G. Aguilar (2009). "Are Drop-Impact Phenomena Described by Rayleigh-Taylor or Kelvin-Helmholtz Theory?" <u>Drying Technology</u> **27**(3): 316-321.

2.4. The Role of Solid Surface Wetting in Disposition of Liquid Following Droplet Impact

As previously stated, the theme of this study is the enhancement of local heat flux via manipulation of the thermal boundary layer. To make this premise, the distinction between 'local' and 'surrounding' must be clear. In essence, it is necessary to understand and predict the area affected by droplet impact, and explore the disposition of the droplet fluid within that working area.

One of the fundamentals of all forms of heat transfer is that the surface area is a governing factor in any heat exchange. In the cooling of a surface by an atomized spray, the droplets strike the surface and then spread and often splash, distributing liquid away from the impact point. The factors controlling the dynamics of the droplet after splashing are numerous and entwined together. For this study, the factors explored are the wettability of the solid surface, the viscosity of the droplet liquid, and the impact velocity. Each is found to play a role in the motion and breakup of liquid after it impacts the surface.

2.4.1. Study: Wetting, Viscosity, and Post-Impact Droplet Oscillation

Wettability plays an intriguing role in droplet impact phenomena. Hydrophobic surfaces tend to increase the likelihood of splashing; as the spreading edge of the droplet is repulsed from the surface, instability based on density and acceleration differences between the liquid and ambient gas are magnified (Vu, Banks et al. 2011). Super-hydrophobic surfaces can cause droplets to bounce as the liquid is repulsed by the action of its own surface tension (Okumura, Chevy et al. 2003). Surfaces with multiple regions of alternating hydrophobic and hydrophilic nature will cause liquid droplets to migrate away from the hydrophobic and onto the hydrophilic regions after impact (Mock, Michel et al. 2005). The dynamic contact angle, one of the measures

of wetting, is explored for the initial spreading and receding of a droplet after impact but could not be directly correlated with the liquid lamella diameter (Bayer and Megaridis 2006).

Upon impact with a solid surface, a droplet typically follows a quasi-periodic progression of events, depicted in Figure 2.7. The droplet spreads radially outward. The layer of liquid formed as the droplet spreads is known as the lamella. This spreading is driven by the impact velocity, and resisted by surface tension around the lamella's rim and viscous shear between the liquid and substrate. The spreading slows and stops, and then surface tension pulls the lamella inward – a recoiling action. During any of these times, splashing may occur in the prompt, corona, or receding breakup forms. The liquid assumes a hemispherical shape, and then begins to flatten again; the process is repeated until viscous effects dissipate the motion.

Figure 2.7. Typical oscillations occurring after droplet impact.

This quasi-periodic spreading and receding of the droplet liquid after impact is recorded for a range of droplet impact conditions. In this study, the focus is on low Weber number impacts (10 < We < 100), and with attention to the effects of elevated droplet viscosity. The low Weber impacts were chosen to maximize oscillation behavior- at higher impact Weber numbers, it was found that oscillations were significantly diminished, possibly due to the droplet liquid spreading farther across the surface.

Noblin, et al studied induced oscillations of a droplet resting on a solid substrate, with a focus on the transition between a static contact line and a moving one (Noblin, Buguin et al. 2004). Using a modified loudspeaker to vibrate an initial quiescent drop, the transition between

an oscillating and a pinned contact line was investigated in the light of the frequency and magnitude of the driving oscillations (Noblin, Buguin et al. 2004). The experimental techniques and vibrational analysis performed by Noblin, et al are similar to the work presented in this paper, except that the focus of this paper is on impacting droplets and unforced oscillations, in contrast to deposited droplets and driven vibrations.

Our goal is to provide better understanding of the oscillations and spreading behaviors during droplet impacts which will lead to improved control of droplet impact heat transfer. The thermal effects of droplet impacts onto liquid films depend on the film thickness (Vu et al. 2009); the oscillations of droplets regulate the thickness of liquid that subsequent droplets strike. Splashing behavior of single droplet impacts depend on the target film thickness, as well- very thin films are more likely to lead to splashing than thicker films (Vander Wal, Berger et al. 2006). Understanding the behavior of the droplet long after impact is critical to applications in some methods of 3-D printing, where droplets are sprayed in layers and solidify into controlled shapes (Martin, Hoath et al. 2008).

2.4.2. Setup

Water and glycerol mixtures are used to explore the effect of viscosity, specifically on the damping of the liquid motion. The surface's wetting characteristics are varied by applying hydrophilic and hydrophobic treatments and using different materials. The impact velocity was varied between 0.5 and 1.5 m/s – strongly influencing the initial spreading of the droplet and the subsequent oscillation.

Droplets were comprised of three liquids: water, 60% glycerol/40% water by mass, and 85% glycerol/15% water by mass. The selection of these three liquids was to cover a wide range of viscosity while only minimally changing the density and surface tension. Table 2.1 provides the

fluid properties of each of these liquids. Using the pneumatic droplet generator and a steel nee-

dle of 1.65 mm outer diameter, the droplets of each of these liquids were 3.3±0.2 mm diameter;

droplets more than 0.1 mm larger or smaller than the mean were rejected. These droplets and

give a range of Weber number of 10-100 and Reynolds number from 15-4000, based on impact

velocities of 0.54±0.01 m/s for examining the effects of fluid properties and surface conditions,

and 0.54-1.5 m/s when investigating the effect of impact velocity.

Table 2.1. Properties of fluids used for post-impact droplet oscillation study.

Fluid	Density (g/cm^3)	Viscosity (cm^2/s)	Surface tension (dyne/cm)
Water	1.00	0.01	72.8
60% Glycerol	1.15	0.09	66.9
85% Glycerol	1.22	0.89	65.1

Three surface conditions were used in this study, listed from most hydrophilic to most hy-

drophobic: bare aluminum, hydrophilic-treated acrylic, and hydrophobic-treated polytetrafluo-

roethylene (PTFE). The hydrophilic treatment was Rain-X Anti-fog wipes. The hydrophobic

treatment was Rain-X Rain Repellant spray. Each surface was cleaned and the treatments re-

applied between each test. The static contact angle for each droplet liquid on each of the three

surface conditions was recorded. Table 2.2 provides the measured static contact angle, along

with the accompanying time-averaged dynamic contact angle in parenthesis.

Table 2.2. Static and (average dynamic) contact angles of droplets on varied substrates.

| Fluid | Surface | | | | |
	Aluminum	Hydrophilic treated acrylic	Untreated Acrylic	Hydrophobic treated Teflon	Untreated Teflon
Water	10° (58°)	29° (51°)	37°	75° (87°)	35°
60% Glycerol	17°	48° (44°)		64°	
85% Glycerol	35°	54° (59°)	45°	66°	55°

The oscillations were characterized by the instantaneous diameter and thickness at the center of each droplet, measured using a high speed video recording of each impact (Figure 2.8). In a cooling situation, the diameter would govern the cooling area covered by the droplet. The thickness of the droplet shouldn't affect the heat transfer as significantly as the splat diameter, although some effect is likely due to thermal boundary layer limitations. However, the thickness of the droplet liquid after impact defines the surface subsequent droplets in a spray or train strike - inextricably controlling their cooling effects and those of the overall spray.
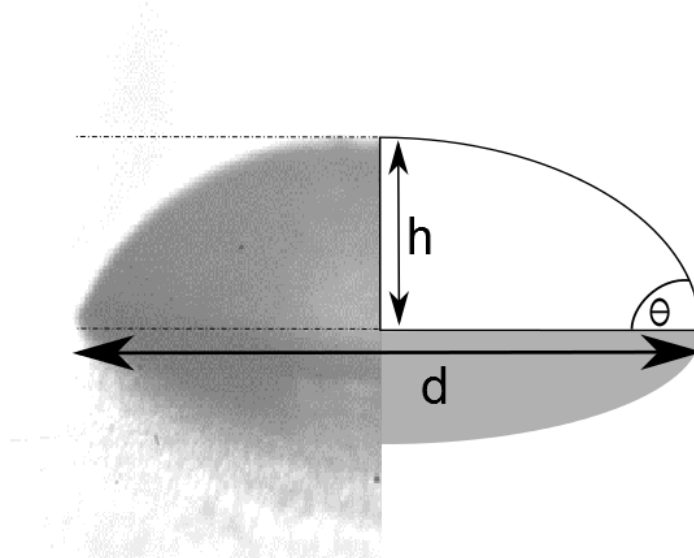
Figure 2.8. Depiction of measurement of contact angle and the droplet center thickness.

The high speed video camera used for these measurements and for the still frames presented in this section is a Phantom V7.1 recording at 5000 fps and 800 x 600 resolution. At the focus and zoom settings employed, measurement of a known distance provided a length resolution of 0.010 mm/pixel. The exposure time per frame is 20 µs.

2.4.3. Results

Oscillations of Dynamic Contact Angle vs. Splat Thickness

The effect of surface wettability on droplet oscillations, with all other characteristics remaining constant, was the first topic of study. Videos of a water droplet striking the aluminum, hydrophilic treated acrylic, and hydrophobic treated Teflon were taken. Figure 2.9 shows the dynamic contact angle and thickness of the water droplet as a function of time on each surface. The dynamic contact angle changes as the droplet oscillates- when the droplet is narrowest, the fluid tries to spread radially, increasing the contact angle; as the droplet recoils, the fluid moves inward, reducing the contact angle.

Viscosity and Wettability's Influence on Oscillations

Viscosity was shown to have a dramatic impact on droplet oscillation behaviors. By varying glycerol content in aqueous mixtures, the viscosity can be changed dramatically without significantly affecting other fluid properties as seen in Table 2.1. Differing-fluid droplets were recorded striking the treated acrylic surface, which is the intermediate surface on the range of wettability. Figure 2.10 shows the dynamic contact angle and oscillations over time for the range of fluids studied on the acrylic surface. Figure 2.9 and Figure 2.10 show that the dynamic contact angle varies at approximately the same frequency but generally opposite in phase to the center thickness for water droplets on all three surface conditions and for each droplet fluid on the acrylic surface. The average dynamic contact angle is generally larger than the corresponding static ones (Table 2.2). The reason for this is that the resting liquid shape is hemispherical, which corresponds to the lower ranges of dynamic contact angle.
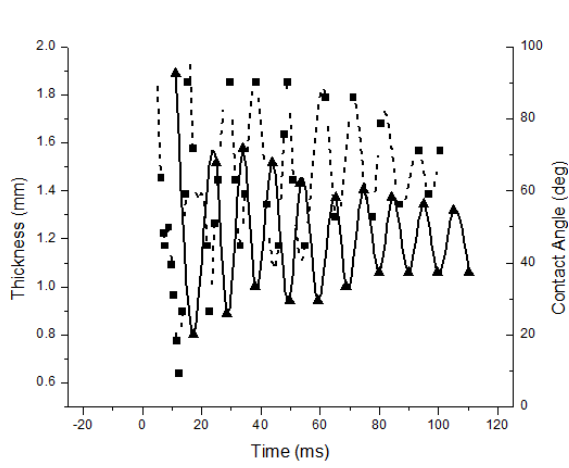
a. Aluminum surface
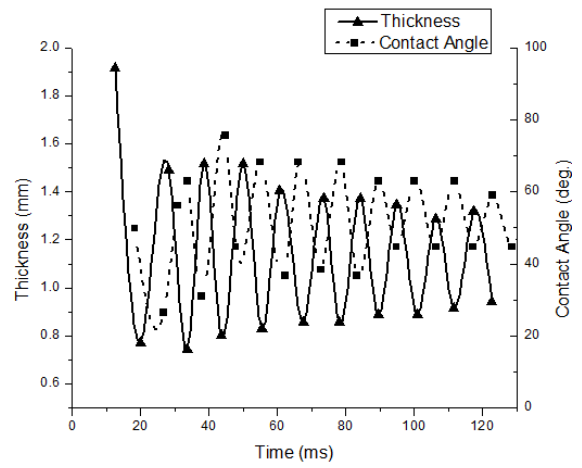
b. Acrylic surface with hydrophilic treatment
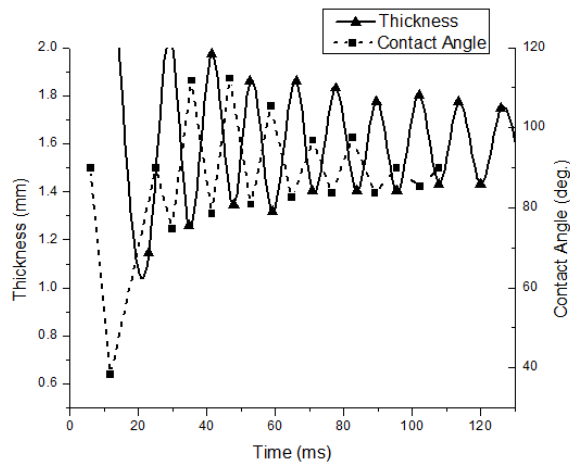
c. PTFE surface with hydrophobic treatment

Figure 2.9. Measured dynamic contact angle and thickness of water droplet on each surface.
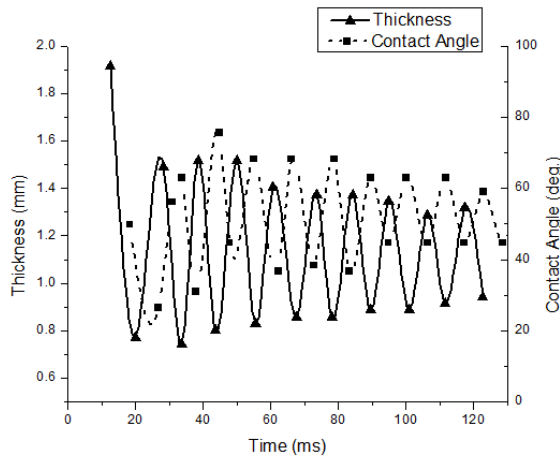
a.   Water droplet
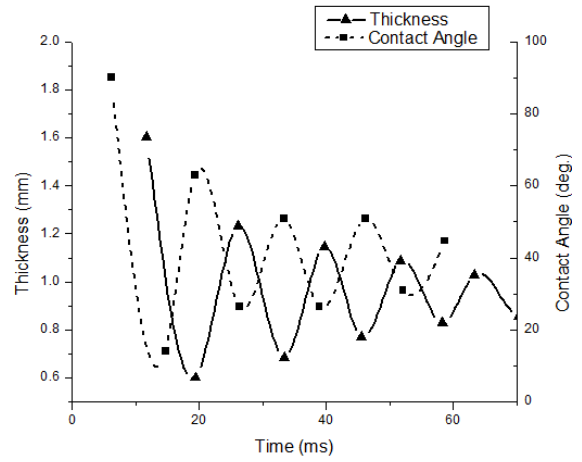
b.   60% glycerol / 40% water droplet
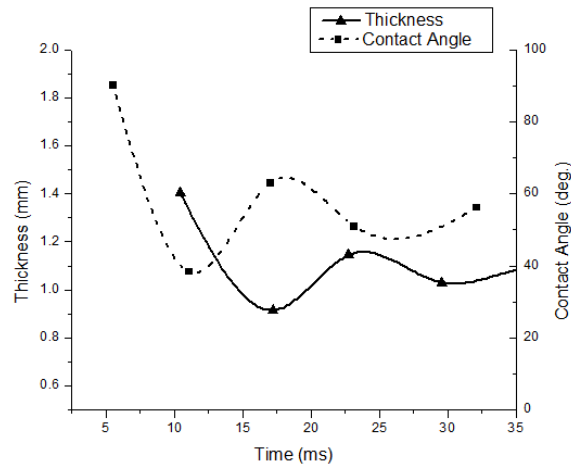
c.   85% glycerol / 15% water droplet

Figure 2.10. Measured dynamic contact angle and thickness of each droplet on the acrylic sur-
face.

Table 2.3. Frequency of oscillation of each droplet on each surface, given in Hz.

| Fluid | Surface | | |
	Aluminum	Hydrophilic Treatment Acrylic	Hydrophobic Treatment Teflon
Water	96	87	81
60% Glycerol	74	79	85
85% Glycerol	83	84	83
Water, 0.57 m/s	-	-	57
Water, 0.81 m/s	-	-	42

Figure 2.11 shows the center thickness over time for all droplets oscillating on the aluminum surface, and Figure 2.12 the same on the hydrophobic treated Teflon surface. Using the average of the peak-to-peak time, the frequency can be calculated from the data presented in these figures. The surface condition influences the frequency differently for each of the three droplet fluids, seen in Table 2.3. For water, the hydrophobic surface (PTFE) produces the lowest frequency (80 Hz). As the surface grows more hydrophilic, the droplet oscillates faster, reaching 96 Hz on aluminum. However, the opposite effect is observed for droplets composed of 60% glycerol- the droplet oscillates fastest on the more hydrophobic surface and decreases in frequency for more hydrophilic ones. The frequencies of oscillation of 85% glycerol droplets seem to ignore the surface conditions- the measured frequencies on all three surfaces vary by approximately 1 Hz.
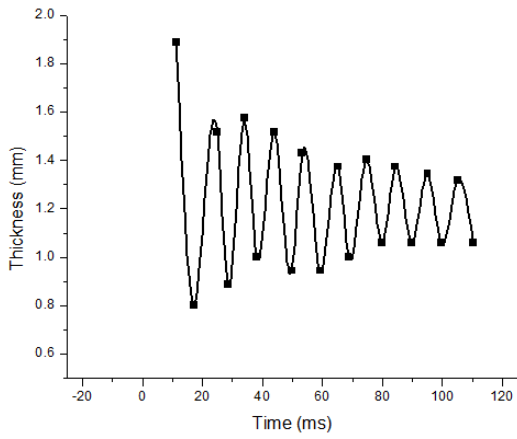
a. Water droplet
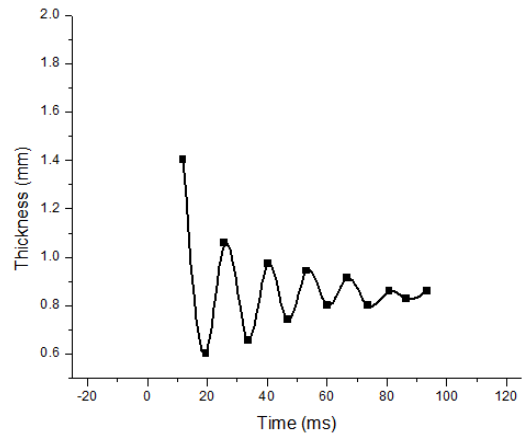
b. 60% glycerol droplet
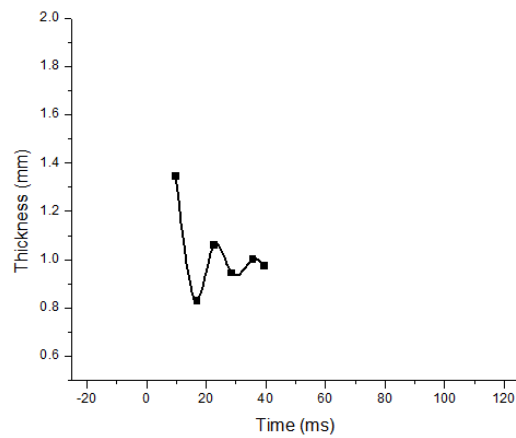
c. 85% glycerol droplet

Figure 2.11. Measured dynamic contact angle and center thickness of each droplet on the aluminum surface.
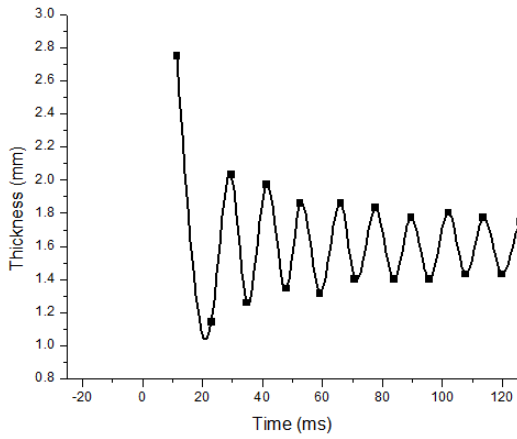
a. Water droplet
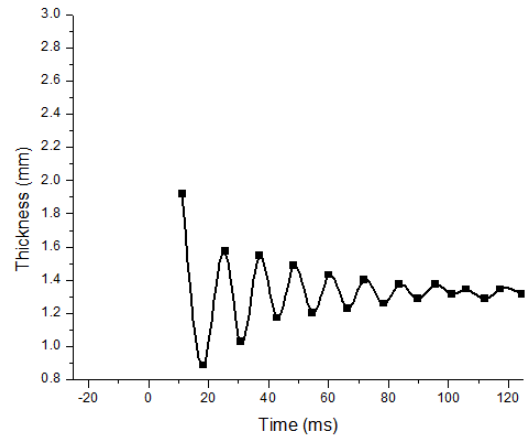
b. 60% glycerol droplet
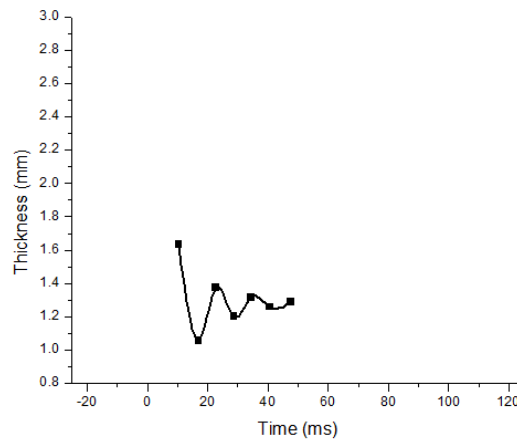
c. 85% glycerol droplet

Figure 2.12. Measured dynamic contact angle and center thickness of each droplet on the PTFE surface.

Both viscosity and wettability seem to affect post impact oscillations, but viscosity seems to have the larger effect over the range of conditions studied. The differences in oscillation amplitude and duration between surfaces for any of the three droplet fluids are much smaller than the corresponding differences between the droplet fluids. Water, having the lowest viscosity, shows the largest amplitude (~±0.4 mm initially on all three surfaces) and most sustained oscillations out of all three droplet fluids (lasting in excess of 120 ms)- visible in Figure 2.10. 60% glycerol has reduced initial amplitude (~±0.3 mm) and oscillations die off before 120 ms. Increasing viscosity further with 85% glycerol droplets leads to initial amplitude of only ~±0.1 mm and no oscillations after only 50 ms, on all surface conditions in this study. In contrast, the differences in initial amplitude between surfaces for each fluid are minimal – on the order of 0.02 mm variation. The surface condition does seem to play a role in the duration of measurable oscillations- for all three droplet species, oscillations die off most quickly on aluminum. The last measurable oscillation occurs 15-25% sooner on aluminum than on the other surfaces for each of the droplet liquids.

On the hydrophobic-treated PTFE surface, all three droplet liquids have the highest mean of their oscillations (Figure 2.12). On that surface, the mean is inversely related to viscosity- water has the largest mean value and 85% glycerol the smallest. Interestingly, on the other two surfaces, 85% glycerol has a higher mean thickness than 60% glycerol. This suggests that as the surface grows more hydrophilic, viscosity plays a larger role in restricting the droplet spreading- similar to the thicker spreading lamella effect observed for high viscosity droplets by Vu, et al (Vu, Banks et al. 2011). Further, the interaction of glycerol with the surface treatments may influence how the droplets spread. However, when considering the differences observed in oscil-

lation frequency and amplitude, it seems probable that viscosity is the dominant factor in controlling droplet spreading in these cases.

Velocity's Influence on Oscillations

Finally, the oscillations of a water droplet after striking a PTFE surface at varying impact velocities were measured over a range of 1.07 to 1.62 m/s (50 < We < 140). Impact velocity was found to play a role in the amplitude, frequency, and mean value of oscillations. Higher impact velocity reduced the amplitude of oscillations, lowered the frequency, and decreased the mean value of the thickness of the droplet. Figure 2.13 shows the oscillations of a water droplet that impacted a treated PTFE surface at 1.07 and 1.34 m/s. The droplets that impacted at higher velocities did not oscillate measurably. The higher-velocity droplets spread thinner initially, but then oscillate and retract, leading to a mean of oscillation that grows over time.
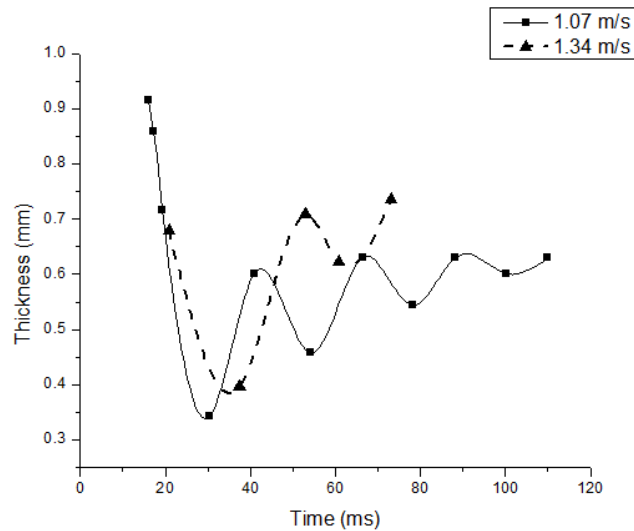
Figure 2.13. Oscillations of a water droplet impacting a PTFE surface at increased velocity.

Increased velocity reduced the amplitude and mean thickness of the droplet for a very simple reason. As the velocity increased, the radius of the droplet when the contact line stopped moving increased correspondingly. The volume of the droplet is virtually identical in each case, so the larger radius results in a droplet that is thinner on average and has less vertical freedom to oscillate. Further, the larger radius means the wavelength of motion in the droplet is longer, leading to an observed decrease in frequency. Similar reasoning may apply in the case of hydrophilic vs. hydrophobic surfaces- both water and 85% glycerol each have higher frequencies and higher amplitudes as the surfaces get more hydrophobic, leading to a smaller pinned contact line diameter and thus thicker volume and shorter wavelength. As the velocity increases, the drop spreads further across the substrate, until the kinetic energy of the impact has been lost. At that point, the surface tension is the only cause of flow, leading to a gradual, non-oscillating retraction of the droplet into a hemisphere.

2.4.4. Vibration Analogy

The behavior of a liquid droplet after impact was compared to a damped harmonic oscillator. If x is the deflection from a neutral state, k is a spring constant, c is a damping coefficient, and m is the mass of the system, the motion of an unforced harmonic oscillator is represented by Equation [2-6], assuming there is no force driving the vibrations (Thomson and Dahleh 1998):

$$m\ddot{x} = -kx - c\dot{x} \qquad \text{[2-6]}$$

This differential equation has an exponentially decaying solution (Thomson and Dahleh 1998):

$$x(t) = \exp\left(-\frac{c}{2m}t\right)\left[A * \exp\left(\sqrt{\left(\frac{c}{2m}\right)^2 - \frac{k}{m}}\,t\right) + B\right.$$
$$\left. * \exp\left(-\sqrt{\left(\frac{c}{2m}\right)^2 - \frac{k}{m}}\,t\right)\right]$$

[2-7]

In Equation [2-7], if an oscillator is 'underdamped', the terms within the radicals will be imaginary, and the equation can be reformulated in terms of trigonometric functions:

$$x(t) = \exp\left(-\frac{c}{2m}t\right)\left[A * \cos\left(\sqrt{\frac{k}{m} - \left(\frac{c}{2m}\right)^2}\,t\right) \pm B * \sin\left(\sqrt{\frac{k}{m} - \left(\frac{c}{2m}\right)^2}\,t\right)\right]$$ [2-8]

Qualitatively, underdamped oscillations are apparent in all of the observed water and 60% glycerol droplet impacts, so oscillations are sustained for many cycles. In contrast, the oscillations of the highly viscous 85% glycerol droplets are more qualitatively overdamped- quiescence occurs after very few oscillations.

In the context of a droplet oscillating on a surface, we hypothesize viscosity ought to play a role primarily in the damping coefficient, c; viscosity will remove energy from the oscillating fluid, acting to diminish the amplitude of the oscillation over time. The spring constant in Equation [2-6], k, is related to how strongly the oscillating system pulls itself towards a neutral state. The surface tension and interactions between the droplet and the surface are what we hypothesize to principally drive the recoiling action of a droplet; as such, k ought to depend on them with limited or no dependence on viscosity.

Using the exponential term in Equation [2-8], the value of c can be computed. That exponential term, when plotted alongside the oscillations, will follow the peaks of the oscillations, as shown in Figure 2.14. By fitting an exponential curve of the form *A*exp(-b*t)* to the peaks of the

39

oscillations, the power of the fitted curve (*b*) can be compared to the value *-c / 2m*. Table 2.4

lists the computed damping coefficients.
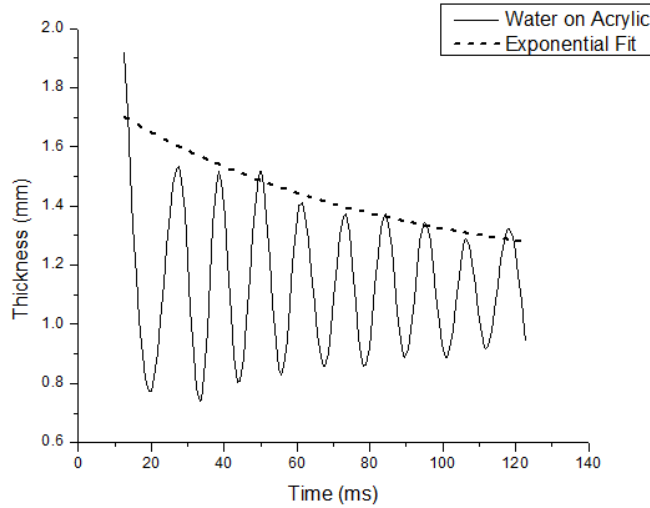
Figure 2.14. Exponential damping curve fitted to the peaks of measured oscillations.

Table 2.4. Damping coefficients (*c*) of droplets onto each surface. Given in N·s/m

| | Surface | | |
Fluid	Aluminum	Treated Acrylic	Treated Teflon
Water, 0.45 m/s	2.50 E -04	2.23 E -04	2.92 E -04
60% Glycerol, 0.45 m/s	7.50 E -04	8.96 E -04	5.36 E -04
85% Glycerol, 0.45 m/s	1.95 E -03	1.47 E -03	1.35 E -03

Correspondingly, the spring constant can be determined by equating the experimentally de-

termined frequency to the frequency term in Equation [2-9]. The factor of 2π converts the fre-

quency to radians/second.

$$2\pi f = \sqrt{\frac{k}{m} - \left(\frac{c}{2m}\right)^2} \qquad\qquad [2\text{-}9]$$

Rearranging Equation [2-9] to find the spring constant:

$$k = m * \left[(2\pi f)^2 + \left(\frac{c}{2m} \right)^2 \right]$$ [2-10]

Table 2.5. Spring constants *(k)* of droplets onto each surface.
Given in N/m. First number is the frequency-predicted spring constant, second number is best-fit spring constant, that is, the closest spring constant that results in RMS error <10% between measurements and predictions.

| | Surface | | |
Fluid	Aluminum	Treated Acrylic	Treated Teflon
Water, 0.45 m/s	2.52/2.52	2.48/2.44	2.14/2.45
60% Glycerol, 0.45 m/s	1.83/1.98	2.16/2.16	2.30/2.30
85% Glycerol, 0.45 m/s	2.24/1.96	2.27/1.64	2.17/1.73

Table 2.5 lists the calculated spring constants for each droplet. That table also contains "best-fit" spring constants. The calculated spring constants do not always fit the observed droplet oscillations very well. To find the best-fit constants, Equation [2-8] was plotted using the damping coefficient from the exponential fit and *k* expected from Equation [2-10]. If the RMS error between the predicted and the measured oscillations was larger than 10%, the spring constant was adjusted in increments of 0.01 N/m until the RMS percentage error between the measured and predicted oscillations was below 10%. Figure 2.15 depicts the measured and predicted oscillations of a 60% glycerol droplet impacting an acrylic surface- a case for which the calculated spring constant qualitatively accurately predicted the oscillations (RMS = 4.2%). Figure 2.16 depicts the measured, predicted, and best-fit spring constant for the 85% glycerol droplet on an acrylic surface. The small increment in spring constant greatly improves the agreement between the measured and predicted curves- RMS error drops from 49% to 9.3%.
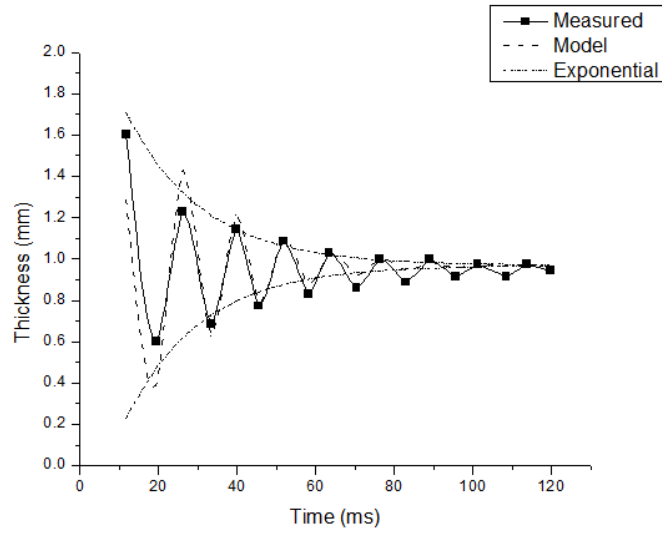
Figure 2.15. Comparison of the measured data points, the damped-oscillation model, and the damping exponential curves.
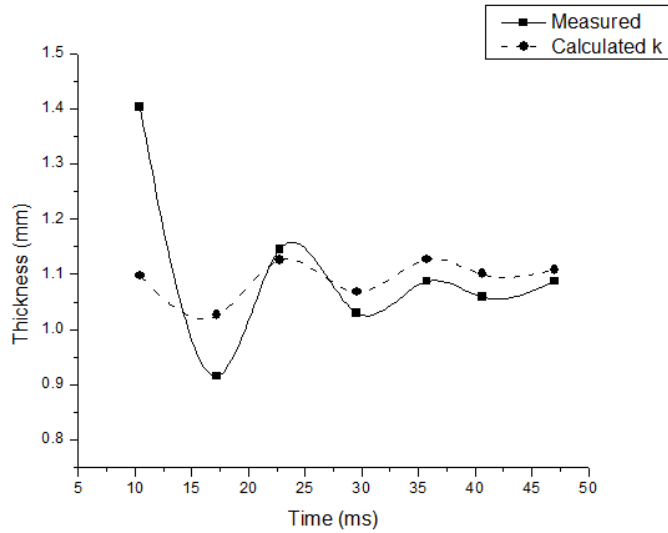
a. With no adjustment to the spring constant.
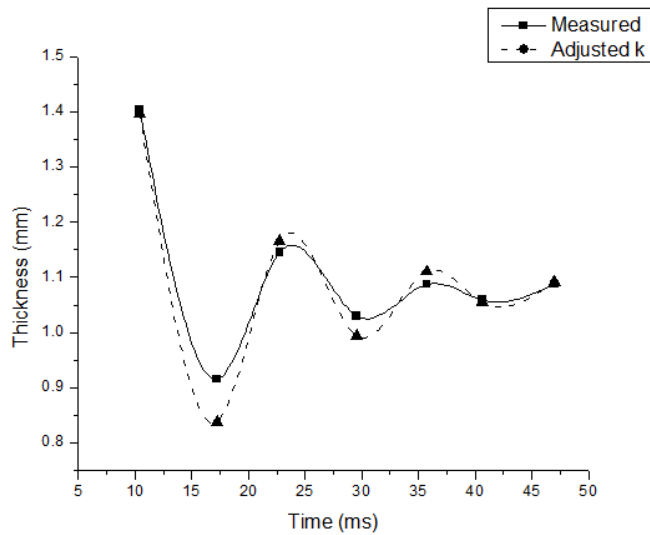
b. Adjusted spring constant.

Figure 2.16. Comparison of the measured data points and predicted oscillation curves for 85% glycerol on an acrylic surface.

The adjustment in the spring constant, k, is from 2.24 to 1.96 N/m, resulting in improved oscillation prediction. The adjustment is needed to account for asymmetry in in the droplet's shape and oscillation that is not purely vertical at the center of the splat.

This inaccuracy appears derive from small asymmetry in the droplet's oscillations. Many times the droplet would oscillate off-center from the point of impact, leading to irregular (fluctuating over time) frequencies. While droplets that visibly exhibited such behavior were rejected for measurement, there is likely to be some asymmetry in the oscillations. Oscillation outside the plane of the video recording would not be apparent. Even a small asymmetry causing a change in frequency would strongly appear in the spring constant. A future study may refine the droplet oscillation model to account for these asymmetries.

From Table 2.4, we observe that all droplets show higher damping coefficients on the more hydrophilic surfaces- in line with the findings discussed about Figure 2.9. The increased viscosity of glycerol contributes to higher damping coefficients- with 85% glycerol having just under an order of magnitude larger damping coefficient than water on all three surfaces, and 60% glycerol approximately bisecting the other two liquids. A quick estimate suggests that the damping coefficient increases approximately following the square root of viscosity; however, a wider range of fluid would be necessary to verify this.

The spring constant does not seem to follow the same trends as the damping coefficient. For the acrylic and the Teflon surfaces, the spring constant is very similar for each of the droplet fluids- less than a 10% difference. This appears to support the hypothesis that the spring constant is related to the surface tension, as the droplet fluids are very similar in that value. A future study will need to use fluids with differing surface tension to verify this. On aluminum, however, the spring constant seems to be influenced significantly by the droplet composition. Water is predicted to have nearly twice as large of a spring constant as 85% glycerol, and the best-fit spring constants are even farther apart.

The higher-velocity water droplets did not follow the same fitting as the other cases because the oscillations were around an increasing mean. The exponential fit could not be used. However, the duration and amplitude of the oscillations can be remarked on. Compared with the lower velocity water droplet impacting on the same surface, the increased velocity seems to result in more rapidly diminishing oscillation amplitude, suggesting a higher effective damping coefficient. At 120 ms after impact, for example, the low-velocity (0.55 m/s) case shows oscillations with amplitudes of approximately 0.2 mm above and below the mean. At the same time after a 1.07 m/s impact, oscillations have faded to less than 0.05 mm around the mean. For a 1.34 m/s impact the oscillations are too small to be measured at 80 ms after impact. The frequency, as well, is influenced by the impact velocity. The frequency of a low velocity water droplet is 87 Hz; the 1.07 m/s droplet oscillates much slower, only 57 Hz, and the 1.34 m/s droplet oscillates at 42 Hz. The decrease in frequency suggests an analogous decrease in the spring constant for these droplets. However, the qualitative increase in damping coefficient may balance out the effect of the frequency change, as each influences the spring constant (Equation [2-10]).

2.4.5. Conclusions

Measurements reveal that the mean of the dynamic contact angle is scales with the static contact angle. Further, hydrophobic surfaces lead to larger changes in dynamic contact angle than hydrophilic ones, suggesting hydrophilic surfaces restrict the droplet motion more effectively.

On all surfaces, the lowest viscosity water droplets show sustained large oscillations relative to higher viscosity fluids- an intuitive result. Increasing viscosity damps oscillations severely. This damping can be qualitatively observed as reduced magnitude and duration of oscillations after

impact. The higher viscosity droplets oscillate less and come to rest more quickly than lower viscosity ones.

Droplet oscillations seem to depend heavily on the radius of the droplet after the contact line has stopped moving. The magnitude of this radius determines the average thickness of the drop, the amount of vertical freedom the droplet fluid has while oscillating- governing the amplitude of oscillations, and the wavelength of motion that governs the oscillation frequency. Higher velocities and more hydrophilic surfaces lead to thinner, slower oscillating, and more severely damped droplet motion. However, the sustaining effect of a hydrophobic surface is greatly outweighed by the damping effect of increased viscosity.

The analogy of droplet impact oscillations to damped harmonic oscillations has been made, with the spring constant and damping coefficient demonstrated to scale with droplet viscosity, surface tension, and velocity. Each of these factors appears to play an intertwined role in the analogy, but generally it can be said that increasing viscosity and velocity corresponds with increased damping and spring coefficients, while increasing contact angles lead to higher damping and spring coefficients in water and the reverse when the droplet is a glycerol mixture.

Connection with the Dissertation Premise

While the droplet oscillations do not directly interrupt the thermal boundary layer, they influence the growth of that boundary layer during the initial stages of spray impact. Droplets that impinge and spread with minimal oscillation become stagnant quickly. The lack of motion will facilitate the growth of the boundary layer. Conversely, sustained oscillation will promote mixing and minimize the layer's thickness.

Figure 2.17 is a segment of the timeline of droplet impact dynamics presented in Figure 2.4. This study has demonstrated the oscillatory behavior and explored the factors that govern this

relatively long-duration dynamic of droplet impingement. Bolded text in the figure indicates findings or conclusions that can be drawn from this study. In the next sections, the focus will be on successively quicker dynamics.

Time Scale	Fluid Dynamics	Thermal Effects
10 – 100 ms	Dry: Receding lamella, high amplitude initial oscillation **Increased impact velocity forces larger lamella, reduces oscillation amplitude.**	Dry: Heating of droplet fluid (boundary layer growth) **Oscillations control liquid layer thickness and motion, setting limits on boundary layer thickness**
> 100 ms	Dry: Oscillation decay **Rate of decay depends on viscosity, wetting characteristics, and impact velocity.**	Dry: droplet fluid heats, reducing heat flux **Faster decay of oscillations allows more rapid heating of liquid at surface**

Figure 2.17. From the timeline previously presented, this study has demonstrated the oscillation in the longer timescales.

References

Bayer, I. S. and C. M. Megaridis (2006). "Contact angle dynamics in droplets impacting on flat surfaces with different wetting characteristics." Journal of Fluid Mechanics **558**: 415.

Martin, G. D., S. D. Hoath and I. M. Hutchings (2008). "Inkjet printing-the physics of manipulating liquid jets and drops." Journal of Physics: Conference Series **105**: 1-15.

Mock, U., T. Michel, C. Tropea, I. Roisman and J. Rühe (2005). "Drop impact on chemically structured arrays." Journal of Physics: Condensed Matter **17**(9): S595-S605.

Noblin, X., A. Buguin and F. Brochard-Wyart (2004). "Vibrated sessile drops: Transition between pinned and mobile contact line oscillations." The European Physical Journal E: Soft Matter and Biological Physics **14**(4): 395-404.

Okumura, K., F. Chevy, D. Richard, D. Quéré and C. Clanet (2003). "Water spring: A model for bouncing drops." Europhysics Letters **62**(2): 237-243.

Thomson, W. T. and M. D. Dahleh (1998). Theory of Vibration with Applications. Upper Saddle River, New Jersey, Prentice-Hall, Inc.

Vander Wal, R., G. Berger and S. Mozes (2006). "Droplets splashing upon films of the same fluid of various depths." Experiments in Fluids **40**(1): 33-52-52.

Vu, H., D. Banks and G. Aguilar (2011). "Examining Viscosity and Surface Wettability in Lamella Lift Dynamics and Droplet Splashing." Atomization and Sprays **21**(4).

2.5. Study: Wetting, Viscosity, and Post-Impact Splashing

Droplet impact with a dry surface often results in splashing rather than the oscillation behavior examined in the previous study. This tends to occur at increased impact velocity, although the exact conditions that lead to splashing are complex and influenced by many factors. Two factors that do influence splashing, in much the same way as they influenced post-impact oscillations in less energetic impacts, are viscosity and surface wettability. This study explores how those factors affect splashing dynamics during single droplet impacts.

Recent research has shown that changing the pressure or density of the surrounding air may significantly alter the threshold of splashing (Xu, Zhang et al. 2005, Jepsen, Yoon et al. 2006, Xu 2007, Liu, Vu et al. 2010). Accordingly, the shear stress between the droplet and the surrounding gas becomes a key parameter for the prediction of splashing. In a recent study, Xu (Xu 2007) provided supporting evidence for this claim by discovering that as the ambient pressure drops to 0.17 atm, splashing was suppressed. Further description of the interaction between a water droplet and ambient gas during impact was presented by Jepsen et al. (Jepsen, Yoon et al. 2006), who used the Schlieren photography method to provide experimental evidence of gas movement, which varied with the ambient pressure during a water slug impact onto a solid surface. Recently, Liu et al. (Liu, Vu et al. 2010) confirmed the validity of this effect, extending Xu's study and proving that for super-atmospheric conditions splashing was intensified. This parallels findings in drop-drop collision studies, where increasing ambient pressure is found to increase the likelihood of the colliding drops coalescing versus bouncing off each other- highlighting changing influence between the liquid surface tension and the surrounding gas (Post and Abraham 2002).

Many experimental correlations exist to predict the quantitative threshold of splashing during droplet impact and most are based on the Weber number (*We*) and the Reynolds number (*Re*) or some combination of the two (Stow and Hadfield 1981, Mundo, Sommerfeld et al. 1995, Vander Wal, Berger et al. 2006, Liu, Vu et al. 2010). These studies have related the threshold of splashing to liquid properties, most importantly the surface tension and viscosity, droplet size and velocity, and to the impact surface characteristics. Correlations may often be divided into those that predict a direct relationship between droplet viscosity and impact kinetics required for splashing (Stow and Hadfield 1981, Mundo, Sommerfeld et al. 1995), and those that predict an inverse relationship (Vander Wal, Berger et al. 2006, Xu 2007, Liu, Vu et al. 2010). A direct relationship means that increasing viscosity would have a tendency to suppress splashing (following intuition) and *vice versa* for an inverse relationship. Clearly these correlations would diverge widely in their splash predictions through a broad range of fluid properties. Xu (Xu 2007) also found a transition point in which the gas density required to initiate splash changes from an inverse to direct function of viscosity.

In this study, fluid viscosity is examined through a wide range of *Re* to determine its effect on splashing. A more in-depth analysis of the mechanisms of splashing is presented by focusing on the spreading lamella, which has been found recently by Bird et al. (Bird, Tsai et al. 2009) to be critical to splashing. By considering the forces acting on the lamella, the as yet unknown mechanism for the vertical velocity component of splashing on dry, smooth surfaces may be determined. This analysis also brings to consideration an adhesive force, dependent upon the chemical affinity or wettability between the liquid and solid surface. Surface wettability has been shown to play an important role in droplet impact dynamics (Ukiwe, Mansouri et al. 2005, Li, Ma et al. 2009), affecting the spreading and receding behavior during impact. But to the au-

thors' knowledge, this effect has not been studied specifically for its influence on splashing. Some additional experiments are performed using water droplets impinging onto surfaces treated to be hydrophilic and hydrophobic to verify the existence and magnitude of an adhesive force. Considering this adhesive force may also explain why within a specific range of viscosity, splashing is promoted. Both higher and lower viscosities than this range inhibit splashing. Eventually, with highly viscous droplets, splashing becomes impossible due to a shortening of a "time window" with respect to a characteristic ligament elongation and breakup time.

2.5.1. Experimental Setup

To supplement available existing experimental data (Vander Wal, Berger et al. 2006, Xu 2007, Liu, Vu et al. 2010), additional droplet impact measurements were performed using FC-72 and aqueous glycerol solutions ranging from 0-100% by weight. Fluid properties are provided in Table 2.6 and were obtained from the manufacturer of FC-72 (perfluorohexane, C_6F_{14}) (3M Specialty Materials, St. Paul, MN) and the CRC Handbook of Chemistry and Physics for the aqueous glycerol solutions (Lide 2006). When necessary, properties were interpolated from available data. The selection of these fluids provides a wide range of fluid viscosity. High glycerol concentrations were chosen because this is where viscosity changes more significantly with changing concentration. A schematic diagram of the experimental apparatus is provided in Figure 2.18. A precision pneumatic micro-liter valve with stainless steel tips of various outer diameters was used to generate droplets of 1.5-3.8 mm diameter. The distance from the nozzle tip to the impact surface was varied from 0.05 to 0.82 m using an adjustable tower to produce impact velocities from 1 to 5 m/s. A smooth Plexiglas surface, approximately 10 cm x 10 cm, with less than 0.8 μm in roughness was used as the impact surface. All experiments were performed isothermally at room temperature and within a custom-made aluminum pressure chamber to vary ambient

pressure from 0.3-6 atm. The chamber was 35 cm long by 30 cm diameter. Clear polycarbonate windows of 15 cm diameter permitted imaging of the impact phenomena with a Phantom V7.1 high-speed camera set at 10000 fps. Images were backlit with a high-power tungsten lamp with light diffuser.

Table 2.6. Fluid Properties of FC-72 and Glycerol Mixtures

	ρ (kg/m^3)	μ (Pa·s)	σ (N/m)
FC-72	1680	0.00064	0.012
Water	998	0.001	0.0728
50% aq. glycerol	1126	0.006	0.0674
60% aq. glycerol	1154	0.0108	0.0669
70% aq. glycerol	1181	0.0225	0.0665
80% aq. glycerol	1209	0.0601	0.0657
85% aq. glycerol	1223	0.1065	0.0652
90% aq. glycerol	1235	0.219	0.0645
Glycerol	1260	1.41	0.0633

Splashing is defined as the appearance of secondary drops. Impact outcomes for each of the tested cases were verified by repeating them at least once. Several repetitions were taken for cases of questionable outcomes or high variability, and the results averaged. Cases where splashing and non-splashing appeared to occur equally were considered "threshold" cases, though this is somewhat subjective.

A wettability study was also performed for water droplets by coating the impact surface to be hydrophilic and hydrophobic using commercially available products (Rain-X, Blue Coral-Slick 50, Ltd., Cleveland, OH). For the hydrophilic case, the water droplets completely wetted the surface; while the hydrophobic case produced a static contact angle of about 130˚ (untreated Plexiglas produces a contact angle of 150˚). Impact outcomes for each of the tested cases were verified by repeating each case 4 times. Again, for cases of questionable outcomes or high variabil-

ity, more measurements were taken and the results averaged, and cases where splashing and non-splashing occurred equally were designated as "threshold".
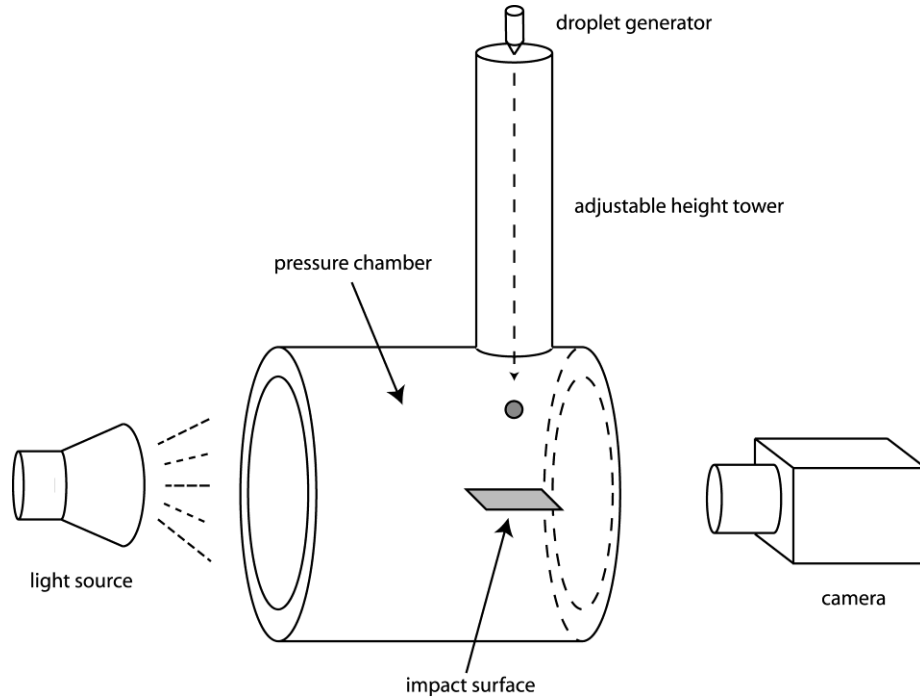
Figure 2.18. High pressure droplet impact apparatus.

2.5.2. Viscosity and Splashing

Figure 2.19 shows the changes in impact dynamics as Re and We are changed at 3 atm. This pressure was chosen because the results are qualitatively clearer than those seen at other pressures. Here, Re and We are used as non-dimensional representations of fluid viscosity and surface tension. The conditions shown are, from left to right: (a) water at 2.5 m/s, (b) water at 3.5 m/s, (c) 50% glycerol at 3.5 m/s, and (d) 90% glycerol at 3.5 m/s. The corresponding Re and We are given below the figure with dimensionless times (defined by Equation [2-11]) given in each frame. Splashing does not occur for the water droplet impacting at 2.5 m/s. But as impact velocity and thus We is increased, some splashing becomes visible at a time of 0.2 after impact.
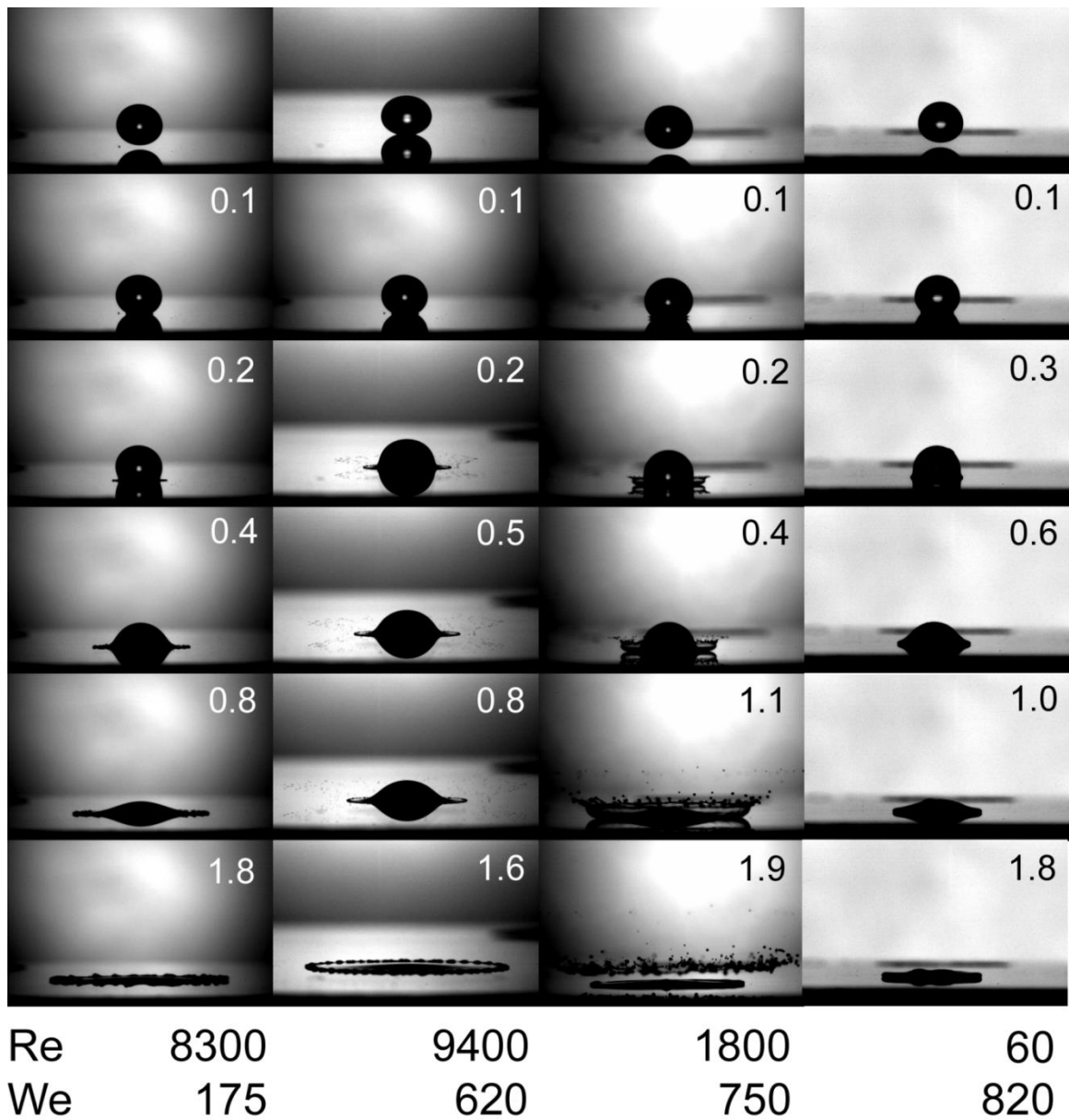
Figure 2.19. Changing splashing characteristics through a range of *Re* and *We* using aqueous glycerol solutions at 3 atm.
The inset numbers are dimensionless times from impact.

$$t_d = \frac{tU_0}{d}$$
[2-11]

This is seen in Figure 2.19 a and b. Interestingly, as Re is decreased significantly for the 50% glycerol with We remaining fairly constant, splashing quantity is increased dramatically (Figure 2.19b and c). Further decrease in Re by increasing viscosity with a 90% glycerol solution, however, inhibits splashing and spreading completely (Figure 2.19c and d). Clearly, a non-obvious combination of Re and We exists that minimizes the impact energy required for splashing.
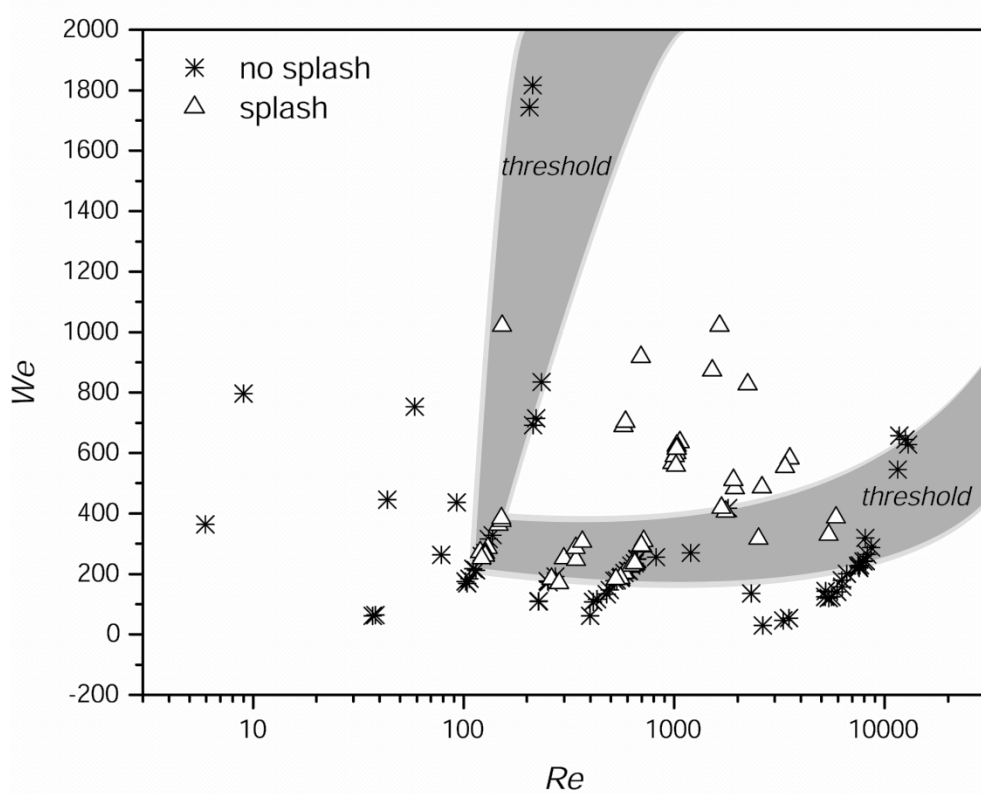
Figure 2.20. Changes in impact kinetic energy (~We) required for splashing as a function of Re at 1 atm for aqueous glycerol solutions.

Figure 2.20 further reinforces this notion for aqueous glycerol solutions in atmospheric conditions by revealing that for a range of *Re* of approximately 100-500, the *We* required for splashing reaches a minimum. Outside this range of *Re*, splashing requires higher impact kinetic energy. The threshold space is defined for the region between consistent splashing and non-splashing. For highly viscous mixtures with *Re* below 100, splashing could not be achieved within the limits of the experimental apparatus so a projected threshold region is proposed.
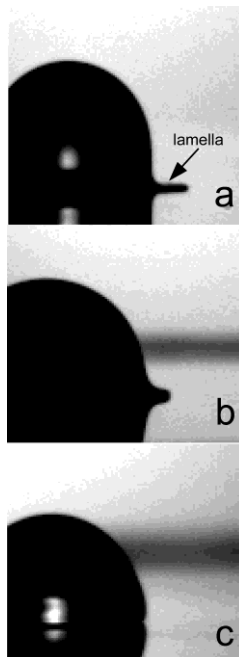
Figure 2.21. A spreading lamella thickness comparison.
Taken at a dimensionless time of approximately 0.2 after impact for (a) water, (b) 50% glycerol and (c) 85% glycerol.

A closer look at the impact dynamics reveals some of the effects of increasing viscosity. As shown in Figure 2.21, the spreading lamella appears to increase in thickness as the fluid viscosity increases. In effect, viscosity may destabilize the lamella by increasing its thickness and reducing the cohesive effect of surface tension. At the same time, however, the opposing effect of

slowing splashing dynamics also occurs with increasing viscosity, as seen by comparison of Figure 2.21 a, b and c, corresponding to pure water, 50% and 85% glycerol solutions, respectively. More evidence for this may be seen in Figure 2.22. The time of actual satellite droplet formation at the location of maximum spreading (fingers' tips) appears to be significantly delayed for the more viscous, 85% glycerol solution (Figure 2.22b) relative to the less viscous, 50% glycerol solution (Figure 2.22a). Thus, while higher viscosity may promote a thicker (Figure 2.21) and consequently more unstable lamella growth that prompts splashing, the simultaneous suppressive mechanism of viscosity delays the onset of splashing beyond a certain "time window" of opportunity. In fact, much of the splashing data for the 85% glycerol solution is inconsistent, which may be an indication that the slow growth rate of instabilities is bordering at this time threshold of opportunity.
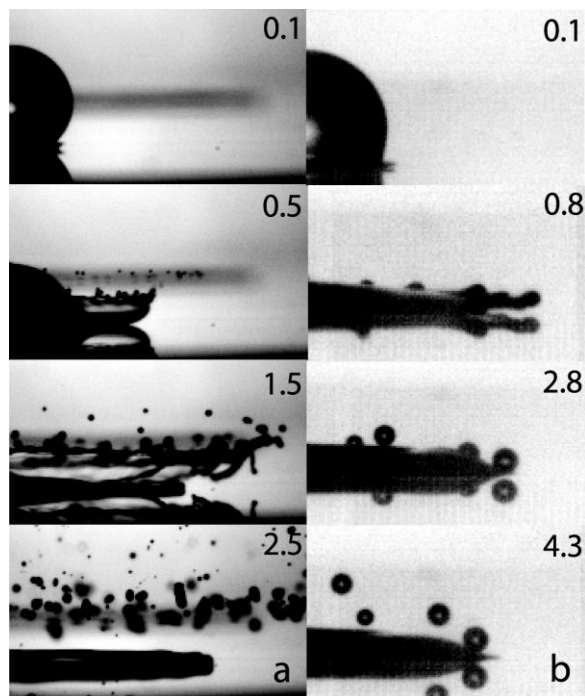
Figure 2.22. A comparison of crown formation and break up times relative to spreading. (a) 50% glycerol at 3 atm and (b) 85% glycerol at 5.5 atm. Dimensionless times from impact are provided.

2.5.3. Lamella Lift Dynamics

As noted before, previous work has suggested that the ambient air pressure has a significant effect on splashing. This has been explained by Jepsen (Jepsen, Yoon et al. 2006) as a compressive effect in which the gas below the droplet is compressed and forced outward, while causing a shearing force on the droplet surface. A closer look at the splashing dynamics, however, reveals that splashing is initiated and continues long after droplet impact. Splashing, under the conditions of interest, is more likely initiated post-impact, at the leading edge of the spreading lamella. Therefore, a closer look at this location is warranted. Splashing requires some vertical momentum in order for satellite droplets to separate from the surface and the bulk droplet. With this as a premise, a requirement for splashing is that the lamella lifts off of the impinged surface.
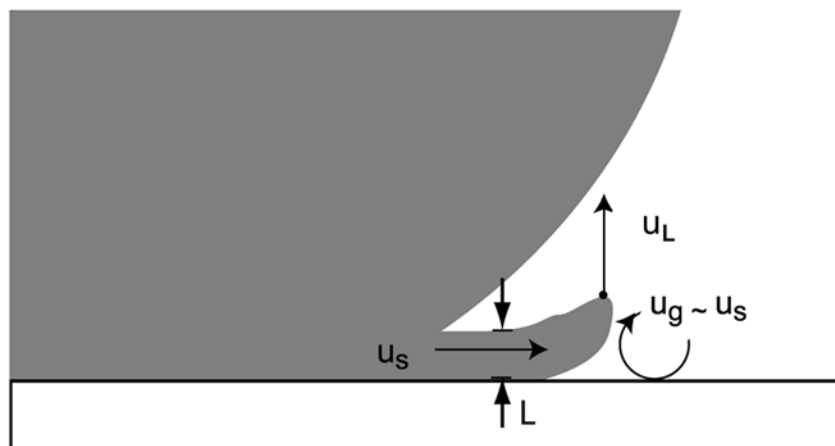
Figure 2.23. Schematic of lamella lift and the relevant velocities.

Referring to Figure 2.23, a momentum balance may be performed at the lamella edge, in the vertical direction:

$$\rho_l V \frac{du_L}{dt} = \frac{1}{2}\rho_g u_g^2 C_d S - \sigma_{lg} L - F_{ls}$$

[2-12]

where F_{ls} is some adhesion or chemical affinity that the liquid has with the impinged surface, which may be related to the dynamic contact angle. (This was not measurable in the videos, however, due to insufficient image resolution and acquisition rate.) The term on the left is the vertical momentum of the lamella. This is equated to the momentum imparted on the lamella by the gas motion minus the opposing effects of surface tension resisting vertical deformation and adhesion holding the lamella to the surface. We may assume that as the lamella spreads radially outward, the surrounding gas is displaced upward at a velocity of the same order of magnitude as the spreading velocity, creating a vertical velocity, $u_g \sim u_L \approx \sqrt{Du_o/4t}$. This is in fact corroborated in the work by Jepsen et al. (Jepsen, Yoon et al. 2006) and later by Liu et al (Liu, Vu et al. 2010). The thickness of the lamella will scale with the boundary layer thickness, so $L \sim \sqrt{\upsilon_l t}$. The surface area, S, is determined by the L and the perimeter of the lamella:

$$P = 2\pi r(t) \approx 2\pi \int \sqrt{\frac{Du_0}{4t}} dt \approx 2\pi\sqrt{Du_0 t}$$

[2-13]

A requirement for lamella lift is that its vertical momentum be greater than zero. Therefore, we may set the LHS of Equation [2-12] to zero to determine the threshold conditions for lift. Substituting and rearranging terms, we have:

$$\frac{\pi}{4}\rho_g (Du_0)^{\frac{3}{2}} C_d \sqrt{\upsilon_l} = \sigma_{lg}\sqrt{Du_0 t} + F_{ls}$$

[2-14]

Lift is most likely to occur at the earliest possible time after impact since the air velocity will decrease significantly with time. This is the moment when a distinct lamella layer extends beyond the outer boundary of the bulk droplet. According to Bird et al. (Bird, Tsai et al. 2009), this time is $t_c \sim \upsilon / u_o^2$. Substituting and simplifying again:

$$\rho_g C_d \mathrm{Re}_{L,l}^{\frac{3}{2}} v_l^2 = \frac{\rho_l \mathrm{Re}_{L,l} v_l^2}{\mathrm{We}_{L,l}} + F_{ls} \qquad [2\text{-}15]$$

Because of the very low *Re* existing with respect to the lamella thickness, C_d may be computed using a well-established correlation for laminar flow over a smooth, flat plate (Çengel and Turner 2001):

$$C_d = \frac{1.328}{\mathrm{Re}_{L,l}^{\frac{1}{2}}} \approx \frac{1.328\sqrt{v_g}}{\left(\frac{Du_0 v_l}{4}\right)^{\frac{1}{4}}} \qquad [2\text{-}16]$$

Interestingly, if we ignore F_{ls}, Equation 4 simplifies to a form very similar to (Mundo, Sommerfeld et al. 1995):

$$\left(\frac{\rho_g \mu_g}{\rho_l \mu_l}\right)^{\frac{1}{4}} \mathrm{Oh}_{L,l} \mathrm{Re}_{L,l}^{\frac{9}{8}} \sim \frac{1}{\mu_l^{\frac{3}{8}}} \qquad [2\text{-}17]$$

which according to Mundo et al., is of order ~1. This analytically derived expression shows that splashing should always decrease with increasing liquid viscosity, following intuition. As will be shown later, the regime in the high *Re* range where viscosity appears to promote splashing may actually be due to the F_{ls} term.

2.5.4. Ligament Dynamics and Satellite Droplet Formation

Lamella lift is a necessary, though insufficient condition for splashing since it provides no provision for satellite droplet formation. Figure 2.24 demonstrates this with a 15% glycerol

droplet where lamella lift occurs without splashing. Here the theoretical framework describing

the physics of a second requirement for splash formation is presented.
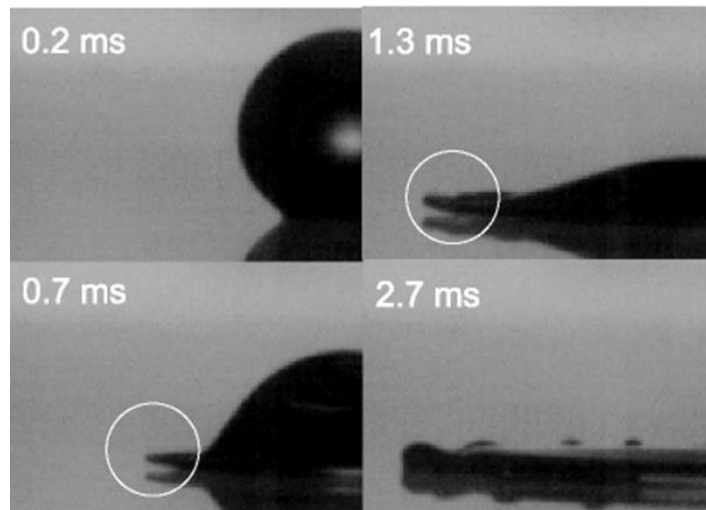
Figure 2.24. Lamella lift without splashing for 15% glycerol solution at 4.5 atm.
Elapsed times from impact are provided.
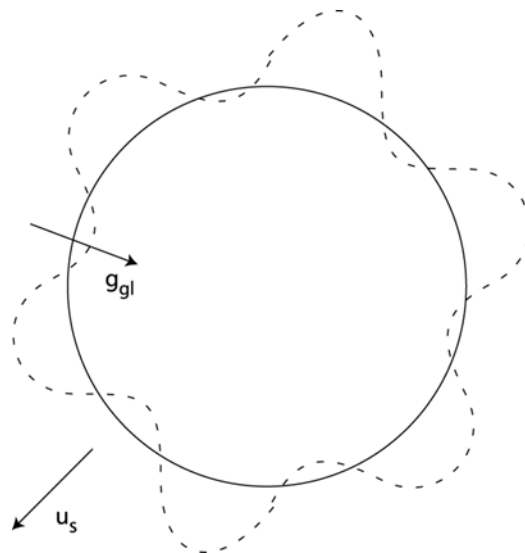
Figure 2.25. Top view of droplet impact with undulations formed under the strong acceleration
field.

Until this point, no mention has been made of the obvious wave-like undulations of the lamella edge during spreading. Analogous to the formation of a spray from an unbroken liquid jet, droplets form from these undulations as they elongate into ligaments, or "fingers", and eventually break by capillary pinching. But the mechanism by which these ligaments initially form has been under debate, though Rayleigh-Taylor (RT) instability theory has been shown to be plausible and simple to apply for this scenario (Allen 1975). RT instability arises at the interface between two fluids of different densities where there is acceleration from the lighter to heavier fluid, as depicted in Figure 2.25. If we assume irrotational, inviscid 2-D flow, we may use the following dispersion relation describing the interfacial wave dynamics (Allen 1975):

$$n^2 = \frac{\rho_l - \rho_g}{\rho_l + \rho_g} a_{gl} k - \frac{\sigma k^3}{\rho_l + \rho_g} \qquad [2\text{-}18]$$

where n is the growth rate of waves and k is wavenumber in inverse length units ($k \equiv 1/\lambda$). Taking $\partial n / \partial k = 0$ and inverting, we get an expression for the fastest growing wavelength:

$$\lambda^2 = \frac{3\sigma}{a_{gl}(\rho_l - \rho_g)} \qquad [2\text{-}19]$$

This is the wavelength most likely to manifest. The acceleration may be determined by taking the time derivative of the expression for spreading velocity:

$$a_{gl} = 0.5 \sqrt{\frac{Du_0}{4}} t^{-1.5} \qquad [2\text{-}20]$$

By combining Equations [2-13], [2-19], and [2-20] and simplifying, a predictive expression for the number of fingers is obtained:

$$N_f = \frac{P}{\lambda} \approx \frac{\pi (Du_0)^{\frac{3}{4}} (\rho_l - \rho_g)^{\frac{1}{2}}}{(3\sigma)^{\frac{1}{2}} t^{\frac{1}{4}}} \qquad [2\text{-}21]$$
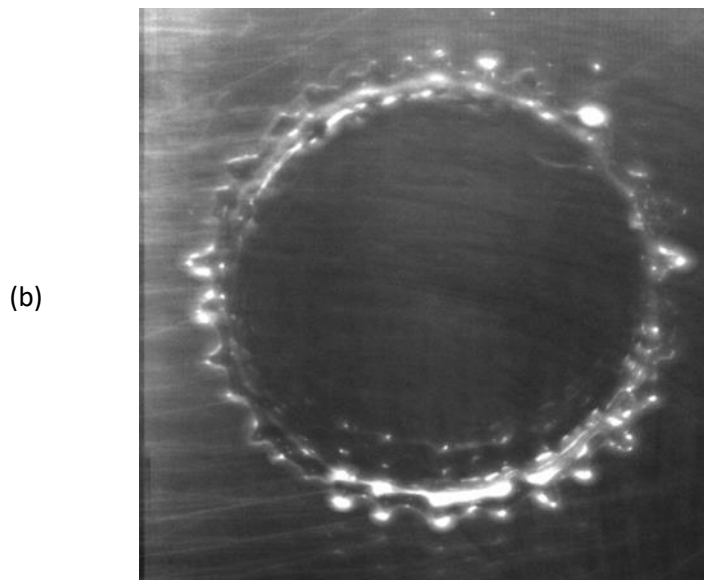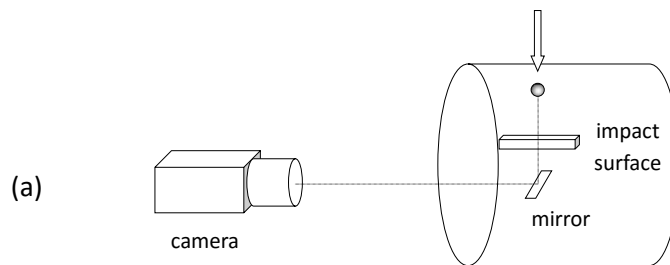
Figure 2.26. Experimental apparatus for imaging (a) and typical image of droplet impact finger-ing (b).

According to Equation [2-21], the wavelength and, thus, number of fingers clearly re-mains a function of time and will theoretically decrease over the course of spreading. This has been shown to be the case by Thoroddsen and Sakakibara (Thoroddsen and Sakakibara 1998). By retrofitting the pressure chamber with a mirror to obtain an axisymmetric view of spreading from below the impact surface (Figure 2.26a), the number of fingers that form at a given in-

stance in time may be counted (Figure 2.26b). Several representative cases for three different

fluids are shown by the symbols in Figure 2.28, where the solid and dashed lines represent the

theoretical predictions by the RT instability theory corresponding to Eq. [2-21] and to an equiva-

lent equation which results from using the angular wavenumber-wavelength relationship:

$k = 2\pi/\lambda$, respectively. It appears that despite the many assumptions of RT theory, the number

of fingers that it predicts is within the same order of magnitude of that observed experimental-

ly, especially when using $k=1/\lambda$, though the counts are subjective and error-prone due to the

image resolution. Furthermore, the experimental counts for all three fluids are similar, though

they show a trend of decreasing number to a steady, asymptotic value as predicted by theory.
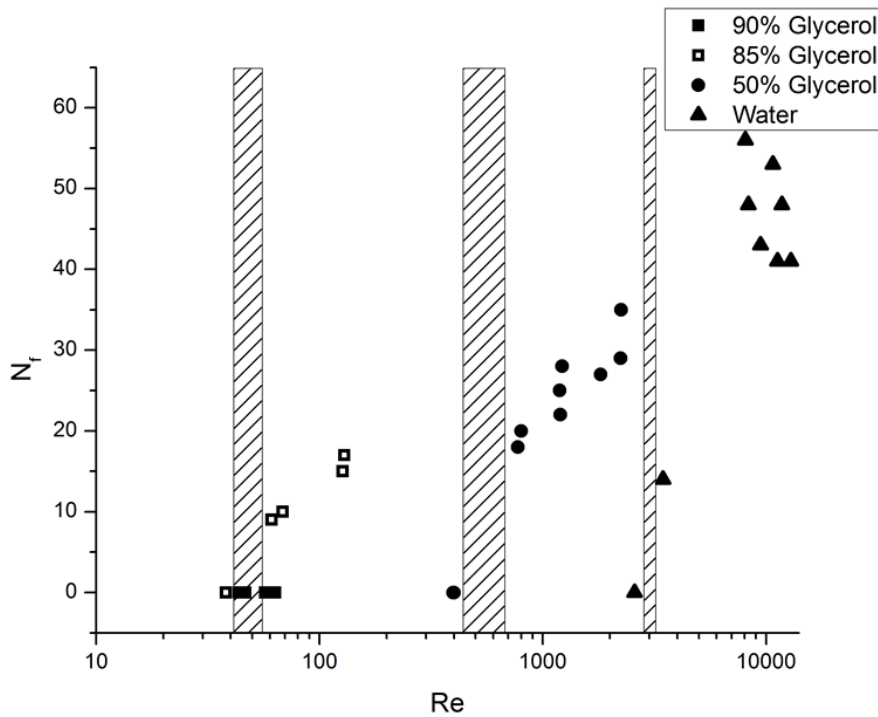
Figure 2.27 Experimentally determined number of fingers as a function of *Re.*
Using water, 50% glycerol and 90% glycerol. The shaded regions represent the thresholds for
finger appearance.
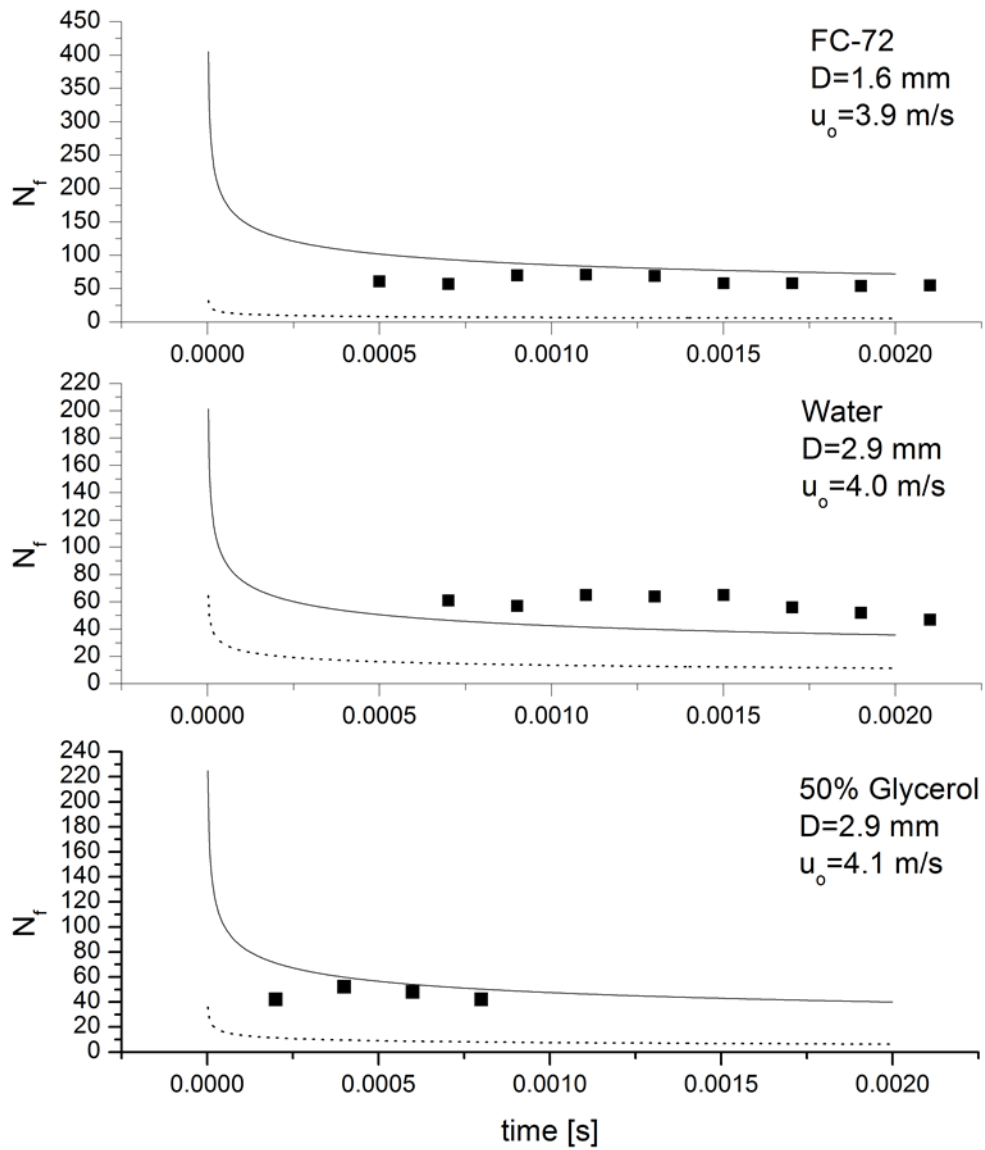
Figure 2.28. Comparison of RT instability predictions of the number of fingers at the lamella edge to experimentally determined values at fixed times.
Solid line is the prediction using linear wavenumber, $k = 1/\lambda$. Dotted line uses angular wavenumber, $k = 2\pi/\lambda$.

It is also interesting to note that viscosity has a non-trivial role in the formation of fingers (Figure 2.27), which is not predicted by RT instability as per Equation [2-21] since it is not a function of viscosity. The number of fingers and minimum value of Reynolds number for fingers to appear changes drastically with viscosity, as all fluids in Figure 2.27 have similar properties except viscosity. Note that as the viscosity of the droplet increases, the transition range of *Re* for the appearance of fingers (denoted by the shaded regions) decreases, seen up to the 85% glycerol drops (μ = 0.107 Pa·s). For the most viscous solution, however, (90% glycerol solution, μ= 0.219 Pa·s), the appearance of fingers is imperceptible for the conditions covered in this study. This supports the idea of a range of viscosity within which splashing is most likely, as seen in Figure 2.20. The reasons for this are currently unknown and beyond the scope of the study.

Alone, RT instability theory cannot predict splashing, and recent research has highlighted that Kelvin-Helmholtz theory may be more suitable as an overall splashing predictor (Yoon, Jepsen et al. 2007, Yoon, Jepsen et al. 2009). However, despite this and other aforementioned limitations, for the purposes of this study, RT theory appears to at least provide a close estimate of the fastest growing wavelength (Eq. [2-19]) and thus ligament thickness, so the focus now moves to the dynamics of elongation and breakup. A momentum balance within the ligament will ensure that breakup can physically occur. The volume of a ligament as a function of time is:

$$\frac{\pi}{4}\lambda^2 \int_t \left(\frac{Du_0}{4t}\right)^{0.5} dt = \frac{\pi}{4}\lambda^2 (Du_0 t)^{0.5} \qquad [2\text{-}22]$$

The momentum of a ligament may then be equated to surface tension to determine a time window of breakup, t_{mom}:

$$\frac{1}{2}\rho_l \left(\frac{\pi}{4}\lambda^2 (Du_0 t)^{0.5}\right)\left(\frac{1}{4}\frac{(Du_0)^{0.5}}{t^{1.5}}\right) = \sigma_{lg}\frac{\pi}{4}\lambda^2 \qquad [2\text{-}23a]$$

$$t_{mom} = \frac{\rho_l D u_0}{8\sigma_{lg}} \qquad\qquad [2\text{-}22b]$$

This time represents the time from impact in which the momentum of the ligament is suffi-cient to break surface tension. Using typical droplet properties of water, we find that t_{mom} is ~20 ms, far longer than the total spreading time, t_s, experimentally measured as ~5 ms. This is, therefore, not a likely limiting factor to ligament breakup.

Another timescale of interest is the capillary of a ligament, as determined by Marmottant and Villermaux in their studies of spray formation (Marmottant and Villermaux 2004):

$$t_\sigma = \sqrt{\frac{\rho_l \lambda^3}{\sigma_{lg}}} \qquad\qquad [2\text{-}24]$$

This is a value representing the time required for the liquid to flow through the ligament as it elongates. If ligament dynamics occur on a shorter timescale, breakage will occur. To test if this is the limiting time to ligament breakage, we take the ratio of t_σ to the experimentally de-termined time of breakup as a function of ligament Re, shown in Figure 2.29. The large error bars represent the uncertainty in measured time of breakup due to the video frame rate. At early times, this error is comparable to the actual time of breakup. Despite significant scatter, the ratios generally are near 1, an indication that t_σ is likely the major limiting time for breakup.

This limiting time may be compared to a "time window" of opportunity for splashing to occur. In light of the analytical developments just presented, this window is most likely the spreading time of the droplet (t_s). For viscous droplets, t_s may be reduced significantly as shown in Figure 2.30. The ligament breakup time, t_σ, must be smaller than t_s for breakup to occur. If not, there is insufficient time for the dynamics of ligament elongation to take place and breakup cannot happen.
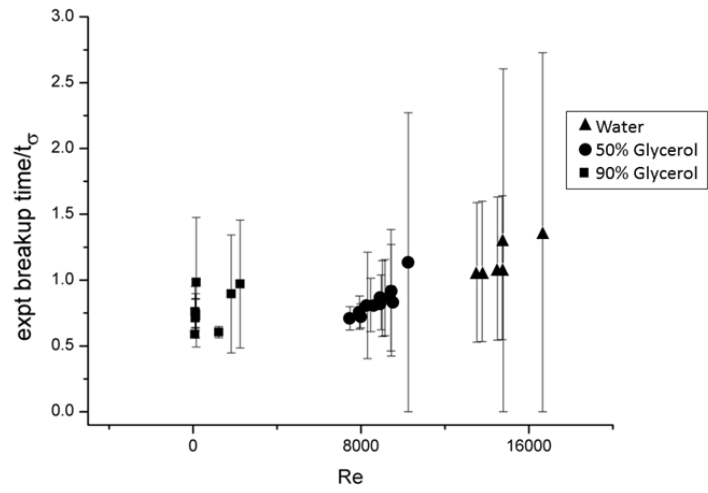
Figure 2.29. Ratio of experimental breakup times to ligament capillary times, t_σ as a function of Re.
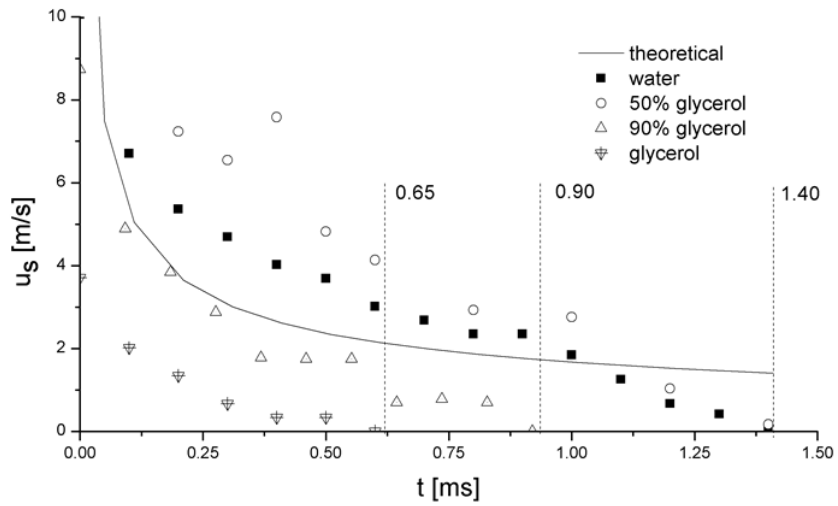
Figure 2.30. Changes in spreading velocity dynamics with increasingly viscous liquids. For all cases, $D \approx 2.9$ mm and $u_o \approx 4$ m/s. Dashed lines indicate times of spreading cessation.

2.5.5. Droplet Surface Wettability Splashing

We now examine the F_{ls} term of Equation [2-12] by experimentally confirming an adhesive effect and discussing its implications on splashing. As shown in Figure 2.31, the adhesive effect is confirmed by the experimental data. The hydrophilic surface clearly requires higher gas density to induce splashing. This is most evident at the 2.6 m/s impact velocity.

The experimental data may also be used to verify the F_{ls} term in Equation [2-15]. Plots of the ratio of the "gas term", a quantity promoting lift, with the suppressive surface tension term reveals a difference in splash threshold ratio between the hydrophilic and hydrophobic surfaces (Figure 2.32a,b). The hydrophilic data requires a higher gas density to induce splashing. The difference in threshold represents a relative quantity for F_{ls}, 4 x 10^{-9} N in this case. Using this value to correct the hydrophilic data brings the threshold to the same level as the hydrophobic data (Figure 2.32c). This suggests that F_{ls} is a constant, dependent only on the chemical affinity of the liquid to the impact surface, and not a function of kinematic properties.

A major implication of recognizing the existence of the F_{ls} term is shown in Figure 2.33 where the lift threshold for various gas pressures is plotted as a function of kinematic viscosity. It reveals that there is a non-obvious viscosity corresponding to the minimum energy necessary to induce lift. This minimum point changes with F_{ls}. A very similar curve was measured experimentally by Xu (Xu 2007) by varying the viscosity of the droplet, drawing attention to the seemingly paradoxical effect of viscosity in which it can both promote and inhibit splashing. As the magnitude of the surface tension term becomes comparable to the F_{ls} term a reversal of the role of viscosity can be seen. In cases of low viscosity such as this, lamella lift appears to be a sufficient condition for splash as the time window for splash is not a limiting factor.
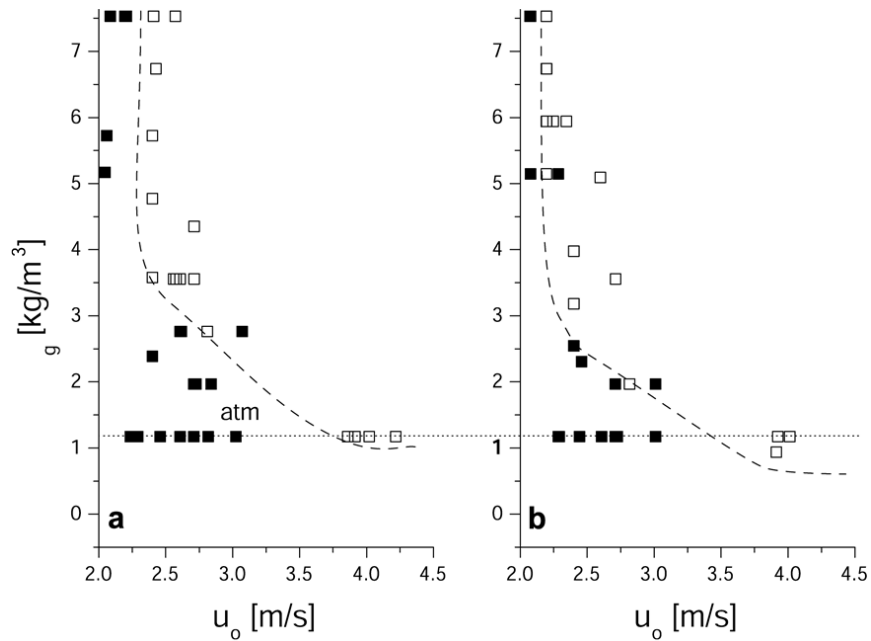
Figure 2.31. Experimental results with (a) hydrophilic and (b) hydrophobic surfaces. Impact diameters are approximately 3.5 mm.
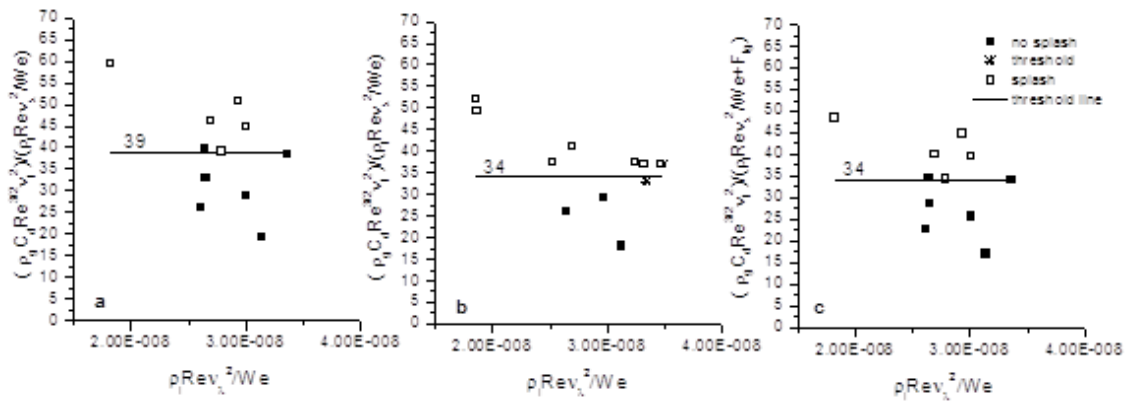
Figure 2.32. Threshold requirements for lamella lift for water droplets impinging onto a (a) hydrophilic and (b) hydrophobic surface. The addition of the F_{ls} term (c) lowers the hydrophilic threshold to that of the hydrophobic surface.
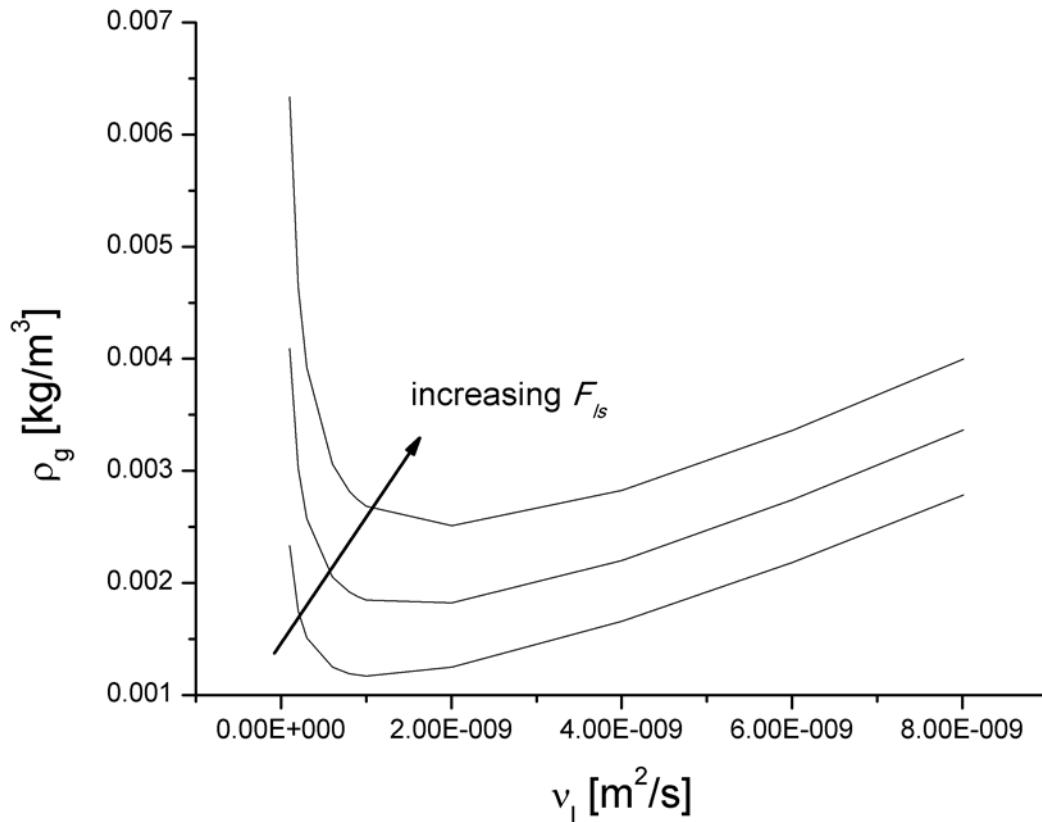
Figure 2.33. A parametric analysis of the effect of v_l on the threshold ρ_g required for lamella lift using a water droplet with D = 3.6 mm and u_s = 2.8 m/s.

2.5.6. Conclusions

Analytical advancements were made in explaining and predicting the onset of splashing of single droplets impinging on a flat smooth surface. Two separate requirements for splashing were revealed: lamella lift, and ligament elongation and breakup. Both must be satisfied for splashing to occur. RT instability theory was found to accurately predict finger formation except for the cases of high liquid viscosity or low gas density, where instabilities appear to cease abruptly. For highly viscous droplets, the "time window" of opportunity of splashing is reduced as

71

the spreading time t_s of the lamella is reduced. The capillary time of the ligament t_σ is the limiting time that must be overcome to for the lamella to break up into droplets (initiation of splashing). If the spreading time is shorter, then the impact dynamics end before the ligament has time to fully elongate and break. The inclusion of an adhesion term, likely associated with the chemical affinity of the liquid to impact surface, in the lift threshold may explain the paradoxical effect of viscosity on splashing.

Connection with the Dissertation Premise

Similar to the prior chapter, the findings of this study do not directly connect to thermal boundary layer dynamics. Instead, the splashing dynamics govern the ultimate disposition of droplet liquid, the subsequent growth of the thermal boundary layer as the liquid heats after deposition, and the condition of the impact surface for subsequent droplets in a spray. A droplet that strongly splashes will deposit cool liquid across a large surface area, providing a non-uniform but widespread cooling effect. Depending on the application, this could be beneficial – e.g., a high thermal conductivity surface that will minimize the non-uniformity while experiencing enhanced cooling due to the additional contact area – or detrimental, e.g., a materials thermal processing procedure that demands even cooling to achieve consistent properties.

Figure 2.34 highlights the timescales investigated in this study, with regard in particular to dry surface impacts. The splashing dynamics and lamella-surface-atmosphere interactions that were the subjects of this study generally occur within the initial impact and spreading timescales, with the exception of receding lamella breakup occurring immediately afterward. The next study complements this one by investigating pool impact splashing.

Time Scale		Fluid Dynamics	Thermal Effects
Impact (0-2 ms)		Dry / pool: Prompt splashing	Dry: Large ΔT at point of impact
2 – 10 ms		Dry: Spreading lamella, corona splashing	Dry: temperature minimum **Splashing and lamella spreading dynamics govern droplet coverage area and local convection between the droplet and the surface.**
10 – 100 ms		Dry: Receding lamella, high amplitude initial oscillation	Dry: Heating of droplet fluid (boundary layer growth)

Figure 2.34. Droplet impact dynamics timeline, dry surface splashing dynamics. Prompt splashing, corona splashing, receding breakup, and other lamella dynamics occur within the first few stages of the timeline.

References

Allen, R. F. (1975). "Role of Surface-Tension in Splashing." <u>Journal of Colloid and Interface Science</u> **51**(2): 350-351.

Bird, J. C., S. S. H. Tsai and H. A. Stone (2009). "Inclined to splash: triggering and inhibiting a splash with tangential velocity." <u>New Journal of Physics</u> **11**(6): 063017.

Çengel, Y. A. and R. H. Turner (2001). <u>Fundamentals of thermal-fluid sciences</u>. Boston, McGraw-Hill.

Jepsen, R. A., S. S. Yoon and B. Demosthenous (2006). "Effects of air on splashing during a large droplet impact: Experimental and numerical investigations." <u>Atomization and Sprays</u> **16**(8): 981-996.

Li, X. Y., X. H. Ma and Z. Lan (2009). "Behavioral Patterns of Drop Impingement onto Rigid Substrates with a Wide Range of Wettability and Different Surface Temperatures." <u>Aiche Journal</u> **55**(8): 1983-1992.

Lide, D. (2006). <u>CRC Handbook of Chemistry and Physics: A Ready-Reference Book of Chemical and Physical Data</u> Boca Raton, Fl, CRC Press.

Liu, J., H. Vu, S. S. Yoon, R. Jepsen and G. Aguilar (2010). "Splashing Phenomena during Liquid Droplet Impact." <u>Atomization and Sprays</u> **20**(4): 297-310.

Marmottant, P. H. and E. Villermaux (2004). "On spray formation." <u>Journal of Fluid Mechanics</u> **498**: 73-111.

Mundo, C., M. Sommerfeld and C. Tropea (1995). "Droplet-Wall Collisions - Experimental Studies of the Deformation and Breakup Process." <u>International Journal of Multiphase Flow</u> **21**(2): 151-173.

Post, S. L. and J. Abraham (2002). "Modeling the outcome of drop-drop collisions in Diesel sprays." <u>International Journal of Multiphase Flow</u> **28**(6): 997-1019.

Stow, C. D. and M. G. Hadfield (1981). "An Experimental Investigation of Fluid-Flow Resulting from the Impact of a Water Drop with an Unyielding Dry Surface." <u>Proceedings of the Royal Society of London Series a-Mathematical Physical and Engineering Sciences</u> **373**(1755): 419-441.

Thoroddsen, S. T. and J. Sakakibara (1998). "Evolution of the fingering pattern of an impacting drop." <u>Physics of Fluids</u> **10**(6): 1359-1374.

Ukiwe, C., A. Mansouri and D. Y. Kwok (2005). "The dynamics of impacting water droplets on alkanethiol self-assembled monolayers with co-adsorbed CH3 and CO2H terminal groups." <u>Journal of Colloid and Interface Science</u> **285**(2): 760-768.

Vander Wal, R. L., G. M. Berger and S. D. Mozes (2006). "The splash/non-splash boundary upon a dry surface and thin fluid film." Experiments in Fluids **40**(1): 53-59.

Xu, L. (2007). "Liquid drop splashing on smooth, rough, and textured surfaces." Physical Review E **75**(5): 056316-056311-056318.

Xu, L., W. W. Zhang and S. R. Nagel (2005). "Drop Splashing on a Dry Smooth Surface." Physical Review Letters **94**(18): 184505.

Yoon, S., R. Jepsen, S. James, J. Liu and G. Aguilar (2009). "Are Drop-Impact Phenomena Described by Rayleigh-Taylor or Kelvin-Helmholtz Theory?" Drying Technology **27**(3): 316-321.

Yoon, S., R. Jepsen, M. Nissen and T. Ohern (2007). "Experimental investigation on splashing and nonlinear fingerlike instability of large water drops." Journal of Fluids and Structures **23**(1): 101-115.

2.6. Study: Effects of Droplet and Film Properties on Dynamics of Single Droplet Impacts

The first objective of this study of droplet impact dynamics is to establish the effects of the fluid physical properties on the behaviors observed after impact. With water, glycerol, and mixtures thereof, a range of viscosity covering three orders of magnitude ($X < \nu < Y$) is investigated. FC-72, ethanol, and methanol are also used, demonstrating the effects of surface tension () and miscibility – FC-72 does not mix with water, while ethanol and methanol easily mix and glycerol does so with agitation. In contrast to most literature, the droplet and pool fluid are varied independently – the droplet can be a different liquid than the pool. This approach allows for individual behaviors to be attributed specifically to the pool or the droplet's characteristics – for example, it will be demonstrated that the crown formation is almost entirely based on the pool properties; splashing from the crown, however, tends to be a function of the droplet's species.

Liquid drop impacts have been studied since the advent of film photography in the nineteenth century, and drop impacts onto films of a different liquid were among the first experiments in this line of research (Worthington and Cole 1897). In more recent times, the thrust of drop–film impact research has concerned same-liquid situations, with little focus on impacts of drops onto differing fluid films (Rein 1993, Yarin 2006). Fedorchenko and Wang examined in detail the effects of viscosity on film and film impact outcomes, but did not separate the effects of film and droplet viscosity (Fedorchenko and Wang 2004). Vander Wal et al. explicitly state that their study is of drop impacts onto same-fluid films (Vander Wal, Berger et al. 2006). It seems that since 1975, little thought has been given to separating the properties of the film and of the drop (Smith 1975). With tremendous advances in imaging and correspondingly in the field of drop impact study, the topic is due for re-examination, especially given the numerous practical applications where drops impact on a different liquid film.

For example, sprays are prevalent means of fire suppression, and when solid material is burning a spray excels at extinguishing the fire. Film-fueled fires are less simple to quench. An incorrectly applied fire retardant can induce splashing, spread the burning liquid, and potentially worsen the fire. One solution is to use very fine sprays that evaporate rapidly and displace the ambient oxygen that combustion requires (Kim and Ryou 2003). Direct quenching of burning pools can extinguish the fire quickly—imperative in kitchen and engine room fires—but the impact outcomes of the spray must be controlled to prevent splashing and subsequent additional damage. In either case of film-fueled fires, the extinguishing spray and the burning pool will never be the same liquid; thus, an understanding of how the drop and film properties individually control impact outcomes is critical in this application of sprays. Another application of dissimilar drop and film fluids is spray freeze drying, especially in the biomedical field, where a feed spray impinges on a cryogen liquid and freezes into useful solid particles (Eslamian and Ashgriz 2011). On a cosmic scale, dissimilar "liquid" impacts are observed with meteor strikes: planetary crusts and atmospherically-superheated meteorites can behave analogously to viscous liquids at the velocity and energy scales observed in these events (Fink, Gault et al. 1984).

Rein defined four immediate outcomes after droplet impact in his review paper: floating, bouncing, coalescence, and splashing. He also defined subsequent outcomes happening after coalescence and splashing: vortex rings and jetting, respectively (Rein 1993). Floating and bouncing rarely occurred in his work's scope of study; these behaviors are typically associated with extremely low impact velocities (Rein 1993). This work instead focuses on the boundary between coalescence and splashing. The modified regimes examined in this study are therefore (1) coalescence, (2) crowning, and (3) crown splashing. In this study, these regimes are exam-

ined in light of varying the drop fluid and the pool fluid independently; drops of a range of fluids impact a corresponding range of films.

Fedorchenko and Wang's analysis of drop impacts on thin films went into significant detail concerning cavity formation and collapse and jet formation, and further proposed a model of crown formation. The maximum cavity depth and the length scales of the central jet are experimentally and analytically related to the Froude number as $Fr^{1/4}$ (Fedorchenko and Wang 2004). However, their analysis did not include the effects of surface tension. Vander Wal et al. noted that in fluids with increased surface tension, the occurrence of prompt splash was lessened, and also that increasing viscosity restricted splashing, both prompt and crown (Vander Wal, Berger et al. 2006). It is worth noting that Vander Wal et al. experimented with a range of viscosity covering one order of magnitude (Vander Wal, Berger et al. 2006), whereas this study covers three orders of magnitude in viscosity (Table 2.7). Both examine similar ranges of surface tension.

A general correlation for splashing on a liquid film was proposed by Cossali et al. for the regime $H^* \equiv \frac{h_{film}}{d_{drop}} < 1$ as (Cossali, Coghe et al. 1997):

$$\text{We} \cdot \text{Oh}^{-0.4} \geq 2100 + 5880 H^{*1.44} \qquad [2\text{-}25]$$

Cossali et al. specify that this correlation works only for $Oh_{drop} > 7 \times 10^{-3}$, which excludes water and FC-72 drops observed in this study. This correlation is also found to be accurate for very shallow films ($H^* < 0.2$) for lower Oh_{drop} numbers. Within that very thin film range of H^*, Vander Wal et al. found that surface roughness plays a significant role in the splashing behavior, with rougher surfaces increasing splashing tendencies (Vander Wal, Berger et al. 2005). That regime of H^* is outside of the range of this study, however. This study extends beyond the film thickness Cossali used, with $H^* = 1$.

Table 2.7. Mechanics properties of liquids for impact dynamics study

Liquid	Density (kg/m^3)	Viscosity (m^2/s)	Surface Tension (N/m)	Typical Ohnesorge
Water	998	1×10^{-6}	0.073	0.0021-0.0023
Glycerol	1260	6.5×10^{-4}	0.064	0.27-0.28
60/40 glycerol/water	1148	9×10^{-6}	0.067	0.020-0.022
85/15 glycerol/water	1222	9×10^{-5}	0.065	0.20-0.21
FC-72	1680	4×10^{-7}	0.010	0.0035-0.0040

On deeper films, Vander Wal et al. ultimately concluded that different splashing modes exist, relating to the film thickness and to fluid viscosity and surface tension, thus no single correlation is able to predict liquid film impact splashing universally (Vander Wal, Berger et al. 2006). Zhang et al. studied the formation of the crown in close detail, finding that splashing depends on the behavior of the immediate post-impact ejecta sheet and the somewhat delayed lamella formation (Zhang, Toole et al. 2011). Here, we focus on the behavior after impact more than the immediate lamella formation; and by separating drop and film properties hope to determine in more detail why a universal correlation for splashing is not practical.

Figure 2.35 shows the progression of crown behavior studied in this paper, based on a regime map by Rein, in order of increasing Weber number (Rein 1996). That study does not provide exact or even approximate values for the Weber number of transitions between the reported behaviors (crown formation, and crown splashing), but instead says that the transition Weber numbers depend on the Froude number; that is, the strength of inertial versus gravitational forces. Based on data from this study, the order of magnitude for the transition between each behavior is approximated in the figure.

In summary, this study seeks to fill in the gaps in the understanding of drop–film impact. A larger range of fluid viscosities is examined than has been used in any previous study, to the best of the authors' knowledge. Existing splashing correlations are found to be unable to address the full range of drops and films in this study, and new empirical correlations are proposed that predict crown formation and splashing based on the data from this study.
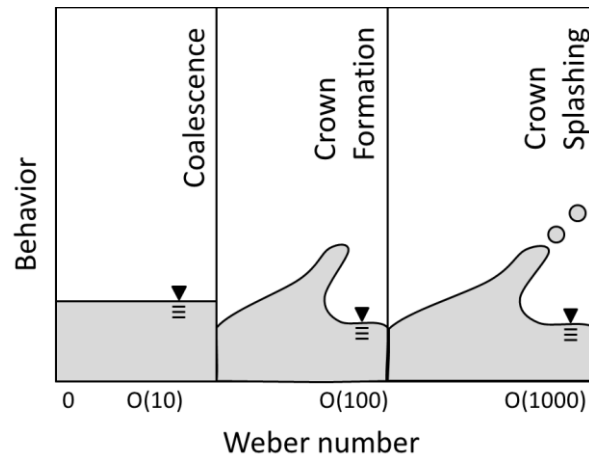
Figure 2.35. Weber-based regime map for drop impact onto liquid pools.
Based on past observations (Rein 1996), fitted to magnitudes found in this study. Diagram depicting the impact outcomes from a horizontal perspective.

2.6.1. Setup

A Phantom V7.1 video camera records the impacts at 512 ₤ 256 pixels resolution at 9000 fps through a Nikon Micro-Nikkor 105 mm f/2.8 lens. The Phantom Camera Control (PCC 1.3, Vision Research, Inc.) software captures impact videos. Using this software to measure objects of known dimensions gives approximately 1% error in length measurements (<±0.05 mm); velocity measurement is expected to have a larger error due to slight blurring due to exposure time (10 µs) and was assumed accurate to within ±0.1 m/s. Drop fluids used are water, 60% glycerol/40% water by weight mixture, 85% glycerol/15% water mixture, pure (>99.9%) glycerol, and

Fluoroinert FC-72 (3M). Table 1 lists the relevant properties of each fluid. As the droplets of water, glycerol, and the mixtures form at the tip of the stainless steel nozzle, they have diameters of 3.3±0.2 mm. FC-72 drops, however, have diameters of 1.7±0.1 mm due to their low surface tension. These conditions give a range of Weber number of 20 to 3,000 and Reynolds number from 20 to 14,000. Film depth is the same as the drop diameter for each experiment, corresponding to the intermediate film depth examined by Vander Wal et al. (Vander Wal, Berger et al. 2006) and the maximum film depth of Cossali et al. (Cossali, Coghe et al. 1997).

Three impact behaviors are classified in this study: (1) coalescence, (2) crown formation, and (3) crown splashing, in accordance with the observations classified by Rein (Rein 1993). Coalescence is defined as the absence of a crown or capillary wave. We categorize crown formation to include the appearance of a capillary wave above the original surface level of the film or an approximately vertical or outward-angled crown ejected from the cavity caused by the impact. Secondary droplets separating from the vertically displaced crown is crown splashing. Figure 2.36 depicts a representative photograph from videos taken for this study of each behavior, using the experimental setup described previously.

Prompt Splashing
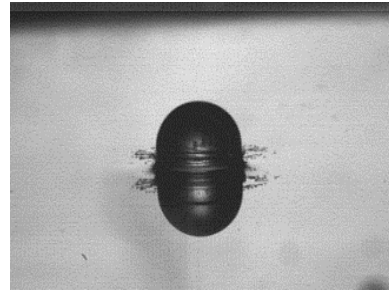
Crown Formation
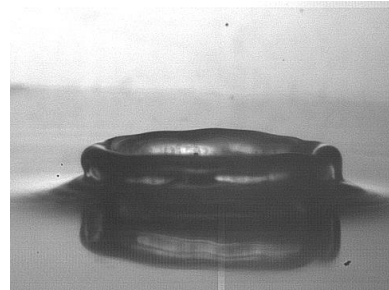
Crown Splashing
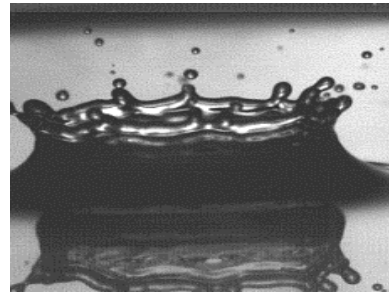
Figure 2.36. Characteristic images of observed impact phenomena.

2.6.2. Results

Since Cossali's (Cossali, Coghe et al. 1997) splashing correlation, as well as many other analyses of film-impact splashing, the Weber and Ohnesorge numbers are used initially as the relevant dimensionless groups to anticipate splashing, and the data for this study have been plotted on those axes as well. These axes distinguish the varying fluids from each other, as the Ohnesorge number is a characteristic of the fluid and a length scale. Each fluid in this study has a distinct range of Ohnesorge number, which is included in the Table 1. In order of increasing Oh, the fluids used in this study are water, FC-72, 60% glycerol, 85% glycerol, and pure glycerol. The

use of film properties in characterizing liquid drop impact is novel; however, when examining the impact of a solid sphere onto a liquid surface, the film properties are always used in relevant dimensionless groups (Thoroddsen, Etoh et al. 2004).

Crown Development and Splashing

Table 2.8 summarizes the findings for crown behavior for each film, in terms of the film Weber number thresholds (We_{film}) for crown formation and splashing. The table presents the transition regions for crown behaviors. Between the We_{film} values for the crown threshold and the lowest crown splashing, crown formation is observed without splashing. Between the lowest crown splashing and universal splashing values, crown formation occurs with as well as without splashing. Above the universal splashing We_{film}, crown splashing appears to occur with every impact.

Table 2.8. Weber number thresholds for crown behavior observed on several types of pools.

Pool Fluid	Crown Threshold	Lowest Splashing	Universal Splashing
Water	100	200	500
60/40 glycerol/water	120	350	600
85/15 glycerol/water	180	350	700
FC-72	550	900	1100

The requirements for crown formation are examined in detail in Figure 2.37. Each depicted region marks the transition between coalescence and crown formation for a film. A wider region means the transition is less clearly defined, with coalescence and crown formation both occurring within that range. For each film, the Weber range at which the transition occurs is approximately constant with regard to drop Oh (Oh_{drop}) for $Oh_{drop} < 1$, suggesting the drop's properties play a minimal role in crown formation. At the upper limits of Oh_{drop} tested in this study, there

starts to be some deviation from the constant crown formation threshold, perhaps due to the highly viscous nature of the drops. In other words, at very high drop viscosity, the magnitude of that viscosity seems to restrict crown formation, while below $Oh_{drop} \gg 1$, drop properties' effect on crown formation is minimal. In contrast, each film's near constant transition We_{film} value is unique to that film. For water, 60% glycerol, and 85% glycerol, the transition value increases with film viscosity. Intuitively, this makes sense; a higher film viscosity ought to restrict highly dynamic behavior like crown formation.
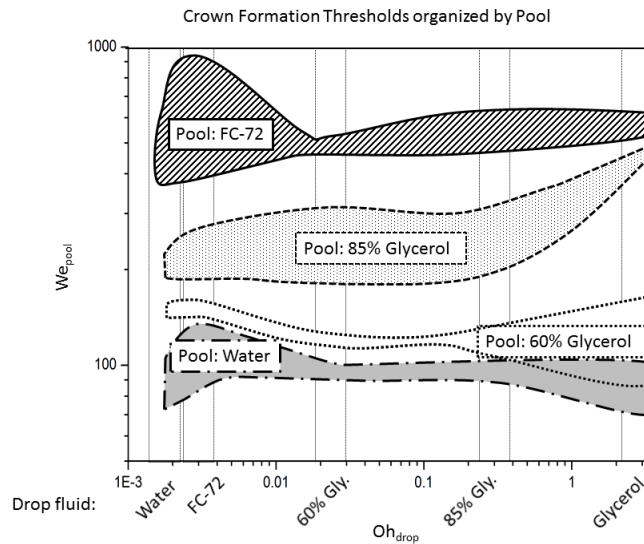
Figure 2.37. Crown formation thresholds, organized by film.
The regions represent the transition from no crown formation to consistent crown formation.
The x-axis includes labels of each droplet species with their respective Oh range represented by the vertical bars on the graph.

However, this trend does not hold for FC-72; as apparent in the figure, the FC-72 film requires a far higher Weber number than the other films for crown formation, despite having a two- to three-fold lower viscosity than water. In fact, FC-72 has the lowest viscosity and surface tension of the studied liquids, so in principle it should require the least amount of energy to

84

form a crown. The other notable feature of the crown formation thresholds in Fig. 4 is the increase in the formation threshold for 85% glycerol for very high drop Oh_{drop}. For $Oh_{drop} > 1$ (pure glycerol, in this study), the 85% glycerol film takes a significantly increased We_{film} to form a crown. The very high viscosities involved in that film–drop pairing serve to severely restrict crown and crown splashing behavior.

Figure 2.38 shows the crown splashing threshold on each film. For the range of film viscosity covered in this study, crown splashing always occurs if We_{film} number is above 1000. Below this value, the onset of crown splashing follows roughly the same trend for all fluids. It starts at lower We_{film} for lower Oh_{drop} values and it reaches seemingly asymptotic values for $Oh_{drop} > 0.04$, albeit a relatively wide spread of splashing threshold We_{film} for all film fluids. It seems that beyond that Oh_{drop}, the effect of viscosity becomes constant regardless of the actual magnitude of viscosity. In contrast to the "crown formation" cases discussed above, the "crown splashing" behavior shows changing threshold values with varying drop fluids. Namely, the splashing threshold is reduced as drop viscosity decreases, suggesting that while the entirety of the corona splashing phenomenon cannot be attributed solely to film or drop viscosity and surface tension, the drop and film fluids' interaction that takes place during the impact that precedes splashing leads to a non-obvious role of dissipation (viscosity) and cohesive (surface tension) forces. As the film grows increasingly viscous, crown formation is inhibited, and therefore crown splashing is prevented.

Impacts onto pure glycerol films (viscosity $»10$ times that of 85% glycerol) resulted in no crown formation within the range of viscosities and surface tensions used in this study, with a single exception: An FC-72 droplet, with $We_{film} = 97$ and $Oh_{drop} = 0.0038$, appeared to crown and splash when it impinged upon the pure glycerol film. We suspect that with such a difference in

viscosity, a ratio of over 103, the glycerol film approximated a solid surface to that particular droplet. None of the other drops tested with that film appeared to crown or splash, having higher respective viscosities.
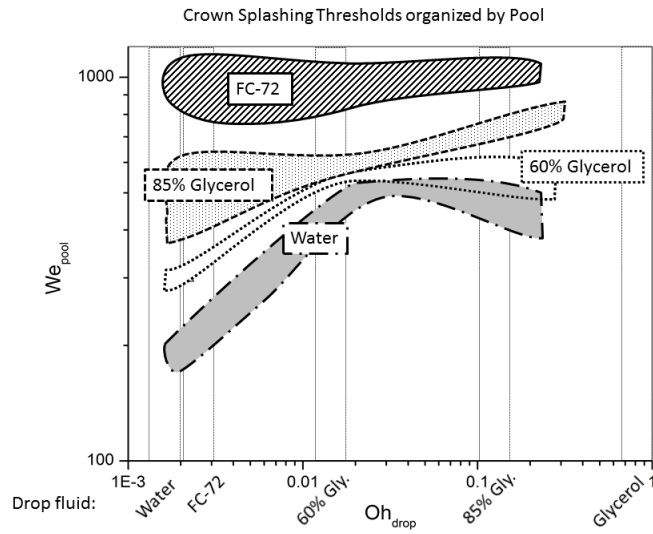
Figure 2.38. Crown splashing behaviors, organized by film.
The regions represent the observed transitions from not splashing to consistently splashing. The x-axis includes labels of each droplet species with their respective Oh range represented by the vertical bars on the graph.

To better illustrate the complex role of viscosity in film impact splashing, crown behaviors are compared for a single type of drop across the range of films in this study in Figure 2.39, organized onto We_{film} / Oh_{film} axes. The film-based Ohnesorge number is used in this case to differentiate the film fluid. The splashing threshold spikes around $Oh_{film} = 0.003$, which corresponds to an FC-72 film; it then decreases as Oh_{film} shifts. Figure 2.40 reorganizes the x-axis directly by film viscosity. The increased splashing threshold at the upper and lower viscous limits becomes obvious, with the lowest splashing threshold occurring on a water pool. Parallels to this intermediate range where splashing is most likely have appeared in dry surface impacts (Vu, Banks et al.

2011), and have been mentioned in other studies of liquid film impacts (Vander Wal, Berger et al. 2006); future work will expand the range of fluids and impact conditions studied to elaborate upon this phenomena. Specifically, the use of FC-72 to categorize viscosity is not ideal, as it has a significantly different surface tension than the other fluids used in this study. Unfortunately, water and glycerol mixtures have uncommonly high surface tension, and few other useful fluids have significant differences in viscosity while having the same range of surface tension. Also apparent is the narrow range of crown formation without splashing on the FC-72 film; if an impact forms a crown it is likely to cause that crown to splash as well. This is hypothesized to be related to the viscous splashing range and the lowered surface tension of FC-72. An impact that produces a crown on an FC-72 pool is likely to develop sufficient instability to break apart. A further possible explanation for FC-72's divergence from other fluids is one of miscibility: FC-72 does not mix with water or glycerol.
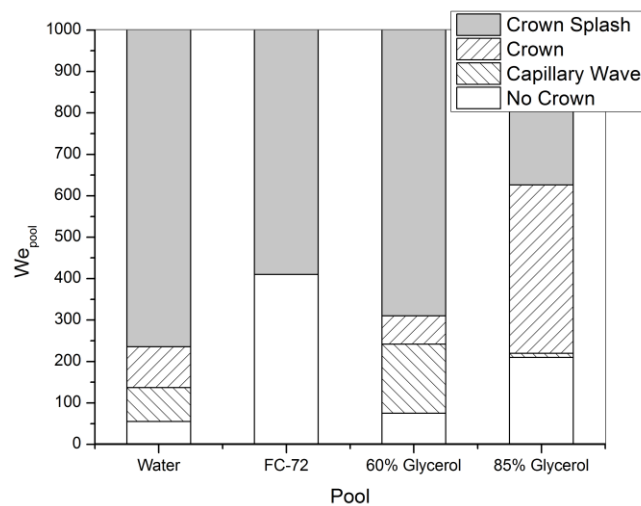
Figure 2.39. Crown splashing behaviors of a water drop onto varying pools, organized by Oh_{pool}.
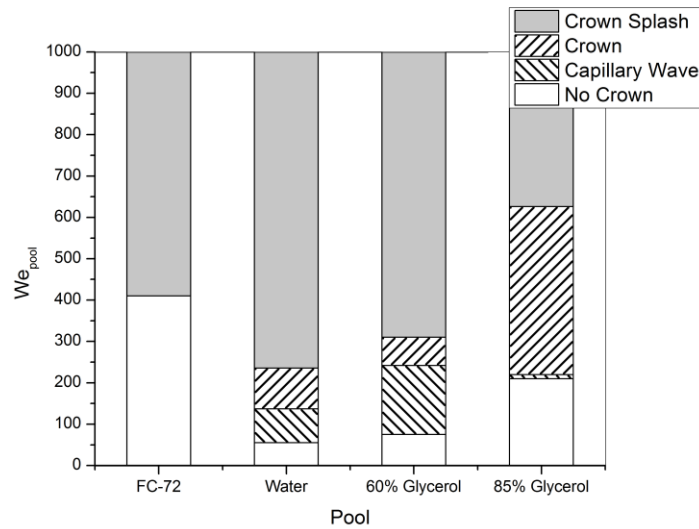
Figure 2.40. Crown behavior observed when water droplets impact varying pools, organized by pool viscosity.

Drop viscosity does influence crown splashing, although it plays less of a role than the film properties. Increasing drop viscosity raises the splashing threshold. To further examine this trend, a solid sphere was used as "infinite-viscosity drop" analogue, and the corresponding splashing thresholds are found. A 4-mm diameter PVC sphere was dropped into a water film of the same depth. The film Weber number for crown splashing was found to be approximately 350; this number is slightly lower than the threshold found using an 85% glycerol drop. While the analogy may be imperfect, as the sphere does not deform at all whereas a liquid drop, even of extremely high viscosity, would deform over longer time scales (a fact which may change the impact outcome), it seems reasonable to believe that there is a limit to the effect of increasing drop viscosity, analogous to the "solid-surface" approximation observed for an FC-72 drop impinging on a highly viscous glycerol film. This limit is seen in Figure 2.38, where each splashing threshold has a significant slope at lower Oh_{drop} but levels off as Oh_{drop} increases. The restrictive

role of high viscosity in splashing has a maximum value: a counterpart to the intermediate viscous range where splashing is promoted.

The data gathered for crown splashing have been compared to the correlation by Cossali et al. (Cossali, Coghe et al. 1997). That relation frequently underestimates the splashing thresholds we observed, since $H*$ in this study is outside the limit of accuracy for that relation. However, we note that with $H*$ being relatively large, the splashing threshold is increased from the Weber number range for splashing reported alongside that correlation (Cossali, Coghe et al. 1997). Vander Wal et al. came to a similar conclusion, finding that in the neighborhood of $H* = 1$, impact behavior undergoes a transition where the liquid film begins to restrict prompt and crown splashing (Vander Wal, Berger et al. 2006). Further, by failing to make a distinction between drop and film viscosity, Cossali et al.'s and other correlations have a non-trivial weakness in addressing dissimilar film impacts.

A New Correlation for Crown Behaviors

As existing correlations have been found to not adequately address crown behavior over the range of fluids used in this study, both by not adequately fitting the data and from the challenge presented by dissimilar fluids, it is necessary to develop a new correlation that can account for drop and film properties and fit the data of this study. From Figure 2.37, it is evident that crown formation depends little on the drop properties (Oh_{drop}), but does depend on We_{film}. Figure 2.38 makes it clear that Oh_{drop} does influence the splashing behavior of the crown.

The three dimensionless groups that seem to play a role in drop impact are the Weber, Reynolds, and Ohnesorge numbers. Further, each of these can be calculated based on the drop or film properties. Cossali's correlation is based on the Weber and Ohnesorge numbers, but does not distinguish the film or drop properties. Starting from the Weber number of the film

and the Ohnesorge number of the drop, the data have been rescaled using combinations of the

drop and film Weber, Reynolds, and Ohnesorge numbers until a criterion that unified the data

was found. Using an exponential fit, the correlation can be written as

$$\frac{We_{film}}{Re_{droplet}^{0.125}} \sim A \cdot Oh_{droplet}^{B}$$ [2-26]

where A and B are the fitting constants. Using this grouping, with Oh_{drop} on the x-axis and

the We_{film} - Re_{drop} grouping on the y-axis, the crown formation and crown splashing thresholds

are plotted in Figure 2.41 respectively.

In Figure 2.41, the crown formation threshold is depicted, along with the curve fit in the

form of Eq. [2-26]. The constants for this fit are A = 152 and B = 0.0754, and the fit has an R^2 val-

ue of 0.50. The crown splashing threshold and fit are also shown, with A = 394, B = 0.139, and an

R^2 value of 0.68. The error bars at each point are used to depict the transition regions (the re-

gimes where different behaviors overlap), i.e., the error bars for the splashing points are formed

by the lowest observed (in terms of the $We_{film}/Re_{drop}^{0.125}$ grouping) splashing occurrence and the

highest observed non-splashing occurrence. The data points presented in Figure 2.41 are the

arithmetic mean of the transition region.

This empirical correlation can be explained from the previous discussion on crown behav-

iors. The drop Reynolds number is taken to a relatively low exponent, reflecting the small but

non-negligible effect of increasing drop viscosity observed in Figure 2.38. The We_{film} and Oh_{drop}

effects are from the original correlation (Cossali, Coghe et al. 1997). In essence, the existing

crown–splashing correlation has been adapted by including the drop properties. While this new

correlation is not an extremely close fit to the data, the range of fluids it covers is unprecedent-

ed, and it predicts both crown formation and crown splashing with reasonable accuracy; existing

correlations usually predict only splashing. This correlation has been found using only $H^* = 1$ and for a range of drop and film Ohnesorge numbers 0.002 > Oh > 3. It does not account for mixing nor has it been tested over a range of surface tension.
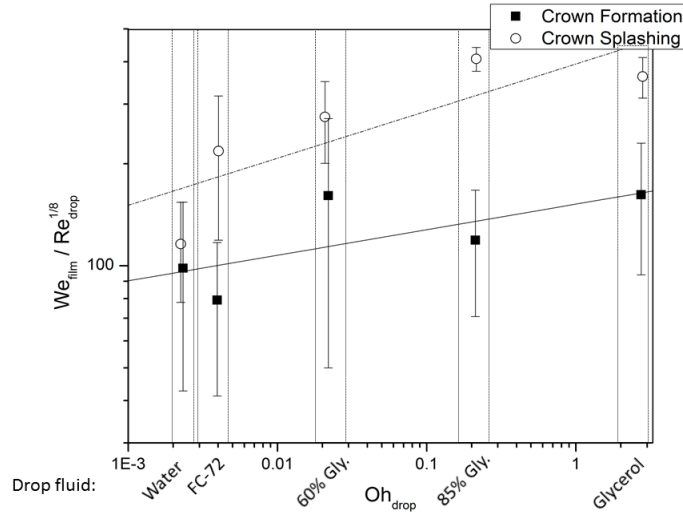
Figure 2.41. Crown formation and splashing behavior in the context of the proposed correlation. Error bars provide the spread of the transition regions.

Distinction between Film and Droplet Properties

Figure 2.42 shows crown behavior based on We_{drop} for a range of drop fluids impacting on a water film, in contrast to Figure 2.37 where We_{film} is used. Generally, there is only minimal difference between the figure below and Figure 2.37. For the water and glycerol mixture drops, the increase in drop Oh leads to increasing splashing thresholds. The exception is FC-72 drops, with its low viscosity and surface tension, which requires unusually high We_{drop} to even produce a crown. Using the film We makes the outcomes for FC-72 impacts fit the trends established with other drops, as seen in Figure 2.38. Similar aberrations appear when crown splashing on other films is presented using the drop-based Weber number.
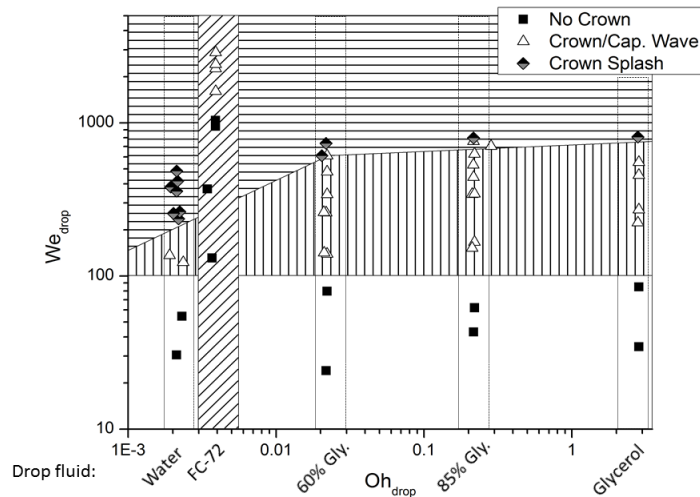
Figure 2.42. Crown behavior with droplet-based Weber number for each droplet fluid onto a water pool.

As crown behavior is mostly decoupled from drop properties, a future thrust of this study would more thoroughly examine crown behavior when a solid sphere strikes a liquid film. Past studies have examined solid sphere impact, but addressed the interior cavity behavior (Marston et al., 2011) or crown behavior at velocities beyond the range of this study (Thoroddsen et al., 2004).

Data from FC-72 droplets often diverges from the trends observed for other droplets. Intuitively, FC-72 should splash more easily than the other liquids, given its lower viscosity (1/2 that of water) and lower surface tension (1/7 that of water). However, for crown splashing in an FC-72 film (Figure 2.38) the splashing threshold is almost always higher than for other liquids. In dry surface drop impacts, viscosity has been observed to have two roles in splashing. First, viscosity induces velocity gradients within the spreading lamella, facilitating the growth of instability. Very low viscosity minimizes velocity gradients, preventing instability development. Further,

viscosity thickens the drop lamella so the drop rim has enough inertia to splash. A drop of lower viscosity has a thinner lamella, so there is less inertia to overcome surface tension (Vu et al., 2011). Similar explanations for the restricted crown splashing may be possible. The crown from an FC-72 film may be sufficiently thin that even the reduced surface tension of that fluid can hold it together.

2.6.3. Conclusions

Few studies in the past have disengaged the film properties from those of the impinging drop. The findings in this paper highlight that these distinctions have potential to transform how drop–film impact phenomena are studied.

Due to the vast range of conditions and complex phenomena associated with drop impingement splashing, it is unusual to find simple criteria such as the observed film based Weber number of approximately 1000 for crown splashing. While extremely high viscosity is a limit of this criterion, it does apply for over three orders of magnitude of film viscosity. Low viscosity drops can splash at lower *We*, but all drops examined splashed above the critical value. This study covered only a single film thickness, where the film is approximately the same as the drop diameter. Future work of crown splash criterion would require investigation of the effects of varying film thickness; we suspect it will at least shift the criterion *We* value. In addition, film viscosity is likely to influence the effect of film thickness, as well; a possible explanation for the lack of crown formation on a glycerol film.

Ongoing work includes exploring the effects of film depth, varying surface tension and miscibility, and refining the new correlation to account for those factors. Further, exploring the dual role of viscosity in all drop impacts, as both an inhibitor and promoter of splashing at different

values, could illuminate the underlying physics that make drop impact such a complex phenomenon that has yet to be solved.

Connection with the Dissertation Premise

This study starts to show how droplet impact influences the thermal boundary layer. In addition to exploring the disposition of droplet fluid after impact, the addition of the liquid pool on the surface and exploration of its interactions with the impinging droplets starts to show how mixing and splashing will influence the growth and restriction of the boundary layer.

Figure 2.43 recalls the general timeline of droplet impact dynamics but depicts only the pool impingement splashing and related behavior. This complements the previous study, where the focus was on dry surface impingement. Looking forward, the next section also examines droplet impact onto liquid pools, but instead of splashing and above-surface dynamics it is concerned with the growth and collapse of the subsurface cavity.
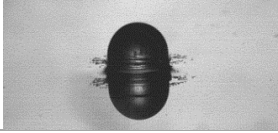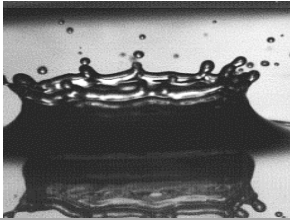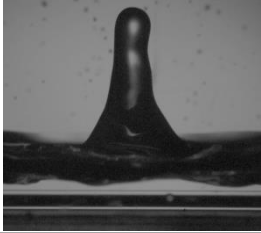
Time Scale		Fluid Dynamics	Thermal Effects
Impact (0-2 ms)		Dry / pool: Prompt splashing	Pool: Little / no effect
2 – 10 ms		Pool: Cavity development, crown splashing	Pool: Decrease of temperature as droplet approaches substrate
10 – 100 ms		Pool: Cavity collapse, jet formation	Pool: Recirculation (secondary cooling) and ejection of droplet fluid
> 100 ms		Pool: Jet ejection, capillary waves on pool surface	Pool: Loss of heat flux as droplet fluid displaced

Figure 2.43. Timeline of droplet impact dynamics, focused on the behaviors observed during impacts onto liquid pools.

References

Cossali, G., A. Coghe and M. Marengo (1997). "The impact of a single drop on a wetted solid surface." <u>Experiments in Fluids</u> **22**: 463-472.

Eslamian, M. and N. Ashgriz (2011). Spray Drying, Spray Pyrolysis and Spray Freeze Drying Handbook of Atomization and Sprays. N. Ashgriz, Springer US**:** 849-860.

Fedorchenko, A. I. and A.-B. Wang (2004). "On some common features of drop impact on liquid surfaces." <u>Physics of Fluids</u> **16**(5): 1349-1365.

Fink, J., D. Gault and R. Greeley (1984). "The Effect of Viscosity on Impact Cratering and Possible Application to the Icy Satellites of Saturn and Jupiter." <u>J. Geophys. Res.</u> **89**(B1): 417-423.

Kim, S. C. and H. S. Ryou (2003). "An experimental and numerical study on fire suppression using a water mist in an enclosure." <u>Building and Environment</u> **38**(11): 1309-1316.

Rein, M. (1993). "Phenomena of liquid drop impact on solid and liquid surfaces." <u>Fluid Dynamics Research</u> **12**: 61-93.

Rein, M. (1996). "The transitional regime between coalescing and splashing drops." <u>Journal of Fluid Mechanics</u> **306**(-1): 145.

Smith, H. J. (1975). <u>The hydrodynamic and physico-chemical basis of the drop picture method</u>. Gottingen, Max Plank Institut fur Stromungsforschung, Bericht Nr. 8.

Thoroddsen, S. T., T. G. Etoh, K. Takehara and Y. Takano (2004). "Impact jetting by a solid sphere." <u>Journal of Fluid Mechanics</u> **499**: 139-148.

Vander Wal, R., G. Berger and S. Mozes (2006). "Droplets splashing upon films of the same fluid of various depths." <u>Experiments in Fluids</u> **40**(1): 33-52-52.

Vander Wal, R. L., G. M. Berger and S. D. Mozes (2005). "The combined influence of a rough surface and thin fluid film upon the splashing threshold and splash dynamics of a droplet impacting onto them." <u>Experiments in Fluids</u> **40**(1): 23-32.

Vu, H., D. Banks and G. Aguilar (2011). "Examining Viscosity and Surface Wettability in Lamella Lift Dynamics and Droplet Splashing." <u>Atomization and Sprays</u> **21**(4).

Worthington, A. M. and R. S. Cole (1897). "Impact with a Liquid Surface, Studied by the Aid of Instantaneous Photography." <u>Philosophical Transactions of the Royal Society of London. Series A, Containing Papers of a Mathematical or Physical Character</u> **189**: 137-148.

Yarin, A. L. (2006). "Drop Impact Dynamics: Splashing, Spreading, Receding, Bouncing..." <u>Annual Review of Fluid Mechanics</u> **38**: 159-192.

Zhang, L. V., J. Toole, K. Fezzaa and R. D. Deegan (2011). "Evolution of the ejecta sheet from the impact of a drop with a deep pool." <u>Journal of Fluid Mechanics</u> **690**: 5-15.

2.7. Single Droplet and Droplet Trains Impact Dynamics onto Liquid Pools

The bridge between single droplet impacts and multiple-droplet spray dynamics is the interaction between impacting droplets. To explore these interactions, high speed videos of trains of droplets were recorded. The dynamics of the impact cavity and the subsequent ejected jet are altered by successive droplets, and the alterations relate to how frequently the droplets impact the substrate. The frequency was varied from a low extreme, where successive droplet impacts were essentially isolated from each other and the pool became fully quiescent between droplets, to a high extreme where each successive droplet impinged into the cavity of the previous, creating a periodically-steady cavity condition. Exploring the transitions between these two extremes reveals several regimes where the cavity collapse and ejected jet interfere with successive droplets.

The behavior of a single droplet impacting any of a wide range of surfaces, under varying conditions (atmospheric, kinetic, etc.), has been very well explored. Connecting a single droplet impact behavior to the cumulative dynamics of a spray, consisting of many thousands or millions of droplets, is the focus of this study. By examining the droplet impact fluid and thermal dynamics in the context of trains of droplets over a range of impact frequencies, the goal of this study is to establish a framework for measuring and comparing the cooling effectiveness of these trains. This framework is necessary due to the range of conditions that occur within a single spray- the droplet frequency or size distribution can change as the spray develops, or the film thickness on the surface can build up, to name a few possible factors.

Existing studies on droplet trains describe a quasi-steady cavity within a pool that develops-the walls of the cavity are nearly quiescent as incoming droplets prevent the collapse of the cavity (Trujillo, Alvarado et al. 2011). That study used high frequency trains (1-10 kHz) of micron

scale droplets and found that the steady condition occurred within milliseconds after the first droplet impact. After a few tens of droplets, heat fluxes ranging from 5 to 35 W/cm2 were measured, increasing proportional to droplet frequency (Trujillo, Alvarado et al. 2011). This study builds upon Trujillo, et al.'s work, extending to larger millimeter-scale droplets and lower (0.5-30 Hz) frequencies. The intent is to provide detailed insight into the interactions between successive droplets that correspond to measured heat transfer.

A recent study by Fujimoto, et al, examined the interaction between two droplets impacting coaxially upon a heated solid surface (Fujimoto, Ogihara et al. 2013). The 0.5-0.6 mm diameter water droplets impacted a few milliseconds apart. Liquid spreading across the dry surface was characterized for various substrate superheats (170 < T_s < 500 °C). At higher temperatures within that range, droplets instantaneously boiled and disintegrated.

2.7.1. Experimental Setup

This study has two principal components: first, the study of cavity development within a liquid film due to single droplet impacts, and second, exploration of how these cavity dynamics contribute to sequential droplet interactions during droplet train impingement over a range of impact frequencies.

The pool and droplets consist of deionized water. Droplets freefall from the needle when they reach a diameter of 4.6±0.1 mm and the impact velocity varies from 1 to 4±0.05 m/s, based on the height of the needle. This results in an impact Weber number range of 42 < *We* < 1064 and an impact Reynolds number range of 4310 < *Re* < 21570. For droplet trains, the Strouhal number range of 0.00115 < *St* < 0.0736 is observed. High speed video is recorded at 1000 fps, 800 x 600 px. resolution, and 40 μs exposure time per frame. The camera is positioned at a height such that the cavity below the surface of the pool is visible as well as well as the droplet

in freefall just before impact. Calibration lengths are taken both above and below the surface of the pool to account for refraction. One pixel above the surface of the pool corresponds to 0.030 mm, and below the surface to 0.028 mm.

To provide repeatability, each droplet was assessed before impact. The impact velocity was measured and required to be ±0.05 m/s of the nominal velocity. The droplet diameter was measured both horizontally and vertically in the video plane, and both axes were required to be within ±0.05 mm of each other and of the nominal diameter for the particular needle used. This ensures comparisons between droplets are not subject to variation due to the pre-impact conditions. Further, the shape of the droplet at impact has been observed to greatly influence subsequent cavity, splashing, and vorticity dynamics (Rein 1996). Ensuring the droplet is spherical at impact will alleviate these geometry effects.

Nondimensionalization

In addition to the aforementioned dimensionless groups (defined in Section 2.2), certain quantities are made dimensionless to ease comparison between scales. First, a dimensionless characteristic H*, given in Equation [2-27], was used to characterize the cavity depth. H* is a ratio of the pool height to the droplet diameter with *H* as the height of the pool and *d* as the diameter of the droplet.

$$H^* = \frac{H}{d} \qquad \text{[2-27]}$$

Time is made dimensionless using Equation [2-11], using the impact velocity and the droplet diameter (pg. 15).

2.7.2. Results

The first experiment is an investigation of cavity-substrate interaction for a single droplet impinging upon a shallow pool. The depth and duration of the cavity is measured via high speed video, and the temperature history is recorded by an RTD directly below the point of impact. Figure 2.44 depicts the cavity depth over time for a droplet impinging upon an (a) 1, (b) 2, and (c) 3 H^* depth pool. The impact velocity in all cases is 2 m/s, corresponding to We = 270. The cavity depth is measured from the point of impact vertically downward. Figure 2.45 shows the cavity at its maximum depth in each of these cases.

Single Droplet Impingement Cavity Dynamics

There appear to be three qualitative regimes of droplet-substrate interaction based on the cavity's behavior. First, the *deep-pool* regime is observed through the cavity behavior of the 15 mm deep pool impact (Figure 2.44c). The cavity does not approach the bottom of the pool- it penetrates approximately halfway through before beginning its collapse. The depth appears to follow a smooth curve with regard to time, with no abrupt changes. In contrast, the 5 mm pool (Figure 2.44a) reveals a *thin-film* regime, where the cavity almost immediately reaches the bottom of the pool after impact. This thin-film regime necessitates that the momentum of the droplet impact be directed radially from the point of impact, leading to an extended period of time when the substrate below the pool is exposed. The quasi-steady cavity condition observed by Trujillo, et al occurs in this regime, as the radial redirection of droplet momentum is what maintains the position of the cavity walls (Trujillo, Alvarado et al. 2011)*.

The 9 mm pool depth (Figure 2.44b) results in a cavity that qualitatively does not appear to be in the either the thin-film regime or the deep pool regime- the cavity does not reach the substrate but the curve is interrupted unlike the deeper pool.
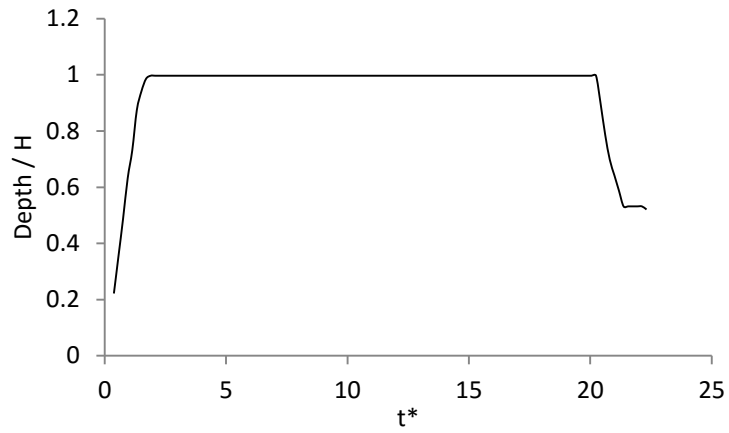
a. Thin film cavity
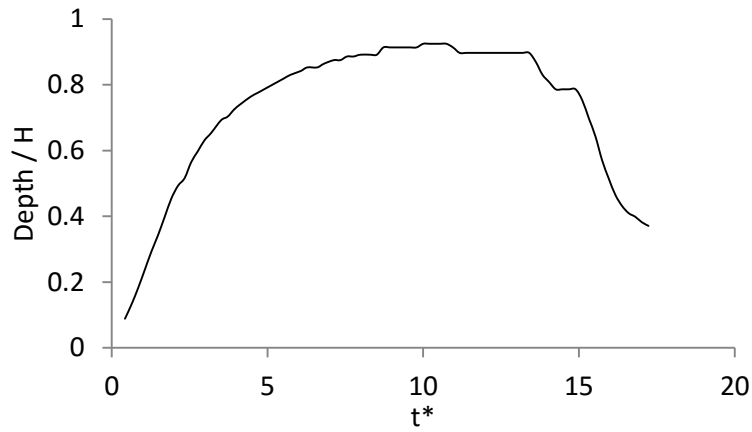
b. Intermediate regime cavity
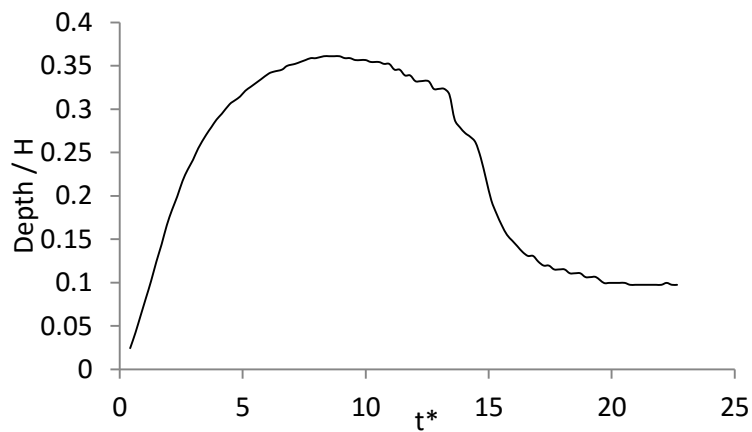
c. Deep pool cavity

Figure 2.44. Cavity measurements for droplets impinging at 2 m/s (We = 270) in pools of varying depths. The dotted line represents the maximum pool depth.

H* = 1

H* = 2
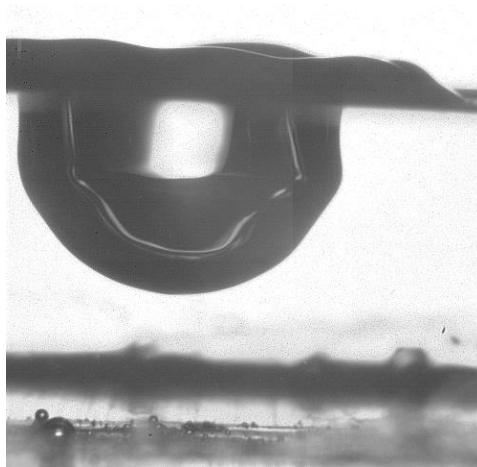
H* = 3

Figure 2.45. Still frames depicting the cavity formation, maximum depth, and collapse.

The smooth curve observed for the deeper pool cavity is replaced with a series of small jumps around the maximum depth, punctuated by a sharp transition to collapse. If the deep pool regime is specified by a lack of droplet-substrate interaction, then this case appears to have some substrate interaction, potentially through viscous effects within the thin layer of fluid that remains between the cavity and the substrate. Figure 2.45b shows the cavity at this instant, with Figure 2.45 a and c representing the same condition- maximum cavity depth - for the thin film and deep pool conditions, respectively. The frame reveals an instant when the bottom of the cavity narrows radially and vertical collapse is delayed momentarily. This narrowing was observed and discussed by Rein (Rein 1996). He describes this radial collapse as occurring in the absence of a vortex ring that forms at lower impact Weber numbers. When it occurs, the vortex redirects flow upward; without the vortex ring the radial collapse becomes more dominant.

To explore and better define the cavity regimes, droplet impacts into a single pool (9 mm depth, $H^* = 2$) and with varying velocities, of 1, 2, and 4 m/s (We = 70, 270, 1064). Figure 2.46 shows the cavity depth those three cases.
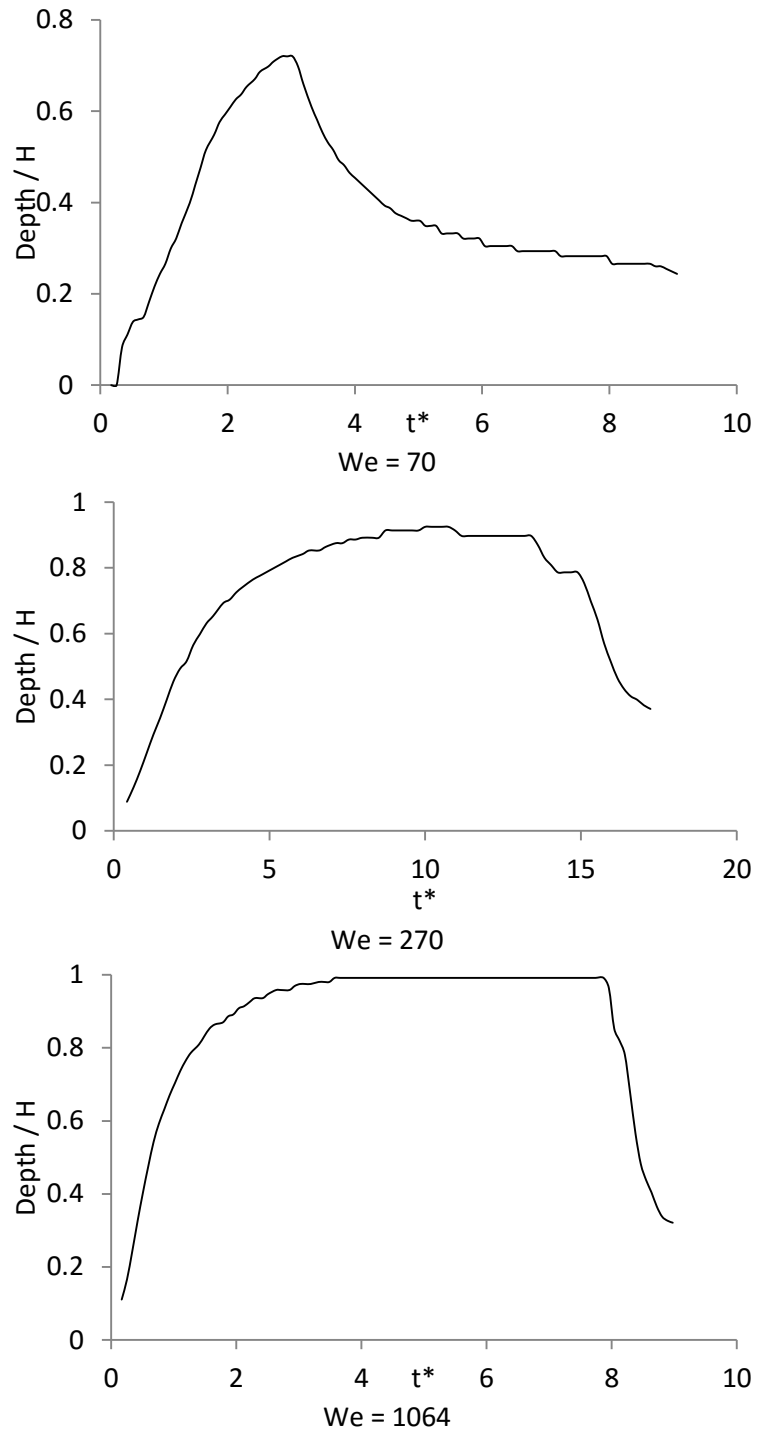
Figure 2.46. Cavity measurements for droplets impinging at varying velocities into an H* = 2 pool.

Figure 2.46a highlights the deep pool regime as caused by a low impact velocity. The cavity is short-lived and reaches less than halfway through the pool. Figure 2.46b shows the previous case of the intermediate regime. Figure 2.46c reveals a cavity that reaches the substrate and rests before collapsing – a thin-film regime cavity caused by elevated impingement *We*.

Single droplet impact studies are minimally useful by themselves. This study aims to connect single droplet impact phenomena with the dynamics of droplet trains – building towards enhanced understanding of spray behavior. These single droplet impacts reveal considerations that must be accounted for when looking at the interactions between subsequent droplets. To that end, the effect of impact velocity on the duration of the cavity has been explored. Figure 2.47 depicts the time from impact to cavity collapse as it relates to the Weber number of an impacting 4.6 mm diameter water droplet. The collapse time is defined as the duration between impact and the instant the cavity has decreased to 50% of its maximum depth.

The collapse time was non-dimensionalized using the impact velocity and droplet diameter:

$$t^* \equiv \frac{t_{collapse} U}{d} \qquad\qquad [2\text{-}28]$$

Figure 2.47 shows a very interesting phenomenon – for the range of pool depths ($1 \leq H^* \leq 5$) and *We* in this study, the dimensionless collapse time as defined in Equation [2-28] varies linearly with *We*, with the collected data points having an R^2 correlation value to a line of 0.82. Intuitively, this makes sense – a higher impact *We* means more inertia to open the cavity, and therefore a cavity that remains open longer. When examining droplet train impingement heat transfer, this finding is essential – a cavity that is open longer provides an extended window for a successive droplet to impact within the pre-existing cavity and enhance cooling.
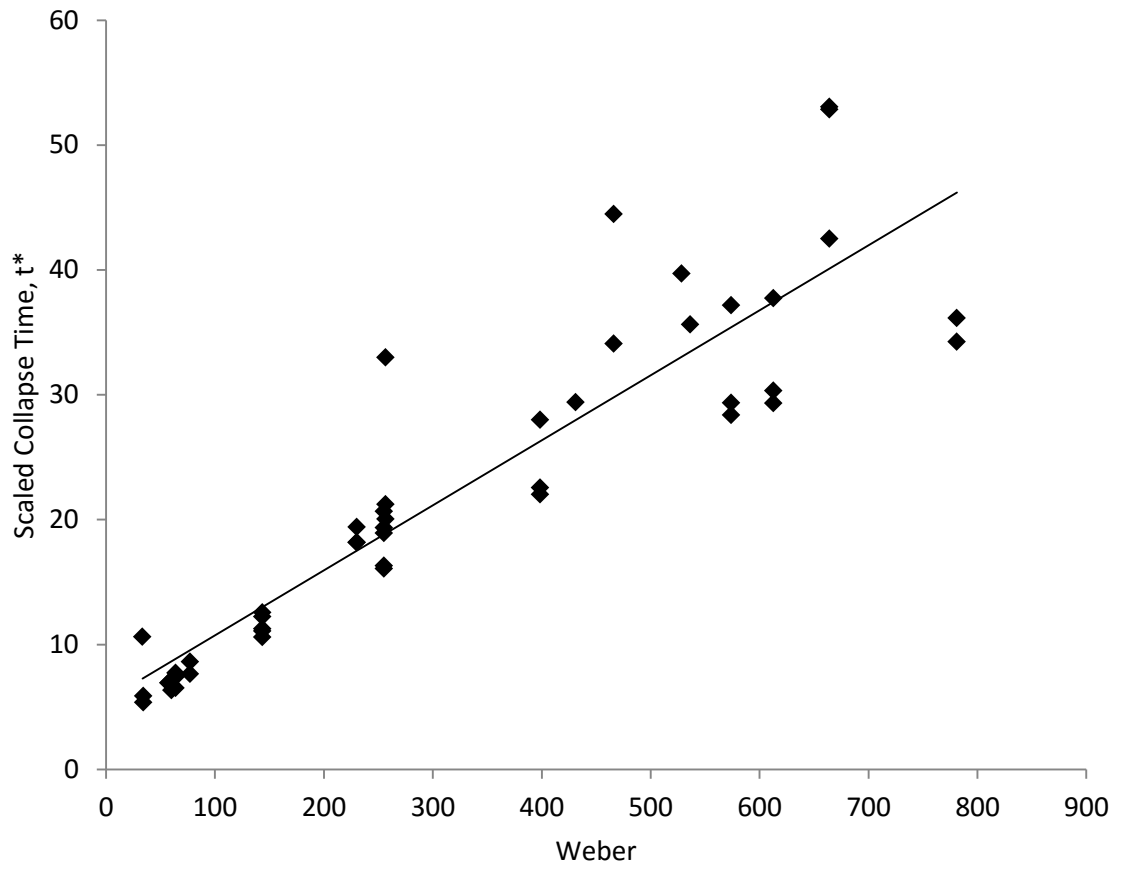
Figure 2.47. Cavity duration as it is affected by impact *We*

The equation of the best-fit line from Figure 2.47 is given in Equation [2-29].

$$t^* \equiv \frac{t_{collapse}U}{d} = 0.052\,We + 5.53 \qquad\qquad [2\text{-}29]$$

Droplet Train Impingement Interaction

Studying the cavity behavior of single droplets helps better understand the interaction between the cavity and successively impinging droplets. For instance, in the thin film regime, the cavity exposes the substrate for a period of time. In a train of droplets of sufficient frequency, the next droplet in the train will fall into the already open cavity and make direct contact with the substrate. The second droplet in this example would then produce a larger cooling effect, as it is effectively a dry-surface impact. The critical frequency for this behavior to occur depends on the duration of the cavity, which relates to the impact Weber number as seen in Figure 7. The radial expansion of the cavity in the thin film regime further acts to improve this phenomenon, as the impinging droplets are able to widen the cavity and hold it open for a longer time.

In the intermediate and deep pool regimes, exposing the substrate is likely to require a higher frequency, as it will take multiple droplets impinging in a short time to widen and deepen the cavity enough to reach the substrate. This necessitates a higher frequency for incoming droplets to impinge upon open cavities.

Droplet trains lasting 6 seconds were used to explore the thermal effects of trains with varying frequencies. The duration of the train was selected as the point by which the train had either reached a thermally quasi-steady condition, or demonstrated that droplet impacts were sufficiently separated that no quasi-steady condition would develop. The trains impacted on a pool of $H^* = 2$, with an impact We of 270. This places the initial impact in the optimal single-droplet cooling regime observed previously. The pool conditions for subsequent droplets are altered by prior impacts. The frequencies ranged from 0.5 to 32 Hz. Figure 2.48 shows still frames of the first four successive droplet impacts for frequencies of $0.5 - 16$ Hz, and Figure 2.49 covers 20, 24, and 32 Hz to explore how the pool conditions change for each impact.

At 0.5 Hz, droplet impacts were isolated from each other. Each droplet impact is virtually identical to the previous. The cavity of one droplet collapsed and the pool settled by the time the next droplet arrived (Figure 2.48a).

At 2 Hz (Figure 2.48b) the impacts are nearly identical, but some agitation of the pool surface is still visible – the pool had not yet returned to quiescence by the time a new droplet arrived. The interaction between droplets is minimal.

Increasing the impingement frequency to 8 Hz (Figure 2.48c), droplets start to strongly interfere with each other. Every second droplet strikes the previous one's post-cavity jet. At this frequency, the jet is collapsing when the successive droplet strikes it. The droplet is impeded from reaching the pool, but is only slowed rather than redirected. This contrasts with the 16 Hz train, where the jet is growing vertically when the successive droplet arrives, leading to a mushroom shape as the liquid is forced radially outward by the opposing inertia.

By 24 Hz, however, the droplets are impinging quickly enough that they occasionally make it into the existing cavity (Figure 2.48d). At this frequency, the pool has not yet become quiescent from one droplet by the time the next has arrived. At 32 Hz (Figure 2.48e), each successive droplet impinged within the cavity of the previous, developing towards the quasi-steady cavity condition reported in literature (Soriano, Zhang et al. 2014). At these elevated frequencies, the second droplet holds open the cavity for a shorter length of time than the first initially opens it; this leads to the third droplet in line striking the cavity collapse jet.

The dimensionless collapse time for an impingement *We*, based on Equation [2-29], is 19.57. A critical train frequency such that successive droplets will impinge into the cavity of the previous ones can be found from this *t**:

$$t^* = \frac{Ut_c}{d} = \frac{U}{df_c} \qquad \text{[2-30]a}$$

$$f_c = \frac{U}{dt^*} \qquad \text{[2-30]b}$$

$$f_{c,We=270} = \frac{2}{0.0046 * 19.57} = 22\ Hz \qquad \text{[2-30]c}$$

At this critical frequency, successive droplets begin to impinge upon an open cavity. Exactly at this frequency, however, the cavity will be collapsing – the inner surface of the cavity will generally be moving upward. This will impede the incoming droplet from reaching the substrate as it has to expend energy re-directing the cavity motion. Observations of trains impinging at slightly higher than this critical frequency (24, 32 Hz) reveal the droplets occasionally impinging into a fully open cavity that has not yet begun to collapse. However, the length of time the cavity is held open by the second droplet is shorter than the dimensionless collapse time. At lower than this critical frequency, the cavity's ejected jet is seen to impede droplet impingement (10 Hz).

0.5 Hz

2 Hz

8 Hz
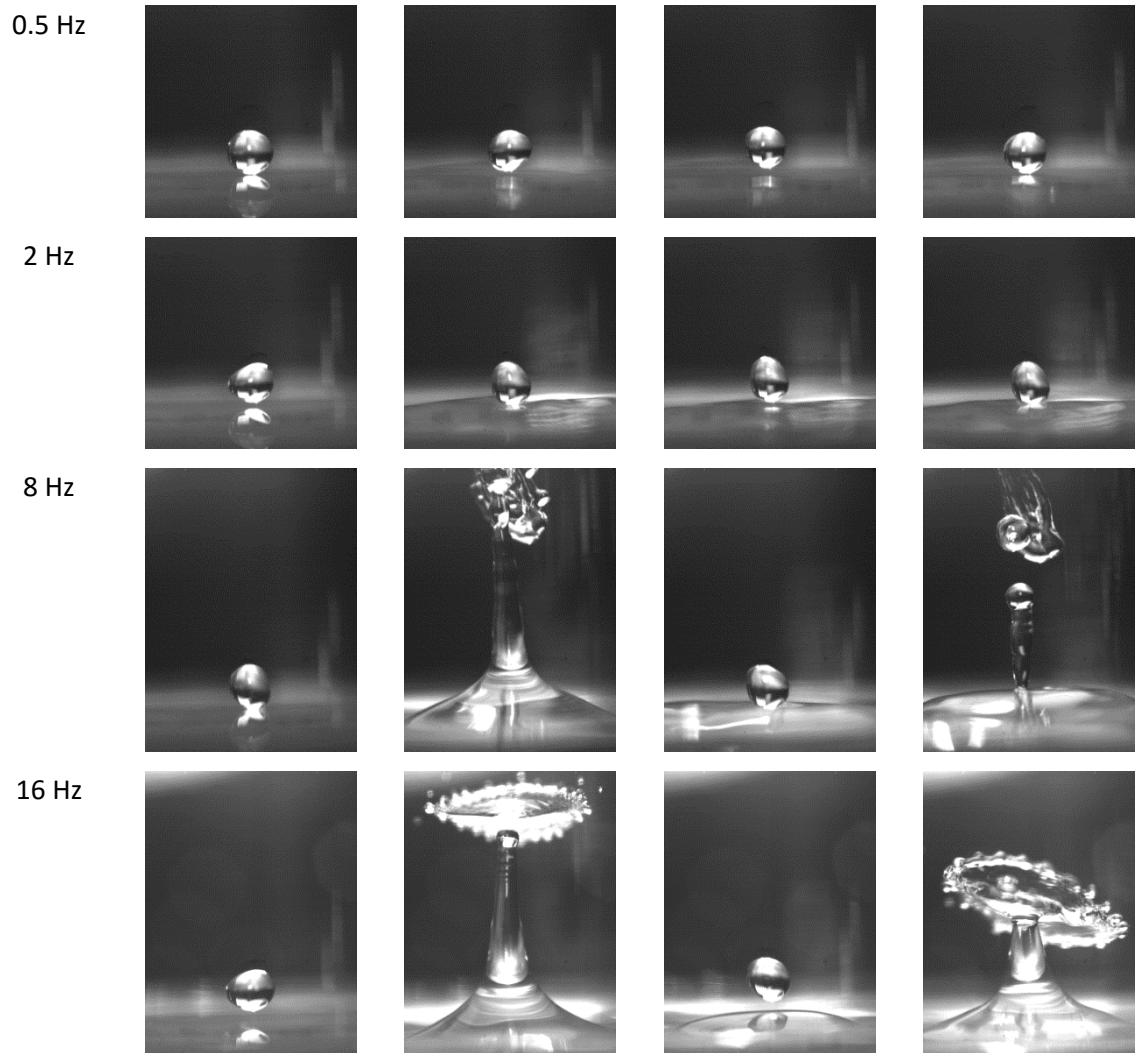
16 Hz

Figure 2.48. Still frames of successive droplet impacts on an $H^* = 2$ with $We = 270$. f = 0.5, 2, 8, and 16 Hz.

20 Hz

24 Hz

32 Hz

Figure 2.49. Still frames of successive droplet impacts on an *H** = 2 with *We* = 270. ƒ = 20, 24, and 32 Hz.

2.7.3. Conclusions

The cavity dynamics of single and train liquid droplet impact have been explored – the sub-surface accompaniment to section 2.6's examination of above-surface splashing behavior. By examining the depth of the cavity produced upon impact as it evolves over time, multiple regimes of droplet-pool-substrate interaction have been identified. The thin film regime describes a condition where the cavity penetrates fully through the pool, exposing the substrate to atmosphere. The deep pool regime occurs when the cavity cannot approach the substrate due to low impingement velocity and/or sufficiently deep pool. The intermediate regime is seen when the cavity approaches the substrate but fails to reach it; additional vorticity produced by the displacement of liquid near the substrate leads to unique radial collapse dynamics not observed in the other regimes.

The length of time which the cavity remains open is found to depend on the impingement *We* and does not seem strongly influenced by the cavity regime. This relationship is useful when examining droplet train impingement over a range of frequencies – above a critical frequency based on the cavity duration, droplets impinge into an open cavity rather than onto the pool surface.

Connection with the Dissertation Premise

As will be demonstrated in the next section, the findings here, especially concerning cavity duration and critical frequency, are key factors governing the heat transfer of impinging cooling droplet trains.

References

Fujimoto, H., T. Ogihara, S. Yoshimoto, T. Hama and H. Takuda (2013). "Successive Collision of Two Water Droplets with a Hot Solid." International Journal of Transport Phenomena **13**(3).

Rein, M. (1996). "The transitional regime between coalescing and splashing drops." Journal of Fluid Mechanics **306**(-1): 145.

Soriano, G. E., T. Zhang and J. L. Alvarado (2014). "Study of the effects of single and multiple periodic droplet impingements on liquid film heat transfer." International Journal of Heat and Mass Transfer **77**(0): 449-463.

Trujillo, M. F., J. Alvarado, E. Gehring and G. S. Soriano (2011). "Numerical Simulations and Experimental Characterization of Heat Transfer From a Periodic Impingement of Droplets." Journal of Heat Transfer **133**(12): 122201-122210.

2.8. Optimizing Droplet Train Heat Transfer

Armed with an understanding of how successive droplets interact with each other and the impact surface, the next step is to explore the cooling dynamics that accompany these interactions. Broadly, as the frequency increases, the heat flux tends to increase as well. However, at certain frequencies, the fluid dynamics accompanying each droplet impact impedes the next droplet from reaching the substrate, minimizing the cooling effects. As the frequency increases past a threshold, successive droplets start having an additive effect, leading to a jump in the effective heat flux, as each droplet impinges into the cavity of the previous and thus is more easily able to reach the substrate. Understanding these positive and negative interferences, and knowing which frequencies produce them, will lead to the ability to tune a spray's droplet size, velocity, and density distributions to get ideal cooling capabilities.

One additional non-dimensionalization is needed to discuss the cooling effects of droplet impingement: a dimensionless temperature. This factor, Θ, is defined as follows:

$$\Theta \equiv 1 - \frac{T_{pool} - T_{measured}}{T_{pool} - T_{droplet}} \qquad [2\text{-}31]$$

A Θ of 1 indicates no cooling has occurred – the measured temperature is unchanged from the initial pool temperature. Similarly, Θ of 0 indicates the measured temperature has decreased to the initial temperature of the droplet – the temperature has reached the minimum possible for that system.

2.8.1. Single Droplet Heat Transfer

Figure 2.50 shows the temperature history from $We = 270$ droplet impingement onto pools of $H^* = 1$, 2, and 3. Despite the cavity not reaching the substrate in the deep pool regime, there is some cooling effect at the substrate. This cooling effect is less than for the other cases, but

non-negligible. All three droplets show a cooling effect- a decrease in temperature occurs, suggesting that at least some cool droplet fluid penetrates completely through the pool and reaches the substrate. The cavity alone is not a reliable indicator of the fate of the droplet fluid. In a past study, Banks, et al established that crown splashing is a function of droplet fluid – suggesting that at least some of the droplet fluid rides up the rim of the cavity and comprises the splashed liquid (Banks, Sanchez et al. 2013). From the fact that cooling effects are observed at the substrate, some of the droplet fluid must also remain below the bottom of the cavity.

Use of these impact regimes can yet be exploited for enhanced cooling. For some impact and pool conditions, some droplet fluid may be deposited near the substrate while the cavity collapses. The droplet fluid will be trapped near the substrate. The cooling period will be prolonged as the droplet heats from its initial cool temperature.
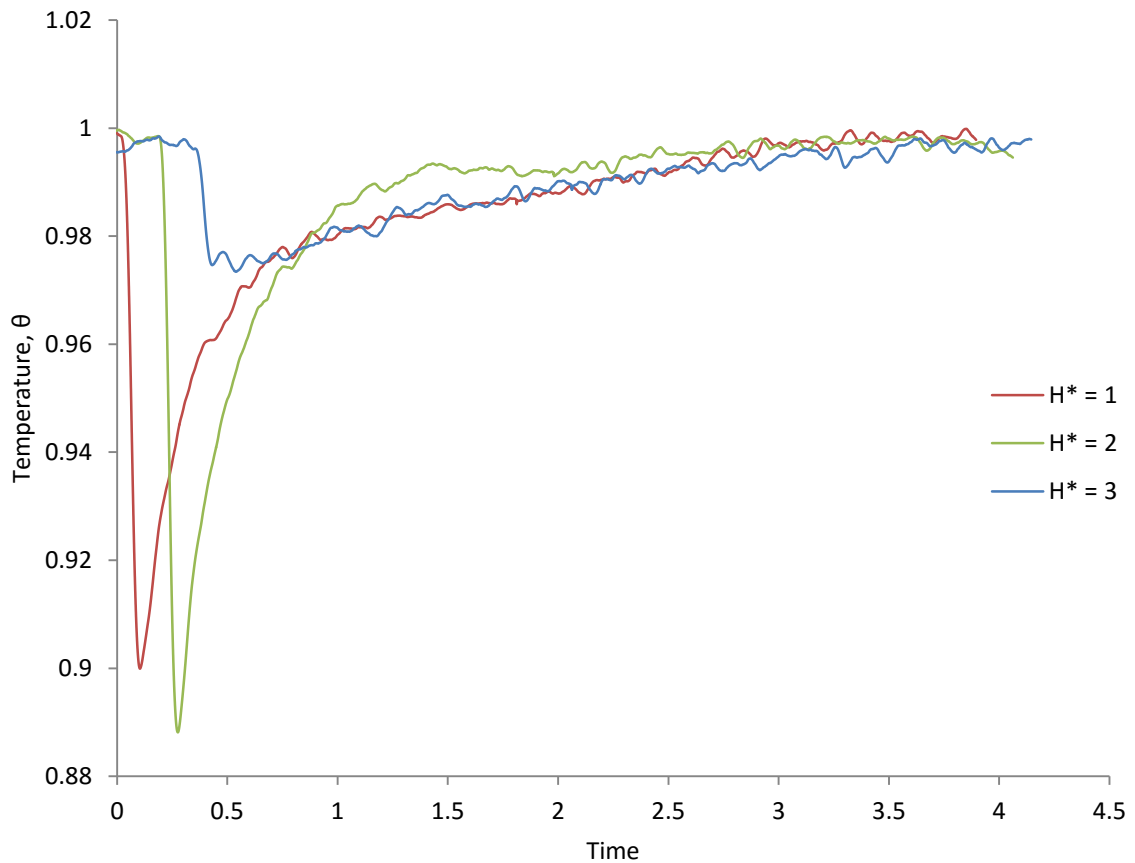
Figure 2.50. Temperature measurements for We = 270 droplet impacts onto pools of 1, 2, and 3 *H** depth.
The droplet fluid is at 22°C and the pool is heated from below to 60°C. The temperature signals are shifted in time to promote clear comparison of the magnitude of effect.

In Figure 2.50, droplet impact into the intermediate pool reduces the temperature at the substrate further than the other two cases. In this case, the cavity approaches but does not reach the substrate – indicating that any droplet fluid comprising the bottom of the cavity is in direct contact with the substrate. The droplet fluid has the most contact with the substrate at the sensor location. The implication is that the sensor location is subjected to a higher heat flux for that case than the others. It is obvious from video why the thin-film regime experiences this-

the droplet liquid is forced radially by the pool substrate, exposing the substrate to air and a drastically weaker convective process. The deep pool, also, has an intuitive reason for lesser cooling effects. While some of the droplet fluid does reach the substrate, the deeper pool does prevent more of the cool fluid from penetrating.

The observation of enhanced cooling for certain pool depths was noted by Vu, et al (Vu, Aguilar et al. 2009). The effect was at that time attributed to a secondary convective phase, due to eddies at the substrate observed using dyed droplet fluid. These eddies are evidence of droplet fluid deposition at the substrate, as the droplet fluid is left behind and subsequently circulated as the cavity recedes. Droplet-film impact vortices are well explored, starting from Thomson and Newell in 1885 (Thomson and Newall 1885) and continuing through the present. Rein, among others, attributes the penetration of these vortices, composed primarily of droplet fluid, to the droplet's shape at impact- a prolate (along impact axis) drop produces a more powerful and penetrating vortex than an oblate one (Rein 1996). Watanabe, et al, discussed these vortices that form around the cavity extensively from the results of their numerical models (Watanabe, Saruwatari et al. 2008). These vortices are one mechanism by which cool-fluid deposition may occur at the substrate, carrying droplet fluid away from the cavity to prevent it from being ejected as the cavity collapses.

Further evidence of vortex-induced mixing is the relatively rapid rise back to the original temperature for H* = 2. Between times 1 and 2.5, the temperature for H* = 2 rises above the other two measurements. In light of the aforementioned vortices, it seems likely that warm pool fluid is swept back in to the sensor site; this effect seems absent for the other pool depths.

Increasing H^* to 7 leads to a minimal cooling effect. The measured temperature decrease is less than 0.5 ^{O}C, nearly negligible. Intuitively, far into the deep pool regime, heat transfer result-

ing from a droplet impact. However, a cooling effect is observed – at least a small portion of the droplet fluid is able to penetrate the full depth of the pool. Due to experimental setup limitations, a sufficiently deep pool to inhibit any measureable cooling effect was not possible.

Figure 2.51 gives the temperature history recorded for the droplet impacts of We = 70, 270, and 1064 into an H^*=2 pool. The most effective cooling is seen the highest velocity/We, where the droplet velocity is high enough that it pushes through the pool allowing for the droplet to reach the substrate for better cooling. In this case, it seems that the increased velocity changes the cooling dynamics such that optimal heat transfer occurs in the thin film regime.
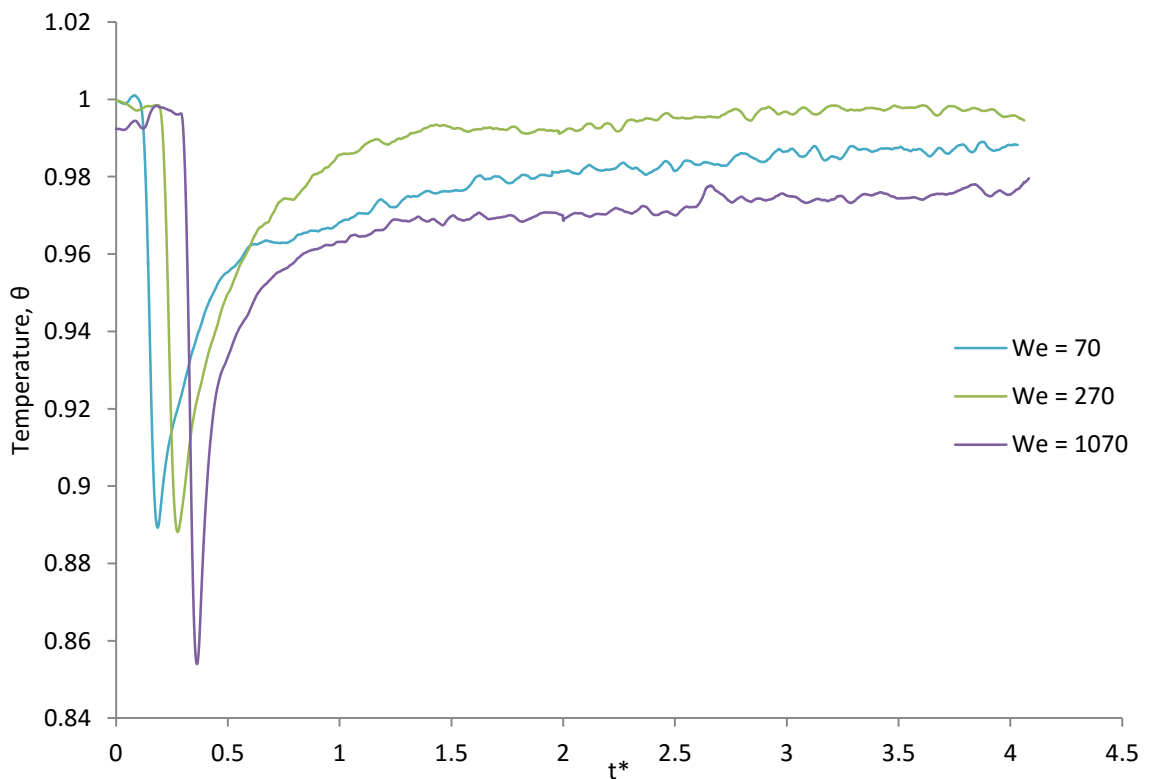
Figure 2.51. Temperature histories for droplet impacting at 1, 2, and 4 m/s, corresponding to Weber numbers of 70, 270, and 1064, into a pool of depth H*=2.
Note: Time is made dimensionless using the intermediate velocity (2 m/s) in this figure.

2.8.2. Droplet Train Heat Transfer

Droplet trains were used to explore the thermal effects of trains with varying frequencies. The trains impacted on an H^*= 2 pool with a constant velocity of 2 m/s for We=270. This places the initial impact in the optimal single-droplet cooling regime observed previously. The pool conditions for subsequent droplets are altered by the prior impact. The frequencies used were 0.5, 8, 16, 24, 32, and 40 Hz. Figure 2.52 shows the temperature history for trains of frequencies 0.5, 2, and 8 Hz. Figure 2.53 shows the same for frequencies of 24, 32, and 40 Hz.

For the 0.5 Hz train, each droplet falls after the temperature has returned to the pool initial temperature from the previous droplet's impact. Consequently, each successive droplet gives a virtually identical temperature effect, with a sharp initial decrease followed by a smooth restitution to the initial temperature. At 2 Hz, the droplet impacts follow the same shape, but the successive droplet impact is able to interrupt the reheating phase, leading to a lower minimum temperature.

By 8 Hz, the cooling effects are shown to overlap and the jet interference observed in Figure 2.48 affects the cooling. No longer can the individual droplet impacts be isolated qualitatively – rather, a chaotic but consistently decreased θ is observed.

At 40 Hz, the lowest values of θ in this study are seen as the droplets impinge on the cavity created by the previous droplet. This constant substrate contact allows for the maximum cooling effect which in turn produces the largest overall temperature drop.
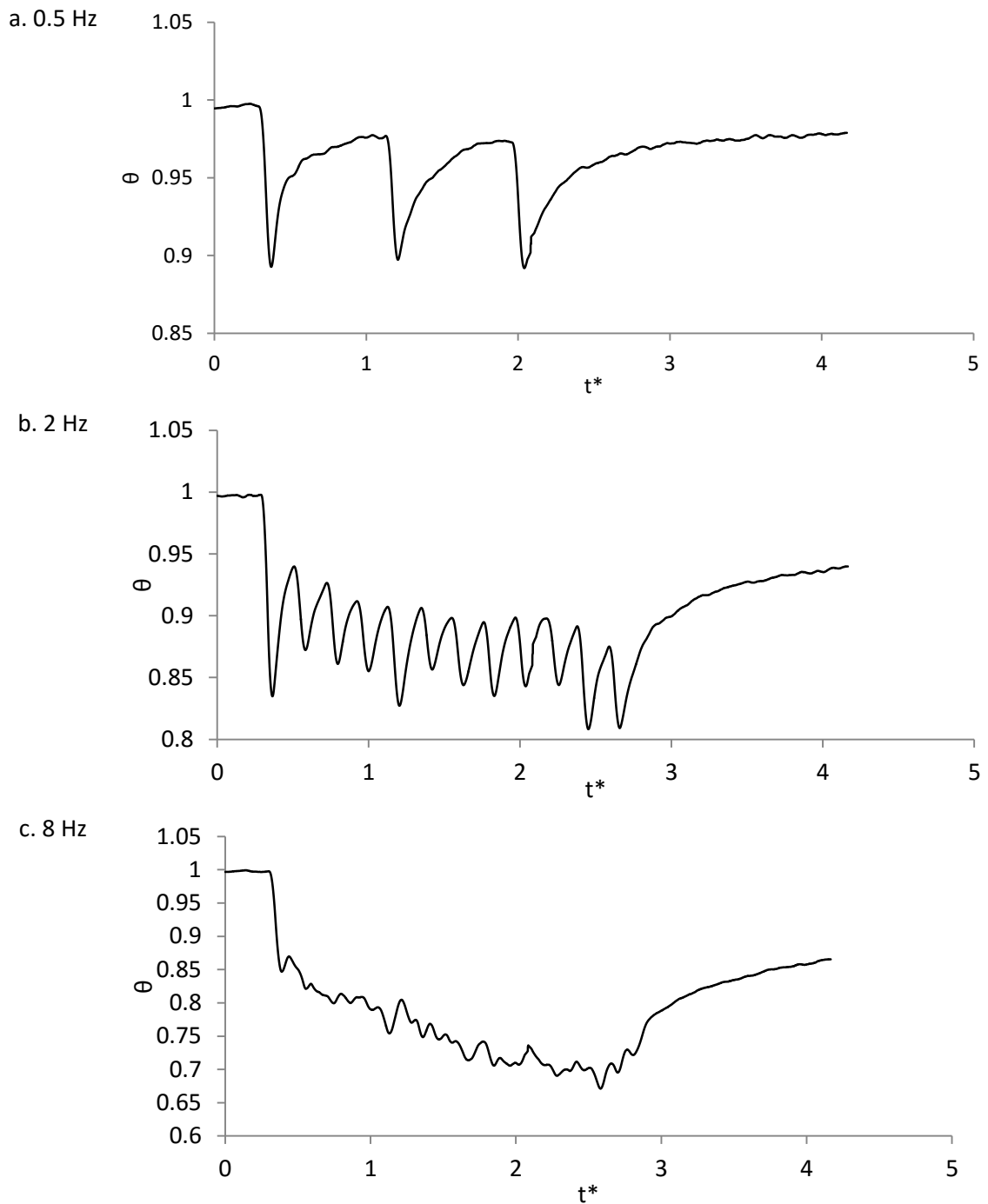
Figure 2.52. Temperature history of droplet trains impacting a heated pool at 0.5, 2, and 8 Hz.
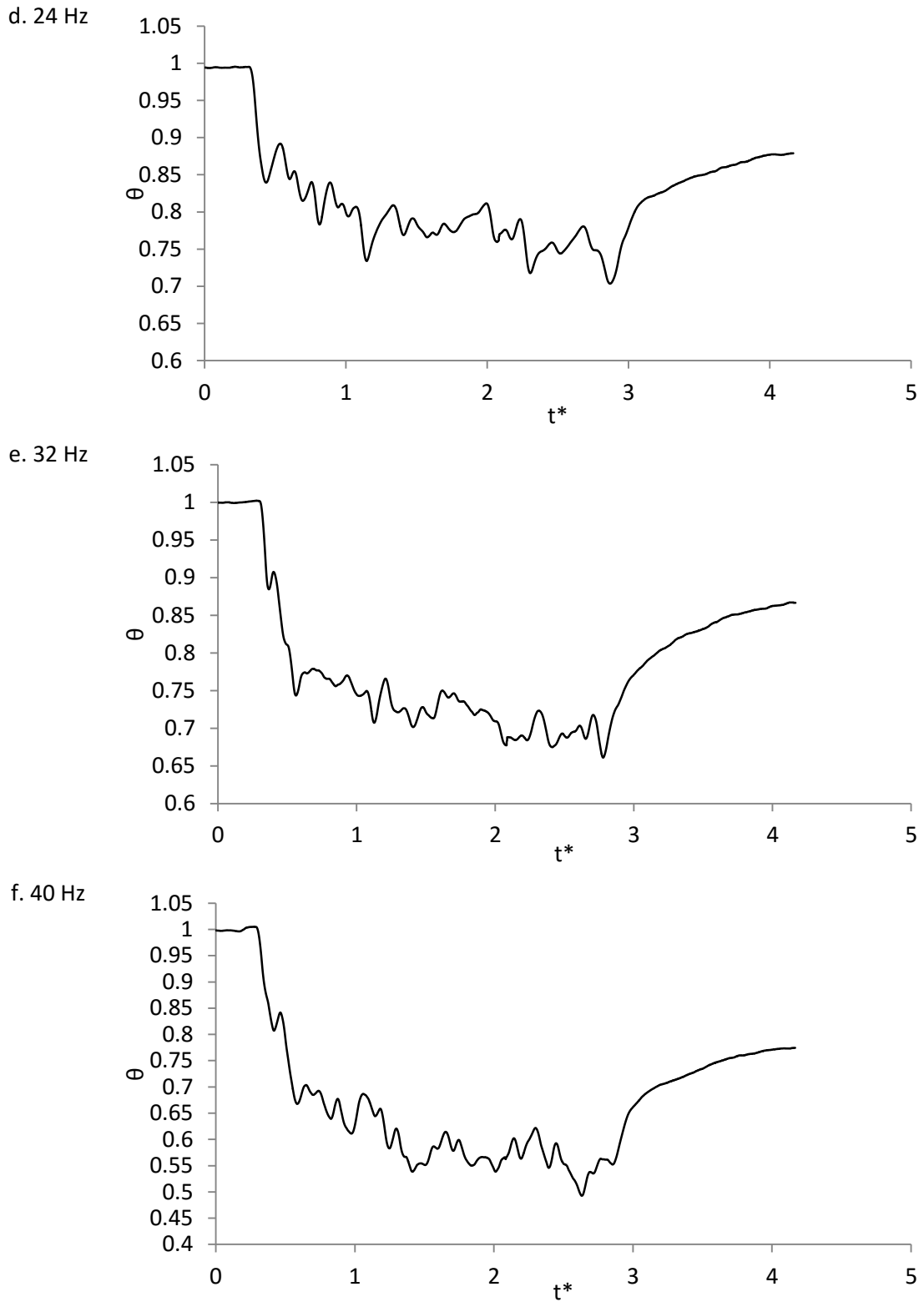
Figure 2.53. Temperature history of droplet trains impacting a heated pool at 24, 32, and 40 Hz.

The calculated heat flux, depicted in Figure 2.54, shows a general trend of increased heat flux as frequency increases. The maximum reduction in temperature is also shown- also following a trend of increasing with frequency, but with a plateau between 8-24 Hz. This covers the range building up to the critical frequency for these trains of 22 Hz (Equation [2-30]c). Within this range, impacts are frequent enough that the dynamics overlap but not yet rapid enough for impingement into a still-open cavity. Heat flux measurement was taken for an $H^*=7$ pool to show that at a deep enough pool, the cooling effects can be deemed negligible.
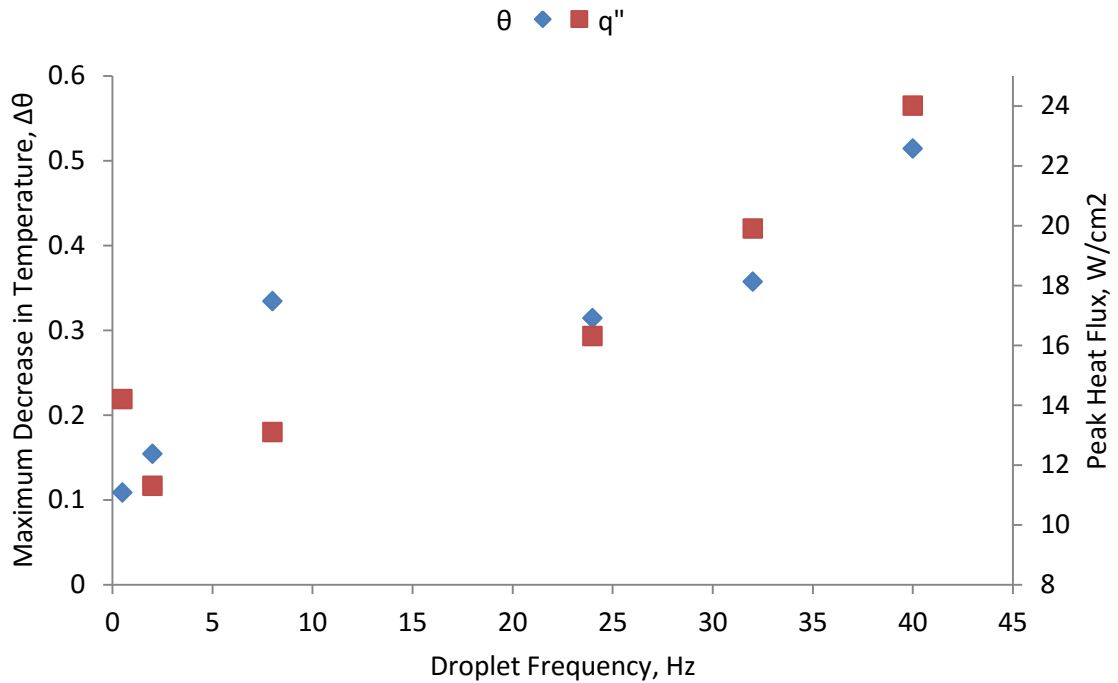
Figure 2.54. Measured heat flux and maximum decrease in temperature of droplet trains over a range of frequencies, for $We = 270$ and a range of H^* from 0 to 2.

For the frequencies studied, the highest cooling in terms of heat flux occurs as the frequency increases. The cooling period of each droplet at higher frequency overlaps with the next, leading to a cumulative high heat flux. However, it is worth examining the heat flux in light of the overall quantity of liquid delivered. By normalizing heat flux against the maximum possible cooling capacity of the droplet liquid (i.e., the heat that would be extracted if the entirety of the droplet liquid heated from its initial temperature to the pool temperature by cooling the sensor), it is possible to examine the cooling effectiveness on a per-droplet basis. Equation [2-32] shows the process by which heat flux is normalized against the cooling capacity of the trains, which is then compared for the trains used in this study in Figure 2.52.

$$q^* \equiv \frac{q''}{q_{capacity}} = \frac{q''}{f * \frac{4}{3}\pi r^3 \left(T_{pool} - T_{droplet}\right)} \qquad [2\text{-}32]$$
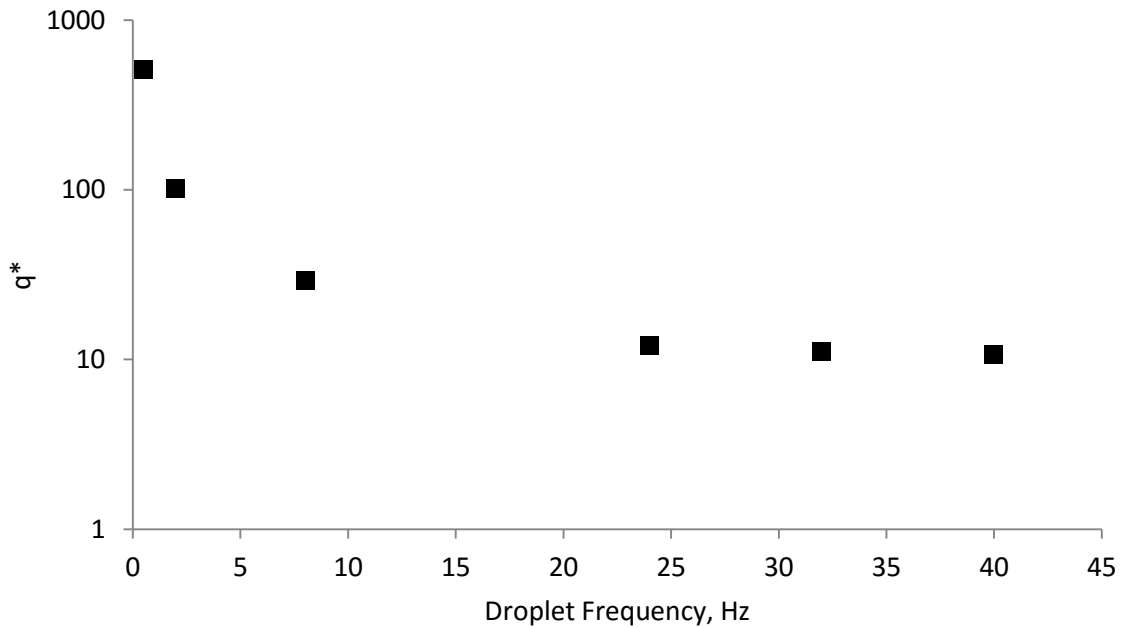
Figure 2.55. Normalized heat flux versus droplet train frequency.

Figure 2.55 shows an interesting trend – lower frequencies produce larger per-droplet cooling effects than higher, despite the elevated peak heat flux observed for higher frequencies in Figure 2.54. The essentially isolated single-droplet impingement of a 0.5 Hz train produces almost 2 orders of magnitude more mass-efficient cooling than trains over 20 Hz.

2.8.3. Conclusions

The main purpose of this study was to investigate the dynamics and heat transfer of single droplet and trains of droplet to better understand spray cooling. This was done by studying and characterizing single droplet and droplet train cavity dynamics as well as the heat transfer of varying surface conditions.

This study found for single droplet impact, the presence of the liquid pool reduces the effective cooling at and near the point of droplet impact. For spray cooling applications where the highest heat flux is needed, the liquid delivered by the spray should be minimized to prevent the buildup of the liquid film on the surface. This is one situation where phase change heat transfer that is often present in spray cooling applications, although not investigated in this study, would be highly beneficial. Evaporation is often accompanied by increased heat flux over convection alone, and it further acts to remove liquid from the sprayed area – a dual effect that should serve to prevent film buildup and maximize the spray's cooling effects.

In cases where a large buildup of a liquid pool is unavoidable, a higher impact frequency should be implemented to not only allow the fluid to penetrate the intended points through the open cavity created by previous impacting droplets and to also avoid interference of developing jets. The ideal cooling configuration where a film is present on the substrate is a spray that produces the quasi-steady cavity condition, allowing incoming droplets to reach the substrate as easily as possible.

Higher impact frequencies in dry surface situations will help minimize the development of the thermal boundary layer, which occurs as the droplet spreads out over larger areas, due to the constant influx of cold liquid pushing heated liquid out of the way. Heat flux findings from the droplet trains are in good agreement with Soriano, et al.'s [Cite Soriano 2014] finding. This good agreement shows that high heat fluxes can be obtained with larger droplets (mm sized) and smaller frequencies (in the tens).

Connection with the Dissertation Premise

Two of the many challenges facing development of spray cooling systems are the rapidly changing cooling dynamics as the surface is coated with liquid, and the interactions between the numerous droplets of the spray. This study tackled both of those challenges – examining how droplets influence the surface by producing a cavity within a liquid pool, and how that cavity primes the surface for subsequent droplets. The thermal boundary layer within the pool is bound to these cavity and pool dynamics – the observed heat flux was seen to change based on interference or facilitation of cooling by sequential droplets.

References

Banks, D., R. Sanchez, C. Ajawara, H. Surti and G. Aguilar (2013). "Effects of drop and film viscosity on drop impacts onto liquid films." <u>Atomization and Sprays</u> **23**(6): 525-540.

Rein, M. (1996). "The transitional regime between coalescing and splashing drops." <u>Journal of Fluid Mechanics</u> **306**(-1): 145.

Thomson, J. and H. Newall (1885). "On the formation of vortex rings by drops falling into liquids, and some allied phenomena." <u>Proceedings of the Royal Society of London</u> **39**(239-241): 417-436.

Vu, H., G. Aguilar and R. Jepsen (2009). <u>Single Droplet Heat Transfer through Shallow Liquid Pools</u>. 11th International Conference on Liquid Atomization and Spray Studies, Vail, CO, Institute of Liquid Atomization and Spray Studies.

Watanabe, Y., A. Saruwatari and D. M. Ingram (2008). "Free-surface flows under impacting droplets." <u>Journal of Computational Physics</u> **227**(4): 2344-2365.

2.9. Conclusion and Future Directions

Droplet impact studies have progressed significantly since the original attempts of Worthington in the 19th Century (Worthington 1876, Worthington 1882, Worthington and Cole 1897). For a complete understanding of droplet impact in spraying applications, however, the multitude of influencing factors have yet to be comprehensively surveyed. In this dissertation, a few of these aspects have been investigated for their effects on cooling and splashing dynamics. Even with the relatively narrow focus on droplet-substrate interactions and heat transfer, the scope of this study was not truly thorough. For example, the effects of surface tension, density, and viscosity on droplet train dynamics were omitted from study – as it stands, the role of these fluid properties in train dynamics may only be extrapolated from single droplet findings. Such inference may be useful but is not a substitute for direct experimental findings.

A two-pronged investigation connecting observations of fluid dynamics with measurements of heat transfer has proven fruitful. In several cases in this study, the range of fluids used exceeds what is commonly found in literature – for example, in Sections 2.5 and 2.6, a range of viscosity covering three orders of magnitude was explored. This led to the discovery of a dichotomous role of viscosity in droplet impact splashing, in particular, where viscosity both restricts motion and prevents splashing while simultaneously acting as the source of instability that permits splashing to exist.

Further, these studies investigated regimes observed regimes found in literature and characterized the development of these regimes – novel findings that deepen the understanding of droplet impact. In particular, the investigation into single droplet splashing revealed the reason between disagreements in literature about the relative influence of viscosity and surface tension in splashing. Also, in the sub-field of droplet train impacts, most literature involves high fre-

quency (kilohertz range) micron-scale droplets (Trujillo, Alvarado et al. 2011). This study combined lower frequency trains with larger scale droplets, allowing for experimental observation of impact dynamics. The high-frequency impacts observed in other studies produce a quasi-steady state cavity within the liquid film on the substrate; in this study the development of train impacts from isolated single droplet events to the steady state cavity was observed. Further, the relation between the impingement Weber number and the necessary frequency to produce the steady state cavity, and achieve the accompanying heat flux, was explored. Future work will expand the relationship to account for a wider range of impact velocities and fluid properties.

References

Trujillo, M. F., J. Alvarado, E. Gehring and G. S. Soriano (2011). "Numerical Simulations and Experimental Characterization of Heat Transfer From a Periodic Impingement of Droplets." Journal of Heat Transfer **133**(12): 122201-122210.

Worthington, A. (1882). "On impact with a liquid surface." Proceedings of the Royal Society of London **34**(220-223): 217-230.

Worthington, A. M. (1876). "On the Forms Assumed by Drops of Liquids Falling Vertically on a Horizontal Plate." Proceedings of the Royal Society of London **25**: 261-272.

Worthington, A. M. and R. S. Cole (1897). "Impact with a Liquid Surface, Studied by the Aid of Instantaneous Photography." Philosophical Transactions of the Royal Society of London. Series A, Containing Papers of a Mathematical or Physical Character **189**: 137-148.

3. Optical Cavitation for Convective Cooling

3.1. Background

Hydrodynamic cavitation – explosive boiling through abrupt pressure or temperature discontinuities - has been explored scientifically for almost a century, at least as far back as Volmer and Weber in 1926 (Volmer and Weber 1926). Optically-induced cavitation was documented shortly following the invention of the laser. In 1964, Carome, et al. reported acoustic signals as a focused pulsed ruby laser irradiated an absorbing liquid (Carome, Clark et al. 1964). Thermal transients in the liquid were believed responsible; phase change is not explicitly mentioned but Carome and his colleagues appear to have been the first to observe optical cavitation. Accompanying the rise of laser photonics, optically-induced cavitation has become a powerful tool in numerous applications.

However, cavitation produces powerful, often damaging shockwaves that often makes it an undesirable phenomenon (notably in watercraft design (Seol, Suh et al. 2005) and spray nozzles (Bergwerk 1959)). To effectively use laser-induced cavitation in almost any application, control of these shockwaves to prevent or selectively target damage is a necessity. Generally, shockwave damage is undesirable, so mitigation of the shockwave is a primary goal. In some cases, such as skin poration (Doukas and Kollias 2004) and materials surface processing, cavitation shockwaves can be beneficial and enhancing the strength of the shockwave is ideal. This study includes exploration of the fluid and optical factors that influence the shockwave dynamics.

Due to the higher, often ionizing energy densities involved in nanosecond and shorter laser pulses, cavitation occurs far more commonly with the use of pulsed lasers over continuous. Pulsed laser cavitation has seen extensive study since Carome, et al.'s pioneering observations using a ruby laser (Carome, Clark et al. 1964). Notably, W. Lauterborn has published extensive

research on pulsed optical cavitation. His research group's work has focused on the behavior of bubbles produced by pulsed laser and the flows around bubbles starting from 1975, with rotating-mirror photography used for imaging of cavitation bubbles (Lauterborn and Bolle 1975), and continuing to the present with measurement of the bubble collapse dynamics via particle tracking velocimetry (Kröninger, Köhler et al. 2009).

Continuous wave (CW) laser-induced cavitation is a much more recent development. CW lasers often have similar time-averaged optical power output as pulsed lasers, but the instantaneous energy density is typically far lower - several orders of magnitude - because pulsed lasers concentrate energy into exceedingly duty cycles. Rastopov and Sukhodolsky observed nucleation of cavitation bubbles induced by CW lasers using water-ethanol solutions as working liquids (Rastopov and Sukhodolsky 1990). The goal was to develop optical cavitation as a mechanism for studying the composition of liquid solutions non-intrusively, by examining how varying proportions of water and ethanol affected cavitation (Rastopov and Sukhodolsky 1990). The absorption coefficients of the solutions were elevated using rhodamine-g dye. Higher ethanol solutions had lower energy thresholds for cavitation, attributed to a reduced temperature for nucleation (Rastopov and Sukhodolsky 1991). The term thermocavitation was coined, referring to rapid superheating which results in cavitation.

Pulsed laser-induced cavitation follows a different bubble nucleation process, wherein the high optical energy density triggers an electron release cascade at the focal point of the pulse, forming superhot plasma that subsequently dissipates heat and forms a bubble (Fujimoto, Lin et al. 1985). Therefore, the term thermocavitation does not apply. Some authors uses the term photoionization or ionocavitation when referring to pulsed laser driven cavitation (Boulais, Lachaine et al. 2012).

CW cavitation is scarce in literature after Rastopov and Sukhodolsky's work in the early 1990s until 2007, when Ramirez-San-Juan, et al. described a process where cavitation was achieved using a low-power CW near-infrared laser in a copper nitrate solution. Cavitation occurred with as little as 60 mW optical power, due to high absorption by copper nitrate at the wavelength used (1024 nm) (Ramirez-San-Juan, Rodriguez-Aboytes et al. 2007). Ramirez, et al. have explored several applications of CW cavitation, producing ultrasound of varying frequency (Korneev, Montero et al. 2011), using cavitation as a metal film perforation mechanism (Ramirez-San-Juan, Padilla-Martinez et al. 2010), to overcome instability limits in liquid jets (Padilla-Martinez, Ramirez-San-Juan et al. 2013), and collaboratively pioneered cavitation for trans-dermal drug delivery, and by perforating the skin with micron-scale holes that allowed drug molecules to penetrate (Padilla-Martinez, Banks et al. 2012).

3.2. PHYSICS

To describe optical cavitation briefly, it is rapid vaporization of a liquid due to absorbed optical energy, followed by the growth and collapse of a vapor bubble. Optical cavitation is not the only mechanism of cavitation. Most cavitation is mechanical, via abrupt local pressure drops caused by flow conditions (Brennen 1995); however electrical (Saranin 1988) and ultrasonic (Doulah 1977, Cochran and Prausnitz 2001) cavitation also occur. The result is the same- a short-lived vapor bubble that often emits a powerful acoustic shockwave upon collapse. For a detailed description of the process, optical cavitation can be broken down into five phases: irradiation, nucleation, growth, collapse, and rebound.

Irradiation

During irradiation, the liquid absorbs optical energy. For a pulsed laser, the laser is active on-ly for the irradiation period; for CW cavitation the laser irradiates the bubble throughout the cavitation process, although the bubble minimizes absorption after it forms (Ramirez-San-Juan, Rodriguez-Aboytes et al. 2010). The irradiation period varies from nanoseconds or shorter for pulsed lasers (Boulais, Lachaine et al. 2012) to >10 milliseconds for low power CW cavitation (Ramirez-San-Juan, Rodriguez-Aboytes et al. 2010). Higher CW laser power reduces the length of the irradiation phase.

Concentrated optical pulses excite liquid molecules to release electrons, resulting in hot plasma formation (Boulais, Lachaine et al. 2012) - similar to the process observed in electrical discharge cavitation (Saranin 1988). Molecular effects are less apparent in CW cavitation; the laser heats the focal volume towards the spinodal superheat limit and the bubble appears to nucleate based on temperature alone (Padilla-Martinez, Aguilar et al. 2011).

Nucleation

Nucleation occurs upon plasma formation or critical superheat. The liquid parcel at the focal volume explosively boils. Metallic and carbon nanoparticles suspended in a liquid enhance cavi-tation by absorbing energy and acting as nucleation sites (Boulais, Lachaine et al. 2012). Nuclea-tion occurs nearly instantly for pulsed laser cavitation, as the molecules of liquid break ionize on the leading edge of the pulse, and the rest of the pulse is absorbed by this quickly-formed plas-ma (Bunkin, Kiseleva et al. 1997).

In CW cavitation, certain additives, especially carbon nanotubes, dramatically reduce the energy density required for cavitation to occur (Dharmadhikari, Dharmadhikari et al. 2011). Car-bon nanotubes strongly absorb near-IR radiation, with absorption coefficients around 105 cm^{-1}.

Using carbon nanotubes suspended in water and a 100x microscope objective as a focusing lens, cavitation occurs with laser power as low as 5 mW (Dharmadhikari, Dharmadhikari et al. 2011).

Growth

The optical energy converts into latent heat, producing a high-pressure vapor, and then the bubble grows rapidly. Pulsed laser cavitation tends to result in small, micron or smaller scale bubbles (Bunkin and Karpov 1990), while CW lasers produce bubbles ranging from sub-millimeter up to approximately 5 mm, with higher laser power resulting in smaller, more frequent bubbles (Ramirez-San-Juan, Rodriguez-Aboytes et al. 2010). Higher CW power heats the liquid to the critical temperature more quickly, minimizing diffusion time (Padilla-Martinez, Aguilar et al. 2011). The growth period lasts up to 200 microseconds, with shorter growth for smaller bubbles (Ramirez-San-Juan, Rodriguez-Aboytes et al. 2010).

Collapse

Collapse occurs when the pressure inside the bubble equalizes and falls below the surrounding liquid pressure. The bubble retracts rapidly back towards the point of nucleation.

For bubbles formed near a solid boundary, the collapse occurs faster opposite the boundary than elsewhere, leading to a toroid shape (Figure 3.2). This was perhaps first reported in an optical cavitation setting by Lauterborn and Bolle (Lauterborn and Bolle 1975). They suggested proximity to a solid boundary as one possible cause of asymmetric collapse, which later research has verified (Thoroddsen, Takehara et al. 2009).

The distance between the center of the bubble and the nearest solid boundary, referred to as the stand-off distance, affects how strongly asymmetric the collapse is (Liu, Cai et al. 2014). The dimensionless stand-off distance (γ) is defined by Equation [3-1], with the initial distance from the bubble center to the wall (D_0) normalized to the maximum radius of the bubble (R).

$$\gamma = \frac{D_0}{R} \qquad\qquad \text{[3-1]}$$

Liu, et al. investigated the convective heat transfer enhancement resulting from the polar jet's impingement upon a heated solid boundary (Liu, Cai et al. 2014). Their model suggests that when bubbles formed near the wall ($1.0 < \gamma < 1.5$), the jet provided a convective cooling effect to the wall. The jet delivers cooler liquid from further within the liquid volume to the heated solid boundary.

The asymmetric collapse of cavitation bubbles formed near a solid boundary is historically attributed to the Kelvin Impulse at the bubble boundary. The Kelvin Impulse describes the inertia of a bubble. Blake defines the impulse, I, based on the liquid density, ρ, the velocity potential, ϕ, and the normal vector to the fluid, n, integrated over the bubble boundary S (Blake 1988):

$$I = \rho \int_S \phi\, n\, dS \qquad\qquad \text{[3-2]}$$

The Kelvin impulse arises from a momentum balance carried out on a finite volume of liquid surrounding a bubble. Blake provides the derivation of the Kelvin impulse near a solid boundary in (Blake 1988); suffice it to say that the smaller the standoff distance, the larger the impulse term. The larger impulse results in the formation of the jet towards the solid boundary (Blake 1988).
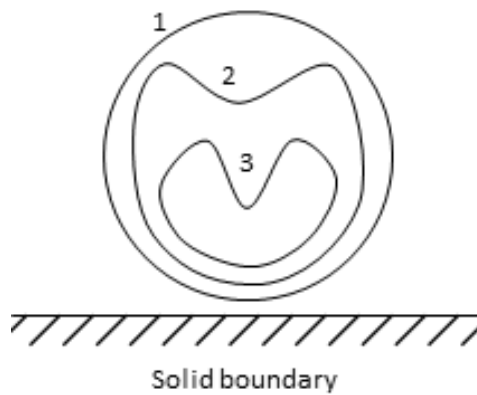
Figure 3.1. Depiction of polar-asymmetric bubble collapse near solid boundary. based on numerical results from (Lauterborn and Bolle 1975). At (1), the bubble is at its maximum diameter and is spherical. The collapse begins, and as the bubble shrinks it begins to deform at the pole opposite the boundary (2). By (3) the bubble has deformed to a nearly toroid shape and the polar jet is clearly defined.

By producing cavitation within liquid droplets resting on a glass slide, polar collapse results in jets which can exceed the Rayleigh-Plateau instability limit (Padilla-Martinez, Ramirez-San-Juan et al. 2013). An observation of Padilla-Martinez, et al. while looking at these jets was that CW laser cavitation appears to always nucleate on the solid boundary and grow in a hemispherical shape, regardless of where the laser's focal point is placed, and the collapse always follows the polar-first collapse shape (Padilla-Martinez, Ramirez-San-Juan et al. 2013).

Shockwave

When the bubble collapses, an acoustic shockwave is emitted- Vogel, et al. discuss acoustic transients after optical cavitation (Vogel and Lauterborn 1988), similar to Carome, et al.'s thermal transients. The shockwave for optical cavitation initially is ~1 MPa (Korneev, Montero et al. 2011). Korneev, et al. used this shockwave as an ultrasound source, using a CW laser to induce cavitation and controlled the strength of the shockwave by adjusting the laser's beam width

(Korneev, Montero et al. 2011). Ramirez-San-Juan, et al. found that smaller bubbles tend to produce weaker shockwaves (Ramirez-San-Juan, Padilla-Martinez et al. 2010).

Rebound

After the collapse of the cavitation bubble, secondary bubbles are often seen rebounding and occasionally moving away from the initial site (Camacho-López, Perez-Gutierrez et al. 2013). Bubble rebound has seen very little research. Fyrillas and Szeri modeled mass transport at the boundary of an oscillating bubble, finding that pressure fluctuations within the bubble affect the solubility of gas in the surrounding liquid (Fyrillas and Szeri 1994). The oscillation in bubble volume is attributed to the rapid local dissolution and escape of gas around the bubble edges. Pressure fluctuations during and after cavitation can cause additional bubbles, likely comprised of dissolved gas, to form near the cavitation site, as seen in Figure 3.2.
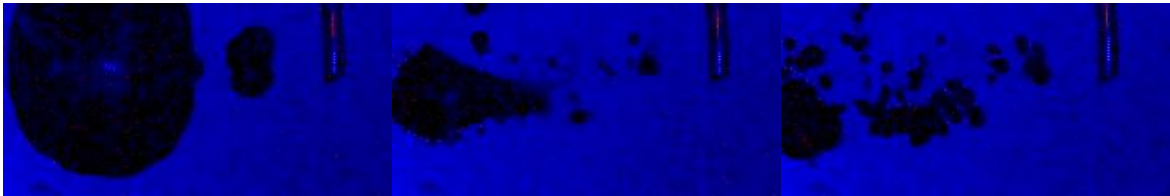
Figure 3.2. High speed video observations of pulsed laser cavitation.
Note secondary bubbles appearing after collapse. Fiber in image is used for length reference and is 125 µm diameter.

Figure 3.3 reviews the processes that occur during optical cavitation, providing an easy reference and comparison of the dynamics of pulsed laser and continuous wave laser-induced bubbles.

Phase	Pulsed Laser	CW Laser
Preheating	Nothing occurs prior to pulse	Duration dependent on laser power, absorptivity, etc. Generally < 100 ms. Heating to near spinode temperature.
Primary Nucleation	Leading edge of pulse reaches critical energy density, ionizes liquid into plasma, which absorbs the remainder of the laser pulse energy.	Near laser focus, a parcel of fluid reaches spinode temperature and flash boils, causing cascade boiling within the superheated volume.
Growth	After nucleation, CW and pulsed laser cavitation proceeds in the same fashion. Starting from a high-temperature, high-pressure volume of vapor, rapid expansion to equalize pressure. Bubble growth lasts up to 200 μs.	
Collapse	Occurs after pressure equalizes and falls. Bubble accelerates inward or towards nearest solid boundary. Acoustic shockwave emitted upon complete collapse.	
Rebound	Pressure fluctuations occasionally cause dissolved gas to nucleate out of liquid temporarily, appearing as oscillation of primary bubble and appearance of secondary bubbles.	

Figure 3.3. A generalized timeline of optical cavitation dynamics, comparing the scales and processes observed for pulsed and continuous wave-laser cavitation.

3.2.1. Challenge to Traditional Models of Bubble Dynamics

Spherical bubble collapse can be well modeled using the Rayleigh-Plesset equation for bubbles formed far from a spherical boundary (Brennen 1995). This model assumes incompressible, inviscous liquid and is derived from Navier-Stokes and the continuity equation.

$$R\ddot{R} + \frac{3}{2}\dot{R}^2 = \frac{P(R) - P_\infty}{\rho}$$

[3-3]

Equation can be solved for the collapse time based on the maximum radius of the bubble:

$$t_c \approx 0.915\, R_{max}\sqrt{\frac{\rho}{P_\infty - P_v}}$$

[3-4]

One other bubble characteristic that arises out of the Rayleigh-Plesset equation is the *bubble energy*. The bubble energy is a form of potential energy, due to the pressure difference from the bubble interior to ambient. The bubble energy E_B depends on the maximum bubble radius:

$$E_B = \frac{4}{3}R_{max}^3(P_\infty - P_v)$$

[3-5]

While Rayleigh-Plesset adapts well to mechanical (i.e., pressure-induced) cavitation, it assumes the bubble is adiabatic and spherical. Deriving an equivalent equation without those assumptions is difficult. In optical cavitation studies, the Rayleigh-Plesset equation and solutions are typically used as a control to which experimental results are compared.

Optical cavitation bubbles, unlike mechanical cavitation bubbles, often have tremendous thermal gradients involved. The temperature differences in the neighborhood of the bubble alter fluid properties significantly, potentially challenging the Rayleigh-Plesset bubble model. Fur-

ther, optical cavitation bubbles, particularly of the CW-laser-induced variety, often occur in the neighborhood of solid boundaries and are highly aspheric – another factor detracting from the Rayleigh-Plesset model. This asymmetry has been found to affect the bubble's fluid dynamics and thermal effects. The standoff distance, γ, can be used to quantitatively characterize the effects of the solid boundary.

Godwin, et al. devised a relationship between γ and a "prolongation time". The prolongation time gives an estimate of the divergence of a near-boundary bubble from the Rayleigh-Plesset model. For values of γ larger than 1, Equation [3-6] provides the modified collapse time:

$$\frac{t_c'}{t_c} = 1 + 0.41\frac{1}{2\gamma} \qquad\qquad [3\text{-}6]$$

For smaller standoff ratios, this model breaks down- it suggests t_c becomes infinitely long. As γ decreases below 1, the bubble becomes increasingly hemispherical, deviating from the spherical assumption of Rayleigh-Plesset that was used to derive the collapse time expression. Godwin, et al. found that for small values of γ, the collapse time is approximately 1.20 of that predicted by Equation [3-4] (Godwin, Chapyak et al. 1999).

One possibility that is not investigated in this study but merits a look is optical cavitation near a free (atmosphere) liquid boundary. There has been some research into that topic, but not nearly as much as the investigation of cavitation near solid boundaries. Jets and droplets can be produced by cavitation near vapor boundaries (Thoroddsen, Takehara et al. 2009, Padilla-Martinez, Ramirez-San-Juan et al. 2013). An investigation into vapor-boundary standoff distance is likely to yield interesting results for fluid control via cavitation.

3.3. Experimental Setup

3.3.1. High Speed Video

Currently, the primary technique for measurement of cavitation bubble dynamics is high speed (HS) video, with framerates of 100,000 frames per second or faster, and exposure times of 10^{-6} seconds are common. For this study, the HS video camera is a Miro m310 by Vision Research. At full 1280 x 800 resolution, the m310 provides a framerate up to 4500 fps; reduced resolution can increase the framerate over 200,000 fps – resolving timescales of approximately 0.5 µs. While adequate for exploring bubble dynamics where timescales are on the order of 10-100 microseconds, HS video is unsuitable to characterize the initial nucleation process and shockwave, which are characteristically nanosecond processes. However, if other techniques are able to provide improved time resolution of the nucleation and shockwave, HS video remains a powerful tool for observing the dynamics during the bubble lifetime

Phase contrast imaging has potential for allowing HS video to explore the thermal gradients around cavitation bubbles as well, although this method has yet to mature in cavitation studies. Phase contrast imaging exploits the change in refractive index as liquid changes temperature and pressure (Hecht 1998). Using a laser as an illumination source, these refractive index changes alter the phase of light as it passes through the liquid. The high speed video camera then sees these phase changes as dark and bright regions (Figure 3.4). At the moment, phase contrast provides only qualitative measurement capabilities – it is possible to observe the ejection of heated liquid form the cavitation site, for example; this is quite clear in Figure 3.4. However, the actual temperature of that liquid is unknown – it is merely certain to be different from ambient temperature.

| Nucleation +50 µs | +920 µs | +2020 µs | +6070 µs |
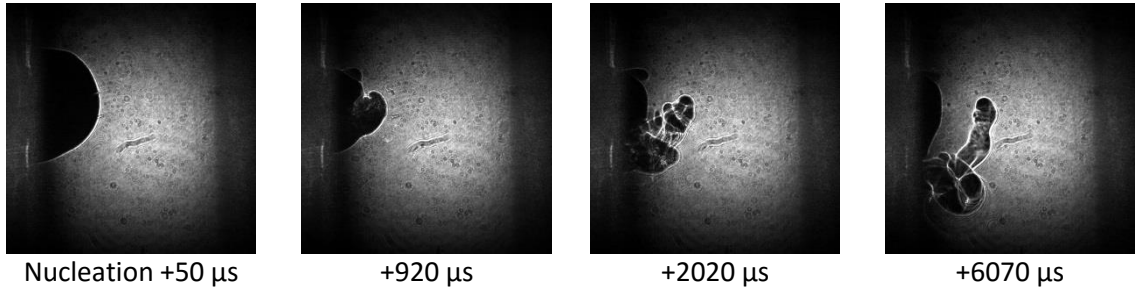
Figure 3.4. Phase contrast imaging of CW induced cavitation.
Phase contrast reveals relative density changes due to temperature differences; quantitative temperature measurement requires a different method.

References

Bergwerk, W. (1959). "Flow Pattern in Diesel Nozzle Spray Holes." Proceedings of the Institution of Mechanical Engineers **173**(1): 655-660.

Blake, J. R. (1988). "The Kelvin impulse: application to cavitation bubble dynamics." The Journal of the Australian Mathematical Society. Series B. Applied Mathematics **30**(02): 127-146.

Boulais, E., R. Lachaine and M. Meunier (2012). "Plasma Mediated off-Resonance Plasmonic Enhanced Ultrafast Laser-Induced Nanocavitation." Nano letters.

Brennen, C. E. (1995). Cavitation and bubble dynamics, Oxford University Press, USA.

Bunkin, N. F. and V. B. Karpov (1990). "Optical cavitation of transparent liquids exposed to broadband laser light." Pis'ma Zh. Eksp. Teor. Fiz. **52**(1): 669-673.

Bunkin, N. F., O. A. Kiseleva, A. V. Lobeyev, T. G. Movchan, B. W. Ninham and O. I. Vinogradova (1997). "Effect of Salts and Dissolved Gas on Optical Cavitation near Hydrophobic and Hydrophilic Surfaces." Langmuir **13**(11): 3024-3028.

Camacho-López, S., F. Perez-Gutierrez, L. Devia-Cruz, D. Garcia, G. Aguilar and D. Banks (2013). "High Resolution Optical Experimental Technique for Computing Pulsed Laser Induced Cavitation Bubble Dynamics in a Single Shot." Atomization and Sprays **23**(6): 475-485.

Carome, E. F., N. A. Clark and C. E. Moeller (1964). "Generation of Acoustic Signals in Liquids by Ruby Laser-Induced Thermal Stress Transients." Applied Physics Letters **4**(6): 95-97.

Cochran, S. A. and M. R. Prausnitz (2001). "Sonoluminescence as an indicator of cell membrane disruption by acoustic cavitation." Ultrasound in medicine & biology **27**(6): 841-850.

Dharmadhikari, A. K., J. A. Dharmadhikari, A. V. Mahulkar, G. Ramanandan, H. Ramachandran, A. B. Pandit and D. Mathur (2011). "Dynamics of Photothermally Created Vaporous, Gaseous, and Mixed Microbubbles." The Journal of Physical Chemistry C **115**(14): 6611-6617.

Doukas, A. G. and N. Kollias (2004). "Transdermal drug delivery with a pressure wave." Advanced Drug Delivery Reviews **56**(5): 559-579.

Doulah, M. S. (1977). "Mechanism of disintegration of biological cells in ultrasonic cavitation." Biotechnology and Bioengineering **19**(5): 649-660.

Fujimoto, J. G., W. Z. Lin, E. P. Ippen, C. A. Puliafito and R. F. Steinert (1985). "Time-resolved studies of Nd:YAG laser-induced breakdown. Plasma formation, acoustic wave generation, and cavitation." Investigative Ophthalmology & Visual Science **26**(12): 1771-1777.

Fyrillas, M. M. and A. J. Szeri (1994). "Dissolution or growth of soluble spherical oscillating bubbles." Journal of Fluid Mechanics **277**: 381-407.

Godwin, R. P., E. J. Chapyak, J. Noack and A. Vogel (1999). Aspherical bubble dynamics and oscillation times.

Hecht, E. (1998). Optics, Addison-Wesley.

Korneev, N., P. R. Montero, R. Ramos-García, J. C. Ramirez-San-Juan and J. P. Padilla-Martinez (2011). "Ultrasound induced by CW laser cavitation bubbles." Journal of Physics: Conference Series **278**: 012029.

Kröninger, D., K. Köhler, T. Kurz and W. Lauterborn (2009). "Particle tracking velocimetry of the flow field around a collapsing cavitation bubble." Experiments in Fluids **48**(3): 395-408.

Lauterborn, W. and H. Bolle (1975). "Experimental investigations of cavitation-bubble collapse in the neighbourhood of a solid boundary." Journal of Fluid Mechanics **72**(2): 391-399.

Liu, B., J. Cai, X. Huai and F. Li (2014). "Cavitation Bubble Collapse Near a Heated Wall and Its Effect on the Heat Transfer." Journal of Heat Transfer **136**(2): 022901.

Padilla-Martinez, J. P., G. Aguilar, J. C. Ramirez-San-Juan and R. Ramos-Garcia (2011). Generation of Micron-Sized Holes on Metallic and Transparent Thin Films Using Thermocavitation. Institute of Liquid Atomization and Spray Studies-Americas. . Ventura, CA.

Padilla-Martinez, J. P., D. Banks, J. C. Ramirez-San-Juan, R. Ramos-Garcia, F. Sun and G. Aguilar (2012). "Towards the enhancement of transdermal drug delivery through thermocavitation." Photonics and Lasers in Medicine **1**(3): 183-193.

Padilla-Martinez, J. P., J. C. Ramirez-San-Juan, N. Korneev, D. Banks, G. Aguilar and R. Ramos-Garci a (2013). "Breaking the Rayleigh-Plateau Limit Using Thermocavitation Within a Droplet." Atomization and Sprays **23**(6): 487-503.

Ramirez-San-Juan, J. C., J. P. Padilla-Martinez, P. Zaca Moran, E. Aboytes-Rodriguez, A. E. Martinez-Canton and R. Ramos-Garcia (2010). "Thermocavitation and its application for fabrication of micron-sized holes on metallic and dielectric thin films." 77621E-77621E-77626.

Ramirez-San-Juan, J. C., E. Rodriguez-Aboytes, N. Korneev, O. Baldovinos-Pantaleon, R. Chiu-Zarate, G. Gutiérrez-Juárez, R. Dominguez-Cruz and R. Ramos-García (2007). Cavitation induced by continuous wave lasers.

Ramirez-San-Juan, J. C., E. Rodriguez-Aboytes, A. E. Martinez-Canton, O. Baldovino-Pantaleon, A. Robledo-Martinez, N. Korneev and R. Ramos-Garcia (2010). "Time-resolved analysis of cavitation induced by CW lasers in absorbing liquids." Opt. Express **18**(9): 8735-8742.

Rastopov, S. F. and A. T. Sukhodolsky (1990). "Cluster nucleation in the process of CW laser induced thermocavitation." Physics Letters A **149**(4): 229-232.

Rastopov, S. F. and A. T. Sukhodolsky (1991). Sound generation by thermocavitation-induced cw laser in solutions. Optical Radiation Interaction with Matter, Leningrad, Russia, SPIE.

Saranin, V. A. (1988). "Cavitation mechanism of high-voltage breakdown formation in liquid dielectrics." Journal of Applied Mechanics and Technical Physics **29**(3): 354-356.

Seol, H., J.-C. Suh and S. Lee (2005). "Development of hybrid method for the prediction of underwater propeller noise." Journal of Sound and Vibration **288**(1–2): 345-360.

Thoroddsen, S. T., K. Takehara, T. G. Etoh and C. D. Ohl (2009). "Spray and microjets produced by focusing a laser pulse into a hemispherical drop." Physics of Fluids **21**(11): 112101-112115.

Vogel, A. and W. Lauterborn (1988). Acoustic transient generation by laser-produced cavitation bubbles near solid boundaries, ASA.

Volmer, M. and A. Weber (1926). "Keimbildung in übersättigten Gebilden." Z. phys. Chem **119**: 277-301.

3.4. Development of the STM and its Adaptation to CW Cavitation

The use of the STM to record cavitation bubble size was developed for use with pulsed laser-induced cavitation and originally did not account for multiple bubbles forming during a recording period (Camacho-López, Perez-Gutierrez et al. 2013). Adapting the STM to continuous-wave induced cavitation had two challenges. First, the optical setup was different – CW lasers require a smaller beam waist to achieve cavitation-producing energy density; the focal length involved is too short to place the dichroic mirror between the lens and the cuvette – thus, the STM probe beam must pass through the focusing lens along with the cavitation driving lens. A further optical consideration is the use of additives to enhance absorption of the cavitation driving laser – the liquid must still be reasonably transparent to the STM probe. Selecting a wavelength that is transmitted by the solution solved part of the problem; adding an additional lens in the STM probe's path solved the other.

The second problem in adapting the STM to CW cavitation was less trivial: adapting the measurement algorithm to handle multiple bubbles. The original code assumed there was a single cavitation event – it found the radius of the initial bubble and any secondary oscillating bubbles but provided no information about sequential cavitation events (Banks, Garcia et al. 2013). A threshold-based filter was developed to allow recognition and measurement of multiple separate bubbles within a single voltage signal.

3.4.1. Fundamentals of the STM System

One newer technique to characterize cavitation dynamics is Spatial Transmission Modulation (STM) (Camacho-López, Perez-Gutierrez et al. 2013). STM transmits a low power continuous laser (the probe) through the liquid volume along the axis of the cavitation-inducing laser. A photodiode reads the strength of the transmitted laser. When a bubble is formed within the

liquid volume, it blocks a portion of the expanded probe, and the photodiode reports a drop in transmitted optical power. Figure 3.5 depicts the components of STM system.
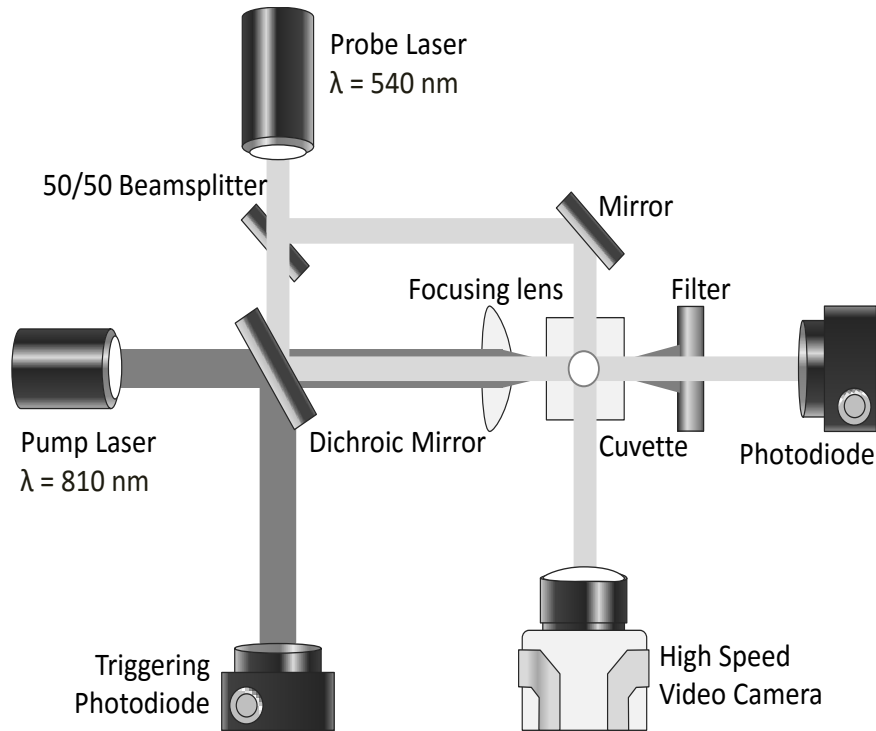
Figure 3.5. Spatial transmission modulation setup.

A low power (0.5 mW at 542 nm), CW laser (the probe) is directed coaxially with the pump laser using a dichroic mirror. The probe has a wavelength that is transmitted by the working fluid, so it passes through the cuvette where the pump is absorbed. The beam of the probe is expanded by two lenses from approximately 1 mm to 7 mm in diameter, so that it is larger than any expected bubbles. It is then directed into a photodiode (Thorlabs DET10A). When a bubble is produced at the focal point of the pump laser, it refracts a portion of the probe away from the photodiode. By approximating the intensity distribution of the probe beam as Gaussian, the drop in the photodiode signal is used to compute the radius of the bubble. The accuracy of the STM was verified by measurements of the bubble taken using a high speed video camera.

The high speed camera is a Miro M310 illuminated by a 542 nm CW laser. The camera records at 25,000 fps and 384 x 288 px. resolution. It observes cavitation perpendicularly to the bubble formation – observing a hemispherical cross section. To verify the STM findings, the hemisphere observed by the camera is assumed to have the same base diameter as the spherical cross-section that the STM measures.

Being limited only by the response time of a photodiode (on the order of single nanoseconds), STM provides better time resolution than HS video. STM can be expanded to multiple axes to provide aspect-ratio measurement of the bubble dimensions: bubbles formed near solid boundaries are often aspheric and STM could adapt to this at much lower cost than using multiple HS cameras (Banks, Garcia et al. 2013). The advantage HS video has over STM appears when the secondary bubbles move away from the nucleation site- on HS video, the movement is immediately obvious, but STM may report a false-negative if the bubble moves out of the measurement volume.

Hydrophones and other pressure transducers provide another means of characterizing cavitation. Specifically, the post-collapse shockwave pressure and duration can be recorded; it was through this method that Ramirez-San-Juan, et al. observed that smaller CW-induced bubbles produced smaller shockwaves than larger ones (Ramirez-San-Juan, Rodriguez-Aboytes et al. 2010). Juhasz, et al. suggest using shorter laser pulses to shrink the cavitation bubble and shockwave, imperative in laser eye therapy (Juhasz, Kastis et al. 1996).

With a Gaussian circular probe laser of known beam diameter, the radius of the bubble blocking that beam can be found. Equation [3-7] shows the relationship between photodiode voltage (V), the probe beam width (w), and the instantaneous bubble radius ($R(t)$) (Camacho-López, Perez-Gutierrez et al. 2013).

$$V(t) \sim \int_{-w}^{w} \exp\left(\frac{r^2}{2w^2}\right) dr - \int_{-R(t)}^{R(t)} \exp\left(\frac{r^2}{2w^2}\right) dr \qquad \text{[3-7]}$$

3.4.2. Overview of Iterative Radius Solver

Equation [3-7] is the starting point for finding the radius of the cavitation bubble. The equation neglects to include any scaling coefficients that arise from optical and experimental factors. To remove these coefficents, the equation and the measured voltage signal are normalized against the nominal voltage reported by the photodiode when no bubble is present (V_{nom}):

$$\frac{V(t)}{V_{nom}} \sim \frac{\int_{-w}^{w} \exp\left(\frac{r^2}{2w^2}\right) dr - \int_{-R(t)}^{R(t)} \exp\left(\frac{r^2}{2w^2}\right) dr}{\int_{-w}^{w} \exp\left(\frac{r^2}{2w^2}\right) dr} \qquad \text{[3-8]}$$

The radius is iteratively found using Equation [3-8]. An estimate of the radius is used to calculate a value for the normalized voltage. This value is then compared to the measured voltage. If the estimated value is larger than the measured one, the radius is increased, and vice-versa, until the values converge within a specified error. To speed computation, after the first radius point is found, the radius for the prior time step is used as the starting point for the successive iteration.

3.4.3. Experimental Verification

Using a single pulse from the Nd:YAG pumping laser, a cavitation bubble was formed within a glass cuvette containing deionized water. The HS camera recorded the event. A sequence of stills from the video is presented in Figure 3.6, with accompanying timestamps and bubble radii, starting from the initiation of the pulse. In the first frame, the green flash of the pulse is observed. In subsequent frames, the growth and collapse of the initial cavitation bubble and subsequent bubbles are depicted.
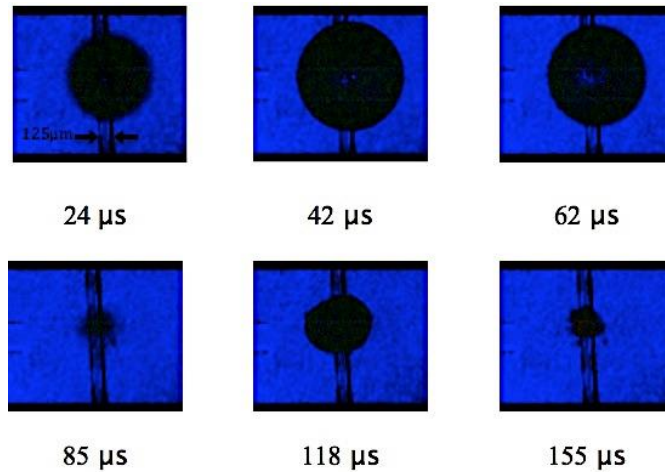
Figure 3.6. Sequence of still frames from a cavitation event induced by a single pulse from the pumping laser.
Time given in µs post-pulse; the fiber visible in the image is 125 microns diameter for scale.

Alongside the high speed recording, the STM photodiode's voltage trace from the same cavitation event was recorded and is shown in Figure 3.7. Prior to the trigger ($t=0$ in the figure), the voltage is constant at approximately 40 mV: a nominal no-bubble signal. There is a spike at the trigger time, corresponding to the pumping laser's pulse, and then the primary cavitation bubble is observed as a large curve below the reference voltage, as the bubble blocks the transmission of the probe beam. As the bubble collapses, the voltage trace goes back towards its nominal value, and subsequent bubbles can be seen as smaller dips in the voltage.
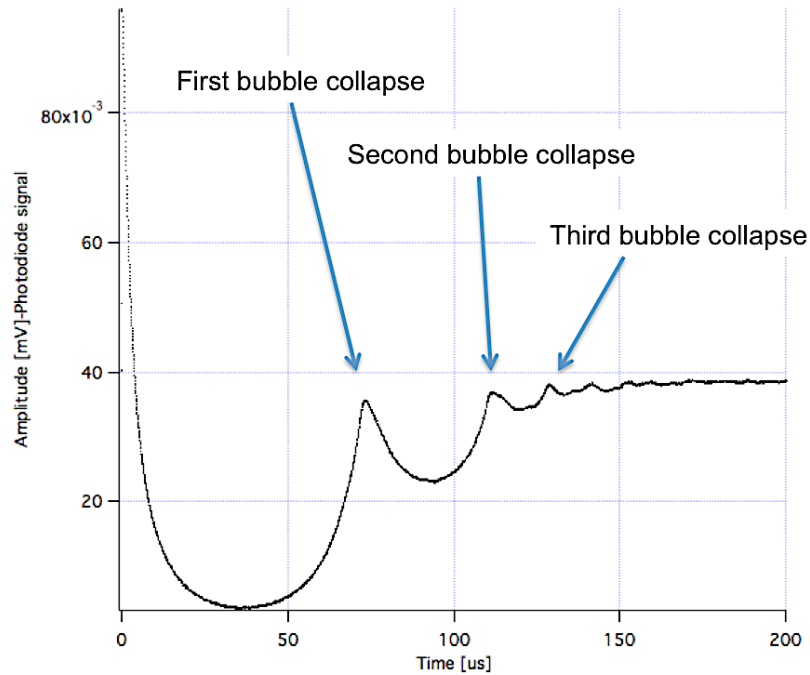
Figure 3.7. STM voltage trace from the cavitation event depicted in Figure 3.6.

In Figure 3.7, the voltage predicted by Equation [3-7] from the radii measured with the camera is superimposed on the voltage readings. The beam width used was 650 μm, based on measurement of the spot size using the HS camera. The predictions match measurements almost exactly.

For a more detailed observation, a frame-by-frame set of high-speed video images are presented in Figure 3.6, and the accompanying STM signal is seen in Figure 3.7 with arrows indicating the point in the signal corresponding to each still frame.
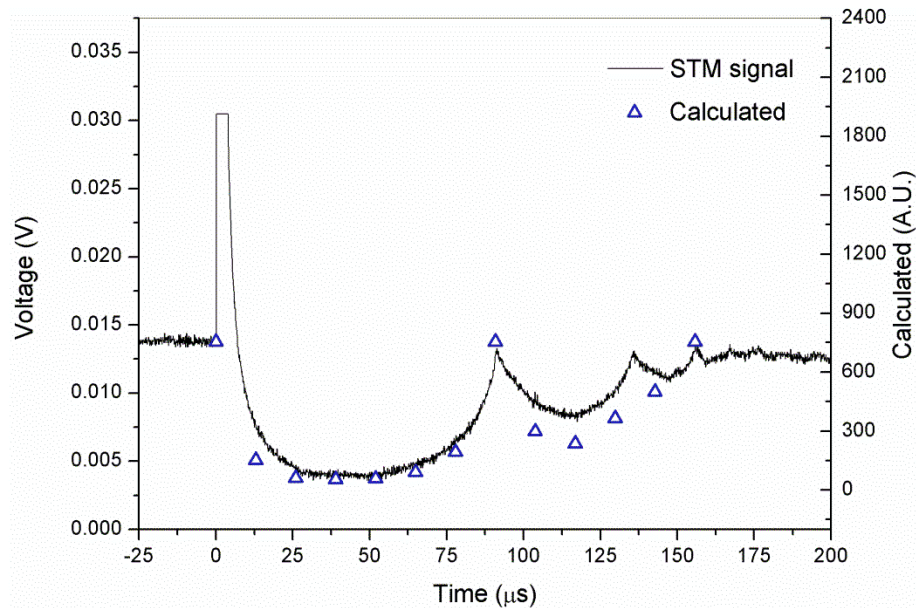
Figure 3.8. Overlay of voltage predictions from Equation [3-7] onto the voltage trace recorded in Figure 3.7.

Figure 3.11 shows the same STM trace after applying the radius calculation algorithm from section 3.4.2. For comparison, the measurements from each frame of the HS video of the same event are presented, as well. Qualitatively, the algorithm and the video agree well with each other. A notable exception to the agreement is when the bubble falls below a minimum radius – for example, a small bubble was still present on video from approximately 300 to 375 µs, but the STM reported no bubble.

The advantage of the high sampling rate of the STM system over the relatively slow video camera is apparent from Figure 3.11. Between 100 and 150 µs, the STM observed two bubble oscillations, where the video misses the intermediate collapse due to the frame interval.

(a) Prior to pulse　　　　　　(b) Laser pulse　　　　　　(c) Bubble growth

(d) Max diameter (0.18 mm)　　(e) Collapsing　　　　　　(f) First collapse

(g) Secondary bubble　　　　(h) Delayed bubble　　　　(i) Delayed bubble
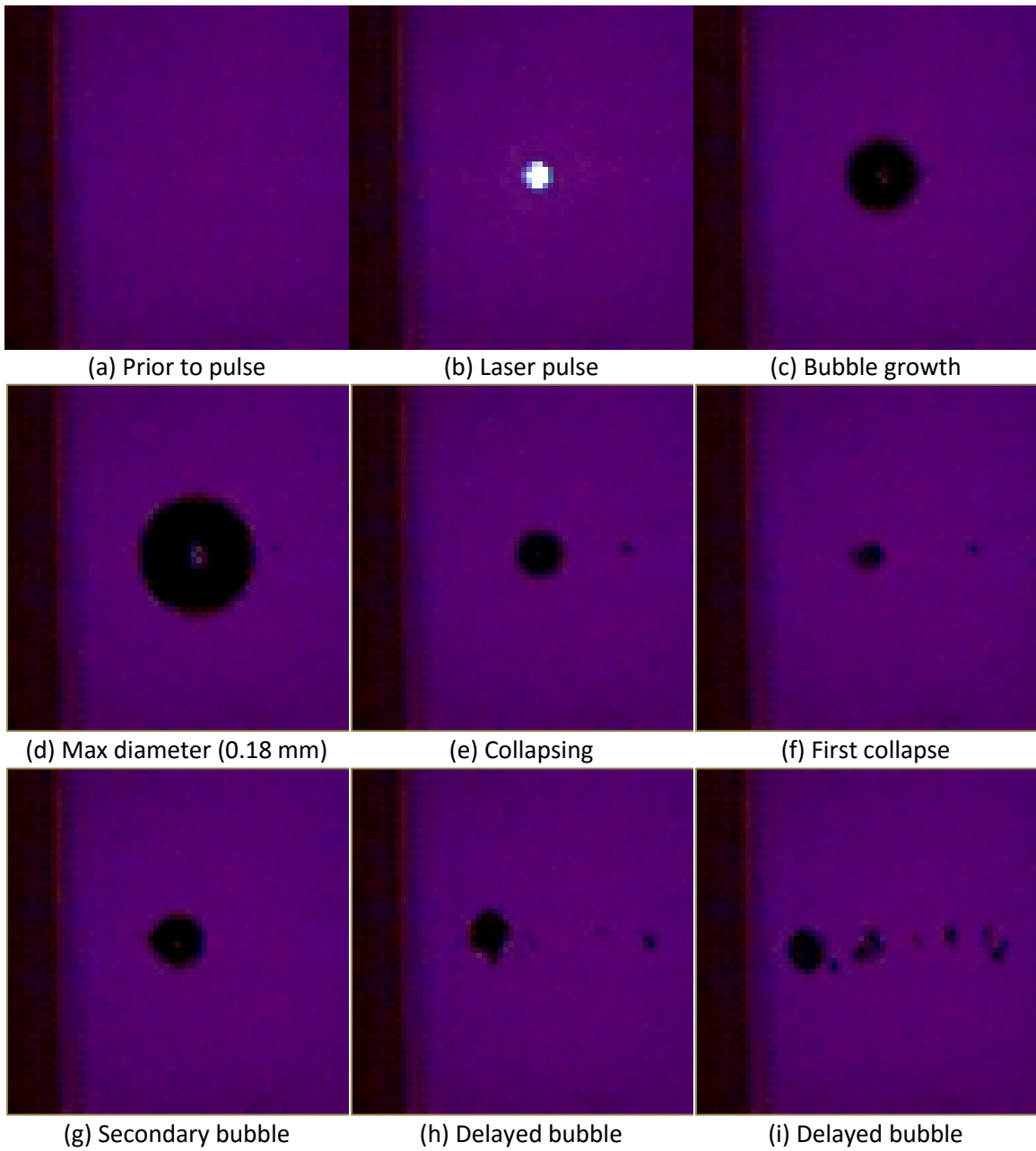
Figure 3.9. Still frames from HS video recording of optical cavitation induced by Nd:YAG (1064 nm, 300 mJ, 5 ns) pulsed laser in water.
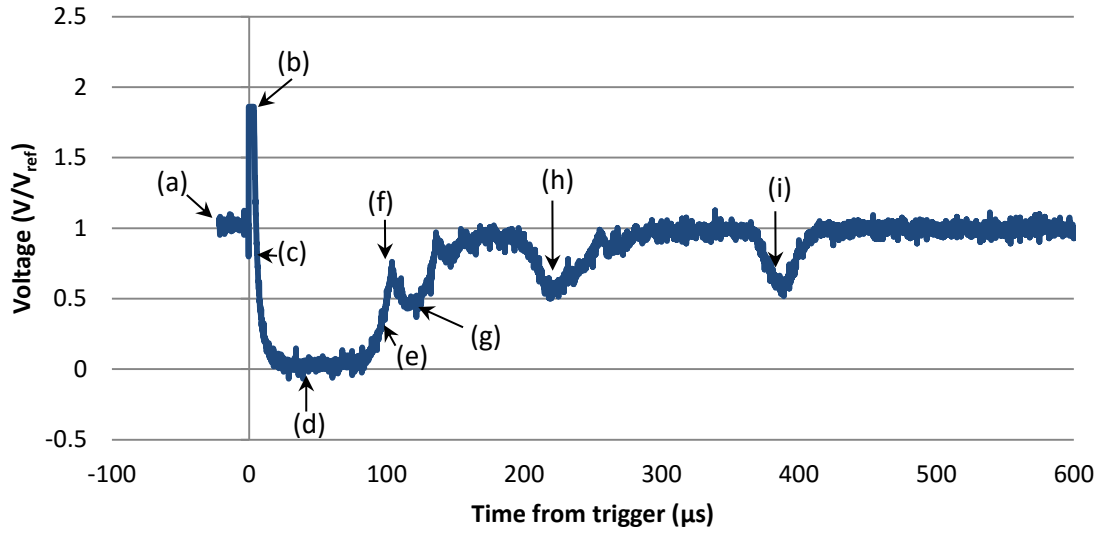
Figure 3.10. STM Voltage corresponding to the still frames presented in Figure 3.9.
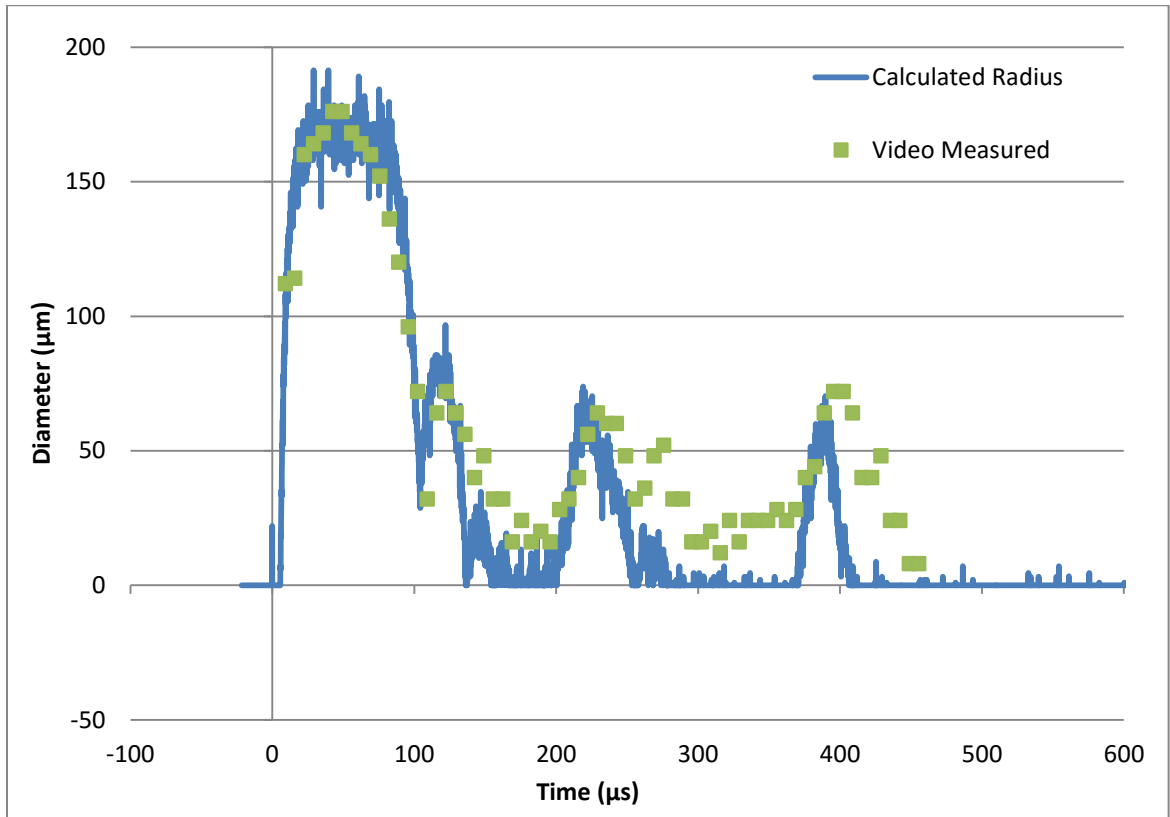
Figure 3.11. Radius calculated from signal using Eq. [3-8] compared to HS video measurements.

3.4.4. Adaptation to CW Cavitation

When moving to study CW-induced optical cavitation rather than pulsed, the STM required both physical and computational alterations. The physical alterations were trivial: selection of a corrected-wavelength dichroic mirror, and one additional lens to correct the STM beam for passing through the primary lens of the cavitation-driving laser.

The algorithm, however, required development to find bubble production frequency. To accomplish this, a threshold-based filter was developed to identify distinct cavitation events, allowing the frequency to be characterized and the radius of individual bubbles to be recorded.

The threshold filter created a binary mask based on the voltage signal. The mask was created using the gap between the nominal (zero-radius) and the minimum (maximum diameter of the largest bubble in the signal) voltage. A criterion of a maximum voltage (i.e., minimum diameter) was set to avoid noise false-positives. The criterion was adjustable; it was set to 25% of the nominal-minimum voltage gap. This value was set by comparing the algorithm-calculated frequency with hand calculation of the frequency – if the algorithm reported more bubbles than were visible, the criteria was increased to reduce false positives. Figure 3.12 shows a typical STM signal, recorded for a 5 second period with multiple bubbles occurring. The placement of the threshold is indicated by a red line; individual bubbles are indicated by arrows.

If the voltage was above the maximum, the mask was set to zero; when it dropped below the maximum, the mask was set to one. The algorithm then identified the time delay between successive patterns of 0 followed by 1 in the mask, as the delay between successive bubble formations. Further, a 0 then series of 1s followed by a 0 indicated a single bubble event; referring back to the corresponding voltage values in the original signal, the radius of individual bubbles could be calculated and compared within the same trial.
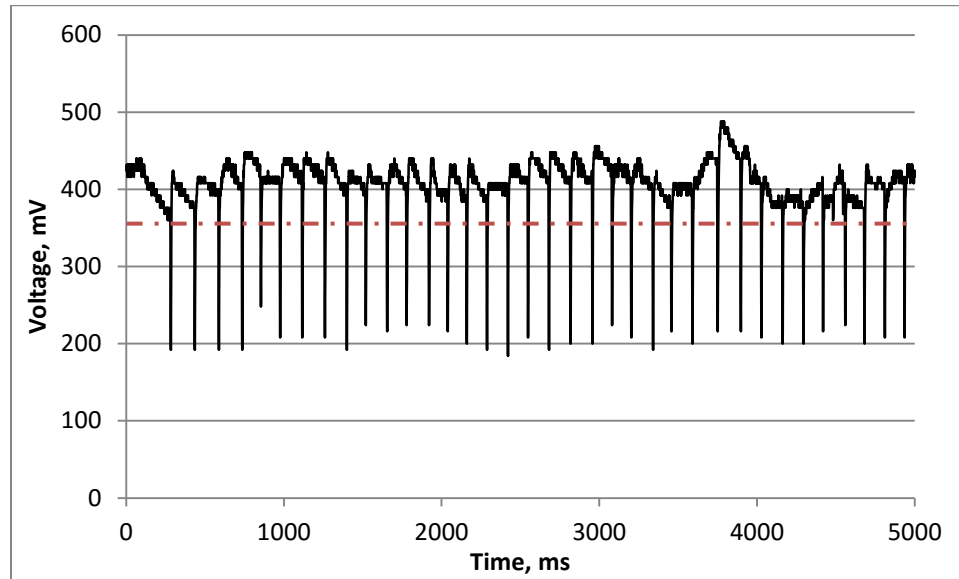
Figure 3.12. Voltage vs. time for a 5 second irradiation period, showing the threshold criteria for creating the filter mask.

Using this method, an algorithm programmed in Python was used to calculate bubble size and frequency for a range of optical conditions (Section 3.5).

3.4.5. Conclusions

The advantage of the STM's tremendous sampling rate becomes obvious when comparing the STM trace to the HS video recording. The STM trace records an additional bubble collapse that occurs between the frames recorded by the camera (Figure 4). The ability for STM to record at many times faster than even the shortest-lived cavitation bubble prove that it is an essential tool in accurate measurement of cavitation.

That advantage, combined with the relative simplicity and minimal cost make the STM method ideal for cavitation studies.

In the past, time resolved imaging has given insight into cavitation (Zysset, Fujimoto et al. 1989). However, such systems get a single frame at set delays over a series of repetitive bubbles. The weakness of this approach is that bubbles differ from shot to shot, interfering with readings. However, due to precise control of the imaging delay, time-resolved imaging provides very good resolution and accurate measurement of bubble diameter. STM provides similar time resolution and avoids the need for multiple bubbles- a single bubble can be measured for its entire lifetime.

However, further comparison of the STM traces with the video recordings highlights a weakness in the STM technique. At times, for reasons as-yet unexplained, the oscillating cavitation bubbles will move away from the nucleation site. Figure 5 shows a series of stills from HS video where the bubble is observed to migrate away from the point of nucleation. Figure 6 is the accompanying STM trace, where the reported bubble radius drops to zero as the bubble leaves the measurement volume, leading to a 'false-negative' reading. Until the migration of the bubble is understood and controlled, the STM requires HS video or another means to identify when the bubble has moved outside of the STM volume. Alternatively, the STM measurement volume may be widened by expanding the probe beam.

The spatial transmission modulation technique presents a high-speed, non-intrusive, and adaptable method of measuring the diameter of cavitation bubbles. Using high speed digital video recording, STM has been demonstrated to accurately reflect the diameter of a cavitation bubble as it grows and collapses. Methods to improve STM have been proposed. Currently, the use of STM in conjunction with HS video seems to be ideal for characterizing optical thermocavitation, with the STM providing very high speed and precise diameter readings and the HS video

as a warning when the bubble leaves the measurement volume. Refinements to the STM technique may reduce the dependence on video supplement.

Connection with the Dissertation Premise

Tackling the thermal effects of optical cavitation is a challenging proposition. Cavitation by nature is difficult to study. This section of the dissertation doesn't deal with the thermal effects of cavitation, but rather documents the development of measurement techniques that later can be used to study cavitation.

References

Banks, D., D. Garcia, F. Devia-Cruz Luis, S. Camacho-López and G. Aguilar (2013). <u>Optical Transmission Measurement of Thermocavitation</u>. Conference on Liquid Atomization and Spray Systems, Pittsburgh, PA.

Camacho-López, S., F. Perez-Gutierrez, L. Devia-Cruz, D. Garcia, G. Aguilar and D. Banks (2013). "High Resolution Optical Experimental Technique for Computing Pulsed Laser Induced Cavitation Bubble Dynamics in a Single Shot." <u>Atomization and Sprays</u> **23**(6): 475-485.

Juhasz, T., G. A. Kastis, C. Suarez, Z. Bor and W. E. Bron (1996). "Time-resolved observations of shock waves and cavitation bubbles generated by femtosecond laser pulses in corneal tissue and water." <u>Lasers in Surgery and Medicine</u> **19**(1): 23-31.

Ramirez-San-Juan, J. C., E. Rodriguez-Aboytes, A. E. Martinez-Canton, O. Baldovino-Pantaleon, A. Robledo-Martinez, N. Korneev and R. Ramos-Garcia (2010). "Time-resolved analysis of cavitation induced by CW lasers in absorbing liquids." <u>Opt. Express</u> **18**(9): 8735-8742.

Zysset, B., J. G. Fujimoto and T. F. Deutsch (1989). "Time-resolved measurements of picosecond optical breakdown." <u>Applied Physics B</u> **48**(2): 139-147.

3.5. Study: Optical Factors that Influence Cavitation Dynamics

The nucleation of a CW-induced cavitation bubble requires a sufficient energy density to superheat the liquid rapidly beyond its boiling point to the liquid-gas spinode temperature. The energy density is a product of four factors – laser power, beam focusing angle or beam waist diameter, spectral absorption by the working fluid, and losses due to optics. The first three can be varied relatively easily; the last is a characteristic of the experimental setup and has a fixed value for this study. In contrast to pulsed laser cavitation, where one laser pulse produces one cavitation event, during CW cavitation many bubbles can occur during an irradiation period. For applications of CW cavitation, then, it is essential to know how to control the bubble formation frequency and the size of the cavitation bubbles.

Since the bubble nucleation frequency is expected to be related primarily to the energy density of irradiation, the experimental setup was designed to vary that energy density in two ways. First, the cavitation driving laser output power was set from 1 to 10 W, in single watt increments. After losses due to the optical configuration, approximately 30% of that nominal power reaches the liquid within the cuvette, as measured by an optical power meter. Second, the cuvette was moved relative to the laser's focusing lens. By moving the cuvette, the effective beam width entering the copper nitrate solution was varied. Correspondingly, the optical power density entering the cuvette is altered.

3.5.1. Results

Varying the optical power and the focal point placement revealed three principal conclusions. First, as expected, increased optical power produces higher cavitation frequencies across all focal points (Figure 3.13). Second, there is a certain focus location that produces the highest cavitation frequency across all tested optical powers (Figure 3.13). This optimal focus is approximately 11.5 mm from the inner wall of cuvette.

At 1 W optical power, cavitation was not observed regardless of focus. Accounting for losses in the optics, approximately 0.3 W was reaching the liquid. This comfortably exceeds the minimum threshold for cavitation observed by Ramirez-San-Juan, et al, for near-IR CW induced cavitation in copper nitrate (Ramirez-San-Juan, Rodriguez-Aboytes et al. 2010). The absence of cavitation in this case is likely due to a less confined focus, using a longer focal length aspheric lens than was used in that study. The presence of the dichroic mirror used for the STM system, in particular, is likely affecting the pump laser beam quality.

At 10 W nominal power, the STM signal began to develop excessive noise, suggesting at least some of the pump laser energy was penetrating the cuvette and filter to reach the STM photodiode. From 2 to 9 W, cavitation was recorded for a 5 second period for at least 3 trials at each focal position. Cavitation occurred for lens-to-cuvette distances of 4.5 – 16.5 mm, with the lens having a focal length 25.4 mm.

Figure 3.13 shows the frequency of cavitation increasing qualitatively linearly as power increases, although the slope changes relative to the focal point. As the focal point gets closer to the 'optimal' location, approximately 11.5 mm lens-to-cuvette distance, the slope of power vs. frequency increases. An increase in optical power produces a greater increase in cavitation frequency near the optimal focus.

The optimal focal point placement presents a challenge to the described process of cavitation – direct heating to a fixed temperature leading to bubble nucleation. By that process, the focal point producing the highest frequency of cavitation should be the one producing the highest laser intensity within the liquid. Placing the beam waist just inside the cuvette would produce this condition.
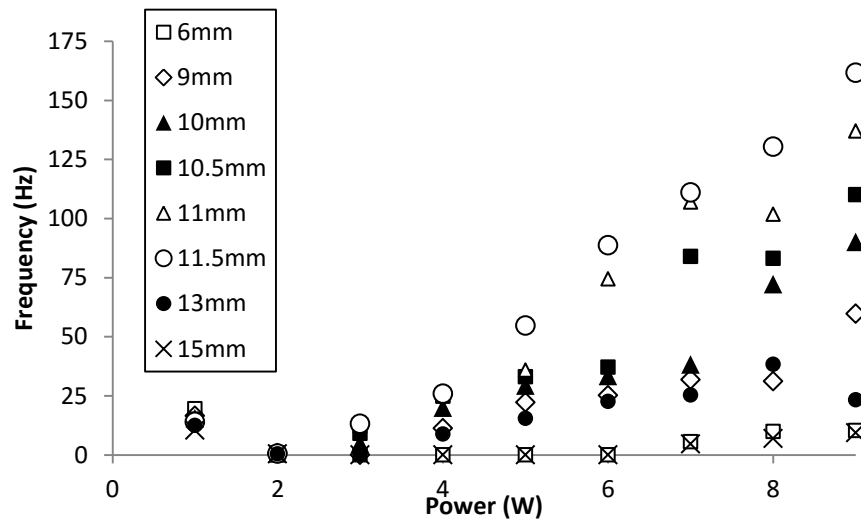
Figure 3.13. Frequency vs. optical power for fixed focal point placements.

However, Figure 3.14 shows that the highest frequency of cavitation occurs when the focal point is significantly displaced from the wall of the cuvette. The hypothesized explanation is that the laser-heated liquid forms a thermal lens as its refractive index changes. Tests to demonstrate this are ongoing. This effect was not observed by Padilla-Martinez, et al, likely due to the range of focal points they used – only a few microns range due to the short focal length of their lens (Padilla-Martinez, Berrospe-Rodriguez et al. 2014). Moving the cuvette closer or farther from the optimum location leads to a decline in cavitation frequency. Outside the range of 4.5-16.5 mm cuvette-to-lens distance, cavitation was not observed.
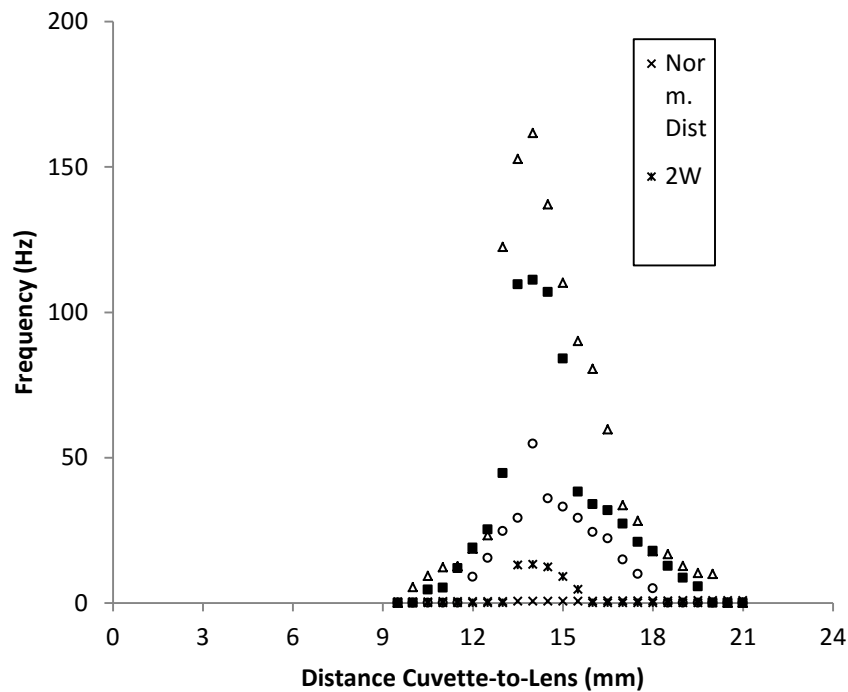
Figure 3.14. Frequency vs. focal point placement for selected optical powers (2, 5, 8, 10 W nom-inal).

Figure 4 shows the average radius of cavitation bubbles at each focal point location as measured by the STM. The error bars represent ±1 standard deviation in the measured radii – the large deviations are likely due to the use of a range of laser power settings. Generally, as the cuvette is moved away from the lens, reducing the irradiated area, the bubbles tend to become slightly smaller. This agrees with the theory that the superheated volume prior to cavitation de-termines the maximum bubble size – a larger irradiated area will heat a larger volume of liquid prior to bubble nucleation (Padilla-Martinez, Berrospe-Rodriguez et al. 2014).
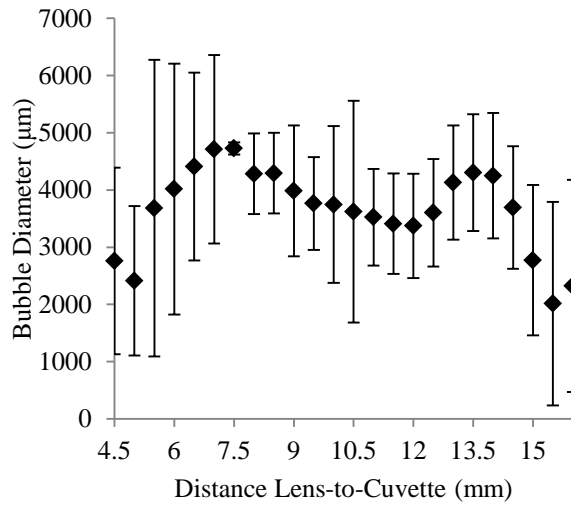
Figure 4. Average bubble size versus focal point position.
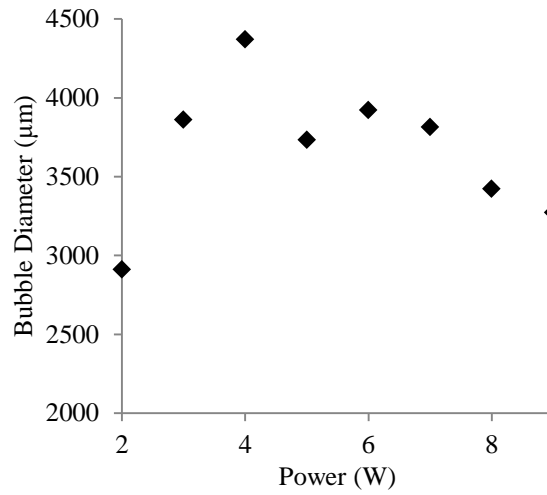
Figure 5. Average bubble size versus optical power.

Figure 5 shows the average bubble size related to the optical power. For higher power settings, the observations match those of Ramirez-San-Juan, et al, of decreasing diameter for increased optical power (Ramirez-San-Juan, Rodriguez-Aboytes et al. 2010), attributed to the smaller timescale of heat diffusion before the critical temperature is reached. However, at the lower end of the power range used in this study, there is a trend towards significantly smaller bubbles, in conflict with the aforementioned study. The exact cause of this is as-yet unknown, but a detailed study of the temperature field and thermal lensing effect that occurs during CW cavitation is likely to reveal some insight.

The thermal lensing involved in CW optical cavitation has been observed using the phase-contrast imaging setup, as well. By moving the illumination laser off-axis by 10° from the camera, a refracted image is produced as the light travels through the cuvette and the solution. The camera receives a distorted image, observing the inner wall of the cuvette (Figure 3.15 a). As the liquid heats under irradiation, a lensing effect is observed at the heating point, indicated by an arrow in Figure 3.15 b. Also in that image, the thermal boundary layer developing from the heating point is visible. Figure 3.15 c shows a cavitation bubble occurring; there is a blurriness near the bubble perimeter suggesting a high pressure region. Finally, in Figure 3.15 d, hot liquid is observed being ejected from the bubble site, and the darkened thermal boundary layer on the cuvette wall and the lensing due to heating have been disrupted temporarily.

| a. Refracted image, no heating. | b. Lensing effect prior to bubble formation. | c. Bubble formation; note disruption of the thermal boundary layer and distortion around bubble. | d. Heated liquid ejected after bubble collapse. |
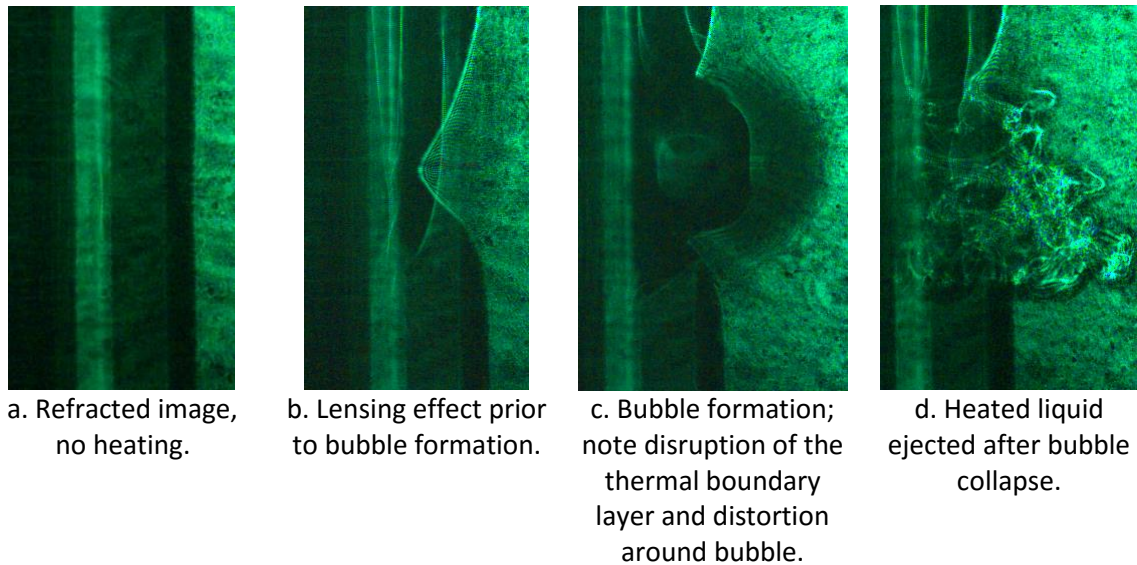
Figure 3.15. Off-axis phase contrast imaging of the CW heating and cavitation process.

3.5.2. Conclusions

The frequency of CW optically-induced cavitation bubbles has been measured for a wide range of focal conditions and optical powers. Cavitation becomes more frequent with increased optical power, because the heating time for the liquid to approach its spinodal temperature is reduced.

The cavitation-driving laser's focus plays a critical role in determining the cavitation frequency. However, unlike in pulsed-laser induced cavitation where there is little thermal effect on the target liquid prior to the end of the optical pulse, the significant heating induced by the CW changes the refractive index of the target liquid, leading to a secondary thermal lensing within the liquid. The effective focal point is thereby altered, producing cavitation when the liquid is much closer to the lens than was otherwise expected.

Further work quantifying the thermal lensing effect is ongoing. Using a pattern of lines and dots of known spacing on a glass slide near the cuvette, the diffraction of the image on video as heating occurs can be quantified.

References

Padilla-Martinez, J. P., C. Berrospe-Rodriguez, G. Aguilar, J. C. Ramirez-San-Juan and R. Ramos-Garcia (2014). "Optic cavitation with CW lasers: A review." Physics of Fluids (1994-present) **26**(12): 122007.

Ramirez-San-Juan, J. C., E. Rodriguez-Aboytes, A. E. Martinez-Canton, O. Baldovino-Pantaleon, A. Robledo-Martinez, N. Korneev and R. Ramos-Garcia (2010). "Time-resolved analysis of cavitation induced by CW lasers in absorbing liquids." Opt. Express **18**(9): 8735-8742.

3.6. Observation of the Temperature Field Surrounding the Bubble Site

To demonstrate the effectiveness of cavitation at drawing cool liquid towards a heated solid boundary, it is necessary to characterize the temperature field surrounding the bubble site before, during, and after cavitation. However, the short timescales of cavitation dynamics challenge conventional temperature measurement methods. The shockwaves produced by cavitation bubbles render sensors submersed in the cavitating liquid useless. To measure the temperature field surrounding cavitation bubbles, a non-intrusive optical technique is ideal. Planar laser induced fluorescence (PLIF) provides an avenue for using the available high speed video camera to measure the temperature field within the working liquid.

PLIF is reasonably simple in principle. A dye is irradiated by a certain wavelength of light, from a laser beam shaped into a sheet. Under this excitation, the dye fluoresces at a different wavelength. Using a video camera and image analysis software, the intensity of fluorescence can be measured. This fluorescence can be correlated with the conditions of the dye: pressure, concentration, or shear. Certain dyes fluoresce with different intensity at different temperatures. Holding everything else approximately constant, then, the fluorescence can be used to measure the local temperature (Crimaldi 2008).

3.6.1. Experimental Setup

A solution of Rhodamine B dye in an aqueous copper nitrate solution is the working liquid for this study, contained in a 1 cm by 1 cm by 4 cm glass cuvette. The cuvette is transparent on all sides in the visible and near-IR spectrum. Cavitation is induced by a laser diode emitting at 810 nm wavelength with a power range of 1 to 30 W, which for this study was set to 5 W (the pump laser), which is focused through a 25.4 mm focal length lens into the cuvette. Copper nitrate is

highly absorptive of near-IR wavelengths, promoting thermocavitation, but is relatively transparent in the violet to yellow visible spectrum which Rhodamine absorbs and fluoresces.

A 440 nm, 2 W diode (the exciter) is shaped into a sheet of less than 1 mm thickness by a cylindrical plano-concave lens (f = 100 mm) in conjunction with an aspheric lens (f = 100 mm) and transmitted through the cuvette along the axis of the pump laser but in the opposite direction. The Rhodamine fluoresces in the exciter's light sheet, with fluorescence wavelengths typically in the range of 550-570 nm (green-yellow). A Miro m310 high speed video camera (Vision Research) records from perpendicular to the pump axis, through a longpass filter with cutoff wavelength of 435 nm, and a shortpass filter with a cutoff wavelength of 600 nm to block the cavitation-driving laser.

The cavitation fluorescence solution consists of 4 mL of copper nitrate solution with Rhodamine B dye added. The concentrations of copper nitrate and Rhodamine B by weight used for temperature measurement are 0.24 g CN and 0.018 mg R-B to 1 g deionized water.
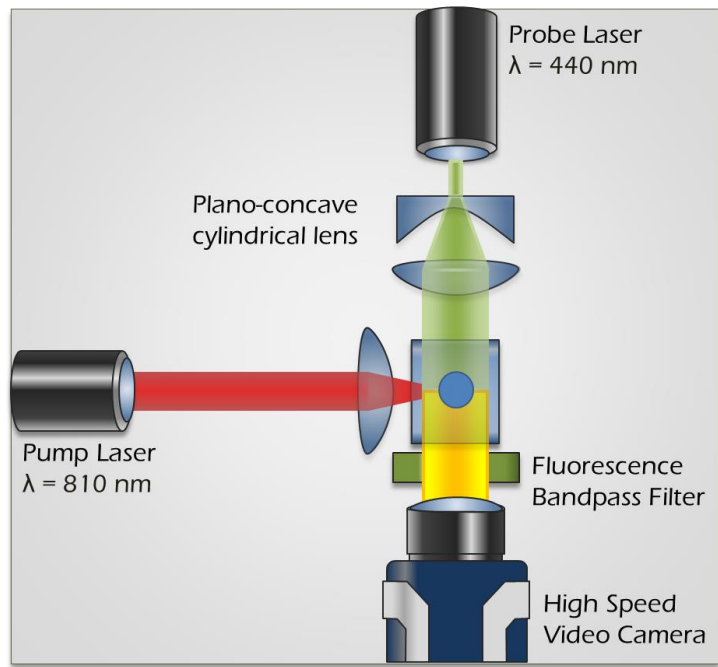
Figure 3.16. Experimental setup for PLIF temperature measurements.

3.6.2. Calibration Procedures

The first challenge facing the development of PLIF is the relatively low intensity of fluorescence compared with the traditional ultra-bright illumination used for most high-speed video recording. As a consequence of the elevated framerate, the exposure time per-frame on high speed video is relatively short; LED panels or lasers are often used as light sources to form images within the short exposure window. In the PLIF setup, it was necessary to optimize the fluorescent intensity to allow high speed video recording.

Excitation was the first factor investigated. Rhodamine B has a reasonably wide excitation band – using various laser diodes, fluorescence was observed to be visible to the naked eye when the solution was illuminated with 405, 440, and 520 nm diodes. By varying the voltage and current supplied to the diodes, it was determined that increased intensity of illumination corre-

sponded directly to increased fluorescent intensity. As such, a high-power diode, nominally 2W at 440 nm, was selected as the excitation source.

Second, the concentration of rhodamine in solution was optimized. Other applications using PLIF often require less intense fluorescence, as the exposure time can be longer; typical concentrations of rhodamine are mg per L or smaller. With such a small concentration, even with multiple watts excitation, there was no fluorescence visible in video. Increasing the concentration to 0.37 µg rhodamine in 10 mL aqueous copper nitrate provided some visibility on video at 1000 fps, so it was used as the starting point for optimization. The intensity was measured using ImageJ software, taking the average RGB values of each of approximately 100 frames of video. Increasing the concentration of rhodamine in increments of 0.37 µg, an approximately linear relationship between the intensity of fluorescence and the concentration of rhodamine was found (Figure 3.17). For purposes of this study, a concentration of 1.8 µg rhodamine to 10 mL copper nitrate solution was used, providing sufficiently bright fluorescence that video can be recorded at 2000 fps.
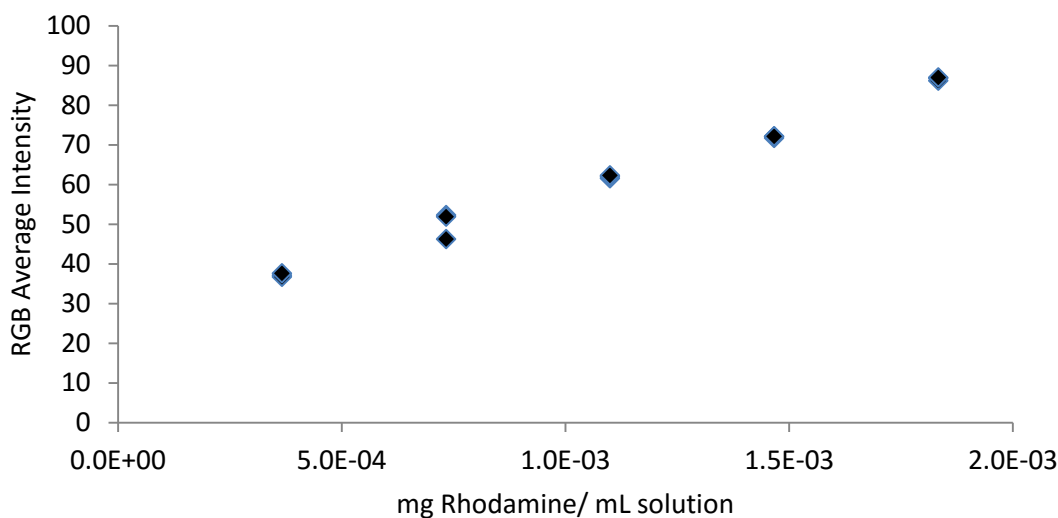
Figure 3.17. The relationship of rhodamine B concentration to average fluorescent intensity.

In addition to examining the feasibility of a range of wavelengths as excitation sources, the spectral absorptivity of the selected aqueous rhodamine copper nitrate solution was measured for several wavelengths in the visible and near-infrared range. The wavelengths used were 405, 440, 520, 638, and 810 nm. To measure the absorptivity, an optical power meter (Newport Model 818) was placed on the opposite side of the cuvette from a laser. The power reported by the meter with no liquid in the cuvette was deemed the nominal intensity (I_0); the cuvette was then filled with solution and the power measured again (I_m). Using Beer's Law (Equation [3-9]), the absorption coefficient α was calculated (Figure 3.18). In the equation, d is the distance the light is transmitted.

$$\alpha = -\frac{1}{d}\ln\left(\frac{I}{I_0}\right)$$
[3-9]
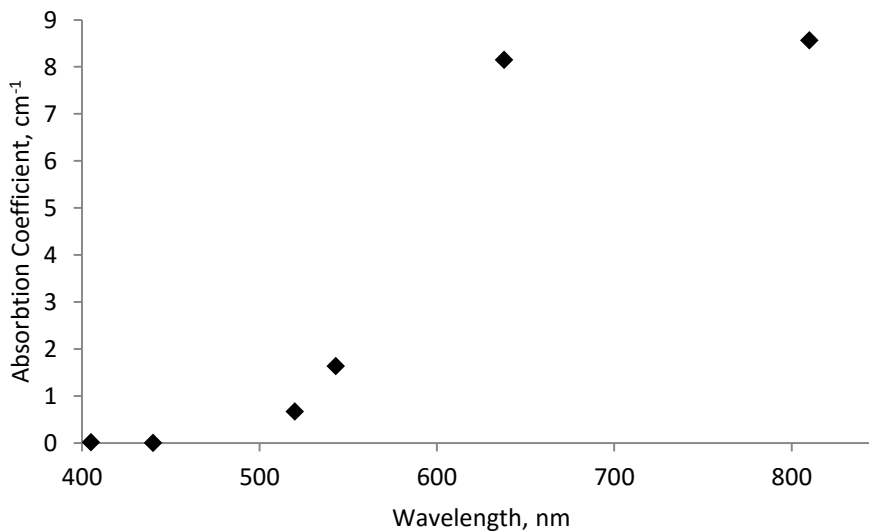
Figure 3.18.Spectral absorption of the aqueous rhodamine copper nitrate solution for selected visible and near-IR wavelengths.

With the excitation laser selected and the concentration of rhodamine set, the setup was then calibrated for temperature. Using a stirring hotplate, a large volume of rhodamine-copper nitrate aqueous solution was prepared and heated to a fixed temperature. The cuvette was filled with liquid from this volume and a video of the fluorescence was recorded within 10 seconds of the liquid being placed in the cuvette. Starting from 25 °C, the average fluorescence within 100 frames at 1000 fps was measured for temperatures up to 75 °C in increments of 10°C. As Figure 3.19 shows, a linear relationship was found relating fluorescent intensity and temperature.
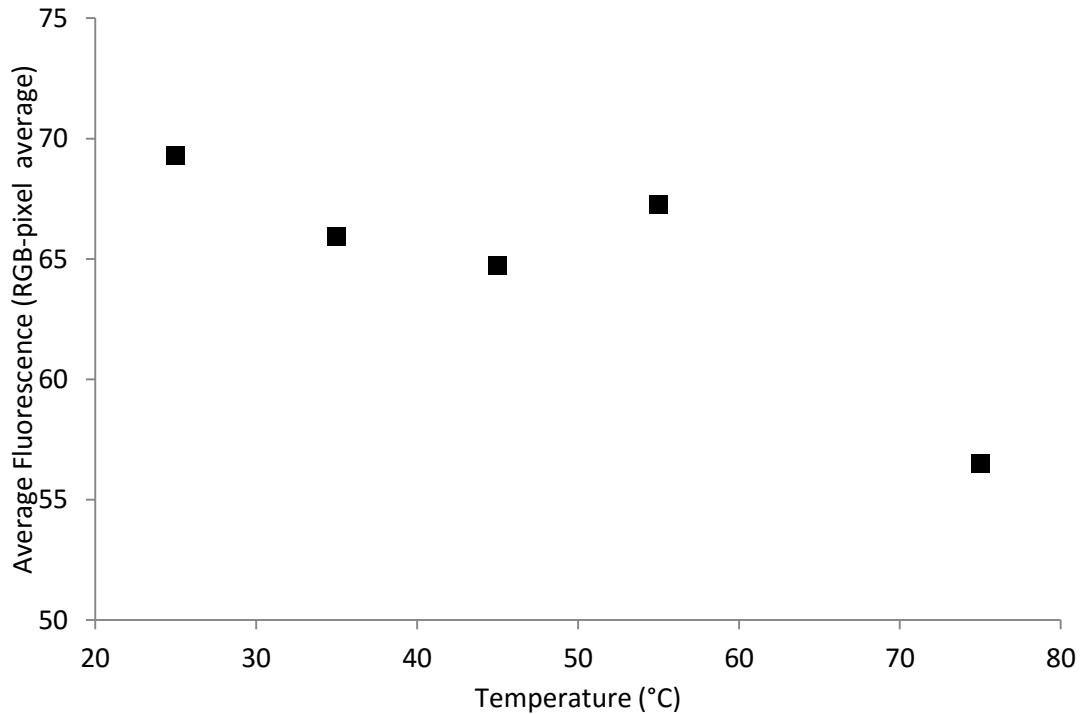
Figure 3.19. Fluorescent intensity versus temperature.

$$I_{RGBAvg} = -0.2191T + 75 \qquad \text{[3-10]}$$

To measure temperature at a given location in video, an ImageJ macro was developed. The macro defined a series of rectangular cells within an image, based on user input (Figure 3.20), and then measured the average RGB intensity of each of those cells over a series of images. The average intensity of each cell correlates with the temperature of the liquid within the excitation sheet at that location. The macro cycles through all images within a stack, providing a chronological evolution of the temperature at all locations recorded.
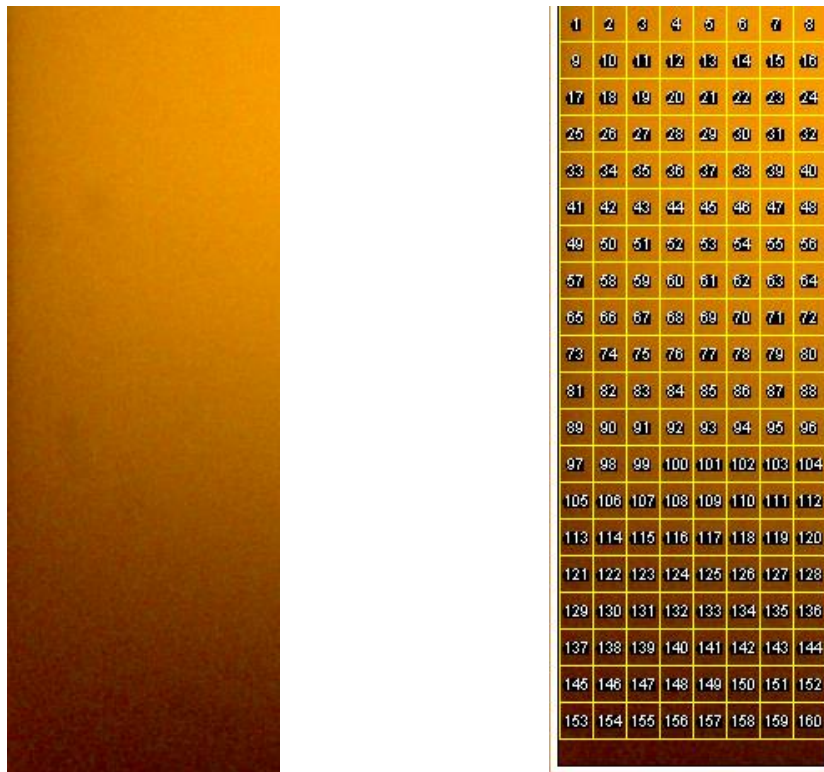
a. Unmodified Image   a.   Cells overlaid on image

Figure 3.20. Depiction of the cells overlaid on a video still frame showing rhodamine b fluorescence.
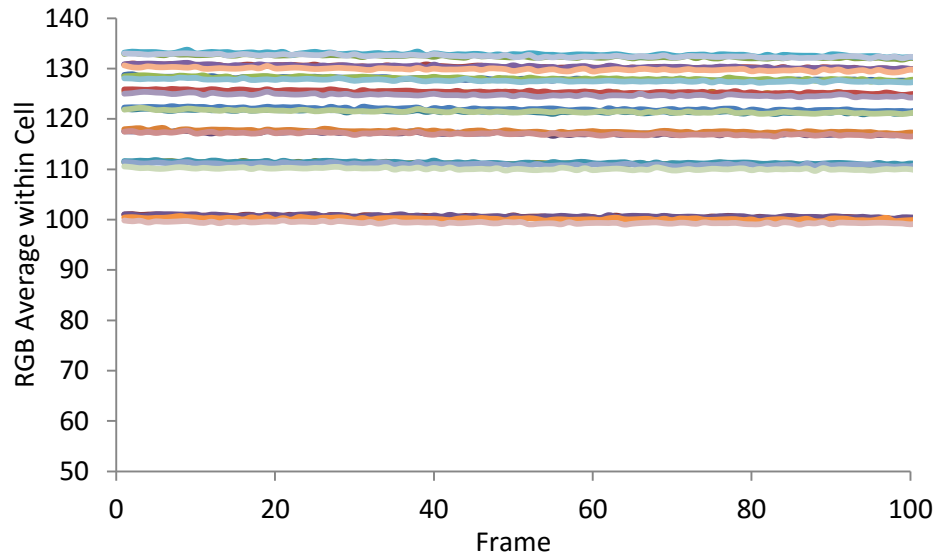
Figure 3.21. Demonstration measurements showing average RGB intensity over 100 frames with no heating from cells from the configuration in Figure 3.20.

Figure 3.20 shows that each cell has a slightly different level of fluorescence. Other than the excitation laser, no irradiation was involved in this measurement. The fluorescence within each cell is seen to remain very nearly constant. Based on this, the procedure for temperature measurements is to collect a reference value for that cell prior to cavitation-laser irradiation and use that reference value and the slope of the fluorescence vs. temperature line to set a calibration to each cell.

The limitation on this measurement technique arises from image noise – small variations in the color of individual pixels. In most photography and videography, this noise can be minimized by the long exposure time and minimal saturation. In high speed video, especially in low-light conditions, the sensor often uses high contrast and sensitivity settings to maximize the light available. This artificially adds noise to the image as individual pixels on the sensor over-react to variations in light. Taking the average intensity over a region minimizes the effect of this noise,

but as the region becomes smaller the effect of single-pixel fluctuations become larger. To establish how much noise affects the calculation, a series of analyses were performed on the same video using progressively smaller cells. The video was 100 frames of unperturbed, unheated liquid fluorescing – there should be negligible or no movement within the liquid, so the only noise arises from the camera sensor. Taking the standard deviation in RGB value of each cell over the range of frames provides an estimate of the magnitude of noise's effect on the measurement of that cell, depicted in Figure 3.22.
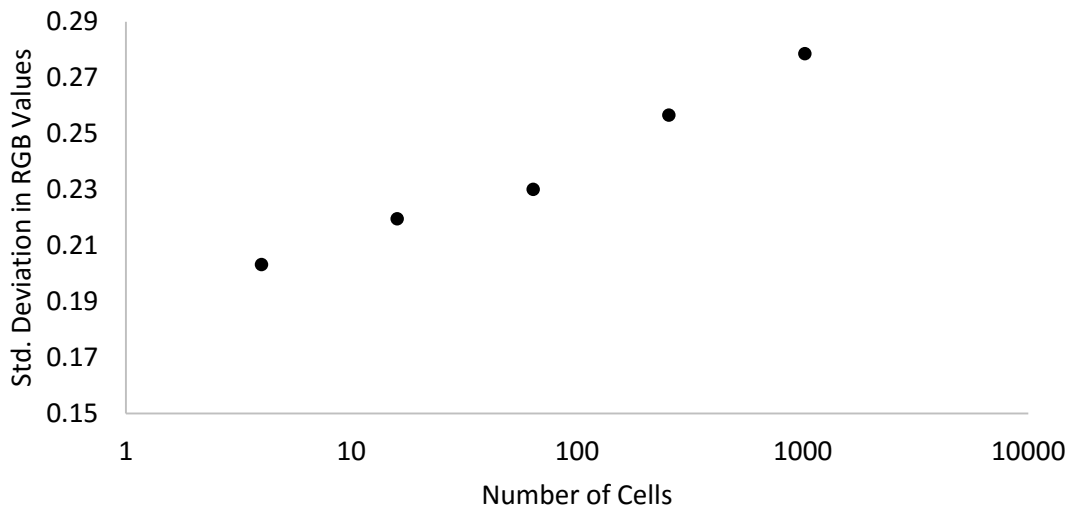
Figure 3.22. Standard deviation of RGB intensity versus cell size.
The same 100 images are analyzed using progressively larger numbers of square cells.

3.6.3. CW Laser Heating Temperature Field Measurements

Temperature measurements were grouped chronologically into three phases: the heating phase, bubble phase, and mixing phase. The heating phase is defined as the time between the pump laser activation and bubble nucleation. The bubble phase starts at nucleation until the bubble collapses. The mixing phase starts after the bubble collapses until no motion is observed.

The current experimental setup can resolve 2000 fps – that is, 500 μs per frame. As typical optical cavitation bubble lifetimes are less than 200 μs, the setup cannot resolve bubble dynamics. Future optimization will improve the time resolution. For this study, the heating and mixing phases will be examined. The frame during which the bubble occurs will be shown and analyzed, although its usefulness may be limited.

For image analysis, a 24 x 32 grid of cells was applied to the PLIF images, and the intensity within each cell was measured. Cavitation was induced using 5W of 810 nm laser power.

Heating

The heating phase for this study lasted approximately 760 ms, from the instant the laser was activated until the first bubble nucleated. During this time, the highest observed temperature was 56°C. Heat diffusion near the wall of the cuvette and the growth of a free convection thermal boundary layer upwards along the cuvette wall from the irradiated area are observed.

The heating as visualized by PLIF is nearly invisible to the naked eye – even magnified on a large screen, the difference in fluorescence is barely visible.

a. Prior to laser activation (0 ms)

b. Development of thermal boundary layer (100 ms)

c. Last frame prior to bubble nucleation (760 ms)
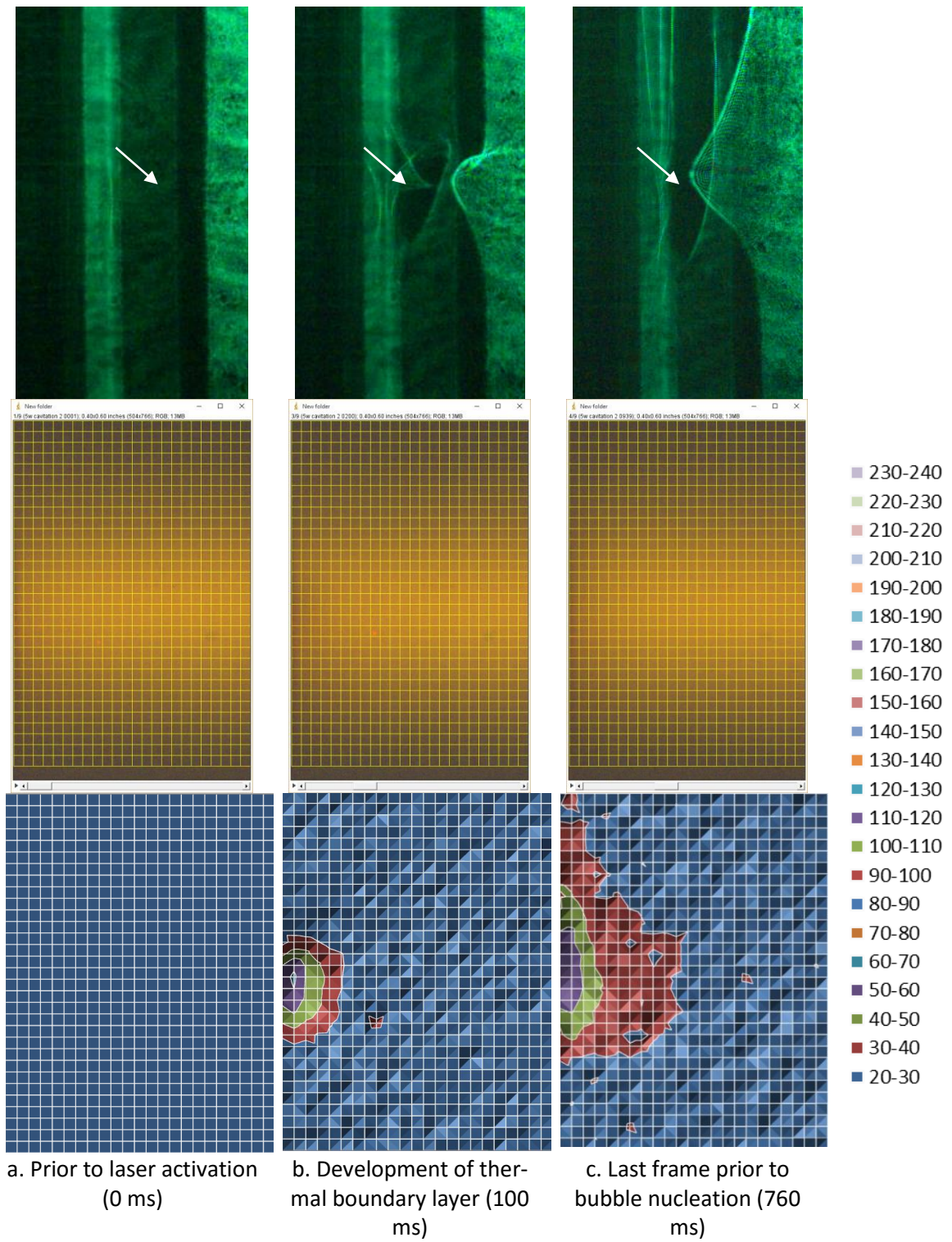
Figure 3.23. Temperature measurements during the heating phase, prior to bubble nucleation.

Top: phase contrast imaging. Middle: PLIF video. Bottom: temperature map.

Bubble

Figure 3.24 shows the cavitation bubble using phase contrast, PLIF, and PLIF-temperature mapped images. The bubble refracts some of the cavitation-driving laser's guide light into the camera, artificially brightening it. This has the unfortunate side effect of rendering temperature measurements essentially meaningless. An improved setup will use a filter to block this unintended light.
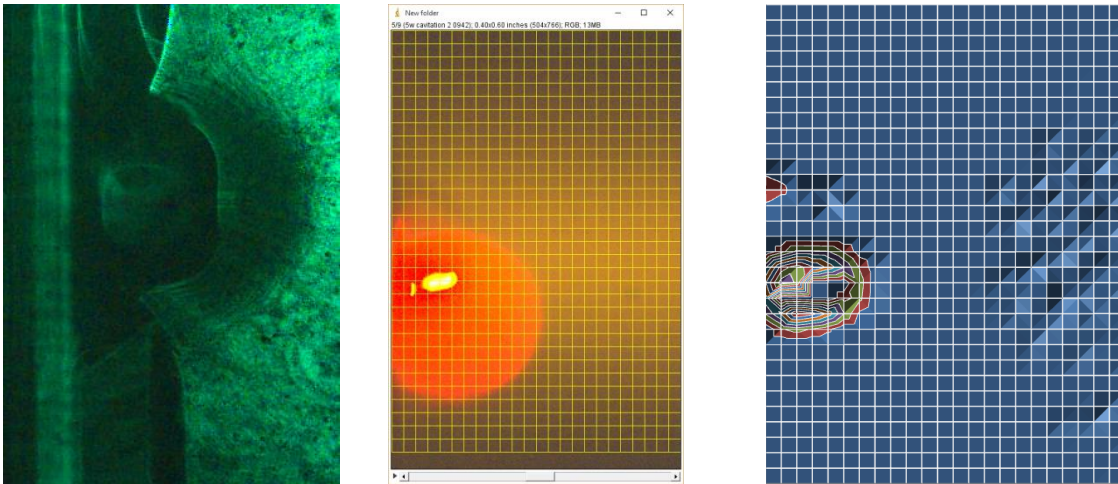
Figure 3.24. Temperature measurement on the frame containing a cavitation bubble. From left to right: phase contrast image, PLIF image, temperature map.

Mixing

The mixing phase extended from the collapse of the bubble for approximately 150 ms, at which point the motion of the liquid had reverted to a similar free convection boundary layer prior to the bubble's appearance. Figure 3.25 shows the collapse of the bubble, the ejection of heated liquid away from the bubble site, and then the gradual return to undisturbed free convection. Again, the images presented include phase contrast, PLIF, and PLIF-calculated temperatures. The gradual return to quiescent free convection provides a key to the enhanced cooling effects sought after in this study. During and for a short period after cavitation, there is relative-

ly rapid motion of fluid around the boundary – in a surface cooling situation, this period should be accompanied by enhanced convective cooling. PLIF reveals that the region of heated liquid near the boundary is significantly dispersed for several milliseconds following cavitation. If cavitation can be induced quickly enough, this agitation can be sustained without interruption, leading to an overall long-term cooling improvement. As described in Section 3.5, increased laser power and focusing conditions combine to control cavitation frequency. Applications of cavitation-driven cooling need only select a combination of liquid, laser power, and focal characteristics to achieve the desired thermal management. This strongly parallels the droplet train cooling study, where the impingement droplet We and train frequency were intertwined in determining overall heat transfer to the impact substrate.
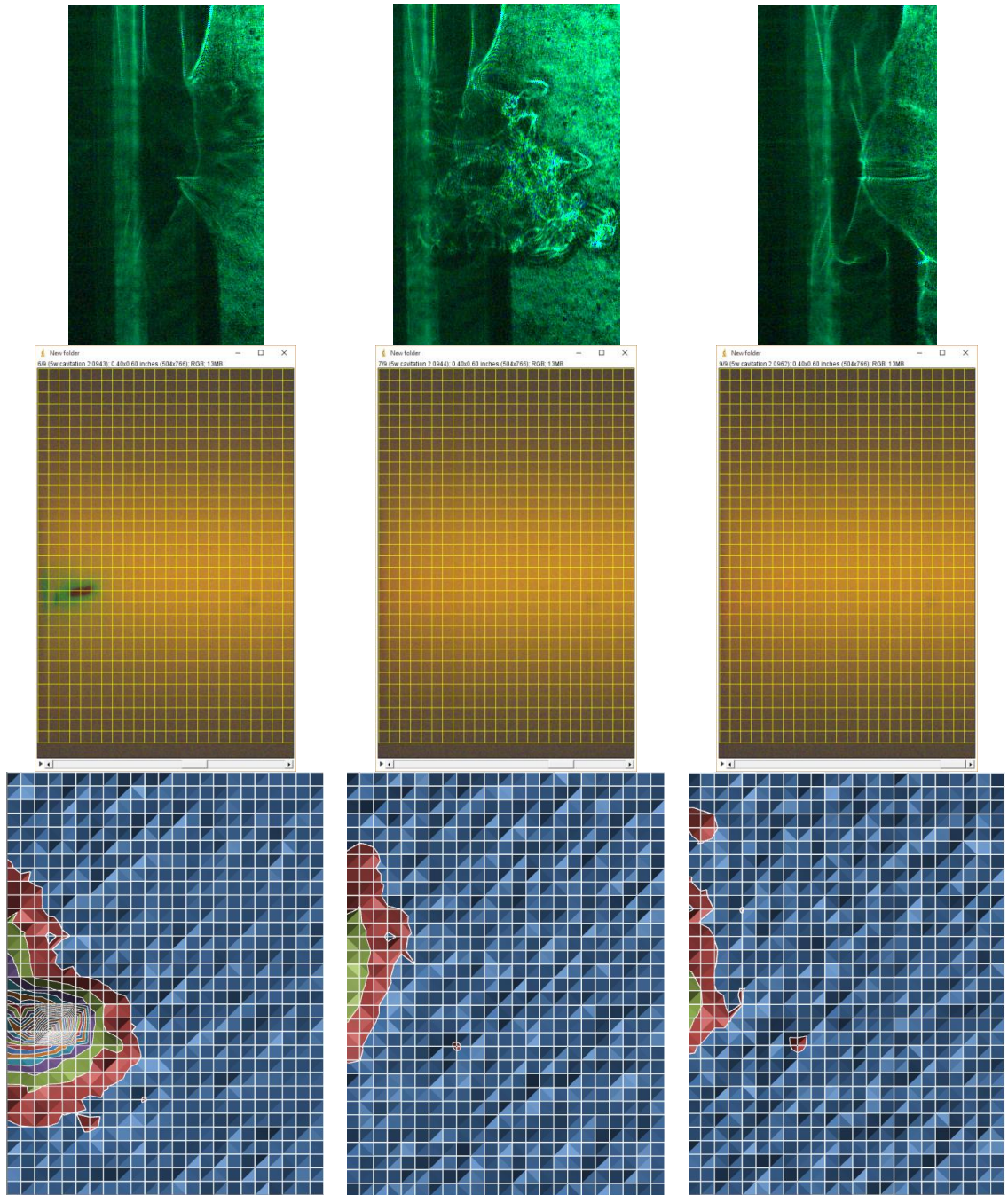
a. First frame after the bubble collapse (0 ms)

b. Ejection of heated liquid (+5 ms)

c. Restoring boundary layer (+30 ms)

Figure 3.25. Temperature measurements during the mixing phase, after the bubble occurred. Top to bottom: Phase contrast, PLIF, temperature map.

3.6.4. Conclusions

PLIF has been demonstrated for measurement of the temperature field surrounding CW optical cavitation bubbles. Experimental limitations currently preclude sufficient time resolution to observe dynamics during the bubble, but the development of the thermal boundary layer during laser heating and the ejection of heated liquid from the bubble site are apparent. After the bubble collapses, ejecta of heated liquid from the bubble site is observed, followed by a return to natural convection conditions stimulated by the continuous irradiation.

In the immediate future, PLIF needs improvement. It agrees well with the phase contrast imaging prior to the bubble. The appearance of the bubble seems to induce error within the temperature measurements. Improved image analysis resolution and optical setup modifications may offset this error.

Future work will combine the findings of this section and Section 3.5, using the period of agitation after a bubble occurs as a convective heat transfer enhancement and seeking to produce cavitation bubbles within this mixing duration to sustain the enhancement.

References

Crimaldi, J. P. (2008). "Planar laser induced fluorescence in aqueous flows." <u>Experiments in Fluids</u> **44**(6): 851-863.

3.7. Thermocavitation as a Needle-less Skin Poration Mechanism

In this study, the potential of thermocavitation is explored as an alternative method to traditional needles to porate the stratum corneum (SC), the outer impermeable layer of the skin. Past literature shows that the shock waves generated immediately after the collapse of thermocavitation bubbles (Korneev, Montero et al. 2011) are energetic enough to produce damage in hard materials such as titanium and indium tin oxide thin films (Ramirez-San-Juan, Padilla-Martinez et al. 2011). In this work, the damage induced on softer materials, such as agar gels and ex-vivo porcine skin is studied to facilitate exploration of thermocavitation for tissue ablation, which may result in the enhancement of transdermal drug delivery (TDD), including that of optical clearing agents (Yoon, Park et al. 2010).

This work demonstrates an application of thermocavitation in the biomedical field, which, while not directly related to the thermal characterization methods developed in the previous sections, demonstrate the use of cavitation and the reasoning behind development of cavitation measurement and control techniques.

3.7.1.   Materials and Methods

Sample Preparation

Two types of samples were used for experiments: (a) tissue phantoms made of agar gel layers (BD Bioscience, Franklin Lakes, NJ, USA) prepared with 1% to 6% agar concentrations and (b) *ex-vivo* porcine skin obtained from Sierra for Medical Science (Whittier, CA, USA). A thin layer of saturated copper nitrate solution (13.78 g of $CuNO_4$ per 10 ml of water) was applied to the surface of each sample and a glass cover slip was placed on top (Figure 3.26A). Using pre-manufactured plastic spacers, it was ensured that the thickness of the solution layer between the cover slip and the sample was 100, 200 or 300 μm.

The agar samples were prepared by weight percentage (e.g., for 2 % concentration, 2 g of agar powder were dissolved in 100 ml of deionized water). For each agar sample, the water was split in two equal parts. The agar was added to one as the other was boiled. Once the second portion was boiling, the first portion with dissolved agar was added, and the combined sample was heated until air bubbles stopped forming within the mixture. The sample was then poured into a container that ensured 7 mm-thick layers once the solution solidified.
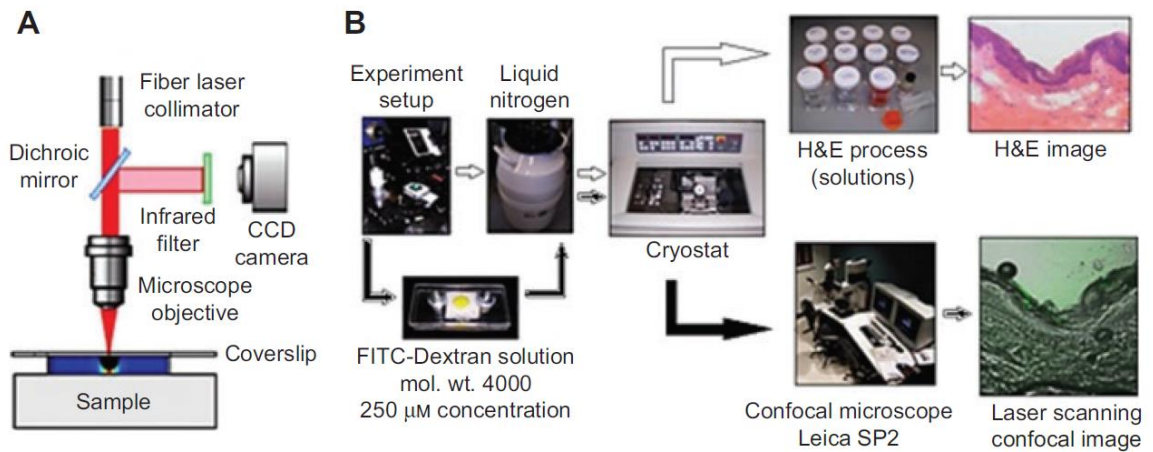
Figure 3.26. (A) Experimental setup to produce cavitation damage on agar gel and porcine skin. (B) Process for studying cavitation damage on skin.

The porcine skin samples of 2 cm^2 were carefully processed in the lab. Hairs were trimmed off using tissue scissors close to the skin surface; the skin surface remained intact to avoid rupturing the SC. Finally, subcutaneous fat and muscle tissue were removed, and the skin sample surface was washed using deionized water. Thereafter, skin samples were snap-frozen in liquid nitrogen (LN$_2$) and stored in the freezer until thawed in phosphate buffer saline (PBS) for 1 hour before experiments.

Thermocavitation Experiments

A CW fiber laser (Model BWF1; B&W TEK Inc., Newark, CN, USA) with a wavelength of 975 nm was collimated and focused on the bottom surface of the cover slip below the solution using a microscope objective (f = 8 mm), which produced a spot of ∼ 2 µm in diameter at the focal point (Figure 3.26A). To observe the position of the beam waist, a dichroic mirror redirected the laser light reflected by the glass-liquid interface onto a CCD camera. Since the Rayleigh distance of the lens is ∼ 13 µm, this reflection is a good indicator of the beam waist diameter on the cover slip, although its exact location is not too critical for measurements (Padilla-Martinez, Aguilar et al. 2011). The absorption coefficient of the solution at this wavelength, $\alpha = 135$ cm^{-1} (Ramirez-San-Juan, Rodriguez-Aboytes et al. 2010), is sufficient to negate any significant irradiation on the skin and thus there is little risk of thermal damage. The laser light is absorbed by the solution near the cover slip, heats the liquid to its spinodal temperature. This leads to the generation of multiple vapor bubbles that grow and collapse very rapidly emitting intense acoustic shock waves (Rastopov and Sukhodolsky 1990, Rastopov and Sukhodolsky 1991, Ramirez-San-Juan, Rodriguez-Aboytes et al. 2010, Korneev, Montero et al. 2011). In CW thermocavitation, the maximum radius of the bubble can be controlled through the beam power or the beam waist position, demonstrated in Section 3.5. To simplify the experiments, the beam waist position was fixed on the cover slip bottom surface and only the laser power and the thickness of the solution layer were varied.

Experiments with Agar Phantoms

Cavitation damage to tissue structures is usually assessed using *ex-vivo* or *in-vivo* tissue. However, this prohibits direct observation of damage as it occurs. Additionally, tissue requires preparation of histology slides to accurately identify lesions caused by cavitation, which is time-

consuming and costly. Agar phantoms, on the other hand, are optically-transparent gels which have similar mechanical properties to skin, allowing real-time visualization of cavitation. Agar gels were used as a simple model to assess the range of parameters (laser power and layer thickness) that would be appropriate for the porcine skin experiments. For this purpose, it was necessary to match the mechanical properties (elastic modulus) of the agar and skin models as closely as possible. The mechanical properties of *ex-vivo* tissue vary widely based on factors such as skin hydration, age, anatomic location, etc., as do the values reported in literature (Subhash, Liu et al. 2011), so we independently measured the stress-strain relationship of all experimental samples. Using a material testing machine (Model 3369, Instron, USA), the strain induced in the samples was measured as a function of the compressing force. 10 mm-thick agar samples with concentrations varying between 1 % and 5 % were made in 52 mm diameter poly-styrene dishes. A PTFE plate was machined to fit tightly on top of the dish for the machine to press on, recording the stress (force) and strain (compression) of each sample.

Subsequently, thermocavitation was induced in solution upon gel samples. The damage in-duced by thermocavitation on the surface of these agar phantoms was observed from the top and side view using an optical microscope (Mod. LSM700; Carl Zeiss MicroImaging, Germany), and assessed as a change in transparency and mass loss. Following this procedure, it was possi-ble to determine that laser power between 170 and 200 mW and thickness of the solution layer fixed at 100 μm would be most appropriate to use for the porcine skin samples.

Experiments with Porcine Skin

To study the cavitation-induced damage on the SC of porcine skin and the subsequent drug penetration, three techniques were used: (1) tape stripping (Lademann, Jacobi et al. 2009), (2) hematoxylin and eosin (H&E) staining (Heyderman 1992), and (3) laser scanning confocal imaging.

Tape Stripping

Tape stripping (Lademann, Jacobi et al. 2009) is a method to observe the penetration of topically applied drugs into the uppermost layer of the skin. By attaching and then peeling back a layer of adhesive tape to the tissue surface, the SC can be removed one cellular layer at a time. The layer of cells is examined for drug content, and the procedure is repeated until there is no evidence of drugs. The procedure was repeated 10 times on the treated skin area. A 250 μm FITC-dextran solution (molecular weight, 4000 Da; Sigma Aldrich), was used as a hydrophilic, fluorescent drug surrogate to assess diffusion into the tissue. It was applied topically on the skin damaged by thermocavitation for 2.5 h before the tape stripping. The amount of topically applied substance removed by each tape strip was observed with a fluorescent microscope (Mod. MZFLIII; Leica, Germany). In order to determine penetration profiles, each digital fluorescent image was post-processed using a MATLAB program (MathWorks, USA); background noise was removed and pixel fluorescence intensity was summed up, which yields the total fluorescence intensity of each tape strip.

H&E Staining

Hematoxylin and eosin staining is a method to differentiate between tissue structures that remain whole and those damaged by cavitation. Samples of porcine skin exposed to thermocavitation were frozen immediately after laser exposure by dipping them into liquid nitrogen (LN_2)

for 5 minutes. The samples were cut to 20 µm thick slices using a motorized cryostat (Mod. HM500 OMV; Mikron Instruments, USA), indicated by white arrows in Figure 3.26B. Half of the skin slices were stained using a typical H&E histological process (Carson and Christa 2009) and then were examined using an optical microscope (Mod. LSM700; Carl Zeiss MicroImaging, Germany). This provided an overview of the structure of the tissue, enabling differentiation between normal or mechanically disrupted structures due to thermocavitation.

Laser Scanning Confocal Images

The samples not used for H&E staining (see black arrows in Figure 1B), were exposed to an FITC-dextran solution for 2.5 hours after laser exposure and before LN_2 freezing. The cryostat was used to create 20 µm slices, which were scanned by a confocal laser scanning microscope (Mod. TCS SP II; Leica, Germany) using 488/532 nm wavelengths for excitation and detection, respectively, to observe the penetration depth of the fluorescent solution into the SC and epidermis. The enhancement of SC permeation by cavitation was determined by comparing the cumulative total fluorescence intensity between the skin damaged by thermocavitation (from different solutions' layers) and the control sample with no cavitation damage.

3.7.2. Results

Agar Gels

Mechanical Properties of Agar versus Porcine Skin

Figure 3.27 shows the stress-strain analysis for the range of agar concentrations. The elastic modulus *E* of agar i.e., the slope of the stress-strain curves, decreases as the concentration of agar increases. The dashed lines indicate a linear fit to the elastic region. The values for *E* were found to be 236, 90, 51, and 17 MPa for the 1, 2, 3, and 5 % agar gel concentrations, respectively. For the particular case of 2 % concentration, the stress-strain curve was consistent with the

stress-strain curves of porcine skin reported in (Uzer, Ho et al. 2009), where an elastic modulus of $\sim$ 95 MPa was obtained, suggesting that this agar concentration possess similar mechanical properties to that of porcine skin. For this reason, most experiments were performed with this agar concentration.
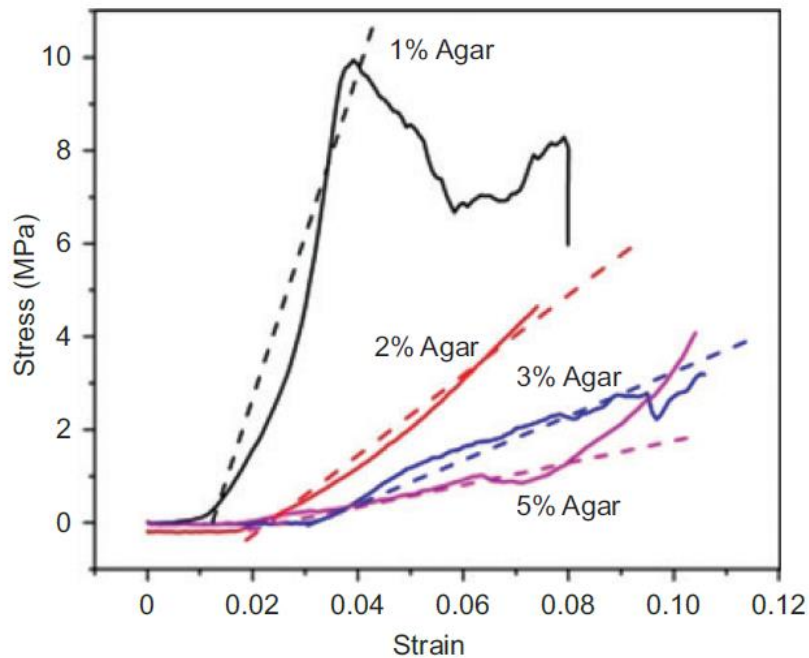
Figure 3.27. Stress-strain curves of several concentrations of agar gel.
Dashed lines indicate an approximate linear fit within the elastic region of deformation.

Effects of Agar Concentration

Figure 3.28A shows holes generated on the agar gels surfaces exposed to the CW laser at 153 mW power, for 10 seconds and for a solution layer of $\sim$ 300 μm. Each image corresponds to agar gel concentrations varying consecutively from 1% to 6%. Based on previous work (Ramirez-San-Juan, Rodriguez-Aboytes et al. 2010), this exposure time and laser parameters correspond to $\sim$ 4 x 10^4 low amplitude cavitation events, each generating maximum pressure waves of ap-

proximately 0.1 MPa. For the 1% and 2% concentrations, the diameter of the holes was almost the same ($\sim$ 1 mm), suggesting that this could be the maximum diameter produced by the shock waves under the conditions described above. This was confirmed through a separate experiment shown in Figure 3.28B, where 2% agar samples with a 100 µm-thick $CuNO_4$ layer solution were irradiated with 193 mW laser power for up to 8 seconds. The resulting hole diameters were normalized because the observed behavior was the same regardless of the agar concentration, laser power or solution layer thickness. When concentration of agar increased, the diameter of the holes became smaller until it disappeared at 6% concentration; the holes became less circular as well. As the concentration increased, the magnitude of the shock wave became insufficient to damage the surface.

Effect of Solution Thickness

Figure 3.29 shows a set of cavitation-produced holes, which were generated on an agar of 5% concentration, but different solution layer thicknesses (300, 200 and 100 µm) using a fixed 170 mW laser power. A 5% agar concentration was employed because damage to that gel ranged between negligible for the thickest solution layer (300 µm) to significant produced by the thinnest layer (100 µm). The shock wave amplitude is greatly attenuated far from its source, i.e., the amplitude decays inversely proportional to its distance from the origin/source (Ramirez-San-Juan, Rodriguez-Aboytes et al. 2010). Shades of gray around the irradiation spots are visible, possibly related to melting and re-gelling and/or entrapment of air bubbles. Only visual inspection of diameter and depth of ablation were used as indicators of damage to the tissue models. Layer thickness smaller than 100 µm were not explored because thermal damage risk increases as the radiation on the sample surface increases.
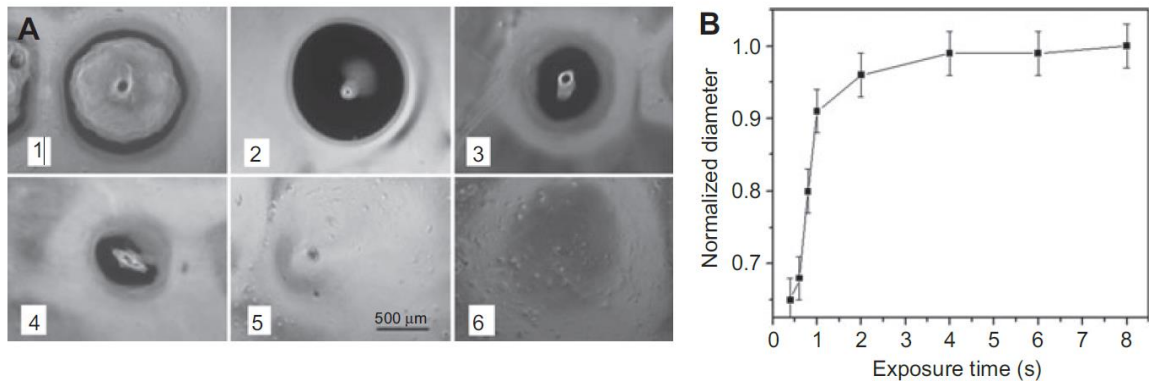
Figure 3.28.Damage generated on agar by thermocavitation-produced shockwaves.
(A) Agar concentrations are percentage by weight, listed in white boxes. The spots visible on 5% and 6% are undissolved agar powder. (B) Normalized diameter of holes as a function of exposure time for 2% agar concentration for a 300 μm solution layer and 153 mW irradiation.

Figure 3.29. Holes on agar gel (5% concentration) for identical irradiation and varying solution thickness.
(A) 300 μm, (B) 200 μm, and (C) 100 μm.

Effect of Laser Power

The inset of Figure 3.30 shows an array of 5 holes generated on 2% concentration agar. Each column corresponds to a different laser power at the output of the microscope objective (see caption) and the exposure time was 10 seconds. At the lowest laser power, the diameter and depth of the holes were the largest, reaching ~ 1 mm diameter and ~ 300 μ m depth, and, as power increased, both the diameter and depth decreased to ~ 650 μm and ~ 150 μm, respec-

tively. In previous work it was shown that bubble's size (and therefore amplitude of the shock wave) increases as the power decreases because of the mismatch in the characteristic times of heat diffusion, τ_{dif} , and cavitation time, τ_{cav} (Ramirez-San-Juan, Rodriguez-Aboytes et al. 2010). When $\tau_{dif} << \tau_{cav}$ (low laser power), heat can be transferred to a larger volume, evaporating a larger volume when the bubble nucleates and producing a larger bubble. A larger bubble creates a higher amplitude shock wave. In contrast, when τ_{dif} is comparable or smaller than τ_{cav} (high power), the vaporization volume is smaller because the bubble formation occurs before heat can diffuse significantly away from the irradiated area. Upon collapse, the shock wave amplitude is also reduced.
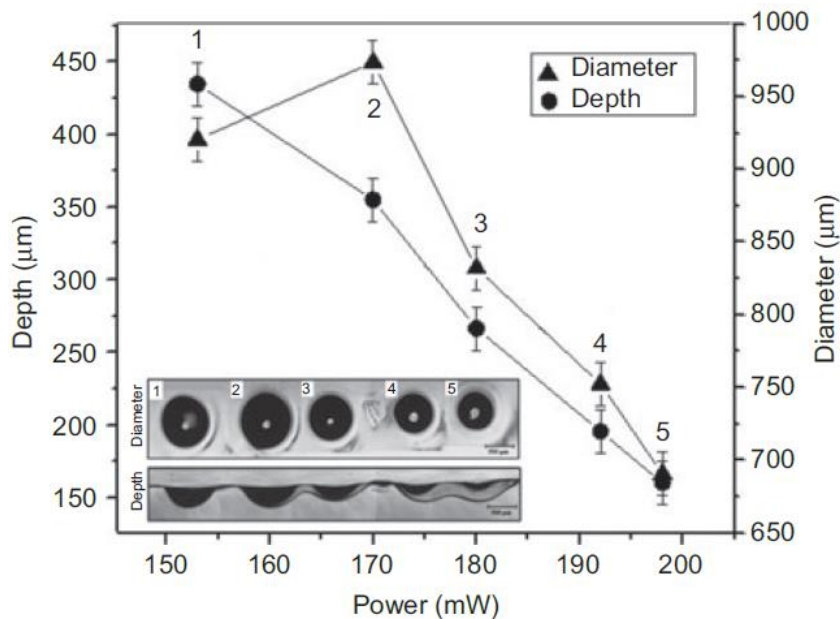
Figure 3.30. Depth and diameter of holes generated by thermocavitation on agar. View from above (top row) and side view (bottom row) generated on 2% concentration agar by laser powers of (1) 153 mW, (2) 170 mW, (3) 180 mW, (4) 192 mW, and (5) 198 mW, using a 300 µm thick liquid solution layer.

As expected, cavitation frequency increases with power because of the shorter time it takes for the bubbles to collapse and make the liquid available for a subsequent evaporation process (Section 3.5). Here, a congruent trend is observed: as laser power increases, the cavitation bubble size and diameter and the depth of the resulting hole in the gel decrease, suggesting that smaller bubbles' craters corresponds to shock waves of lower amplitude.
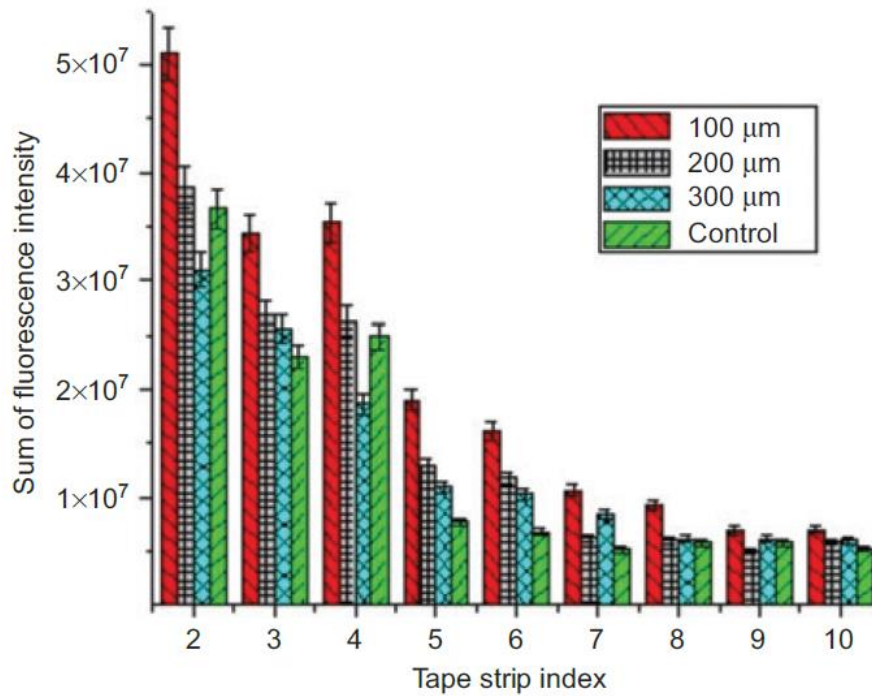
Figure 3.31. Penetration profiles of topically applied FITC-dextran on the stratum corneum. The porcine skin was exposed to 193 mW laser radiation and the liquid layer thickness was varied as indicated.

Porcine Skin

Tape Stripping

Figure 3.31 shows the fluorescence intensity distribution of each successive tape strip, which is correlated to the penetration of FITC-dextran solution into the skin. The first tape strip contained almost a complete cell layer of SC, and it rejected because its fluorescence is influenced by highly variable skin surface conditions. The size of the error bars denotes the standard deviation of the intensity measurements of the samples measured, which for all experiments was between 3 and 5. The inherent randomness of the tests means the true uncertainty and repeatability of the tests is much larger. Estimating a maximum significance level of 30%, a *t*-test of two independent populations comparing the control to the 100 µm layer experiments reveals a *p*–value of 0.26, indicating that these two populations were statistically different. Despite the variability of this method and its partially qualitative nature, these results suggest that the penetration of FITC-dextran into the skin is greater when thermocavitation is induced within the thinnest layer of solution (100 µm), congruent with the cavitation-induced damage on the agar skin phantoms.
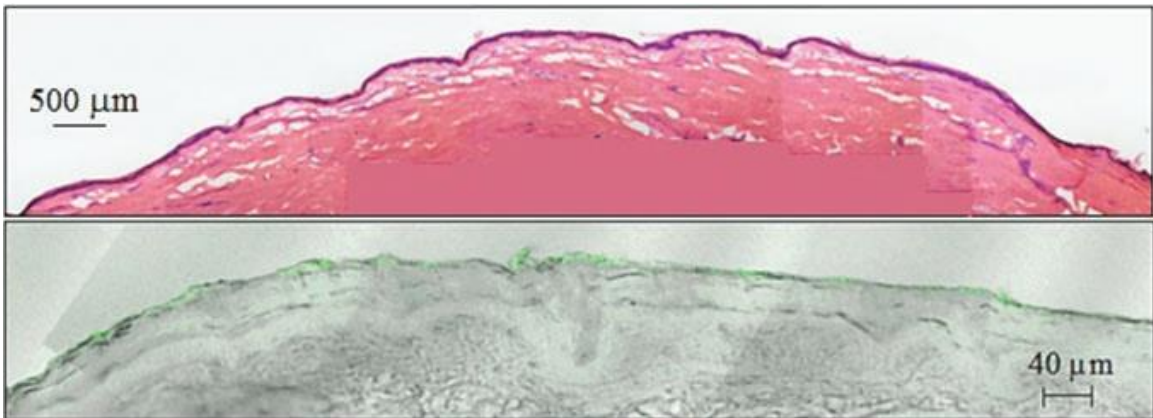
Figure 3.32. Porcine skin not exposed to cavitation. H&E control (top) and confocal microscope fluorescent image (bottom).

H&E and Confocal Fluorescent Imaging: Control

Figure 3.32 shows the images of the histological structure of the tissue by the H&E technique (top), and the confocal fluorescent microscope to observe the penetration of the FITC-dextran solution topically applied on the porcine skin surface (bottom) for 2.5 hours. Each image was taken from adjacent 20 μm thick slices of porcine skin samples that were not exposed to thermocavitation. The H&E image shows intact SC and epidermis, and the confocal fluorescent image shows the solution's fluorescence (FITC-dextran) is confined to the surface of the SC, confirming that the SC is the principal barrier to FITC-dextran's permeation into the skin.
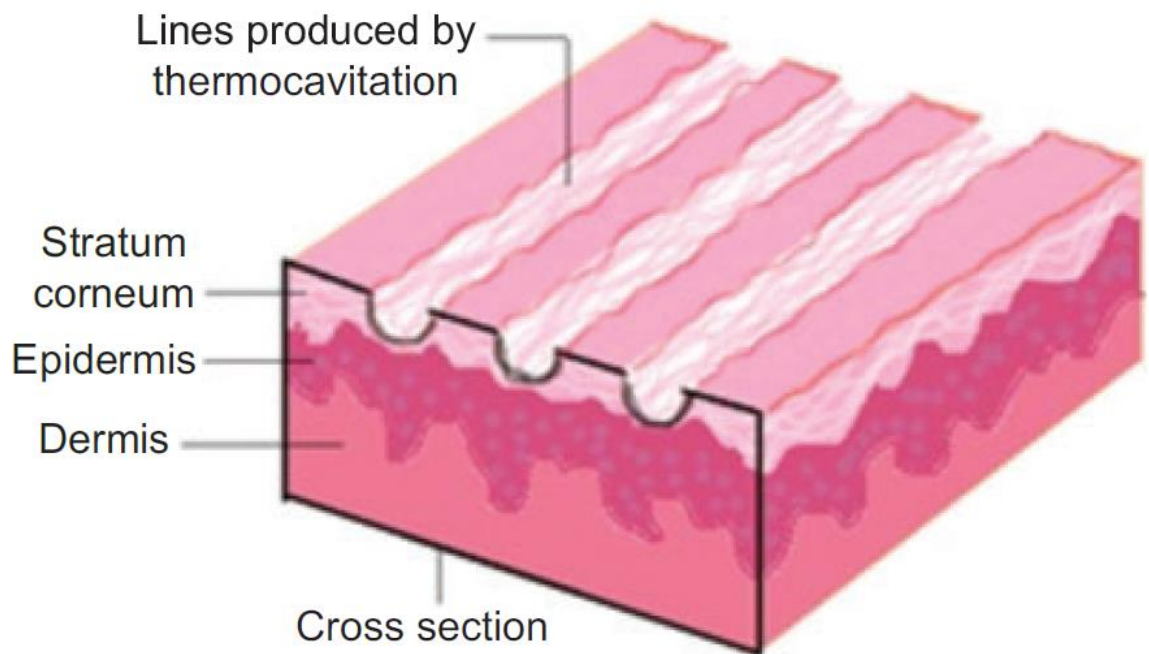
Figure 3.33. Diagram of damage channels produced on the SC by thermocavitation.
The skin sample was then cut tranversally by a cryostat to 20 μm thick slices for analysis.

H&E and Confocal Fluorescent Imaging: Cavitation

The experiments described above were repeated but this time the samples were exposed to thermocavitation, using a ~ 100 μm thick solution topically applied on the skin surface for 2.5 hours. To make damage more apparent, the laser beam was displaced along the surface to generate lines on the surface of the SC (Figure 3.33), as opposed to the holes created on the agar gels by keeping the laser beam fixed. The damage generated by thermocavitation can be observed by taking cross-section samples. The displacement was achieved by moving the skin sample at a speed of 0.5 mm/s while irradiating the solution with the maximum power available from the laser system (193 mW). This ensures continuous lines over the SC because the cavitation's occurs very frequently relative to the displacement velocity. Two adjacent slices (20 μm thick) were obtained from the same sample; the first was H&E stained and the second was analyzed in the confocal microscope to observe the penetration of the fluorescent solution into the SC (Figure 3.34 and Figure 3.35).

Figure 3.34 is a complete view of an H&E stained tissue slice, where it is possible to observe the damage on the SC in at least three locations, marked by 1, 2 and 3. This damage is assessed, first, by the clearly evident peeling of the uppermost skin layers (SC and epidermis) and then verified using the optical microscope. Figure 3.35A–C magnifies these three locations on the H&E slice (top) and the corresponding confocal fluorescent images (bottom). Location 1 in Figure 3.34 shows that the damage generated along this channel is almost superficial (H&E image) and, consequently, the solution penetration depth is minimal (fluorescent image). However, in locations 2 and 3, the damage increases. There is an abrupt tearing of the SC of ~ 80 − 100 μm in diameter, and possible damage to the upper epidermis. This damage allows the FITC-dextran

solution to penetrate deeper into the skin ($\sim 40 - 60$ μm) as shown in the fluorescent images of

Figure 3.35B and C.
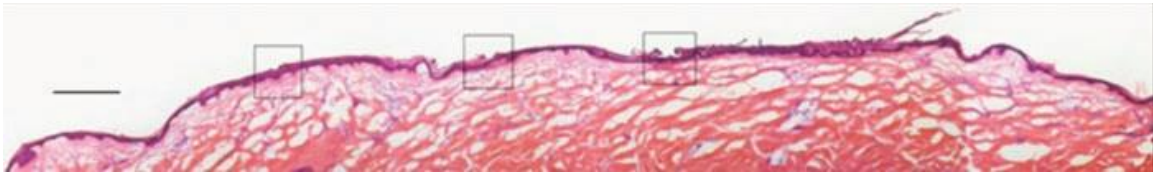
Figure 3.34. Hisotological structure of porcine skin exposed to thermocavitation.
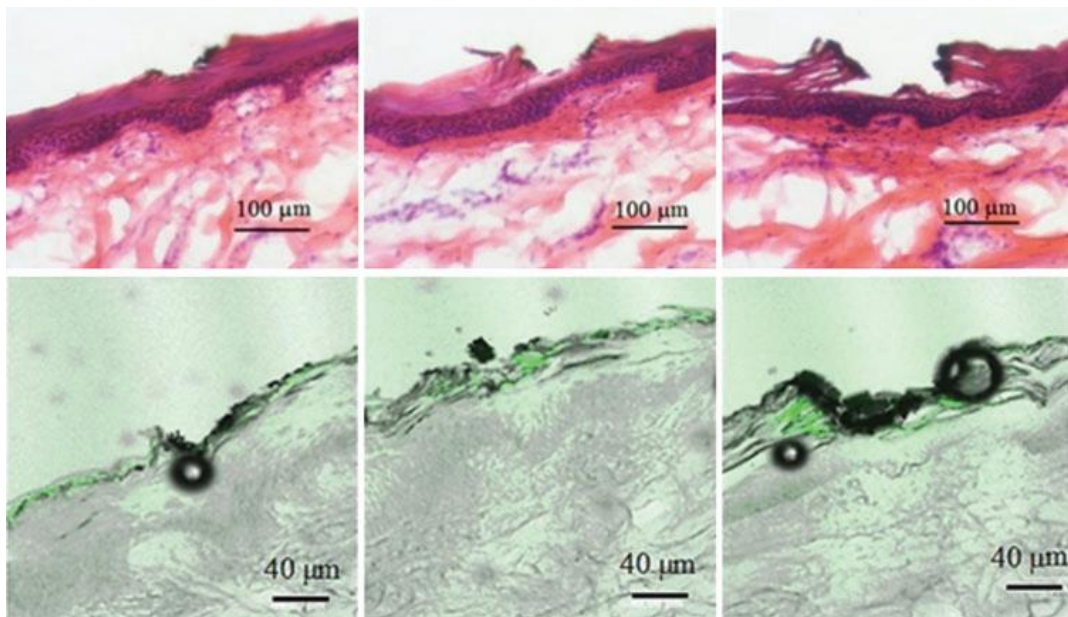
Figure 3.35. Magnified regions of Figure 3.34. H&E images (top) and laser confocal microscopy (bottom) of skin exposed to FITC-dextran solution for 2.5 hours.

3.7.3. Discussion

The discrepancy between regions 1 and 2–3 (Figure 3.34) is at first glance unusual, as each site was subject to the same experimental conditions. Similar damage was expected in all three cases. However, it is likely that the maximum bubble radius and, consequently, the shock wave amplitude is influenced by variations in the sample thickness, flatness, and even a slight tilt of the sample from its ideal perpendicular position with respect to the laser beam. These variables affect the bubble size and therefore shock wave amplitude, producing different damage scenarios for each channel. Also, the maximum damage obtained on the SC ($\sim 80 - 100$ μm diameter) is much smaller than that obtained in the agar, possibly due to subtle differences on mechanical properties between both materials and the mismatch in the number of cavitation events between the two experiments. A modest increase in the number of cavitation events by slowing the sample displacement and/or a reduction of the laser power should increase the hole depth.

Of concern was the dark region noticeable in the H&E and fluorescent images near the periphery of the ruptured tissue. Such damage could be induced by excessive heat transfer from the solution layer or direct laser absorption, potentially burning the skin surface. Further, since the SC has lower water content than epidermis, ablative damage could be induced on the SC at lower temperatures and shorter exposure times than those reported needed to damage the epidermis. To investigate this hypothesis, two analyses were performed using a finite element heat transfer model (COMSOL Multiphysics, V 4.2; COMSOL, USA). Human skin thermos-physical properties reported in (Shafirstein, Bäumler et al. 2004) were used and the $CuNO_4$ solution was assumed to have identical properties to water. The first study computed the theoretical maximum temperature reached within a 100 μm thick solution layer during exposure to a focused 193 mW CW laser. With the maximum solution temperature, the second study estimated the

cumulative thermal damage to the tissue underneath using an Arrhenius tissue damage model (Shafirstein, Bäumler et al. 2004).

Figure 3.36A shows the computed thermal map within the 110 µm thick solution layer after 240 µs irradiation. This corresponds to the cavitation time, i.e., the time between the laser activation and the nucleation of the first cavitation bubble (Ramirez-San-Juan, Rodriguez-Aboytes et al. 2010). Figure 3.36B shows the temperature distribution at the skin surface (i.e., the SC) and illustrates that the maximum temperature reached is approximately 72 ° C in 240 µs. After nucleation, the temperature decreases as the bubble expands and collapses, mechanically dispersing heat. The cycle repeats again at a frequency of $\sim$ 4 kHz for these conditions. Upon bubble collapse, due to convective mixing, an even higher rate of cooling is expected, but this model does not accommodate for this agitation. Nevertheless, measurements indicate that after several minutes of irradiation, the solution heats by only about 5 ° C, and the Arrhenius model suggests that thermal damage is unlikely to occur within the epidermis for sub-millisecond temperature spike to 72 ° C.
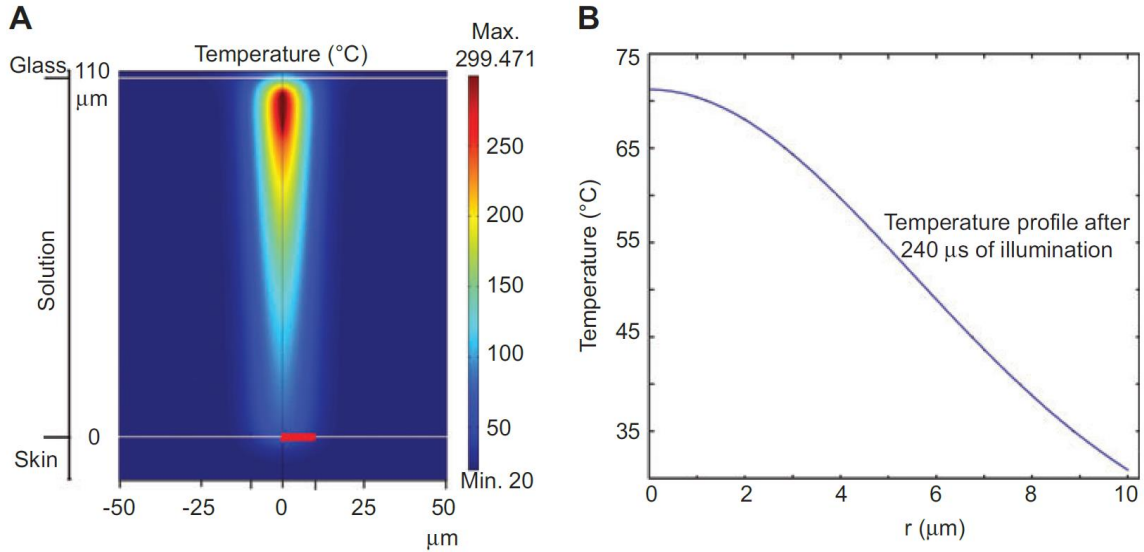
Figure 3.36. (A) Temperature profile within a 110 μm thick CuNO₄ solution and (B) at the SC at the end of a 240 μs, 193 mW irradiation period.
The simulation ends when 300 °C is reached, the nucleation temperature.

In order to assess the thermal damage on the skin, the Arrhenius damage integral (Ω) was then computed, represented by Equation [3-11]:

$$\Omega(ti) = \ln\left(\frac{C(0)}{C(ti)}\right) = A \int_{0}^{ti} \exp\left(-\frac{E_a}{RT(x,z,t)}\right) dt \qquad [3\text{-}11]$$

where $\Omega(ti)$ is the thermal damage parameter at $t = ti$; $C(0)$ is the number of undamaged cells at time 0; $C(ti)$ is the number of undamaged cells at time ti; A is the frequency factor or the molecule collision rate; E_a is the activation energy in J/mol; and R is the universal gas constant of 8.3144 J/mol/K.

Visual inspection of the histology samples reveals a region of damage of ∼ 100 μm in diameter (Figure 3.35C), which means that ∼ 800 cavitation events took place during approximately 200 ms. Using this time and the maximum temperature computed before (72 °C), the Ω values

203

shown in Table 1 were computed. These values correspond to the mean thermal damage calculated over a region of 10 µm in radius at the interface skin solution (the horizontal red line in Figure 3.36A) for skin harvested from different anatomic locations.

Table 3.1. Mean thermal damage induced to porcine skin after 200 ms of CW laser exposure to a constant temperature of 72°C. From (Xu, Seffen et al. 2008)

Specimen		E_a (J/mol*K)	A (1/s)	Ω (ti = 200 ms)
Porcine skin	Back	525,500	2.126E+81	1.14203
	Belly	393,500	1.151E+61	0.75226
	Ear	586,700	5.240E+91	13.88818
	Face	471,000	4.575E+72	0.47972
	Flank	401,200	1.501E+61	0.06598

Note that only values of $\Omega \geq 1$ correspond to cell damage >63 % relative to the existing undamaged cells before exposure, and lesser values are normally considered inconsequential or reversible damage. Two values >1 were computed, for ear and back skin. Although there is always uncertainty as to the anatomic location of the skin samples, back and ear skin is generally recognizable, and the samples used for this study did not appear to be from those locations. Therefore, the damage observed in the samples is unlikely due to heated solution or laser-induced epidermal burning. Finally, burning by light absorption is also unlikely since the beam diameter at the skin ($\sim$ 20 µm) is smaller than the damaged region ($\sim$ 100 µm). The reason for the darker region in Figure 3.35 remains to be determined, but laser burning or thermal damage by a hot liquid seems unlikely.

3.7.4. Conclusions

The damage observed on agar and porcine skin appears to be congruent with the relation-ship between laser power, focal point, cavitation frequency and extent of damage observed in previous studies and related to the emission of shock waves produced at the collapse of the thermocavitation bubbles (Rastopov and Sukhodolsky 1991, Ramirez-San-Juan, Rodriguez-Aboytes et al. 2010). In particular, the shockwave amplitude produced by thermocavitation de-creases with laser power, but the increase in cavitation frequency with laser power means the width and depth of the damaged zone increases.

In this study, the greatest damage induced to the agar phantoms is produced with the low-est laser power ($\sim$ 153 mW) and thinnest solution layer ($\sim$ 100 μm). Similar laser power and solution layer thickness led to porcine skin damage of $\sim$ 80–100 μm in diameter, sufficient to break the SC and allow penetration of 4 kDa, FITC-dextran to depths of $\sim$ 40–60 μm. However, the extent of damage induced on porcine (and presumably human) skin seems dependent on variations in the sample thickness, flatness, and angle from normal to the laser beam. A system-atic study to assess this issue is warranted.

Uncertainty remains regarding the dark region in the H&E and fluorescent images near the periphery of the ruptured tissue. First-approach numerical simulations suggest that those re-gions are not caused by the temperatures and exposures corresponding to laser absorption within the solution.

From an application point of view, this combination of CW laser and absorbing solution is quite convenient, being much less expensive and complex than contemporary TDD methods.

References

Carson, F. and H. Christa (2009). "Histotechnology. A Self-Instructional Text." <u>American Society for Clinical Pathology Press: Hong Kong</u>.

Heyderman, E. (1992). "Histotechnology. A self-instructional text." <u>Histopathology</u> **20**(1): 91-91.

Korneev, N., P. R. Montero, R. Ramos-García, J. C. Ramirez-San-Juan and J. P. Padilla-Martinez (2011). "Ultrasound induced by CW laser cavitation bubbles." <u>Journal of Physics: Conference Series</u> **278**: 012029.

Lademann, J., U. Jacobi, C. Surber, H.-J. Weigmann and J. Fluhr (2009). "The tape stripping procedure–evaluation of some critical parameters." <u>European Journal of Pharmaceutics and Biopharmaceutics</u> **72**(2): 317-323.

Padilla-Martinez, J., G. Aguilar, J. Ramirez-San-Juan and R. Ramos-García (2011). <u>Temporal evolution of thermocavitation bubbles using high speed video camera</u>. SPIE NanoScience+ Engineering, International Society for Optics and Photonics.

Ramirez-San-Juan, J., J. Padilla-Martinez, P. Zaca-Moran and R. Ramos-Garcia (2011). "Micro-hole drilling in thin films with cw low power lasers." <u>Optical Materials Express</u> **1**(4): 598-604.

Ramirez-San-Juan, J. C., E. Rodriguez-Aboytes, A. E. Martinez-Canton, O. Baldovino-Pantaleon, A. Robledo-Martinez, N. Korneev and R. Ramos-Garcia (2010). "Time-resolved analysis of cavitation induced by CW lasers in absorbing liquids." <u>Opt. Express</u> **18**(9): 8735-8742.

Rastopov, S. F. and A. T. Sukhodolsky (1990). "Cluster nucleation in the process of CW laser induced thermocavitation." <u>Physics Letters A</u> **149**(4): 229-232.

Rastopov, S. F. and A. T. Sukhodolsky (1991). <u>Sound generation by thermocavitation-induced cw laser in solutions</u>. Optical Radiation Interaction with Matter, Leningrad, Russia, SPIE.

Shafirstein, G., W. Bäumler, M. Lapidoth, S. Ferguson, P. E. North and M. Waner (2004). "A new mathematical approach to the diffusion approximation theory for selective photothermolysis modeling and its implication in laser treatment of port-wine stains." <u>Lasers in surgery and medicine</u> **34**(4): 335-347.

Subhash, G., Q. Liu, D. Moore, P. Ifju and M. Haile (2011). "Concentration dependence of tensile behavior in agarose gel using digital image correlation." <u>Experimental Mechanics</u> **51**(2): 255-262.

Uzer, G., A. Ho, R. Clark and C. Fu-pen (2009). <u>Mechanical properties of pig skin</u>. Proceedings of the Society for Experimental Mechanics Annual Conference.

Xu, F., K. Seffen and T. Lu (2008). "Temperature-dependent mechanical behaviors of skin tissue." <u>IAENG International Journal of Computer Science</u> **35**(1): 92-101.

Yoon, J., D. Park, T. Son, J. Seo, J. S. Nelson and B. Jung (2010). "A physical method to enhance transdermal delivery of a tissue optical clearing agent: combination of microneedling and sonophoresis." <u>Lasers in surgery and medicine</u> **42**(5): 412-417.

3.8. Conclusions and Future Directions

The unique and potent dynamics of cavitation bubbles provide a novel avenue for forced mixing and convection near heated surfaces. The challenge in making use of cavitation is controlling it and studying its effects. Direct measurement is difficult, as sensors fast enough to characterize the microsecond dynamics are by physical necessity small and fragile, and are destroyed upon exposure to cavitation shockwaves. This study by necessity includes the development of non-intrusive optically-based measurement techniques, for both the fluid flows (Section 3.4) and temperature fields (Section 3.6) surrounding cavitation bubbles.

Cavitation induced by pulsed lasers has been studied since the development of such lasers in the mid-20th Century. Continuous wave laser induced cavitation is a much more novel development; the nucleation process differs somewhat from pulsed-laser induced cavitation and the repetitive bubble formation during a single irradiation period is not a factor when using a pulsed laser. In this study, the behavior of CW-induced cavitation bubbles as it relates to the optical conditions used to induce cavitation has been explored (Section 3.5). The study explored bubble frequency and radius as they relate to laser power and focus. The development of a liquid lens as the liquid heats up is observed; this lens is unreported in literature as the related studies use far shorter focal lengths and lower laser power.

The use of optical cavitation as a method of needle-less drug delivery is explored using porcine skin as a human skin analog (Section 3.7). The use of cavitation to create temporary, painless micron-scale skin poration is shown to facilitate drug diffusion into the skin. This can be applied in many clinical procedures; a nascent application where cavitation skin poration would be very beneficial is the delivery of skin optical clearing agents for imaging of subdermal tissues.

Currently, optical clearing agents are delivered using arrays of microneedles to puncture the skin. Cavitation can be induced within the clearing agent itself, simplifying the process.

Continuous wave-induced cavitation is a novel and growing field. Future work should perfect the measurement techniques demonstrated in this dissertation and develop new ones to address the challenge of characterizing cavitation bubbles. Building on the examination of the temperature field surrounding cavitation events, quantitative measurement of the cooling effects induced by cavitation bubbles is needed. Control over the bubble size and formation frequency can be improved – introducing factors such as nanoparticles (acting as absorption enhancers and nucleation sites) and dissolved gases into the cavitation solution can potentially reduce the optical energy required or affect the size and collapse rates of the cavitation bubbles.

4. Collected References

Allen, R. F. (1975). "Role of Surface-Tension in Splashing." Journal of Colloid and Interface Science **51**(2): 350-351.

Banks, D., D. Garcia, F. Devia-Cruz Luis, S. Camacho-López and G. Aguilar (2013). Optical Transmission Measurement of Thermocavitation. Conference on Liquid Atomization and Spray Systems, Pittsburgh, PA.

Banks, D., R. Sanchez, C. Ajawara, H. Surti and G. Aguilar (2013). "Effects of drop and film viscosity on drop impacts onto liquid films." Atomization and Sprays **23**(6): 525-540.

Bayer, I. S. and C. M. Megaridis (2006). "Contact angle dynamics in droplets impacting on flat surfaces with different wetting characteristics." Journal of Fluid Mechanics **558**: 415.

Beck, J. V., C. R. St Clair and B. F. Blackwell (1985). Inverse Heat Conduction: Ill-Posed Problems, John Wiley & Sons, Inc.

Bergwerk, W. (1959). "Flow Pattern in Diesel Nozzle Spray Holes." Proceedings of the Institution of Mechanical Engineers **173**(1): 655-660.

Bird, J. C., S. S. H. Tsai and H. A. Stone (2009). "Inclined to splash: triggering and inhibiting a splash with tangential velocity." New Journal of Physics **11**(6): 063017.

Blake, J. R. (1988). "The Kelvin impulse: application to cavitation bubble dynamics." The Journal of the Australian Mathematical Society. Series B. Applied Mathematics **30**(02): 127-146.

Boulais, E., R. Lachaine and M. Meunier (2012). "Plasma Mediated off-Resonance Plasmonic Enhanced Ultrafast Laser-Induced Nanocavitation." Nano letters.

Brennen, C. E. (1995). Cavitation and bubble dynamics, Oxford University Press, USA.

Bunkin, N. F. and V. B. Karpov (1990). "Optical cavitation of transparent liquids exposed to broadband laser light." Pis'ma Zh. Eksp. Teor. Fiz. **52**(1): 669-673.

Bunkin, N. F., O. A. Kiseleva, A. V. Lobeyev, T. G. Movchan, B. W. Ninham and O. I. Vinogradova (1997). "Effect of Salts and Dissolved Gas on Optical Cavitation near Hydrophobic and Hydrophilic Surfaces." Langmuir **13**(11): 3024-3028.

Camacho-López, S., F. Perez-Gutierrez, L. Devia-Cruz, D. Garcia, G. Aguilar and D. Banks (2013). "High Resolution Optical Experimental Technique for Computing Pulsed Laser Induced Cavitation Bubble Dynamics in a Single Shot." Atomization and Sprays **23**(6): 475-485.

Carome, E. F., N. A. Clark and C. E. Moeller (1964). "Generation of Acoustic Signals in Liquids by Ruby Laser-Induced Thermal Stress Transients." Applied Physics Letters **4**(6): 95-97.

Carson, F. and H. Christa (2009). "Histotechnology. A Self-Instructional Text." <u>American Society for Clinical Pathology Press: Hong Kong</u>.

Çengel, Y. A. and R. H. Turner (2001). <u>Fundamentals of thermal-fluid sciences</u>. Boston, McGraw-Hill.

Cochran, S. A. and M. R. Prausnitz (2001). "Sonoluminescence as an indicator of cell membrane disruption by acoustic cavitation." <u>Ultrasound in medicine & biology</u> **27**(6): 841-850.

Cossali, G., A. Coghe and M. Marengo (1997). "The impact of a single drop on a wetted solid surface." <u>Experiments in Fluids</u> **22**: 463-472.

Crimaldi, J. P. (2008). "Planar laser induced fluorescence in aqueous flows." <u>Experiments in Fluids</u> **44**(6): 851-863.

Dharmadhikari, A. K., J. A. Dharmadhikari, A. V. Mahulkar, G. Ramanandan, H. Ramachandran, A. B. Pandit and D. Mathur (2011). "Dynamics of Photothermally Created Vaporous, Gaseous, and Mixed Microbubbles." <u>The Journal of Physical Chemistry C</u> **115**(14): 6611-6617.

Doukas, A. G. and N. Kollias (2004). "Transdermal drug delivery with a pressure wave." <u>Advanced Drug Delivery Reviews</u> **56**(5): 559-579.

Doulah, M. S. (1977). "Mechanism of disintegration of biological cells in ultrasonic cavitation." <u>Biotechnology and Bioengineering</u> **19**(5): 649-660.

Eslamian, M. and N. Ashgriz (2011). Spray Drying, Spray Pyrolysis and Spray Freeze Drying Handbook of Atomization and Sprays. N. Ashgriz, Springer US**:** 849-860.

Faulkner, D., M. Khotan and R. Shekarriz (2003). <u>Practical design of a 1000 W/cm^2 cooling system [high power electronics]</u>. Semiconductor Thermal Measurement and Management Symposium, 2003. Ninteenth Annual IEEE.

Fedorchenko, A. I. and A.-B. Wang (2004). "On some common features of drop impact on liquid surfaces." <u>Physics of Fluids</u> **16**(5): 1349-1365.

Ferain, I., C. A. Colinge and J. P. Colinge (2011). "Multigate transistors as the future of classical metal-oxide-semiconductor field-effect transistors." <u>Nature</u> **479**(7373): 310-316.

Fink, J., D. Gault and R. Greeley (1984). "The Effect of Viscosity on Impact Cratering and Possible Application to the Icy Satellites of Saturn and Jupiter." <u>J. Geophys. Res.</u> **89**(B1): 417-423.

Fujimoto, H., T. Ogihara, S. Yoshimoto, T. Hama and H. Takuda (2013). "Successive Collision of Two Water Droplets with a Hot Solid." <u>International Journal of Transport Phenomena</u> **13**(3).

Fujimoto, J. G., W. Z. Lin, E. P. Ippen, C. A. Puliafito and R. F. Steinert (1985). "Time-resolved studies of Nd:YAG laser-induced breakdown. Plasma formation, acoustic wave generation, and cavitation." Investigative Ophthalmology & Visual Science **26**(12): 1771-1777.

Fyrillas, M. M. and A. J. Szeri (1994). "Dissolution or growth of soluble spherical oscillating bubbles." Journal of Fluid Mechanics **277**: 381-407.

Godwin, R. P., E. J. Chapyak, J. Noack and A. Vogel (1999). Aspherical bubble dynamics and oscillation times.

Hecht, E. (1998). Optics, Addison-Wesley.

Hellman, A. N., K. R. Rau, H. H. Yoon, S. Bae, J. F. Palmer, K. S. Phillips, N. L. Allbritton and V. Venugopalan (2007). "Laser-Induced Mixing in Microfluidic Channels." Analytical Chemistry **79**(12): 4484-4492.

Heyderman, E. (1992). "Histotechnology. A self-instructional text." Histopathology **20**(1): 91-91.

Jepsen, R. A., S. S. Yoon and B. Demosthenous (2006). "Effects of air on splashing during a large droplet impact: Experimental and numerical investigations." Atomization and Sprays **16**(8): 981-996.

Jian, A. Q., K. Zhang, Y. Wang, S. P. Lau, Y. H. Tsang and X. M. Zhang (2012). "Microfluidic flow direction control using continuous-wave laser." Sensors and Actuators A: Physical **188**(0): 329-334.

Juhasz, T., G. A. Kastis, C. Suarez, Z. Bor and W. E. Bron (1996). "Time-resolved observations of shock waves and cavitation bubbles generated by femtosecond laser pulses in corneal tissue and water." Lasers in Surgery and Medicine **19**(1): 23-31.

Kim, J. (2007). "Spray cooling heat transfer: The state of the art." International Journal of Heat and Fluid Flow **28**(4): 753-767.

Kim, S. C. and H. S. Ryou (2003). "An experimental and numerical study on fire suppression using a water mist in an enclosure." Building and Environment **38**(11): 1309-1316.

Korneev, N., P. R. Montero, R. Ramos-García, J. C. Ramirez-San-Juan and J. P. Padilla-Martinez (2011). "Ultrasound induced by CW laser cavitation bubbles." Journal of Physics: Conference Series **278**: 012029.

Kröninger, D., K. Köhler, T. Kurz and W. Lauterborn (2009). "Particle tracking velocimetry of the flow field around a collapsing cavitation bubble." Experiments in Fluids **48**(3): 395-408.

Lademann, J., U. Jacobi, C. Surber, H.-J. Weigmann and J. Fluhr (2009). "The tape stripping procedure–evaluation of some critical parameters." European Journal of Pharmaceutics and Biopharmaceutics **72**(2): 317-323.

Lauterborn, W. and H. Bolle (1975). "Experimental investigations of cavitation-bubble collapse in the neighbourhood of a solid boundary." Journal of Fluid Mechanics **72**(2): 391-399.

Li, X. Y., X. H. Ma and Z. Lan (2009). "Behavioral Patterns of Drop Impingement onto Rigid Substrates with a Wide Range of Wettability and Different Surface Temperatures." Aiche Journal **55**(8): 1983-1992.

Lide, D. (2006). CRC Handbook of Chemistry and Physics: A Ready-Reference Book of Chemical and Physical Data Boca Raton, Fl, CRC Press.

Liu, B., J. Cai, X. Huai and F. Li (2014). "Cavitation Bubble Collapse Near a Heated Wall and Its Effect on the Heat Transfer." Journal of Heat Transfer **136**(2): 022901.

Liu, J., H. Vu, S. S. Yoon, R. Jepsen and G. Aguilar (2010). "Splashing Phenomena during Liquid Droplet Impact." Atomization and Sprays **20**(4): 297-310.

Mack, C. A. (2011). "Fifty Years of Moore's Law." Semiconductor Manufacturing, IEEE Transactions on **24**(2): 202-207.

Marmottant, P. H. and E. Villermaux (2004). "On spray formation." Journal of Fluid Mechanics **498**: 73-111.

Martin, G. D., S. D. Hoath and I. M. Hutchings (2008). "Inkjet printing-the physics of manipulating liquid jets and drops." Journal of Physics: Conference Series **105**: 1-15.

Mock, U., T. Michel, C. Tropea, I. Roisman and J. Rühe (2005). "Drop impact on chemically structured arrays." Journal of Physics: Condensed Matter **17**(9): S595-S605.

Mundo, C., M. Sommerfeld and C. Tropea (1995). "Droplet-Wall Collisions - Experimental Studies of the Deformation and Breakup Process." International Journal of Multiphase Flow **21**(2): 151-173.

Nagel, M., P.-T. Brun and F. Gallaire (2014). "A numerical study of droplet trapping in microfluidic devices." Physics of Fluids (1994-present) **26**(3): -.

Noblin, X., A. Buguin and F. Brochard-Wyart (2004). "Vibrated sessile drops: Transition between pinned and mobile contact line oscillations." The European Physical Journal E: Soft Matter and Biological Physics **14**(4): 395-404.

Okumura, K., F. Chevy, D. Richard, D. Quéré and C. Clanet (2003). "Water spring: A model for bouncing drops." Europhysics Letters **62**(2): 237-243.

Padilla-Martinez, J., G. Aguilar, J. Ramirez-San-Juan and R. Ramos-García (2011). <u>Temporal evolution of thermocavitation bubbles using high speed video camera</u>. SPIE NanoScience+ Engineering, International Society for Optics and Photonics.

Padilla-Martinez, J. P., G. Aguilar, J. C. Ramirez-San-Juan and R. Ramos-Garcia (2011). Generation of Micron-Sized Holes on Metallic and Transparent Thin Films Using Thermocavitation. <u>Institute of Liquid Atomization and Spray Studies-Americas. </u>. Ventura, CA.

Padilla-Martinez, J. P., D. Banks, J. C. Ramirez-San-Juan, R. Ramos-Garcia, F. Sun and G. Aguilar (2012). "Towards the enhancement of transdermal drug delivery through thermocavitation." <u>Photonics and Lasers in Medicine</u> **1**(3): 183-193.

Padilla-Martinez, J. P., C. Berrospe-Rodriguez, G. Aguilar, J. C. Ramirez-San-Juan and R. Ramos-Garcia (2014). "Optic cavitation with CW lasers: A review." <u>Physics of Fluids (1994-present)</u> **26**(12): 122007.

Padilla-Martinez, J. P., J. C. Ramirez-San-Juan, N. Korneev, D. Banks, G. Aguilar and R. Ramos-Garci a (2013). "Breaking the Rayleigh-Plateau Limit Using Thermocavitation Within a Droplet." <u>Atomization and Sprays</u> **23**(6): 487-503.

Post, S. L. and J. Abraham (2002). "Modeling the outcome of drop-drop collisions in Diesel sprays." <u>International Journal of Multiphase Flow</u> **28**(6): 997-1019.

Ramirez-San-Juan, J., J. Padilla-Martinez, P. Zaca-Moran and R. Ramos-Garcia (2011). "Micro-hole drilling in thin films with cw low power lasers." <u>Optical Materials Express</u> **1**(4): 598-604.

Ramirez-San-Juan, J. C., J. P. Padilla-Martinez, P. Zaca Moran, E. Aboytes-Rodriguez, A. E. Martinez-Canton and R. Ramos-Garcia (2010). "Thermocavitation and its application for fabrication of micron-sized holes on metallic and dielectric thin films." 77621E-77621E-77626.

Ramirez-San-Juan, J. C., E. Rodriguez-Aboytes, N. Korneev, O. Baldovinos-Pantaleon, R. Chiu-Zarate, G. Gutiérrez-Juárez, R. Dominguez-Cruz and R. Ramos-García (2007). <u>Cavitation induced by continuous wave lasers</u>.

Ramirez-San-Juan, J. C., E. Rodriguez-Aboytes, A. E. Martinez-Canton, O. Baldovino-Pantaleon, A. Robledo-Martinez, N. Korneev and R. Ramos-Garcia (2010). "Time-resolved analysis of cavitation induced by CW lasers in absorbing liquids." <u>Opt. Express</u> **18**(9): 8735-8742.

Rastopov, S. F. and A. T. Sukhodolsky (1990). "Cluster nucleation in the process of CW laser induced thermocavitation." <u>Physics Letters A</u> **149**(4): 229-232.

Rastopov, S. F. and A. T. Sukhodolsky (1991). <u>Sound generation by thermocavitation-induced cw laser in solutions</u>. Optical Radiation Interaction with Matter, Leningrad, Russia, SPIE.

Rein, M. (1993). "Phenomena of liquid drop impact on solid and liquid surfaces." <u>Fluid Dynamics Research</u> **12**: 61-93.

Rein, M. (1996). "The transitional regime between coalescing and splashing drops." Journal of Fluid Mechanics **306**(-1): 145.

Saranin, V. A. (1988). "Cavitation mechanism of high-voltage breakdown formation in liquid dielectrics." Journal of Applied Mechanics and Technical Physics **29**(3): 354-356.

Seol, H., J.-C. Suh and S. Lee (2005). "Development of hybrid method for the prediction of underwater propeller noise." Journal of Sound and Vibration **288**(1–2): 345-360.

Shafirstein, G., W. Bäumler, M. Lapidoth, S. Ferguson, P. E. North and M. Waner (2004). "A new mathematical approach to the diffusion approximation theory for selective photothermolysis modeling and its implication in laser treatment of port-wine stains." Lasers in surgery and medicine **34**(4): 335-347.

Smith, H. J. (1975). The hydrodynamic and physico-chemical basis of the drop picture method. Gottingen, Max Plank Institut fur Stromungsforschung, Bericht Nr. 8.

Soriano, G. E., T. Zhang and J. L. Alvarado (2014). "Study of the effects of single and multiple periodic droplet impingements on liquid film heat transfer." International Journal of Heat and Mass Transfer **77**(0): 449-463.

Stow, C. D. and M. G. Hadfield (1981). "An Experimental Investigation of Fluid-Flow Resulting from the Impact of a Water Drop with an Unyielding Dry Surface." Proceedings of the Royal Society of London Series a-Mathematical Physical and Engineering Sciences **373**(1755): 419-441.

Subhash, G., Q. Liu, D. Moore, P. Ifju and M. Haile (2011). "Concentration dependence of tensile behavior in agarose gel using digital image correlation." Experimental Mechanics **51**(2): 255-262.

Thomson, J. and H. Newall (1885). "On the formation of vortex rings by drops falling into liquids, and some allied phenomena." Proceedings of the Royal Society of London **39**(239-241): 417-436.

Thomson, W. T. and M. D. Dahleh (1998). Theory of Vibration with Applications. Upper Saddle River, New Jersey, Prentice-Hall, Inc.

Thoroddsen, S. T., T. G. Etoh, K. Takehara and Y. Takano (2004). "Impact jetting by a solid sphere." Journal of Fluid Mechanics **499**: 139-148.

Thoroddsen, S. T. and J. Sakakibara (1998). "Evolution of the fingering pattern of an impacting drop." Physics of Fluids **10**(6): 1359-1374.

Thoroddsen, S. T., K. Takehara, T. G. Etoh and C. D. Ohl (2009). "Spray and microjets produced by focusing a laser pulse into a hemispherical drop." Physics of Fluids **21**(11): 112101-112115.

Trujillo, M. F., J. Alvarado, E. Gehring and G. S. Soriano (2011). "Numerical Simulations and Experimental Characterization of Heat Transfer From a Periodic Impingement of Droplets." Journal of Heat Transfer **133**(12): 122201-122210.

Trujillo, M. F. and S. R. Lewis (2012). "Thermal boundary layer analysis corresponding to droplet train impingement." Physics of Fluids **24**(11): 112102-112102-112122.

Ukiwe, C., A. Mansouri and D. Y. Kwok (2005). "The dynamics of impacting water droplets on alkanethiol self-assembled monolayers with co-adsorbed CH3 and CO2H terminal groups." Journal of Colloid and Interface Science **285**(2): 760-768.

Uzer, G., A. Ho, R. Clark and C. Fu-pen (2009). Mechanical properties of pig skin. Proceedings of the Society for Experimental Mechanics Annual Conference.

Vander Wal, R., G. Berger and S. Mozes (2006). "Droplets splashing upon films of the same fluid of various depths." Experiments in Fluids **40**(1): 33-52-52.

Vander Wal, R. L., G. M. Berger and S. D. Mozes (2005). "The combined influence of a rough surface and thin fluid film upon the splashing threshold and splash dynamics of a droplet impacting onto them." Experiments in Fluids **40**(1): 23-32.

Vander Wal, R. L., G. M. Berger and S. D. Mozes (2006). "The splash/non-splash boundary upon a dry surface and thin fluid film." Experiments in Fluids **40**(1): 53-59.

Vogel, A. and W. Lauterborn (1988). Acoustic transient generation by laser-produced cavitation bubbles near solid boundaries, ASA.

Volmer, M. and A. Weber (1926). "Keimbildung in übersättigten Gebilden." Z. phys. Chem **119**: 277-301.

Vu, H., G. Aguilar and R. Jepsen (2009). Single Droplet Heat Transfer through Shallow Liquid Pools. 11th International Conference on Liquid Atomization and Spray Studies, Vail, CO, Institute of Liquid Atomization and Spray Studies.

Vu, H., D. Banks and G. Aguilar (2011). "Examining Viscosity and Surface Wettability in Lamella Lift Dynamics and Droplet Splashing." Atomization and Sprays **21**(4).

Watanabe, Y., A. Saruwatari and D. M. Ingram (2008). "Free-surface flows under impacting droplets." Journal of Computational Physics **227**(4): 2344-2365.

Worthington, A. (1882). "On impact with a liquid surface." Proceedings of the Royal Society of London **34**(220-223): 217-230.

Worthington, A. M. (1876). "On the Forms Assumed by Drops of Liquids Falling Vertically on a Horizontal Plate." Proceedings of the Royal Society of London **25**: 261-272.

Worthington, A. M. and R. S. Cole (1897). "Impact with a Liquid Surface, Studied by the Aid of Instantaneous Photography." Philosophical Transactions of the Royal Society of London. Series A, Containing Papers of a Mathematical or Physical Character **189**: 137-148.

Wu, T.-H., L. Gao, Y. Chen, K. Wei and P.-Y. Chiou (2008). "Pulsed laser triggered high speed microfluidic switch." Applied Physics Letters **93**(14): 144102-144102-144103.

Xu, F., K. Seffen and T. Lu (2008). "Temperature-dependent mechanical behaviors of skin tissue." IAENG International Journal of Computer Science **35**(1): 92-101.

Xu, L. (2007). "Liquid drop splashing on smooth, rough, and textured surfaces." Physical Review E **75**(5): 056316-056311-056318.

Xu, L., W. W. Zhang and S. R. Nagel (2005). "Drop Splashing on a Dry Smooth Surface." Physical Review Letters **94**(18): 184505.

Yarin, A. L. (2006). "Drop Impact Dynamics: Splashing, Spreading, Receding, Bouncing..." Annual Review of Fluid Mechanics **38**: 159-192.

Yoon, J., D. Park, T. Son, J. Seo, J. S. Nelson and B. Jung (2010). "A physical method to enhance transdermal delivery of a tissue optical clearing agent: combination of microneedling and sonophoresis." Lasers in surgery and medicine **42**(5): 412-417.

Yoon, S., R. Jepsen, S. James, J. Liu and G. Aguilar (2009). "Are Drop-Impact Phenomena Described by Rayleigh-Taylor or Kelvin-Helmholtz Theory?" Drying Technology **27**(3): 316-321.

Yoon, S., R. Jepsen, M. Nissen and T. Ohern (2007). "Experimental investigation on splashing and nonlinear fingerlike instability of large water drops." Journal of Fluids and Structures **23**(1): 101-115.

Zhang, K., A. Jian, X. Zhang, Y. Wang, Z. Li and H.-y. Tam (2011). "Laser-induced thermal bubbles for microfluidic applications." Lab on a chip **11**(7): 1389-1395.

Zhang, L. V., J. Toole, K. Fezzaa and R. D. Deegan (2011). "Evolution of the ejecta sheet from the impact of a drop with a deep pool." Journal of Fluid Mechanics **690**: 5-15.

Zhou, P., J. Hom, G. Upadhya, K. Goodson and M. Munch (2004). Electro-kinetic microchannel cooling system for desktop computers. Semiconductor Thermal Measurement and Management Symposium, 2004. Twentieth Annual IEEE.

Zysset, B., J. G. Fujimoto and T. F. Deutsch (1989). "Time-resolved measurements of picosecond optical breakdown." Applied Physics B **48**(2): 139-147.